



ISTITUTO NAZIONALE DI FISICA NUCLEARE
Laboratori Nazionali di Frascati

FRASCATI PHYSICS SERIES

Workshop sulla fisica



IL WORKSHOP ITALIANO SULLA FISICA DI ATLAS E CMS

Editors
G. Carlino, P. Paolucci

**IL WORKSHOP ITALIANO
SULLA FISICA DI ATLAS E CMS**

FRASCATI PHYSICS SERIES

Series Editor

Stefano Bianco

Technical Editor

Luigina Invidia

Volume XXXVIII

*Istituto Nazionale di Fisica Nucleare – Laboratori Nazionali di Frascati
Divisione Ricerca – SIS – Ufficio Pubblicazioni
P.O. Box 13, I-00044 Frascati (Roma) Italy
email: sis.publications@lnf.infn.it*

FRASCATI PHYSICS SERIES
IL WORKSHOP ITALIANO SULLA FISICA DI ATLAS E CMS

Copyright © 2005, by INFN Laboratori Nazionali di Frascati
SIS – Ufficio Pubblicazioni

All rights reserved. No part of this publication may be reproduced, stored in a retrieval system or transmitted, in any form or by any means, electronic, mechanical, photocopying, recording or otherwise, without the prior permission of the copyright owner.

ISBN — 88-86409-44-3

Printed in Italy by Poligrafica Laziale, P.le della Stazione 1, 00044 Frascati

FRASCATI PHYSICS SERIES

Volume XXXVIII

**IL WORKSHOP ITALIANO
SULLA FISICA DI ATLAS E CMS**

Editors

Gianpaolo Carlino and Pierluigi Paolucci



**Istituto Nazionale
di Fisica Nucleare**



**Università di Napoli
"Federico II"**



**Regione
Campania**

University "Federico II", in the Monte Sant'Angelo campus
Napoli, October 13 – 15, 2004

Scientific Committee

Riccardo Barbieri	(SNS Pisa, Italy)
Mario Calvetti	(Università di Firenze, Italy)
Rino Castaldi	(INFN Pisa, Italy)
Marcella Diemoz	(INFN Roma I, Italy)
Umberto Dosselli	(INFN Padova, Italy)
Lorenzo Foà	(SNS Pisa, Italy)
Ugo Gasparini	(Università di Padova, Italy)
Fabiola Gianotti	(CERN, Switzerland)
Michelangelo Mangano	(CERN, Switzerland)
Leonardo Merola	(Università di Napoli, Italy)
Sergio Patricelli	(Università di Napoli, Italy)
Giacomo Polesello	(INFN Pavia, Italy)
Francesco Ragusa	(Università di Milano, Italy)
Gigi Rolandi	(CERN, Switzerland)
Crisostomo Sciacca	(Università di Napoli, Italy)
Roberto Tenchini	(INFN Pisa, Italy)
Guido Tonelli	(Università di Pisa, Italy)
Fabio Zwirner	(Università di Padova, Italy)

Organising Committee

Giovanni Bagliesi	(INFN Pisa, Italy)
Gianpaolo Carlino	(INFN Napoli, Italy)
Aleandro Nisati	(INFN Roma, Italy)
Fabrizio Palla	(INFN Pisa, Italy)
Pierluigi Paolucci	(INFN Napoli, Italy)

Secretariat and Support

Studio Congressi Cicala - De Pertis
Via dei Mille 16, 80121 Napoli
Tel. 0039 081 400520 – 0039 081 414119
e-mail: congressi@studiocongressi.it

PREFACE

The series of Italian Workshops on the Physics of ATLAS and CMS was established in 2003 with its first edition in Pisa from June 10th to 11th following the example of the series of Italian Workshops devoted to the LEP physics. The second edition took place in 2004 in Napoli, from October 13th to 15th, in the Conference Hall of the University “Federico II” in the Monte Sant’Angelo campus.

The aim of the meeting was to offer the Italian community of physicists, both experimentalists and theoreticians, the opportunity to discuss about the physics of the LHC project, in particular about the difficulties the ATLAS and CMS experiments have to face during the commissioning of the experimental apparatus and the first year(s) of data-taking when the detectors will not be in their final stage and the LHC machine will not reach its full luminosity.

The structure of the Workshop was based on three days of plenary sessions. The first day was dedicated to talks of general interest in order to review the perspectives on the first years of LHC physics from both the experimentalists and theoreticians points of view, the status of the current high energy experiments at Tevatron hadron collider and the Monte Carlo and Computing challenges for the new era. The talks of the second day were more “experiment-oriented” reporting the trigger strategies and the physics tools for particle reconstruction and identification. The status of physics studies in both the experiments was also discussed with special emphasis on the physics of the Standard Model and Beyond. These talks were attributed, as in the first edition, to two young physicists one from ATLAS and the other from CMS collaborations; they collaborated in the preparation of the talks sharing the presentation and discussion responsibilities. This structure had, as in the past, a very good feedback from the audience and allowed a closer collaboration between the two experiments. The status of theoretical QCD was the main topic of the final day. A round table discussion, chaired by Gigi Rolandi, closed the meeting with a discussion, among many other items, on the perspectives of the High Energy Physics for the young generation of researchers.

The social program included of a visit to the museum of “La Città della Scienza” (<http://www.cittadellascienza.it>) and a dinner to the restaurant “La Sacrestia” where a selection of typical Neapolitan food was offered to our guests.

The formula of the workshop raised enthusiastic reactions in the Italian High Energy Physics community such to convince Lorenzo Foà and his colleagues from Pisa to continue the series. The third edition will be hosted in Bari in October 2005.

The conference has been sponsored by the Istituto Nazionale di Fisica Nucleare (INFN), by the Dipartimento di Fisica of the “Federico II” University of Naples and by Regione Campania.

We wish to express our gratitude to Nicoletta de Pertis’ “Studio Congressi” agency that made an excellent job in the preparation of the workshop and during the meeting itself.

We are also grateful to INFN and Dipartimento di Fisica secretariats for the help they gave us. The preparation of a conference is a very difficult task and we are sure that everything would have been easier if Mirella Russo, in charge of the organization of many conferences for the INFN Napoli, were still among us.

The conference proceedings, as well as the presentations, are available on the web at <http://wifac.na.infn.it>.

September 2005

Gianpaolo Carlino and Pierluigi Paolucci

 CONTENTS

Preface	VII
Introduction		
F. Gianotti and M. Mangano	LHC Physics: the first one-two year(s) ...	3
F. Bedeschi	Physics at Tevatron today	27
S. Frixione	Recent progress in event generators	29
T. Boccali	The transition from Geant3 to Geant4	47
P. Capiluppi	Data challenging	57
L. Rossi	LHC, status of the construction and perspectives	59
Session I – Triggers		
S. Marcellini and F. Pastore	First level triggers for Atlas and CMS experiments at the LHC	63
A. Di Mattia and M. Zanetti	The high level triggers in ATLAS and CMS	73
Session II – Physics Tools		
N. Amapane and M. Biglietti	Muon reconstruction and identification in ATLAS and CMS	91
M. D’Alfonso and F. Sarri	Jet and missing E_T reconstruction and calibration in ATLAS and CMS	103
L. Carminati and P. Meridiani	Electrons and photons reconstruction in ATLAS and CMS	115
S. Cucciarelli and C. Schiavi	Selection of events with Beauty and Tau with the ATLAS and CMS detectors	131
B. Mangano and I. Vivarelli	Status of energy flow algorithms in ATLAS and CMS	141
Session III – Standard Model		
A. Giammarco and G. Gagliardi	The Top quark at LHC	153
M. Vos and P. Ferrari	W and Z physics at the LHC	165
Session IV – Higgs and Beyond		
S. Gennai and E. Meoni	Standard Model and MSSM Higgs bosons searches at LHC	181
M. Chiorboli and D. Costanzo	Search for physics beyond the Standard Model at the Large Hadron Collider	191

Session V – QCD

V. Del Duca	QCD at LHC	209
M. Cacciari	Bottom production from past to future	225

Concluding Remarks

G. Altarelli	Status of the Standard Model and beyond	239
Participants	253

Introduction

LHC PHYSICS: THE FIRST ONE-TWO YEAR(S) ...

Fabiola Gianotti and Michelangelo Mangano
CERN, PH Department, Geneva, Switzerland

Abstract

We discuss the strategy to commission the LHC experiments and understand standard physics at $\sqrt{s} = 14$ TeV before data taking starts and in the early phases of the LHC operation. In particular, we review the various steps needed to understand and calibrate the ATLAS and CMS detectors, from construction quality checks, to beam tests, to cosmic runs, to first collisions. We also review the preparation and tuning of Monte Carlo tools, and present a few examples of physics goals for integrated luminosities of up to a few fb^{-1} .

1 Introduction

When the LHC will start providing data to the experiments, unprecedented opportunities to explore the frontier of high energy physics as we know it today will suddenly become available ¹⁾. It will take some time before the accelerator ramps up in luminosity and the Collaborations debug and understand

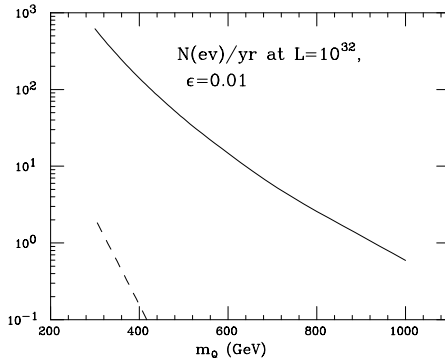


Figure 1: *Production rates for heavy quark pairs, as a function of the quark mass, at the Tevatron (dashed) and at the LHC (solid), during one year of data taking at $10^{32} \text{ cm}^{-2} \text{ s}^{-1}$, and assuming a detection efficiency of 1%.*

luminosity already accumulated by UA1 and UA2. Over 100 nb^{-1} would have been necessary to improve on, say, the top quark search, as the production cross section at the Tevatron was “only” a factor of 10-20 larger than at CERN, in the relevant range of masses.

When the LHC will start, the situation will be much more like that at the time of the $S\bar{p}pS$ turn on. In spite of the multi- fb^{-1} luminosity which we expect CDF and D0 to collect by that time, rates for new particles (heavy quarks, gluinos, new gauge bosons, etc.) with mass beyond the discovery reach of the Tevatron will allow their abundant production already with typical start-up luminosities of 1% of the design, namely $\mathcal{L} \sim 10^{31-32} \text{ cm}^{-2} \text{ s}^{-1}$. This is clearly shown in fig. 1, which plots the production rate for pairs of new heavy quarks (already at the rather low mass of the top quark the rate at the LHC is over 100 times larger than at the Tevatron!). Knowing that cross sections for gluinos are typically one order of magnitude larger than for quarks of equal mass, this figure gives also a clear picture of the immense Supersymmetry (SUSY) discovery potential of early LHC data!

So, we have phase-space, we have large rates for new physics. But should we seriously expect something to show up at the LHC energy scale and at luminosities reachable early on? The Tevatron and LEP’s heritage is a strong confirmation of the Standard Model (SM), and at the same time an apparent paradox⁴⁾, illustrated in the following paragraphs. Electroweak (EW) precision tests and the value of the top mass are consistent with, and require, a rather light Higgs mass: $m_H = 117_{-68}^{+45}$ GeV; EW radiative corrections in the

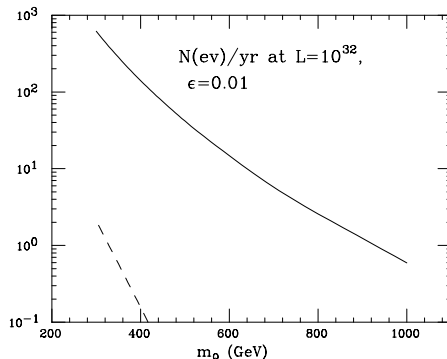


Figure 1: Production rates for heavy quark pairs, as a function of the quark mass, at the Tevatron (dashed) and at the LHC (solid), during one year of data taking at $10^{32} \text{ cm}^{-2} \text{ s}^{-1}$, and assuming a detection efficiency of 1%.

luminosity already accumulated by UA1 and UA2. Over 100 nb^{-1} would have been necessary to improve on, say, the top quark search, as the production cross section at the Tevatron was “only” a factor of 10-20 larger than at CERN, in the relevant range of masses.

When the LHC will start, the situation will be much more like that at the time of the $S\bar{p}pS$ turn on. In spite of the multi-fb $^{-1}$ luminosity which we expect CDF and D0 to collect by that time, rates for new particles (heavy quarks, gluinos, new gauge bosons, etc.) with mass beyond the discovery reach of the Tevatron will allow their abundant production already with typical start-up luminosities of 1% of the design, namely $\mathcal{L} \sim 10^{31-32} \text{ cm}^{-2} \text{ s}^{-1}$. This is clearly shown in fig. 1, which plots the production rate for pairs of new heavy quarks (already at the rather low mass of the top quark the rate at the LHC is over 100 times larger than at the Tevatron!). Knowing that cross sections for gluinos are typically one order of magnitude larger than for quarks of equal mass, this figure gives also a clear picture of the immense Supersymmetry (SUSY) discovery potential of early LHC data!

So, we have phase-space, we have large rates for new physics. But should we seriously expect something to show up at the LHC energy scale and at luminosities reachable early on? The Tevatron and LEP’s heritage is a strong confirmation of the Standard Model (SM), and at the same time an apparent paradox⁴⁾, illustrated in the following paragraphs. Electroweak (EW) precision tests and the value of the top mass are consistent with, and require, a rather light Higgs mass: $m_H = 117_{-68}^{+45} \text{ GeV}$; EW radiative corrections in the

SM, integrated up to a scale Λ , shift the bare value of m_H by:

$$\delta m_H^2 = \frac{6G_F\Lambda^2}{\sqrt{2}\pi^2} \left(m_t^2 - \frac{1}{2}m_W^2 - \frac{1}{4}m_Z^2 - \frac{1}{4}m_H^2 \right) \sim (115 \text{ GeV})^2 \left(\frac{\Lambda}{400 \text{ GeV}} \right)^2. \quad (1)$$

The integration in principle can extend up to very large values of Λ , where new particles may appear, changing eq. (1). As Λ gets significantly larger than 400 GeV, however, the presence of a counterterm (CT) should be assumed, to ensure that the overall value of m_H is consistent with its bounds. This CT can be interpreted as a low-energy manifestation of the physical mechanisms which, at some scale $\bar{\Lambda}$, modify eq. (1). Ensuring that the residual of the cancellation between eq. (1) and the CT is in the 100 GeV range, however, forces a fine tuning which becomes more and more unbelievable as $\bar{\Lambda}$ grows. Assuming that no new physics appears before the GUT scale of 10^{16} GeV would lead to a level of fine tuning of 10^{-28} ! By and large theorists believe that this is unlikely enough to call for the existence of new physics at scales in the range of 1–few TeV, so as to maintain the fine tuning level to within $\mathcal{O}(10^{-3})$. This belief however clashes (and this is where the paradox arises) with the staggering agreement between EW data and the SM. The inclusion of generic new physics, parameterized in terms of low-energy effective couplings between the SM particles, and the analysis of the effects induced on EW observables, set lower limits to the scale $\bar{\Lambda}$ in the range of 5-10 TeV⁵, at the extreme limit of the fine-tuning window. The solution to the paradox could only be obtained with new physics which cancels the large radiative contributions to m_H and, at the same time, manages to leave all other EW parameters and observables unaffected. SUSY provides one such example! The cancellation of large loop effects between SM particles and their SUSY partners modifies eq. (1) and leads to an upper limit on m_H , given in a simplified approximation here:

$$m_H^2 \lesssim m_Z^2 + \frac{3G_F m_t^4}{\sqrt{2}\pi^2} \log \left(\frac{m_{\tilde{t}}^2}{m_t^2} \right) \quad (2)$$

where $m_{\tilde{t}}^2$ is the average squared mass of the two stop states. At the same time, the structure of the theory is such that indeed generic choices of the SUSY parameters, consistent with current experimental limits on new particles, lead to negligible effects in the EW observables. In the minimal realization of SUSY (MSSM), when eq. (2) is improved with 2-loop and non-logarithmic corrections,

the experimental limit on m_H pushes however the scale of SUSY in the multi-TeV domain. Once again this is at the edge of being acceptable as a “natural” solution to the fine-tuning problem, and for many theorists the room left for SUSY is becoming too tight. As a result, new scenarios for EW symmetry breaking, particularly some where the upper limits on the Higgs mass are looser compared to the MSSM, have been proposed (as reviewed in ⁴).

While these alternative scenarios could take much longer to be identified experimentally, the SUSY framework provides a strong and appealing physics case for possible early discovery, and therefore should be given maximum priority in the planning for the first data analyses. SUSY is in fact expected to manifest itself with abundant and striking signals, such as the production of multijets with large missing transverse energy (\cancel{E}_T), multileptons (possibly same-charge), or prompt photons with large \cancel{E}_T . Because of rates, background levels, and nature of the observables, searches for SUSY are expected to be less demanding from the experimental point of view than the quest for the Higgs in the $m_H < 140$ GeV range. In addition, SUSY provides a natural candidate for dark matter, namely the lightest neutralino χ_1^0 , the neutral SUSY partner of the photon and Z . Proving the direct link between dark matter and SUSY would be, perhaps even more than the Higgs discovery, the flagship achievement of the LHC! Last but not least, an early detection of SUSY could immediately provide clear directions to the field of experimental high-energy physics, and allow a robust planning for future facilities.

3 Machine start-up scenario

According to the present LHC schedule (see ⁶) for more details), the machine will be cooled down in Spring 2007, and will then be commissioned for a few months starting with single beams. A first run with colliding beams is expected in the second half of 2007, and will likely be followed by a shut-down of a few months, and then by a seven-month physics run in 2008 at instantaneous luminosities of up to 2×10^{33} cm⁻² s⁻¹.

There are several uncertainties on this plan (in particular because of the recent problems with the production of the cryogenic line) and on how the machine commissioning and performance will actually evolve. Therefore we assume here that the integrated luminosity collected by the end of 2008 will range between a very modest 100 pb⁻¹ per experiment and a very ambitious

10 fb⁻¹ per experiment, and we discuss the LHC physics potential for this range.

4 Initial detectors and initial performance

The first question to address is which detectors will be available at the beginning. Indeed, because of missing resources, and in some cases of construction delays, several components of ATLAS and CMS will not be complete at the beginning of data taking. ATLAS will start with two pixel layers (instead of three) and without Transition Radiation Tracker in the region $2 < |\eta| < 2.4$. CMS will start without muon trigger chambers (RPC) in the region $1.6 < |\eta| < 2.1$ and without the fourth layer of the end-cap muon chambers. Furthermore, the CMS end-cap electromagnetic calorimeter and pixel detector will be installed during the shut-down period after the 2007 run. In addition, in both experiments part of the high-level trigger and data acquisition processors will be deferred, with the consequence that the output rate of the level-1 trigger will be limited to 50 kHz (instead of 100 kHz) in CMS and to 35 kHz (instead of 75 kHz) in ATLAS.

The impact of this staging on physics will be significant but not dramatic. The main loss is a descoped B -physics programme because, due to the reduced level-1 bandwidth, the thresholds of the single-muon triggers will have to be raised from a few GeV (as originally chosen to address B -physics studies) to $p_T=14-20$ GeV.

The second question concerns the detector performance to be expected on “day 1”, i.e. at the moment when data taking starts. Some predictions, based on construction quality checks, on the known precision of the hardware calibration and alignment systems, on test-beam measurements and on simulation studies, are given in tab. 1 for illustration. The initial uniformity of the electromagnetic calorimeters (ECAL) should be at the level of 1% for the ATLAS liquid-argon calorimeter and 4% for the CMS crystals, where the difference comes from the different techniques and from the limited time available for test-beam measurements in CMS. Prior to data taking, the jet energy scale may be established to about 10% from a combination of test-beam measurements and simulation studies. The tracker alignment in the transverse plane is expected to be known at the level of 20 μm in the best case from surveys, from the hardware alignment systems, and possibly from some studies with cosmic

Table 1: *Examples of expected detector performance for ATLAS and CMS at the time of the LHC start-up, and of physics samples which will be used to improve this performance.*

	expected performance on “day 1”	data samples (examples) to improve the performance
ECAL uniformity	$\sim 1\%$ ($\sim 4\%$) in ATLAS (CMS)	minimum-bias, $Z \rightarrow ee$
electron energy scale	1-2%	$Z \rightarrow ee$
HCAL uniformity	2-3%	single pions, QCD jets
jet energy scale	$\leq 10\%$	$Z(\rightarrow \ell\ell)+\text{jet}$, $W \rightarrow jj$ in $t\bar{t}$ events
tracker alignment	20-200 μm in $R\phi$	generic tracks, isolated μ , $Z \rightarrow \mu\mu$

muons and beam halo events.

This performance should be significantly improved as soon as the first data will be available (see last column in tab. 1) and, thanks to the huge event rates expected at the LHC, the ultimate statistical precision should be achieved after a few days/weeks of data taking. Then the painful battle with the systematic uncertainties will start. This is illustrated in fig. 2 which shows that, by measuring the energy flow in about 18 million minimum-bias events (which can be collected in principle in a few hours of data taking), the non-uniformity of the CMS ECAL should be reduced from the initial 4% to about 1.5% in the barrel region. Therefore the systematic limit coming from the non-uniformity of the upstream tracker material will be hit very quickly.

5 Strategy to achieve the goal detector performance

Are the performance expectations presented in the previous section realistic? This is discussed below with the help of a concrete example.

The ATLAS and CMS detectors have been subject to stringent requirements and detailed quality controls at the various steps of the construction phase. Extensive test-beam measurements have been performed with prototype and final detector modules, which have also allowed the validation of the simulation packages (e.g. GEANT4) used for instance to extrapolate the detector response from the test-beam to the collider environment. Such detailed

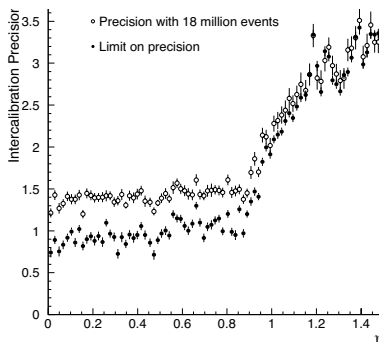


Figure 2: *Inter-calibration precision of the CMS electromagnetic calorimeter achievable with 18 million minimum-bias events ⁷⁾, as a function of rapidity (open symbols). The closed symbols show the limit coming from the non-uniformity of the upstream material.*

checks and tests represent an unprecedented culture in our field. In addition, *in situ* commissioning and calibrations after installation in the pits will be needed to understand the experiments as a whole, to account for the presence of e.g. upstream material and magnetic field, to cure long-range effects, etc. These calibrations will be based on cosmic muons, beam-halo muons and beam-gas events during the pre-collision phase (i.e. in the first half of 2007, during the machine cool-down and single-beam commissioning). Then, as soon as first collisions will be available, well-known physics samples (e.g. $Z \rightarrow \ell\ell$ events, see tab. 1) will be used.

As an example of the above procedure, the case of the ATLAS lead-liquid argon electromagnetic calorimeter ⁸⁾, for which the construction phase is completed, is discussed below.

One crucial performance issue for the LHC electromagnetic calorimeters is to provide a mass resolution of about 1% in the hundred GeV range, needed to observe a possible $H \rightarrow \gamma\gamma$ signal as a narrow peak on top of the huge $\gamma\gamma$ irreducible background. This requires a response uniformity, that is a total constant term of the energy resolution, of $\leq 0.7\%$ over the full calorimeter coverage ($|\eta| < 2.5$). Achieving this goal is challenging, especially at the beginning, but is necessary for a fast discovery, and can hopefully be accomplished in four steps:

- Construction quality. Test-beam measurements performed with proto-

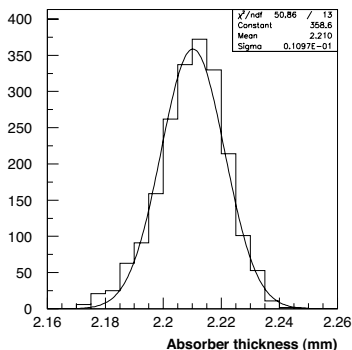


Figure 3: Distribution of the thickness of the 2048 absorber plates (3 m long and 0.5 m wide) of the ATLAS barrel ECAL, as obtained from ultrasound measurements. The mean value of the distribution is 2.2 mm and the r.m.s. is 11 μm .

types of the ATLAS ECAL in the early '90s showed that a 1% excess in the thickness of the lead plates produces a drop of the calorimeter response by 0.7%. Therefore, in order to keep the maximum response non-uniformity coming from the detector mechanics alone below 0.3%, the thickness of the lead plates must be uniform to about 0.5%, i.e. $\sim 10 \mu\text{m}$. This goal has been achieved, as shown in fig. 3.

- Test-beam measurements. About 15% of the final calorimeter modules have been exposed to electron beams, in order to verify the construction uniformity and to prepare correction factors to the detector response. Figure 4 shows the results of a position scan of one module performed with high-energy test-beam electrons. For all tested modules, the response non-uniformity was found to be about 1.5% before correction, i.e. at the exit of the construction chain, and better than 0.7% after calibration with test-beam data.
- Pre-collision phase. Before data taking starts, the calorimeter calibration can be checked *in situ* with physics-like signals by using cosmic muons. Table 2 shows the expected rates of cosmics in ATLAS⁹⁾ as obtained from a full simulation of the detector inside the underground cavern (including the overburden, the access shafts and the surface buildings). These results have also been validated by direct measurements of the cosmics flux in the pit made with a scintillator telescope. It can be seen that rates between

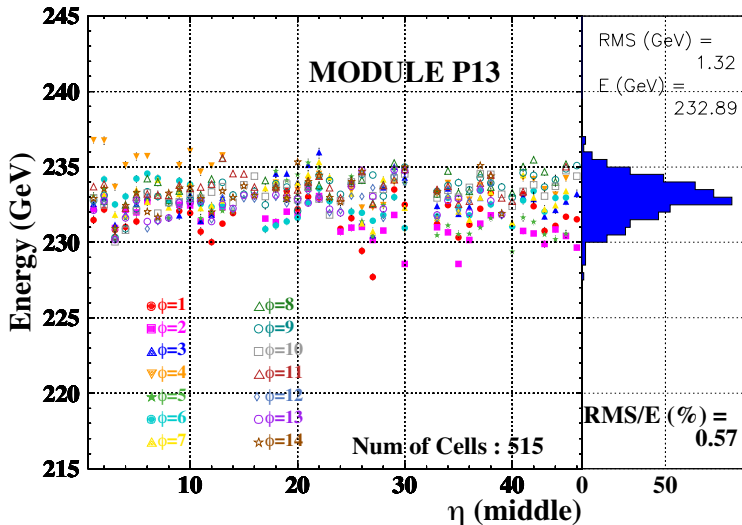


Figure 4: Energy response of one module (of size $\Delta\eta \times \Delta\phi = 1.4 \times 0.4$) of the ATLAS barrel ECAL, as a function of rapidity, as measured from a scan with test-beam electrons. The various symbols indicate different ϕ rows.

0.5 Hz and 30 Hz are expected, depending on the requirements on the muon trajectory. Therefore, in about three months of cosmic runs in 2007 during the machine cool-down and commissioning, a few million events should be collected, a data sample large enough to catalog and fix several problems, gain operational experience, check the relative timing and position of the various sub-detectors, etc., hopefully in a more relaxed environment than during the collision phase.

In particular, for what concerns the electromagnetic calorimeter, the signal-to-noise ratio for muons is large enough ($S/N \sim 7$ from test-beam measurements) that cosmic muons can be used to check the calibration uniformity of the barrel calorimeter as a function of rapidity. The calorimeter is equipped with an electronics calibration system delivering pulses uniform to 0.25%. However, the calibration signals and the physics signals do not have exactly the same shape, and the difference depends on the rapidity of a given calorimeter cell. This induces a non-uniformity

Table 2: *Expected rates of cosmic muons in ATLAS for various requirements on the muon trajectory, as obtained from a full simulation of the detector inside the pit.*

topology	rate (Hz)	comments
through-going muons	~ 25	muons giving hits on top and bottom RPC's and in inner detector
close to interaction vertex	~ 0.5	muons passing within $ z < 60$ cm and $R < 20$ cm from the interaction centre
useful for ECAL calibration	~ 0.5	muons with $ z < 20$ cm, $E_{\text{cell}} > 100$ MeV

of the ECAL response to incident particles as a function of η . Test-beam studies show that the expected sample of cosmic muons is large enough to allow measurements of these effects down to the 0.5% level.

- **First collisions.** As soon as first collider data will be available, $Z \rightarrow ee$ events, which are produced at the rate of ~ 1 Hz at a luminosity of $10^{33} \text{ cm}^{-2} \text{ s}^{-1}$, will be used to correct long-range response non-uniformities from module to module, possible temperature effects, the impact of the upstream material, etc. Full simulation studies indicate that, since the calorimeter is already quite uniform on “day 1” by construction and thanks to the previous steps, about 10^5 $Z \rightarrow ee$ events should be sufficient to achieve the goal overall constant term of 0.7%. In addition, this $Z \rightarrow ee$ sample should fix the absolute energy scale to about 0.5%. Therefore, after a few weeks of data taking the ATLAS ECAL should in principle be fairly well calibrated.

As an academic exercise, one could consider a very pessimistic (actually unrealistic...) scenario. That is, ignoring the results and expectations discussed above, one could assume that no corrections (neither based on test-beam data, nor using $Z \rightarrow ee$ events) will be applied. In this case, the intrinsic calorimeter constant term would be given by the uncorrected non-uniformity from detector construction (measured to be $\sim 1.5\%$, as mentioned above), to which another $\sim 1.5\%$ from uncorrected material effects has to be added. This would give a

total constant term of the energy resolution of about 2% instead of 0.7%. As a consequence, the significance of a $H \rightarrow \gamma\gamma$ signal would be reduced by about 30%, and a factor 1.7 more integrated luminosity would be needed to achieve the same sensitivity.

6 How well will LHC physics and Monte Carlos be known before data taking starts?

While we cannot anticipate which new physics is waiting for us at the LHC, we do know that there is plenty of SM processes to be observed. In many cases, these processes offer themselves the potential for important measurements (e.g. improved determinations of the W and top-quark masses, parton densities). More in general, they will provide dangerous backgrounds to most signals of new physics. A solid physics programme at the LHC will therefore require a robust understanding of SM processes, and of QCD in particular. Significant improvements have taken place in the past few years, as reviewed in ¹⁰⁾ and shortly summarized here.

By far the cleanest process in pp collisions, theoretically as well as experimentally, is the production of W and Z bosons. In addition to the full NNLO predictions for the total cross sections, achieved long ago ¹¹⁾, NNLO calculations for the experimentally more interesting rapidity distributions have recently been obtained ¹²⁾, reducing the intrinsic theoretical uncertainty for Drell-Yan cross sections to the level of 1-2%. At this level of accuracy, EW effects start playing a role, as recently evaluated in ¹³⁾, and a precise knowledge of the parton densities (PDF) becomes essential. Progress in this field, in addition to the availability of much more accurate data from HERA ¹⁴⁾, has been driven by the development of formalisms which allow a proper account of systematic uncertainties ¹⁵⁾.

The production of $t\bar{t}$ pairs, which at the Tevatron represents a rather exotic signature, will become at the LHC a dangerous background, with an inclusive rate of the order of 1 Hz. The cross section is known from theory with an accuracy of about 5% ¹⁶⁾, enough to allow an indirect estimate of the top mass with an accuracy of ± 2 GeV (excluding experimental uncertainties). The ability to precisely model the structure of the final states has improved recently with the development of the MC@NLO code, where the complete NLO parton-level matrix elements are consistently incorporated in a full shower Monte Carlo

(MC) ¹⁷⁾. Also the description of bottom quark production appears now to be under better theoretical control, after improvements in the inputs of the calculations (fragmentation functions and resummation of large logarithms) have led to excellent agreement ¹⁸⁾ with the most recent results from CDF ¹⁹⁾.

Complex multijet topologies can be described today more reliably, thanks to recent advances in the calculation of multiparton final states ²⁰⁾, their inclusion in parton level codes ^{21, 22)}, and the development of techniques to deal with the problem of properly merging with shower MCs ²³⁾. In addition, the well known and tested shower MC codes which dominated the LEP and Tevatron era are being updated, with inclusion of better algorithms for the development of the shower or for the description of the underlying event ²⁴⁾.

Validation of these new tools using Tevatron data will be possible before the LHC starts, but only the very large statistics and the huge dynamic range of the LHC will allow complete studies and proper tunings.

7 Early physics goals and measurements

Table 3 shows the data samples expected to be recorded by ATLAS and CMS for some example physics processes and for an integrated luminosity of 10 fb^{-1} . The trigger selection efficiency has been included. Already over the first year (even days in some cases) of operation, huge event samples should be available from known SM processes, which will allow ATLAS and CMS to commission the detectors, the software and the physics itself, and also from several new physics scenarios. We stress that this will be the case even if the integrated luminosity collected during the first year were to be a factor of hundred smaller, i.e. $\sim 100 \text{ pb}^{-1}$.

In more detail, the following goals can be addressed with such data samples¹:

- Commission and calibrate the detectors *in situ*, as already mentioned. Understanding the trigger performance in as an unbiased way as possible, with a combination of minimum-bias events, QCD jets collected with

¹It should be noted that the total amount of data recorded by each experiment in one year of operation corresponds to about 1 Petabyte, which represents an unprecedented challenge also for the LHC computing and offline software.

Table 3: For some physics processes, the numbers of events expected to be recorded by ATLAS and CMS for an integrated luminosity of 10 fb^{-1} per experiment.

channel	recorded events per experiment for 10 fb^{-1}
$W \rightarrow \mu\nu$	7×10^7
$Z \rightarrow \mu\mu$	1.1×10^7
$t\bar{t} \rightarrow \mu + X$	0.08×10^7
QCD jets $p_T > 150 \text{ GeV}$	$\sim 10^7$ (assuming 10% of trigger bandwidth)
minimum bias	$\sim 10^7$ (assuming 10% of trigger bandwidth)
$\tilde{g}\tilde{g}, m(\tilde{g}) \sim 1 \text{ TeV}$	$10^3 - 10^4$

various thresholds, single and dilepton samples, is going to be one of the most challenging and crucial steps at the beginning. $Z \rightarrow \ell\ell$ is a gold-plated process for a large number of studies, e.g. to set the absolute electron and muon scales in the ECAL and tracking detectors respectively, whereas $t\bar{t}$ events can be used for instance to establish the absolute jet scale and to understand the b -tagging performance.

- Perform extensive measurements of the main SM physics processes, e.g. cross sections and event features for minimum-bias, QCD dijet, $W, Z, t\bar{t}$ production, etc. These measurements will be compared to the predictions of the MC simulations, which will already be quite constrained from theory and from studies at the Tevatron and HERA energies. Typical initial precisions may be 10-20% for cross section measurements, and 5-7 GeV on the top-quark mass, and will likely be limited by systematic uncertainties after just a few weeks of data taking.
- Prepare the road to discoveries by measuring the backgrounds to possible new physics channels. Processes like W/Z +jets, QCD multijet production and $t\bar{t}$ are omnipresent backgrounds for a large number of searches and need to be understood in all details. In addition, dedicated control samples can be used to measure specific backgrounds. For instance, $t\bar{t}jj$ production, where the jets j are tagged as light-quark jets, can be used to gauge the irreducible $t\bar{t}b\bar{b}$ background to the $t\bar{t}H \rightarrow t\bar{t}b\bar{b}$ channel.

As an example of initial measurement with limited detector performance, fig. 5 shows the reconstructed top-quark signal in the gold-plated $t\bar{t} \rightarrow bj\bar{j} b\ell\nu$

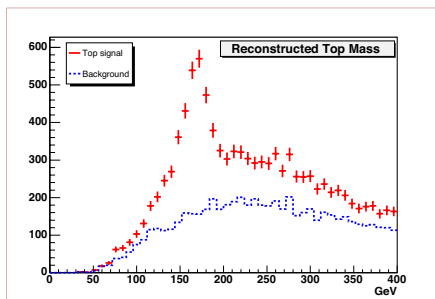


Figure 5: *Three-jet invariant mass distribution for events selected as described in the text, as obtained from a simulation of the ATLAS detector. The dots with error bars show the expected signal from $t\bar{t}$ events plus the background, the dashed line shows the $W+4$ -jet background alone (ALPGEN Monte Carlo ²²). The number of events corresponds to an integrated luminosity of 150 pb^{-1} .*

semileptonic channel, as obtained from a simulation of the ATLAS detector. The event sample corresponds to an integrated luminosity of 150 pb^{-1} , which can be collected in less than one week of data taking at $L = 10^{33} \text{ cm}^{-2} \text{ s}^{-1}$. A very simple analysis was used to select these events, requiring an isolated electron or muon with $p_T > 20 \text{ GeV}$ and four and only four jets with $p_T > 40 \text{ GeV}$. The invariant mass of the three jets with the highest p_T was then plotted. No kinematic fit was made, and no b -tagging of some of the jets was required, assuming conservatively that the b -tagging performance would not have been well understood yet. Figure 5 shows that, even under these over-pessimistic conditions, a clear top signal should be observed above the background after a few weeks of data taking (30 pb^{-1} would be sufficient). In turn, this signal can be used for an early validation of the detector performance. For instance, if the top mass is wrong by several GeV, this would indicate a problem with the jet energy scale. Furthermore, top events are an excellent sample to understand the b -tagging performance of ATLAS and CMS. It should be noted that, unlike at the LHC, at the Tevatron today the statistics of $t\bar{t}$ events is not sufficient to use these samples for detector calibration purposes.

8 Early discoveries

Only after the three steps outlined in section 7 will have been fully addressed can the LHC experiments hope to extract a convincing discovery signal from their data. Three examples of new physics are discussed briefly below, ranked

by increasing difficulty for discovery in the first year(s) of operation: an easy case, namely a possible $Z' \rightarrow e^+e^-$ signal, an intermediate case, SUSY, and a difficult case, a light Standard Model Higgs boson.

8.1 $Z' \rightarrow e^+e^-$

A particle of mass 1-2 TeV decaying into e^+e^- pairs, such as a possible new gauge boson Z' , is probably the easiest object to discover at the LHC, for three main reasons. First, if the branching ratio into leptons is at least at the percent level as for the Z boson, the expected number of events after all experimental cuts is relatively large, e.g. about ten for an integrated luminosity as low as 300 pb^{-1} and a particle mass of 1.5 TeV. Second, the dominant background, dilepton Drell-Yan production, is small in the TeV region, and even if it were to be a factor of two-three larger than expected today (which is unlikely for such a theoretically well-known process), it would still be negligible compared to the signal. Finally, the signal will be indisputable, since it will appear as a resonant peak on top of a smooth background, and not just as an overall excess in the total number of events. These expectations are not based on ultimate detector performance, since they hold also if the calorimeter response is understood to a conservative level of a few percent.

8.2 Supersymmetry

Extracting a convincing signal of SUSY in the early phases of the LHC operation is not as straightforward as for the previous case, since good calibration of the detectors and detailed understanding of the numerous backgrounds are required. As soon as these two pre-requisites are satisfied, observation of a SUSY signal should be relatively easy and fast. This is because of the huge production cross sections, and hence event rates, even for squark and gluino masses as large as $\sim 1 \text{ TeV}$ (see tab. 3), and the clear signature of such events in most scenarios. Therefore, by looking for final states containing several high- p_T jets and large \cancel{E}_T , which is the most powerful and model-independent signature if R-parity is conserved, the LHC experiments should be able to discover squarks and gluinos up to masses of $\sim 1.5 \text{ TeV}$ in only one month of data taking at $L = 10^{33} \text{ cm}^{-2} \text{ s}^{-1}$, as shown in the left panel of fig. 6.

Although detailed measurements of the SUSY particle masses will likely take several years, it should nevertheless be possible to obtain a first determi-

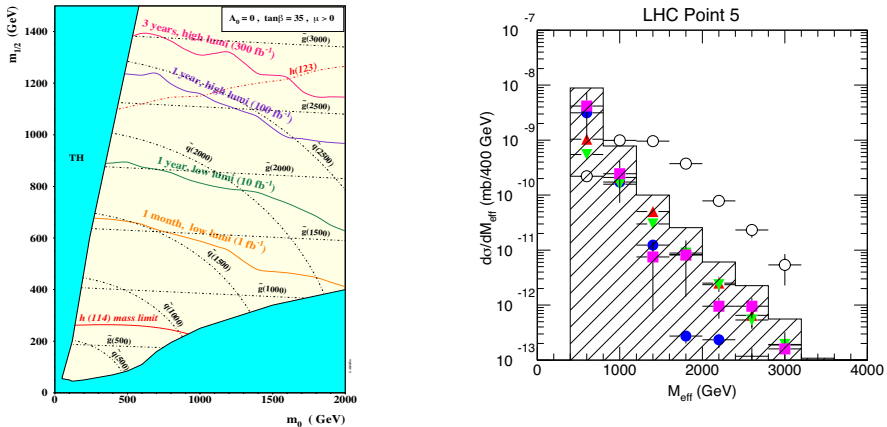


Figure 6: *Left:* The CMS discovery potential²⁵⁾ for squarks and gluinos in $mSUGRA$ models, parametrized in terms of the universal scalar mass m_0 and universal gaugino mass $m_{1/2}$, as a function of integrated luminosity. Squark and gluino mass isolines are shown as dot-dashed lines (masses are given in GeV). *Right:* The expected distribution of the effective mass (see text) for the SUSY signal at “Point 5”²⁶⁾ of the $mSUGRA$ parameter space (open circles), as obtained from a simulation of the ATLAS detector. The histogram shows the total SM background, which includes $t\bar{t}$ (solid circles), W +jets (triangles), Z +jets (downward triangles), and QCD jets (squares).

nation of the SUSY mass scale quickly after discovery. This is illustrated in the right panel of fig. 6, which shows the striking SUSY signal on top of the SM background, expected at a point in the minimal SUGRA parameter space where squark and gluino masses are about 700 GeV. The plotted variable, called “effective mass” (M_{eff}), is defined as the scalar sum of the event \cancel{E}_T and of the transverse energies of the four highest p_T jets, and thus reflects the “heaviness” of the particles produced in the final state. More precisely, the position of the peak of the M_{eff} signal distribution (see fig. 6) moves to larger/smaller values with increasing/decreasing squark and gluino masses. Therefore a measurement of the signal peak position should provide a first fast determination of the mass scale of SUSY. The expected precision is about 20% for an integrated luminosity of 10 fb^{-1} , at least in minimal models like $mSUGRA$.

A crucial detector performance issue for an early SUSY discovery is a reliable reconstruction of the event \cancel{E}_T , which is *a priori* prone to contamination from several instrumental effects (calorimeter non-linearities, cracks in the detector, etc.). Final states with non-genuine \cancel{E}_T can be rejected by requiring the event primary vertex to be located close to the interaction centre (which

also helps to suppress the background from cosmic and beam-halo muons), no jets pointing to detector cracks, and that the missing p_T vector is not aligned with any jet. The calorimeter response linearity can be understood to a large extent by using “calibration” samples like $Z(\rightarrow \ell\ell)+\text{jet}$ events (with $\ell = e, \mu$), where the lepton pair and the jet are back-to-back in the transverse plane, so that the well-measured p_T of the lepton pair can be used to calibrate the jet p_T scale over a large dynamic range.

Concerning the physics backgrounds (e.g. $Z \rightarrow \nu\bar{\nu}+\text{jets}$, $t\bar{t}$ production, QCD multijet events), most of them can be measured by using control samples. For instance, $Z \rightarrow \ell\ell+\text{jet}$ production provides a normalization of the $Z \rightarrow \nu\bar{\nu}+\text{jets}$ background. More difficult to handle is the residual background from QCD multijet events with fake \cancel{E}_T produced by the above-mentioned instrumental effects. The technique used at the Tevatron consists of normalizing the Monte Carlo simulation to the data in the (signal-free) region at low \cancel{E}_T , and then use the Monte Carlo to predict the background in the (potentially signal-rich) region at large \cancel{E}_T .

A crucial element in the ability to calibrate these backgrounds using the theoretical MC predictions to extrapolate from the signal-free to the signal-rich regions is the reliability of the MC themselves. As mentioned earlier, their level of accuracy and their capability to describe complex final states, such as the multijet topology typical of new phenomena like SUSY, have improved significantly over the past few years¹⁰⁾. In some cases, the predictions obtained with the new tools are very different from those derived in the past. In particular, the description of multijet final states, which until the recent past could only be achieved in a rather approximate way with shower MCs, is now performed starting from exact matrix-element calculations of the multiparton emission amplitudes. This typically results in higher production rates, increasing therefore the difficulty of extracting in a robust way the signals of new physics from the QCD backgrounds. An example of this is shown in fig. 7: the diamond plot represents the matrix-element prediction²²⁾ of the $Z(\rightarrow \nu\bar{\nu})+4\text{jet}$ background to a possible multijet+ \cancel{E}_T SUSY signal, compared to estimates (the grey histogram, which also includes the contribution of \cancel{E}_T -mismeasurement in pure multijet events) obtained in the past with standard shower MC simulations. Not only is the rate larger than previously expected, but the shape of the distribution is different, and much closer to that of the signal itself. A calibration

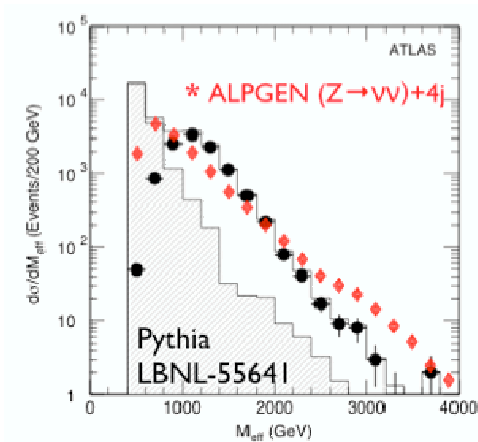


Figure 7: M_{eff} distributions for a potential SUSY signal (histogram), separated into signal (dark points) and the background prediction from shower MC (shaded histogram), compared to the $Z(\rightarrow \nu\bar{\nu})+4\text{jet}$ background evaluated with exact matrix elements (grey diamonds).

of the absolute rate using $(Z \rightarrow \ell^+\ell^-)+4\text{jet}$ data is still possible where the statistics allow (up to $M_{\text{eff}} \sim 1-2$ TeV), but a validation of the MCs is clearly required to ensure a robust extrapolation to the highest values of M_{eff} .

8.3 Standard Model Higgs boson

The possibility of discovering a SM Higgs boson at the LHC during the first year(s) of operation depends very much on the Higgs mass, as shown in fig. 8. If the Higgs mass is larger than 180 GeV, discovery may be relatively easy thanks to the gold-plated $H \rightarrow 4\ell$ channel, which is essentially background-free. The main requirement in this case is an integrated luminosity of at least $5-10 \text{ fb}^{-1}$, since the signal has a cross section of only a few fb.

The low-mass region close to the LEP limit is much more difficult. The expected sensitivity for a Higgs mass of 115 GeV and for the first good (i.e. collected with well-calibrated detectors) 10 fb^{-1} is summarized in tab. 4. The total significance of about 4σ per experiment ($4_{-1.3}^{+2.2} \sigma$ including the expected systematic uncertainties) is more or less equally shared among three channels: $H \rightarrow \gamma\gamma$, $t\bar{t}H$ production with $H \rightarrow b\bar{b}$, and Higgs production in vector-boson

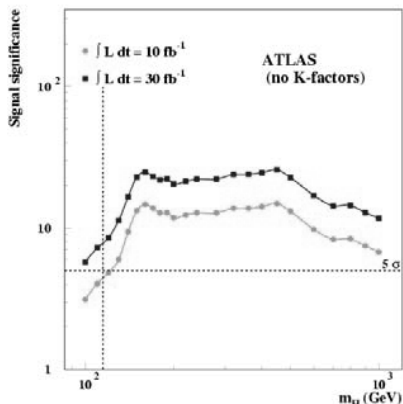


Figure 8: The expected signal significance for a SM Higgs boson in ATLAS as a function of mass, for integrated luminosities of 10 fb^{-1} (dots) and 30 fb^{-1} (squares). The vertical line shows the lower limit from searches at LEP. The horizontal line indicates the minimum significance (5σ) needed for discovery.

Table 4: For a Higgs boson mass of 115 GeV and an integrated luminosity of 10 fb^{-1} , the expected numbers of signal (S) and background (B) events after all cuts and signal significances (S/\sqrt{B}) in ATLAS for the three dominant channels.

	$H \rightarrow \gamma\gamma$	$t\bar{t}H \rightarrow t\bar{t}b\bar{b}$	$qqH \rightarrow qq\tau\tau \rightarrow \ell + X$
S	130	15	~ 10
B	4300	45	~ 10
S/\sqrt{B}	2.0	2.2	~ 2.7

fusion followed by $H \rightarrow \tau\tau$. A conservative approach has been adopted in deriving these results. For instance, very simple cut-based analyses have been used, and higher-order corrections to the Higgs production cross sections (the so-called K-factors), which are expected to increase for example the $gg \rightarrow H \rightarrow \gamma\gamma$ rate by a factor of about two compared to leading order, have not been included. Nevertheless, it will not be easy to extract a convincing signal with only 10 fb^{-1} , because the significances of the individual channels are small, and because an excellent knowledge of the backgrounds and close-to-optimal detector performances are required, as discussed below. Therefore, the contribution of both experiments, and the observation of possibly all three channels, will be crucial for an early discovery.

The channels listed in tab. 4 are complementary. They are characterized

by different Higgs production mechanisms and decay modes, and therefore by different backgrounds and different detector requirements. Good uniformity of the electromagnetic calorimeters is crucial for the $H \rightarrow \gamma\gamma$ channel, as already mentioned. Powerful b -tagging is the key performance issue for the $t\bar{t}H$ channel, since there are four b -jets in the final state which all need to be tagged in order to reduce the background. Efficient and precise jet reconstruction over ten rapidity units ($|\eta| < 5$) is needed for the $H \rightarrow \tau\tau$ channel, since tagging the two forward jets accompanying the Higgs boson and vetoing additional jet activity in the central region of the detector are necessary tools to defeat the background. Finally, all three channels demand relatively low trigger thresholds (at the level of 20-30 GeV on the lepton or photon p_T), and a control of the backgrounds to a few percent. These requirements are especially challenging during the first year(s) of operation.

9 Conclusions

The LHC offers the potential for very interesting physics and major discoveries right from the beginning. We note that for some standard physics processes, a single day of data taking at $L = 10^{33} \text{ cm}^{-2} \text{ s}^{-1}$ corresponds, in terms of event statistics, to ten years of operation at previous machines. SUSY may be discovered quickly, a light Higgs boson will be much more difficult to observe, unexpected scenarios and surprises may also be round the corner at an unprecedented collider exploring a completely new territory.

The machine luminosity performance will be the crucial issue at the beginning. Hopefully, an instantaneous luminosity of up to $L \sim 10^{33} \text{ cm}^{-2} \text{ s}^{-1}$, and an integrated luminosity of a few fb^{-1} per experiment, can be achieved by the end of 2008, as estimated by the accelerator team.

Concerning the experiments, a lot of emphasis has been given to quality checks in the various phases of the construction and to tests with beams. The results indicate that the detectors “as built” should give a good starting-point performance already on “day 1”. However, a lot of data and time will be needed to commission the detectors, the triggers and the software *in situ*, to reach the performance required to address serious physics studies, to understand standard physics and the Monte Carlo tools at $\sqrt{s}=14 \text{ TeV}$, and to measure the backgrounds to possible new physics processes.

The next challenge is therefore an efficient and timely detector commis-

sioning, from cosmic runs to first collisions, where the experiments try to learn and fix as much as possible as early as possible. In parallel, efforts to improve and tune the Monte Carlo generators, based on theoretical developments as well as on comparisons with data from past and present experiments, should be pursued with vigor. Indeed, both activities will be crucial to reach quickly the discovery phase, and to extract convincing signals of new physics in the first year(s) of operation.

References

1. M. L. Mangano, Comments Nucl. Part. Phys. **2**, A153 (2002).
2. G. Arnison *et al.* [UA1], Phys. Lett. B **122** (1983) 103; M. Banner *et al.* [UA2], Phys. Lett. B **122** (1983) 476.
3. M. Banner *et al.* [UA2], Phys. Lett. B **118** (1982) 203; G. Arnison *et al.* [UA1], Phys. Lett. B **123** (1983) 115.
4. R. Barbieri, arXiv:hep-ph/0410223.
5. R. Barbieri and A. Strumia, Phys. Lett. B **462** (1999) 144; R. Barbieri, A. Pomarol, R. Rattazzi and A. Strumia, Nucl. Phys. B **703** (2004) 127.
6. L. Rossi, these Proceedings.
7. D. Futyan, CMS Note CMS CR 2003/005.
8. ATLAS Collaboration, Liquid Argon Calorimeter Technical Design Report, CERN/LHCC/96-41.
9. M. Boonekamp *et al.*, ATLAS Note ATL-GEN-2004-001.
10. M. L. Mangano, eConf **C030614** (2003) 015.
11. R. Hamberg, W. L. van Neerven and T. Matsuura, Nucl. Phys. B **359** (1991) 343 [Erratum-ibid. B **644** (2002) 403].
12. C. Anastasiou, L. Dixon, K. Melnikov and F. Petriello, arXiv:hep-ph/0312266.

13. U. Baur, S. Keller and D. Wackerroth, *Phys. Rev. D* **59** (1999) 013002; U. Baur *et al.*, *Phys. Rev. D* **65** (2002) 033007; S. Dittmaier and M. Kramer, *Phys. Rev. D* **65** (2002) 073007.
14. M. Klein, plenary talk at the 2004 ICHEP, Beijing.
15. A. D. Martin, R. G. Roberts, W. J. Stirling and R. S. Thorne, *Eur. Phys. J. C* **28** (2003) 455; J. Pumplin, D. R. Stump, J. Huston, H. L. Lai, P. Nadolsky and W. K. Tung, *JHEP* **0207** (2002) 012; M. Botje, *Eur. Phys. J. C* **14** (2000) 285; S. I. Alekhin, hep-ph/0211096.
16. R. Bonciani, S. Catani, M. L. Mangano and P. Nason, *Nucl. Phys. B* **529** (1998) 424; M. Cacciari *et al.*, hep-ph/0303085.
17. S. Frixione and B. R. Webber, *JHEP* **0206** (2002) 029; S. Frixione, P. Nason and B. R. Webber, *JHEP* **0308** (2003) 007.
18. M. Cacciari, S. Frixione, M. L. Mangano, P. Nason and G. Ridolfi, *JHEP* **0407** (2004) 033.
19. D. Acosta *et al.* [CDF Collaboration], *Phys. Rev. D* **71** (2005) 032001.
20. F. Caravaglios and M. Moretti, *Phys. Lett. B* **358** (1995) 332; F. Caravaglios, M. L. Mangano, M. Moretti and R. Pittau, *Nucl. Phys. B* **539** (1999) 215; P. Draggiotis, R. H. Kleiss and C. G. Papadopoulos, *Phys. Lett. B* **439** (1998) 157; hep-ph/0202201.
21. T. Stelzer and W. F. Long, *Comput. Phys. Commun.* **81** (1994) 357; F. Maltoni and T. Stelzer, *JHEP* **0302** (2003) 027; A. Pukhov *et al.*, hep-ph/9908288; M. L. Mangano, M. Moretti and R. Pittau, *Nucl. Phys. B* **632** (2002) 343; F. Krauss, R. Kuhn and G. Soff, *JHEP* **0202** (2002) 044; S. Tsuno *et al.*, hep-ph/0204222.
22. M. L. Mangano *et al.*, *JHEP* **0307** (2003) 001.
23. S. Catani, F. Krauss, R. Kuhn and B. R. Webber, *JHEP* **0111** (2001) 063; L. Lonnblad, *JHEP* **0205** (2002) 046; F. Krauss, *JHEP* **0208** (2002) 015; S. Mrenna and P. Richardson, *JHEP* **0405** (2004) 040; A. Schaliche and F. Krauss, arXiv:hep-ph/0503281.

24. L. Lonnblad, *Comput. Phys. Commun.* **71** (1992) 15; S. Gieseke *et al.*, hep-ph/0311208; hep-ph/0310083; T. Sjostrand, L. Lonnblad, S. Mrenna and P. Skands, hep-ph/0308153; T. Gleisberg *et al.*, hep-ph/0311263.
25. CMS Collaboration, Technical Proposal, CERN/LHCC/94-38.
26. ATLAS Collaboration, Detector and Physics Performance Technical Design Report, CERN/LHCC/99-15.

Frascati Physics Series Vol. XXXVIII (2005), pp. 27

II WORKSHOP ITALIANO SULLA FISICA DI ATLAS E CMS – Napoli, October 13 - 15, 2004

PHYSICS AT TEVATRON TODAY

Franco Bedeschi
INFN Sezione di Pisa, Italy

Written contribution not received

RECENT PROGRESS IN EVENT GENERATORS

Stefano Frixione

INFN, Sezione di Genova, Via Dodecaneso 33, 16146 Genova, Italy

Abstract

Standard parton shower Monte Carlos are designed to give reliable descriptions of low- p_T physics. In the very high-energy regime of modern colliders, this may lead to largely incorrect predictions for the basic reaction processes. This motivated the theoretical efforts aimed at improving Monte Carlos through the inclusion of matrix elements computed beyond the leading order in QCD. I discuss some of the ideas involved, emphasizing the role of higher-order QCD corrections and their interplay with parton showers.

1 Introduction

Event Generators (denoted as EvG's henceforth) have been the workhorses of all modern experiments in high-energy physics. For good reasons: in spite of being conceptually simple, they provide fairly good descriptions of the real

events occurring in detectors, allowing experimenters to perform a variety of tasks, from computing efficiencies to design strategies for achieving given measurements or searches. On the other hand, EvG's may not be the ideal tools for predicting the physical observables with high accuracy, something that is needed in order to – say – extracting the non-computable parameters of the theory from data; traditionally, this task is performed by a class of codes that can be called *cross section integrators* (CSI's). In a loose sense, CSI's can also output events; however, such events can be used only to predict a limited number of observables (for example, the transverse momentum of single-inclusive jets) and are not a faithful description of actual events taking place in real detectors.

Although complementary in nature, EvG's and CSI's are based on the same simple description of an elementary process (the *hard subprocess*), which doesn't even need to be a physically-observable one. To clarify this point, let us consider a gedanken experiment which, at an imaginary accelerator that collides 45 GeV u -quarks with 45 GeV \bar{u} -quarks, observes a $d\bar{d}$ quark pair produced through the decay of a Z^0 . The process of interest is therefore $u\bar{u} \rightarrow Z^0 \rightarrow d\bar{d}$ at 90 GeV. Any theoretical model describing this process must start from the knowledge of its cross section

$$d\sigma(u\bar{u} \rightarrow Z^0 \rightarrow d\bar{d}) = \frac{1}{2\hat{s}} |\mathcal{M}(u\bar{u} \rightarrow Z^0 \rightarrow d\bar{d})|^2 d\Phi_2, \quad (1)$$

where $d\Phi_2$ is $d\bar{d}$ phase space, \mathcal{M} is the relevant matrix element and \hat{s} is the centre-of-mass energy squared. Equation (1) can be used to write an EvG or a CSI. After sampling the phase space, i.e. choosing a point in $d\Phi_2$, one has a complete description of the $u\bar{u} \rightarrow d\bar{d}$ kinematics – a *candidate event*. The candidate event's differential cross section (or *event weight*) $d\sigma$ is calculated from eq. (1) and is directly related to the probability of this event occurring. The information on such a probability can be exploited in two ways to get the distributions of the physical observables: (A) the event weights may be used to create histograms representing physical distributions, or (B) the events may be *unweighted* such that they are distributed according to the theoretical prediction. Procedure (A) is very simple and is what is done for CSI's. A histogram of some relevant distribution (e.g. the transverse momentum of the d quark) is filled with the event weights from a large number of candidate events. The individual candidate events do *not* correspond to anything observable but,

in the limit of an infinite number of candidate events, the distribution is exactly the one predicted by eq. (1). Procedure (B) is a bit more involved, has added advantages, and is what is done in EvG's. It produces events with the frequency predicted by the theory being modelled, and the individual events represent what might be observed in a trial experiment—in this sense unweighted events provide a genuine simulation of an experiment. Strictly speaking, it would be desirable to talk about events only in the case of unweighted events; it is important to keep in mind that CSI's, no matter what their specific nature is, cannot output unweighted events.

What done so far is theoretically well defined, but scarcely useful, the process in eq. (1) being non physical. In fact: *a)* The kinematics of the process is trivial; the Z^0 has transverse momentum equal to zero. *b)* Quark beams cannot be prepared and isolated quarks cannot be detected. Items *a)* and *b)* have a common origin. In eq. (1) the number of both initial- and final-state particles is fixed, i.e. there is no description of the radiation of any extra particles. This radiation is expected to play a major role, especially in QCD, given the strength of the coupling constant.

In the case of item *a)*, the extra radiation taking place on top of the hard subprocess corresponds to considering higher-order corrections in perturbation theory. In the case of item *b)*, it can be viewed as an effective way of describing the dressing of a bare quark which ultimately leads to the formation of the bound states we observe in Nature (*hadronization*). Thus, any EvG or CSI which aims at giving a realistic description of collision processes must include: *i)* A way to compute exactly or to estimate the effects of higher-order corrections in perturbation theory. *ii)* A way to describe hadronization effects. Different strategies have been devised to solve these problems. They can be quickly summarized as follows. For higher orders: **HO.1)** Compute exactly the result of a given (and usually small) number of emissions. **HO.2)** Estimate the dominant effects due to emissions at all orders in perturbation theory. For hadronization: **HAD.1)** Use the QCD-improved version of Feynman's parton model ideas (the *factorization theorem*) to describe the parton \leftrightarrow hadron transition. **HAD.2)** Use phenomenological models to describe the parton \leftrightarrow hadron transition at mass scales where perturbation techniques are not applicable.

The simplest way to implement strategy **HO.1)** is to consider only those diagrams corresponding to the emission of real particles. Basically, the number

of emissions coincides with the perturbative order in α_s . This choice forms the core of *Tree Level Matrix Element* generators. These codes can be used either within a CSI or within an EvG. A more involved procedure aims at computing all diagrams contributing to a given perturbative order in α_s , which implies the necessity of considering virtual emissions as well as real emissions. Such $N^k LO$ computations are technically quite challenging and satisfactory general solutions are known only for the case of one emission (i.e., NLO). Until recently, these computations have been used only in the context of CSI's; their use within EvG's is a brand new field, and I'll deal with it in what follows.

Strategy **HO.2**) is based on the observation that the dominant effects in certain regions of the phase space have almost trivial dynamics, such that extra emissions can be recursively described. There are two vastly different classes of approaches in this context. The first one, called *resummation*, is based on a procedure which generally works for one observable at a time and, so far, has only been implemented in cross section integrators. The second procedure forms the basis of the *Parton Shower* technique and is, by construction, the core of EvG's. This procedure is not observable-specific, making it more flexible than the first approach, but it cannot reach the same level of accuracy as the first, at least formally.

At variance with the solutions given in **HO.1** and **HO.2**, solutions to the problem posed by hadronization always involve some knowledge of quantities which cannot be computed from first principles (pending the lattice solution of the theory) and must be extracted from data. The factorization theorems mentioned in **HAD.1** are the theoretical framework in which CSI's are defined. Parton shower techniques, on the other hand, are used to implement strategy **HAD.2** in the context of EvG's.

2 Event Generators at TeV Colliders

As discussed in the previous section, EvG's and those CSI's which are based upon strategy **HO.2** for the description of higher-order corrections (i.e. those that implement some kind of resummation) give exactly the same description for the observables for which the analytical computations required by the CSI's

are feasible¹, provided that the logarithmic accuracy of the shower and of the resummation is the same. This is basically never the case; analytical resummations are more accurate than parton showers. In practice, some of the (formally uncontrolled) higher logarithms sneak in the showers, and the effective resummation performed by EvG's is seen to give, in many cases, results which are very close to those obtained with analytical resummation techniques. For this reason, the so-far unknown solution of the interesting and fairly challenging problem of improving the logarithmic accuracy of the showers would presumably give only marginal effects in phenomenological predictions. On the other hand, the improvement in the treatment of soft emissions at large angles would have a more visible effect, although on a more restricted class of observables.

The multiple emissions of quarks and gluons performed by the showers change the kinematics of the hard subprocess. The Z^0 of eq. (1) acquires a non-zero transverse momentum p_T by recoiling against the emitted partons. Since the parton shower is based upon a collinear approximation, one must expect the predictions of an EvG for, say, $p_T(Z^0) > 100$ GeV to be completely unreliable. Fortunately, the bulk of the cross section occurs at much smaller values of p_T , where EvG's do provide a sensible description of the production process. In the energy range involved in the collider physics program up to now, this was sufficient for the vast majority of the experimenters' needs.

The situation has now changed considerably. Tevatron Run II and especially LHC will feature very high-energy, high-luminosity collisions, and the events will have many more energetic well-separated particles/jets than before. An accurate description of these is necessary, especially in view of the fact that signals for many beyond-the-SM models involve in fact a large number of jets, resulting from the decay chains of particles of very high mass. The complexity of the LHC environment will be such that an incorrect description of the hard processes *may* even jeopardize the discovery potential of the machine, and will certainly prevent the experiments from performing detailed studies of the collision processes.

The collinear nature of the parton shower implies that EvG's cannot do well in predicting high- p_T processes. The fact that the description of the hard process is achieved using a leading-order picture, as outlined in the previous

¹An alternative approach to resummation, based on numerical methods, has been recently proposed in ref. 1).

sections, has also a second implication: estimates of the rates (i.e., of the number of particles to be detected by the experiments) will be largely underestimated, since many processes have large K factors. Troubles arise when not only the K factors are large, but differ sizably between the various processes, since this complicates enormously the task of normalizing the signal using the background. It should be clear that ⁴¹⁻⁵⁰the K factors needed here are those relevant to the visible regions of the detectors. It is usually assumed that the ratios of these is equal to ratios of the fully inclusive K factors. This crude approximation usually works decently, but may fail dramatically when a complex kinematics is at play.

The bottom line is that the EvG's, which have been one of the fundamental building blocks of the very successful collider physics program of the 80's and the 90's, will not perform well with the new generation of experiments. They will need either to be improved, or to be replaced.

The emphasis on large- p_T emissions implies that the only candidates for the replacement of EvG's are the CSI's that implement exactly the kinematics of the higher-order QCD corrections, thus performing N^k LO computations (strategy **HO.1**). Unfortunately, it is at present unknown how to cancel systematically, and without any reference to a specific observable, the infrared and collinear singularities beyond NLO. Besides, the description of the hadronization phenomena in such computations is very crude, and cannot match the sophistication of the hadronization model implemented in EvG's. Furthermore, as already mentioned, N^k LO computations cannot output events, which is what is absolutely needed.

Barring the possibility of replacing EvG's with something else, the only solution left is to improve them; the improved EvG's will be able to predict sensibly the large- p_T emissions, without losing their capability of treating fairly the low- p_T region, performing resummations there. Clearly, since the large- p_T region is associated with higher-order diagrams, the improvement of EvG's will be equivalent to answering the following question: *How can we insert higher-order QCD corrections into EvG's?* As I will soon discuss, there are two different, largely complementary ways, to solve this problem.

3 Matrix Element Corrections and CKKW

Since the large- p_T emissions are due to the real emission diagrams, the first strategy (denoted as Matrix Element Corrections, MEC henceforth) is that of considering only these diagrams among those contributing to higher-order QCD corrections, in this way neglecting⁴¹⁻⁵⁰ the diagrams with one or more virtual loops. In doing so, the possibility is given up of including the K factor consistently in the computations.

The starting point for including real emission diagrams in EvG's is that of computing them efficiently, which includes efficient samplings of very complex final-state phase spaces. Fortunately, techniques are known to highly automatize such computations, which are nowadays performed by specialized codes (the Tree Level Matrix Element generators), external to proper EvG's and interfaced to them in a standardized way for FORTRAN-based event generators by the Les Houches Accord (LHA) event record²⁾ (the LHA standard is supported in C++ by the HepMC³⁾ event record). Tree-level matrix element generators can be divided into two broad classes, which I will briefly review below; the interested reader can find more information in ref.⁴⁾.

The codes belonging to the first class feature a pre-defined list of partonic processes. Multi-leg amplitudes are strongly and irregularly peaked; for this reason the phase-space sampling has typically been optimized for the specific process. The presence of phase space routines implies that these codes are always able to output partonic events (weighted or unweighted). Popular packages are AcerMC⁵⁾, AlpGEN⁶⁾, Gr@ppa⁷⁾, MadCUP⁸⁾.

The codes belonging to the second class may be thought of as automated matrix element generator authors. The user inputs the initial and final state particles for a process. Then the program enumerates Feynman diagrams contributing to that process and writes the code to evaluate the matrix element. The programs are able to write matrix elements for *any* tree level SM process. The limiting factor for the complexity of the events is simply the power of the computer running the program. Typically Standard Model particles and couplings, and some common extensions are known to the programs. Many of the programs include phase space sampling routines. As such, they are able to generate not only the matrix elements, but to use those matrix elements to generate partonic events (some programs also include acceptance-rejection routines to unweight these events). Codes belonging to this class are AMEGIC++⁹⁾,

CompHEP 10), Grace 11), MadEvent 12).

The use of one of the codes listed above allows one to generate a final-state configuration made of hard quarks, gluons, and other non-coloured particles such as Higgs or gauge bosons. This final state is thus not directly comparable to what is observed in a detector. A drastic simplification is that of assuming that there is a one to one correspondence between hard partons and physical jets.

However, this assumption may cause problems when interfacing these codes to EvG's such as HERWIG 13) or PYTHIA 14); a step which is necessary in order to obtain more sensible descriptions of the production processes. In fact, a kinematic configuration with n final-state partons can be obtained starting from $n - m$ partons generated by the tree-level matrix element generator, with the extra m partons provided by the shower. This implies that, although the latter partons are generally softer than or collinear to the former, there is always a non-zero probability that the *same* n -jet configuration be generated starting from *different* $(n - m)$ -parton configurations. Since tree-level matrix elements do have soft and collinear singularities, a cut at the parton level is necessary in order to avoid them²; I will symbolically refer to this cut as y_{cut} in what follows. Physical observables should be independent of y_{cut} , but they are not; the typical dependence is of leading-log nature (i.e., $\alpha_s^k \log^{2k} y_{cut}$).

To clarify this issue with a simple example, let me consider again the hard subprocess of eq. (1), $u\bar{u} \rightarrow Z^0$. One of the NLO real contributions to this process is $u\bar{u} \rightarrow Z^0 g$. Events from these two processes should never be blindly combined, since a fraction of the latter events are already included in the former process via gluon radiation in the parton shower. Combining the two processes without special procedures amounts to *double counting* some portion of phase space.

The first approaches to the technique of MEC, which allows one to solve the double counting problem, limited themselves to the case of at most one extra hard parton wrt those present at the Born level 15, 16). These MEC can be implemented either as a strict partition of phase space between two processes, or as an event reweighting (re-evaluation of the event probability using the matrix element) using the higher order tree level matrix element for the related process. In either case the effect is the same: the event shapes are

²It is actually this cut that defines the “hardness” of the primary partons.

dominated by the parton shower in the low- p_T region, the shapes are NLO-like in the high- p_T region, and the total cross section remains leading order (i.e. for our example the total cross section will be the same as that for $u\bar{u} \rightarrow Z^0$). The trouble with such versions of MEC is that they can be applied only in a very limited number of cases, which are relatively simple in terms of radiation patterns and colour connections.

The way in which MEC can be achieved in the general case of n_E extra hard partons, with $n_E \geq 1$, has been clarified in ref. ¹⁷⁾ for the case of e^+e^- collisions (referred to as CKKW after the names of the authors). The idea is the following: *a)* Integrate all the $\gamma^* \rightarrow 2 + n_E$ ME's by imposing $y_{ij} > y_{cut}$ for any pairs of partons i, j , with $y_{ij} = 2 \min(E_i^2, E_j^2)(1 - \cos\theta_{ij})/Q^2$ the interparton distance defined according to the k_T -algorithm. *b)* Choose statistically an n_E , using the rates computed in *a)*. *c)* Generate a $(2 + n_E)$ -parton configuration using the exact $\gamma^* \rightarrow 2 + n_E$ ME, and reweight it with a suitable combination of Sudakov form factors (corresponding to the probability of no other branchings). *d)* Use the configuration generated in *c)* as initial condition for a *vetoed* shower. A vetoed shower proceeds as the usual one, except that it forbids all branchings $i \rightarrow jk$ with $y_{jk} > y_{cut}$ without stopping the scale evolution. Although the selection of an n_E value has a leading-log dependence on y_{cut} , it can be proved that this dependence is cancelled up to next-to-next-to-leading logs in physical observables (i.e., $\alpha_S^k \log^{2k-2} y_{cut}$), plus terms suppressed by powers of y_{cut} . It is clear that, in order to be internally consistent, matrix elements must be available for any value of $2 + n_E$. In practice, $n_E \leq 3$ is a good approximation of $n_E < \infty$.

After CKKW proposed their implementation of MEC for e^+e^- collisions, an extension to hadronic collisions has been presented, without formal proof, in ref. ¹⁸⁾; an alternative method for colour-dipole cascades has been presented in ref. ¹⁹⁾. There is a considerable freedom in the implementation of the CKKW prescription in the case of hadronic collisions. This freedom is used to tune (some of) the EvG's parameters in order to reduce as much as possible the y_{cut} dependence, which typically manifests itself in the form of discontinuities in the derivative of the physical spectra. A discussion on these issues, with practical examples of the implementation of CKKW in HERWIG and PYTHIA, can be found in ref. ²⁰⁾. CKKW has also been implemented in SHERPA ²¹⁾; an alternative procedure, proposed by Mangano, is being implemented in AlpGEN.

I stress that the complete independence of y_{cut} cannot be achieved; this would be possible only by including all diagrams (i.e., also the virtual ones) contributing to a given order in α_s .

4 Adding virtual corrections: NLOwPS

The point made at the end of the previous section appears obvious; it is well known, and formally established by the BN and KLN theorems, that the infrared and collinear singularities of the real matrix elements are cancelled by the virtual contributions. One may in fact be surprised by the mild y_{cut} dependence left in the practical implementation of CKKW (see for example ref. ²⁰); however, we should keep in mind that parton showers do contain part of the virtual corrections, thanks to the unitarity constraint which is embedded in the Sudakov form factors. However, to cancel exactly the y_{cut} dependence there is no alternative way to that of inserting the exact virtual contributions to the hard process considered. In doing so, one is also able to include consistently in the computation the K factor. It is important to realize that this is *the only way* to obtain this result in a theoretically consistent way. The procedure of reweighting the EvG's results to match those obtained with CSI's for certain observables must be considered a crude approximation (since no CSI is able to keep into account all the complicated final-state correlations that are present when defining the cuts used in experimental analyses).

The desirable thing to do would be that of adding the virtual corrections of the same order as all of the real contributions to CKKW implementations. Unfortunately, this is unfeasible, for practical and principle reasons. The practical reason is that, at variance with real corrections, we don't know how to automatize efficiently the computations of loop diagrams in the Minkowskian kinematic region. The principle reason is that there's no known way of achieving the cancellation of infrared and collinear divergences in an universal and observable-independent manner beyond NLO. We have thus to restrict ourselves to the task of including NLO corrections in EvG's; I'll denote the EvG improved in this way as NLO with Parton Showers (NLOwPS).

The fact that only one extra hard emission can be included in NLOwPS's is the reason why such codes must be presently seen as complementary to MEC. When one is interested in a small number of extra emissions, then NLOwPS's must be considered superior to MEC; on the other hand, for studying processes

with many hard legs involved, such as SUSY signals or backgrounds, MEC implementations should be used. A realistic goal for the near future is that of incorporating the complete NLO corrections to all the processes with different n_E 's in CKKW.

Before turning to a technical discussion on NLOwPS's, let me specify in more details the meaning of "NLO" in the context on an EvG. To do so, let me consider the case of SM Higgs production at hadron colliders, which at the lowest order, $\mathcal{O}(\alpha_s^2)$, proceeds through a loop of top quarks which is the only non-negligible contribution to the ggH effective vertex. When the p_T distribution of the Higgs is studied, we get what follows:

$$\frac{d\sigma}{dp_T} = (A\alpha_s^2 + B\alpha_s^3) \delta(p_T) + C(p_T)\alpha_s^3, \quad (2)$$

which means

$$\int_{p_T^{min}}^{\infty} dp_T \frac{d\sigma}{dp_T} = \mathcal{C}_3\alpha_s^3, \quad p_T^{min} > 0 \quad (3)$$

$$= \mathcal{D}_2\alpha_s^2 + \mathcal{D}_3\alpha_s^3, \quad p_T^{min} = 0. \quad (4)$$

In the language of perturbative computations, the result for $p_T^{min} > 0$ would be denoted as LO, that for $p_T^{min} = 0$ as NLO. This is not appropriate for EvG's, since such a naming scheme depends on the observable considered, and EvG's produce events without any prior knowledge of the observable(s) which will eventually be reconstructed. Thus, in the context of EvG's, we generally define N^k LO accuracy with k the number of extra (real or virtual) gluons or light quarks wrt those present at the Born level.

Apart from this, there is a certain freedom in defining NLOwPS's. I follow here the definitions given in ref. 22), where the NLOwPS MC@NLO was first introduced:

- Total rates are accurate to NLO.
- Hard emissions are treated as in NLO computations.
- Soft/collinear emissions are treated as in MC.
- NLO results are recovered upon expansion of NLOwPS results in α_s .
- The matching between hard- and soft/collinear-emission regions is smooth.

- The output is a set of events, which are fully exclusive.
- MC hadronization models are adopted.

The fourth condition above defines the absence of double counting in NLOwPS's. In other words: *An NLOwPS is affected by double counting if its prediction for any observable, at the first order beyond the Born approximation in the expansion in the coupling constant, is not equal to the NLO prediction.* According to this definition, double counting may correspond to either an excess or a deficit in the prediction, at any point in phase space. This includes contributions from real emission and virtual corrections.

Let me now consider a generic hard production process, whose nature I don't need to specify, except for the fact that its LO contribution is due to $2 \rightarrow 2$ subprocesses, which implies that real corrections will be due to $2 \rightarrow 3$ subprocesses; these conditions are by no means restrictive, and serve only to simplify the notation. Let O be an observable whose value can be computed by knowing the final-state kinematics emerging from the hard processes. At the NLO, we can write the distribution in O as follows:

$$\left(\frac{d\sigma}{dO}\right)_{\text{subt}} = \sum_{ab} \int dx_1 dx_2 d\phi_3 f_a(x_1) f_b(x_2) \left[\delta(O - O(2 \rightarrow 3)) \mathcal{M}_{ab}^{(r)}(x_1, x_2, \phi_3) + \delta(O - O(2 \rightarrow 2)) \left(\mathcal{M}_{ab}^{(b,v,c)}(x_1, x_2, \phi_2) - \mathcal{M}_{ab}^{(c.t.)}(x_1, x_2, \phi_3) \right) \right]. \quad (5)$$

Here, $\mathcal{M}_{ab}^{(r)}$ is the contribution of the real matrix elements, whereas $\mathcal{M}_{ab}^{(b,v,c,c.t.)}$ are the contributions of the Born, virtual, collinear reminders and collinear counterterms; $O(2 \rightarrow n)$, with $n = 2, 3$, is the value of the observable O as computed with 2- and 3-body final states. The form of eq. (6) is borne out by the universal formalism for cancelling the infrared and collinear divergences proposed in refs. 23, 24), upon which MC@NLO is based. Other equivalent forms could be used at this point, without changing the conclusions.

In order to predict the distribution of O using an EvG, one computes the value of O for each event generated by the shower. The most compact way of describing how an EvG works is through the generating functional, which is

basically the incoherent sum of all possible showers

$$\mathcal{F}_{\text{MC}} = \sum_{ab} \int dx_1 dx_2 d\phi_2 f_a(x_1) f_b(x_2) \mathcal{F}_{\text{MC}}^{(2 \rightarrow 2)} \mathcal{M}_{ab}^{(b)}(x_1, x_2, \phi_2), \quad (6)$$

where $\mathcal{F}_{\text{MC}}^{(2 \rightarrow 2)}$ is the generating functional for parton-parton scattering, with a $2 \rightarrow 2$ configuration as a starting condition for the showers.

In the attempt of merging NLO and EvG, we observe that in eqs. (6) and (6) the short distance matrix elements serve to determine the normalization of the results, and the hard process kinematics. Such kinematics configurations are evolved by the showers $\mathcal{F}_{\text{MC}}^{(2 \rightarrow 2)}$ in eq. (6), and the resulting final states eventually used to compute the value of O . A similar “evolution” is performed in the context of the NLO computations by the δ functions appearing in eq. (6); clearly, the evolution is trivial in this case. However, this suggests that the incorporation of NLO results into EvG’s may simply amount to replacing in eq. (6) $\delta(O - O(2 \rightarrow n))$ with $\mathcal{F}_{\text{MC}}^{(2 \rightarrow n)}$, i.e. with the generating functionals of the showers whose initial conditions are $2 \rightarrow 2$ and $2 \rightarrow 3$ hard kinematics configurations. It should be stressed that this strategy, that I’ll call the *naive NLOwPS prescription*, actually works at the LO, since eq. (6) can be obtained from eq. (6) following this prescription, if terms beyond LO are dropped from the latter equation.

Unfortunately, things are more complicated than this. Basically, when $\mathcal{F}_{\text{MC}}^{(2 \rightarrow 2)}$ acts on $\mathcal{M}_{ab}^{(b)}$ in the analogue of eq. (6) obtained by applying the naive NLOwPS prescription, it generates terms that contribute to the NLO prediction of O , which are not present in eq. (6). According to the definition given above, this amounts to double counting. Furthermore, the weights associated with $\mathcal{F}_{\text{MC}}^{(2 \rightarrow 2)}$ and $\mathcal{F}_{\text{MC}}^{(2 \rightarrow 3)}$ (i.e., the coefficients multiplying $\delta(O - O(2 \rightarrow 2))$ and $\delta(O - O(2 \rightarrow 3))$ in eq. (6) respectively) are separately divergent. These divergences are known to cancel thanks to the KLN theorem and the infrared safeness of O ; however, this happens efficiently in the case of the NLO computations, thanks to the fact that the final-state configurations with which the values of O are computed coincide with the hard configurations. This is not the case when the showers are attached, since the evolutions implicit in $\mathcal{F}_{\text{MC}}^{(2 \rightarrow 2)}$ and $\mathcal{F}_{\text{MC}}^{(2 \rightarrow 3)}$ are not correlated (and must not be so). This means that the naive prescription outlined above, apart from double counting, requires an infinite amount of CPU time in order for the cancellation of the infrared divergences to occur. I’ll now show how these problems are solved in the context of MC@NLO (22, 25). We

observe that, if the shower evolution attached to the Born contribution in the naive prescription results in spurious NLO terms, one may try to remove “by hand” such terms. Denoting by $\mathcal{M}_{\mathcal{F}(ab)}^{(\text{MC})}$ the terms that we’ll actually remove, the following equation holds:

$$\mathcal{M}_{\mathcal{F}(ab)}^{(\text{MC})} = \mathcal{F}_{\text{MC}}^{(2\rightarrow 2)} \mathcal{M}_{ab}^{(b)} + \mathcal{O}(\alpha_s^2 \alpha_s^b), \quad (7)$$

where α_s^b is the perturbative order corresponding to the Born contribution. Clearly, eq. (7) leaves a lot of freedom in the definition of $\mathcal{M}_{\mathcal{F}(ab)}^{(\text{MC})}$ (which I denote as *MC counterterms*), in that all terms of NNLO and beyond are left unspecified. In MC@NLO, we defined the MC counterterms using eq. (7), and requiring all terms beyond NLO to be zero. With this, we define the MC@NLO generating functional as follows:

$$\begin{aligned} \mathcal{F}_{\text{MC@NLO}} = & \sum_{ab} \int dx_1 dx_2 d\phi_3 f_a(x_1) f_b(x_2) \\ & \left[\mathcal{F}_{\text{MC}}^{(2\rightarrow 3)} \left(\mathcal{M}_{ab}^{(r)}(x_1, x_2, \phi_3) - \mathcal{M}_{ab}^{(\text{MC})}(x_1, x_2, \phi_3) \right) + \right. \\ & \mathcal{F}_{\text{MC}}^{(2\rightarrow 2)} \left(\mathcal{M}_{ab}^{(b,v,c)}(x_1, x_2, \phi_2) - \mathcal{M}_{ab}^{(c.t.)}(x_1, x_2, \phi_3) + \right. \\ & \left. \left. \left. \mathcal{M}_{ab}^{(\text{MC})}(x_1, x_2, \phi_3) \right) \right]. \end{aligned} \quad (8)$$

Eq. (8) is identical to what one would have got by applying the naive NLOwPS prescription discussed above to eq. (6), except for the fact that the short-distance coefficients have been modified by adding and subtracting the MC counterterms; for this reason, MC@NLO is said to be based upon a modified subtraction method. At the first glance, it may appear surprising that the MC counterterms have been added twice, with different signs, since their role is that of eliminating the spurious terms arising from the evolution of the Born term. However, this is what they do indeed. In fact, the evolution of the Born term also includes a contribution due to the so-called non-branching probability, i.e. the probability that nothing happens. This corresponds to a would-be deficit of the naive NLOwPS prediction, which is taken into account by our definition of double counting.

Remarkably, the solution of the problem of double counting also solves the problem of the cancellation of the infrared and collinear divergences in a finite amount of time. In fact, the weights attached to the two generating functionals on the r.h.s. of eq. (8) are now separately finite locally in the phase

space. This is so since the showers are constructed to reproduce the behaviour of the collinear emissions as predicted by perturbation theory, and this in turn implies that the MC counterterms locally match the singular behaviour of the real matrix elements, hence the name “counterterms” (there are subtleties due to the peculiar treatment of soft emissions in showers, which are technically too involved to be discussed here; the interested reader can find all the details in ref. ²²). This fact also implies that MC@NLO produces events identical in nature to those of standard EvG’s, since unweighting can be performed at the level of short-distance contributions. As a consequence, the convergence properties (i.e., the smoothness of the physical distributions) are much better than those of the corresponding NLO codes; typically, to achieve the same level of fluctuations, MC@NLO has to sample the phase space about 50 times less than the NLO code from which it is derived. This pattern is followed by all of the processes so far implemented in MC@NLO, whose (growing) list can be found with the package at <http://www.hep.phy.cam.ac.uk/theory/webber/MCatNLO/>.

An important point to stress is that the computation of the MC counterterms requires a detailed knowledge of what the EvG does when performing the shower. This means that the MC counterterms are specific to a given Monte Carlo implementation: those corresponding to HERWIG differ from those corresponding to PYTHIA. Presently, MC@NLO can only be interfaced to HERWIG, since only the MC counterterms relevant to HERWIG have been computed. It is also worth mentioning that the form of the MC counterterms doesn’t depend on the hard process considered; thus, their computation is performed once and for all. A second point is that NLOwPS’s are in general not positive definite, i.e. a fraction of the generated events will have negative weights. Fortunately, this fraction is fairly small, and future work may lead to its further reduction.

In spite of attracting a considerable amount of theoretical interest in the past few years, at the moment there are only a couple of codes, plus MC@NLO, that can be used to produce actual events in hadronic collisions. Phase-space veto has been introduced in ref. ²⁶, elaborating on an older idea presented in ref. ²⁷, and applied to Z^0 production. The approach is interesting since no negative-weight events are produced. However, as shown in ref. ²², this is obtained at the price of double counting in certain regions of the phase space. Although the practical impact of such double counting seems to be modest for

the physical process considered, it remains to be seen how the method can be generalized in order to treat processes more complicated from the point of view of kinematics and colour configurations. The code `gcnLO` ²⁸⁾ is characterized by the numerical computation of all the matrix elements involved. In order not to do double counting, the short distance cross sections have to be interfaced with an *ad-hoc* shower, i.e., the interfacing with HERWIG or PYTHIA does produce double counting. The method has so far been applied to Z^0 production, and efforts are being made in order to implement $Z^0 + 1$ jet production.

5 Conclusions

The new event generators include many theoretical ideas developed in the last few years, and represent a significant improvement with respect to the Monte Carlo's of the 80's and the 90's. Such an improvement is necessary in order for the new generators to give a correct description of the production processes involved in Tevatron Run II and LHC physics.

References

1. A. Banfi, G. P. Salam and G. Zanderighi, arXiv:hep-ph/0407286.
2. E. Boos, *et al.*, arXiv:hep-ph/0109068.
3. M. Dobbs and J. B. Hansen, Comput. Phys. Commun. **134**, 41 (2001).
4. M. A. Dobbs *et al.*, arXiv:hep-ph/0403045.
5. B. P. Kersevan and E. Richter-Was, Comp. Phys. Commun. **149** (2003) 142 [arXiv:hep-ph/0201302].
6. M. L. Mangano, M. Moretti, F. Piccinini, R. Pittau and A. D. Polosa, JHEP **0307** (2003) 001 [arXiv:hep-ph/0206293].
7. S. Tsuno, K. Sato, J. Fujimoto, T. Ishikawa, Y. Kurihara, S. Odaka and T. Abe, Comput. Phys. Commun. **151** (2003) 216 [arXiv:hep-ph/0204222].
8. K. Cranmer, T. Figy, W. Quayle, D. Rainwater, and D. Zeppenfeld, <http://pheno.physics.wisc.edu/Software/MadCUP/>.

9. F. Krauss, R. Kuhn and G. Soff, JHEP **0202** (2002) 044 [arXiv:hep-ph/0109036].
10. A. Pukhov *et al.*, arXiv:hep-ph/9908288.
11. J. Fujimoto *et al.*, Comput. Phys. Commun. **153** (2003) 106 [arXiv:hep-ph/0208036].
12. F. Maltoni and T. Stelzer, JHEP **0302** (2003) 027 [arXiv:hep-ph/0208156].
13. G. Corcella *et al.*, JHEP **0101** (2001) 010 [arXiv:hep-ph/0011363].
14. T. Sjostrand, P. Eden, C. Friberg, L. Lonnblad, G. Miu, S. Mrenna and E. Norrbin, Comput. Phys. Commun. **135** (2001) 238 [arXiv:hep-ph/0010017].
15. M. Bengtsson and T. Sjostrand, Nucl. Phys. B **289** (1987) 810.
16. M. H. Seymour, Comput. Phys. Commun. **90** (1995) 95 [arXiv:hep-ph/9410414].
17. S. Catani, F. Krauss, R. Kuhn and B. R. Webber, JHEP **0111** (2001) 063 [arXiv:hep-ph/0109231].
18. F. Krauss, JHEP **0208** (2002) 015 [arXiv:hep-ph/0205283].
19. L. Lonnblad, JHEP **0205** (2002) 046 [arXiv:hep-ph/0112284].
20. S. Mrenna and P. Richardson, JHEP **0405** (2004) 040 [arXiv:hep-ph/0312274].
21. T. Gleisberg, S. Hoeche, F. Krauss, A. Schaelicke, S. Schumann, J. Winter and G. Soff, arXiv:hep-ph/0407365.
22. S. Frixione and B. R. Webber, JHEP **0206** (2002) 029 [arXiv:hep-ph/0204244].
23. S. Frixione, Z. Kunszt and A. Signer, Nucl. Phys. B **467** (1996) 399 [arXiv:hep-ph/9512328].
24. S. Frixione, Nucl. Phys. B **507** (1997) 295 [arXiv:hep-ph/9706545].

25. S. Frixione, P. Nason and B. R. Webber, JHEP **0308** (2003) 007 [arXiv:hep-ph/0305252].
26. M. Dobbs, Phys. Rev. D **65** (2002) 094011 [arXiv:hep-ph/0111234].
27. H. Baer and M. H. Reno, Phys. Rev. D **44** (1991) 3375.
28. Y. Kurihara, J. Fujimoto, T. Ishikawa, K. Kato, S. Kawabata, T. Munehisa and H. Tanaka, Nucl. Phys. B **654** (2003) 301 [arXiv:hep-ph/0212216].

THE TRANSITION FROM GEANT3 TO GEANT4

Tommaso Boccali

Scuola Normale Superiore and INFN Pisa, Piazza dei Cavalieri 7, 56126 Pis

Abstract

In the last two years the High Energy Physics (*HEP*) community has completed the transition from simulation programs based on Geant3 to the new Geant4 framework. The status of the current understanding and the comparison with test beam data is presented, outlining a possible strategy for the continuation of the effort.

1 Introduction

The realization of simulation programs for the soon-to-come LHC experiments presents huge problems, due to the complexity of the apparatus and to the high multiplicity events which will contaminate the trigger event.

In this review, I try and sketch the evolution of such simulation programs from the Fortran Geant3¹⁾ framework, to the new C++ Geant4²⁾ framework. The current status of physics validation is then presented.

2 From Geant3 to Geant4

The previous HEP experiments, *e.g.* the LEP ones, had simulation programs based on Geant3, a Fortran framework for the simulation of the interactions of particles with matter, developed starting from 1982 for the OPAL ³⁾ experiment.

The success of the LEP physics program for precision measurements, where the availability of a detailed Monte Carlo simulation is unavoidable, shows that the Geant3 framework could fulfill to the expectations.

In 1993 a parallel project started to port the Geant3 code to C++; at the same time, any further development of Geant3 was stopped to focus the efforts on the new product.

The transition from Fortran to C++ was needed since C++ was already understood as the language for the LHC experiments; moreover, recent techniques of computer science were claiming an easier control of the code base and an easier release sequence.

3 About Physics Validation

The complete validation of the Geant4 framework by the experiments is a long and complex process. It involves

- validation of the components (geometry building, beam simulation, interface to generators, interface to databases);
- validation of physics (hadronic physics, electromagnetic physics);
- validation of performance (C++ is known to be slower than Fortran, and possibly more prone to crashes).

The first type of validation is more interesting for Computer Scientists, having not much to do with physics itself. The second point is the core of the problem and is covered in details in the next sections. The third one is again not really linked to physics, but is utterly important when massive productions have to be carried out.

4 Physics Validation

A physics validation program must be based on the comparison of Geant4 simulations with real data. A comparison Geant3 vs Geant4 does not have much sense here, since, at least in principle, Geant4 should be superior to Geant3 *a priori*, since it incorporates 10 years of further studies.

A comparison with data, on the other hand, is much more complicated from the practical point of view. Test beam data, for example, is often taken with non final detectors and electronics, and in unstable situations (beam, environment ...). Any attempt to extract valuable information about the underline physics must address and simulate this problems before drawing any conclusion.

Then, when can be a physics validation program considered accomplished? Various definitions could be used, but one seems natural: a physics simulation can be considered adequate if any systematic errors introduced by residual discrepancies in a benchmark analysis (after proper calibration) is not the dominant one on the total error.

4.1 Hadronic Physics

In Geant4 a single hadronic model valid for all processes and energies is not available; instead, a collection of models is present, which cover a wide range of use cases.

Moreover, various models can be available for the same energy range. Differences can be in the modelling, either based on theoretical arguments or fits to existing data, in speed and in accuracy. While in principle the user is entitled to *build* the hadronic model combining model with different validity range, in practice a group of experts (*Hadronic Physics Working Group*) has provided *Physics Lists* for general use and validity from thermal neutrons to HEP applications. These are:

- LHEP: *Data Driven Low-High Energy Parameterization*. It is a low/high energy parameterization of the available data, and describes in a fairly accurate way the final states, while neglecting intermediate states like resonances. It is, to a large extent, a porting in C++ of the existing hadronic model of Geant3.

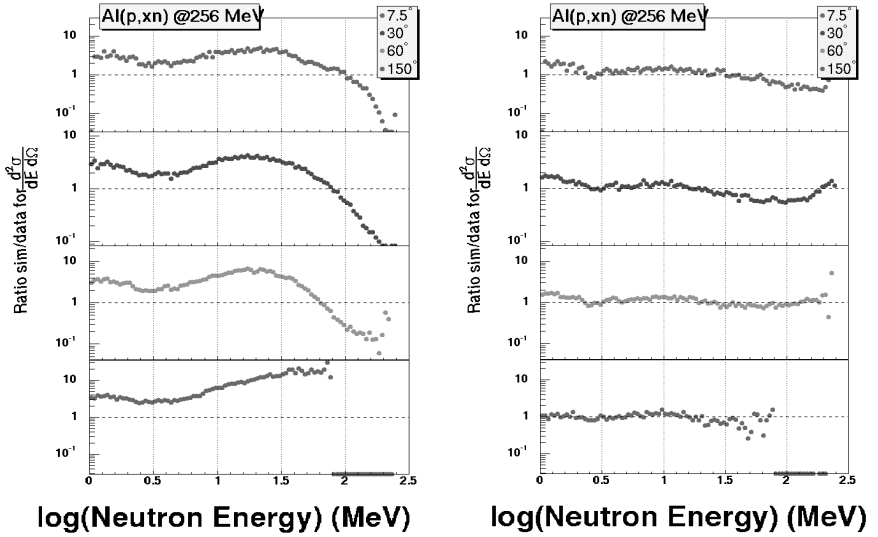


Figure 1: Differential cross section of neutrons out of proton(256 MeV)-Al. Left: using LHEP hadronic model; right: QGSP model.

- QGSP: a theory-driven model, based on the *Quark Gluon String Model* with Bertini/Binary cascade under 3 GeV.

Validation has been carried out using these two models, with data from low energy experiments from nuclear physics and test beams of LHC (up to 200 GeV); higher energy data will be available during the commissioning of the LHC accelerator.

Low-Energy Hadronic Physics The ALICE Collaboration ⁴⁾ has studied Los Alamos data about proton (up to 800 MeV) scattering on fixed targets, looking at the produced neutrons at different energy and angle. Figure 1 shows one example of such distributions. The conclusion by ALICE states that the LHEP model is not able to describe the experimental data, while the QGSP model is adequate, giving an agreement between data and Monte Carlo Simulation within 20% everywhere, and better in most cases.

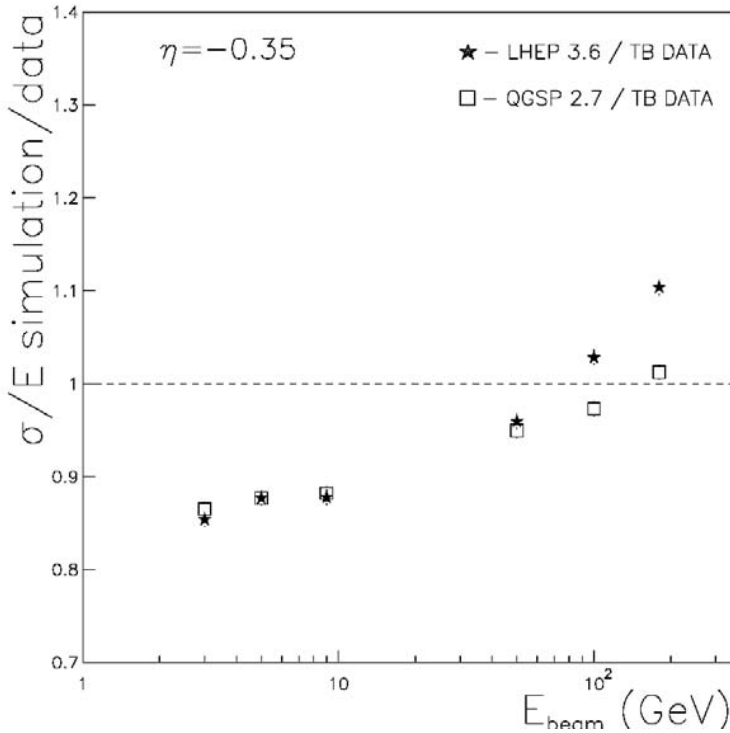


Figure 2: Energy resolution simulation/data for pions on ATLAS TileCal.

High-Energy Hadronic Physics Data is available from ATLAS ⁵⁾ and CMS ⁶⁾ LHC test beams (SPS Collider), and studies the response of the hadronic and electromagnetic calorimeters for electrons, muons and pions in the energy range 1-200 GeV. Quantities under study are

- reconstructed energy: linearity and resolution;
- e/π energy response separation;
- shower profiles.

Figures 2,3 shows the energy resolution from the ATLAS TileCal calorimeter; while neither LHEP nor QGSP agree at the percent level, QGSP is able to give a description within less than 5%.

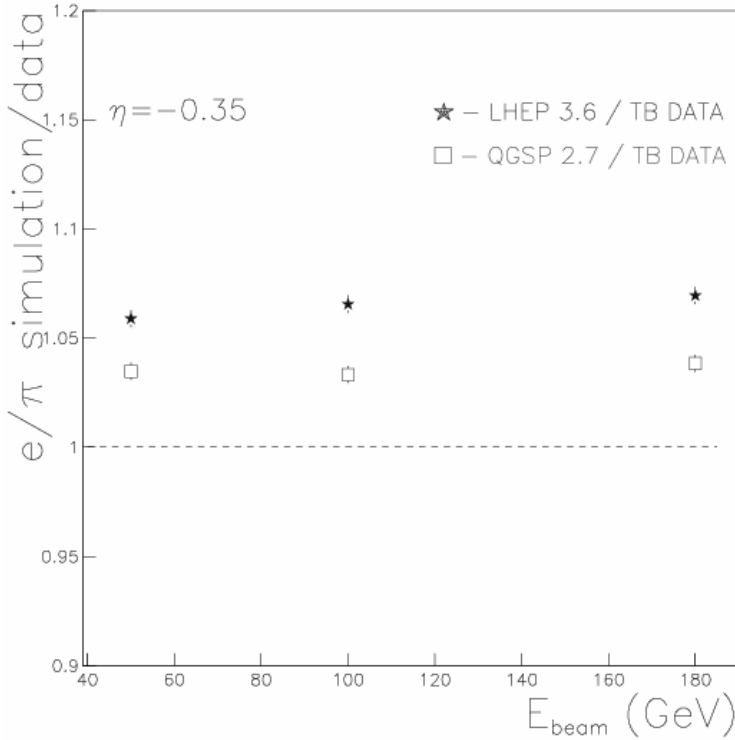


Figure 3: Relative response to pions and electron, simulation/data.

Figure 4 shows shower profiles from the ATLAS HEC calorimeter. Only in one case the Geant3 simulation seems in better agreement with data.

Figure 5 shows shower profiles from the CMS HCAL calorimeter; again the conclusions are not straightforward, but Geant4 simulations are in each case quite in agreement with data.

While conclusions are not always easy to draw, the general trend is that when data is compared with Geant3 and Geant4, Geant4 shows a better agreement with both the Physics Lists. Moreover, the complex theory-driven QGSP is generally better than the simple parameterization offered by LHEP.

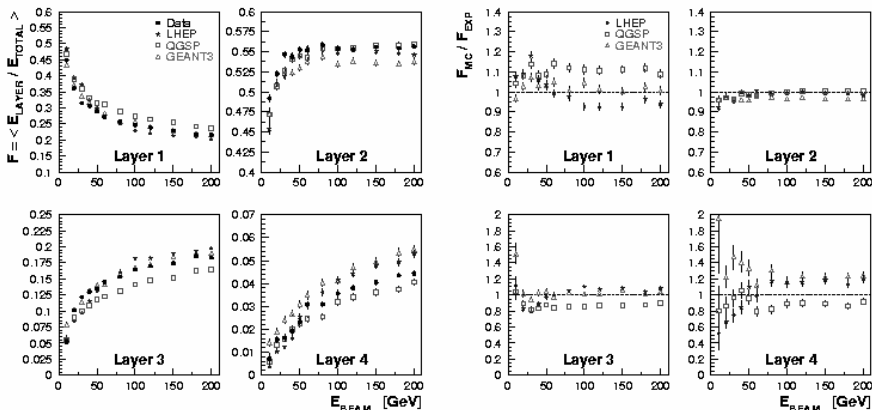


Figure 4: Longitudinal shower shapes in 4 HEC layers. Left: distributions as a function of pion energy; right: simulation/data.

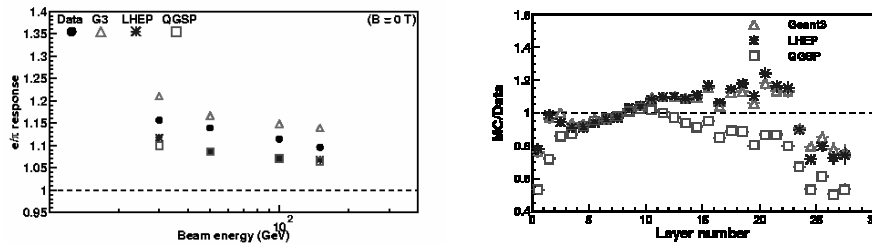


Figure 5: Left: e/π response in the CMS HCAL. Right: longitudinal shower evolution, simulation/data.

4.2 Hadronic Physics in Thin Layers

A correct modelling of the hadronic physics is at the base of calorimetry simulations, but can be important also in the simulation of thin detectors, like silicon tracking devices. The response of such detectors is mainly due to Em interactions, but the rare ($O(10^{-3})$) occurrence of hadronic interactions can generate problems. In fact, the energy deposition of these is in the MeV range, at least

10 times more than the corresponding Em one, and can generate saturations in the front end electronics. On the other hand, these can be valuable in studying hadronic interactions: with detectors less than 1 mm thick, an hypothesis of single interaction can be used.

ATLAS, in a test beam with pixel detectors, has selected events with pions colliding in a detector, which generate at least three tracks downstream. In such a trigger condition, kinematic distributions such as the number of tracks coming out of the layer, the relative height of the hit pixels (shape of the cluster) and the angular distributions of such tracks are compared to the simulation of the setup.

Also in this case, the Geant4 based simulation is able to reproduce the data within a few percent.

4.3 Em Physics

The electromagnetic physics simulation is an easier task, since the model is well known and understood since long. In fact, Geant4 provides virtually no options for the model, apart from the choice of the precision level.

On thin layers, like tracking devices, the level of accuracy must be such has to correctly reproduce the elementary interaction up to very small energies: in pixel detectors, the expected resolution is of the order of 10 μm , which is comparable to the range in silicon of 30 keV electrons. Delta ray emission must be allowed and correctly simulated up to this level. CMS has shown with recent test beams that resolutions, cluster shapes and energy deposits are well in agreement with the simulations (see Figure 6).

In Em calorimeters, on the other hand, the hadronic showers must be correctly simulated from the pile-up scale (100 MeV) to the energy of the jets (TeV scale). Quantities which need to be checked in the simulation are energy, linearity and resolution, but also shower shapes, needed to separate electrons from jets, and position resolutions, used to identify the correct primary interaction vertex.

CMS has compared test beam data with electrons 20-180 GeV in ECAL to the simulation, comparing confinement and resolutions to the Geant4 simulation. The agreement is considered satisfactory. Figure 7 shows the agreement data/simulation for what concerns confinement, while Figure 8 shows the resolution in energy.

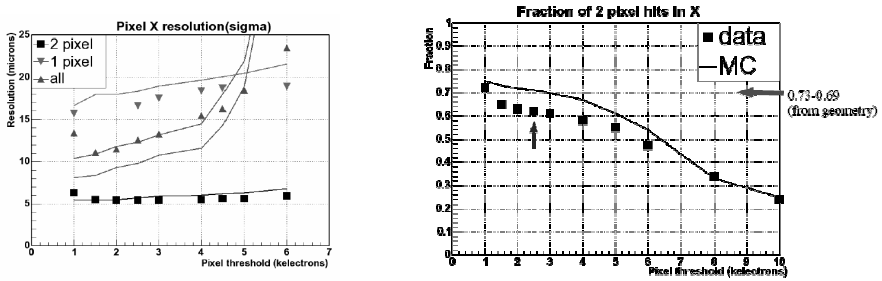


Figure 6: Left: resolution in X coordinate in a CMS pixel detector; right: fraction of hits with 2 pixels as a function of the pixel threshold.

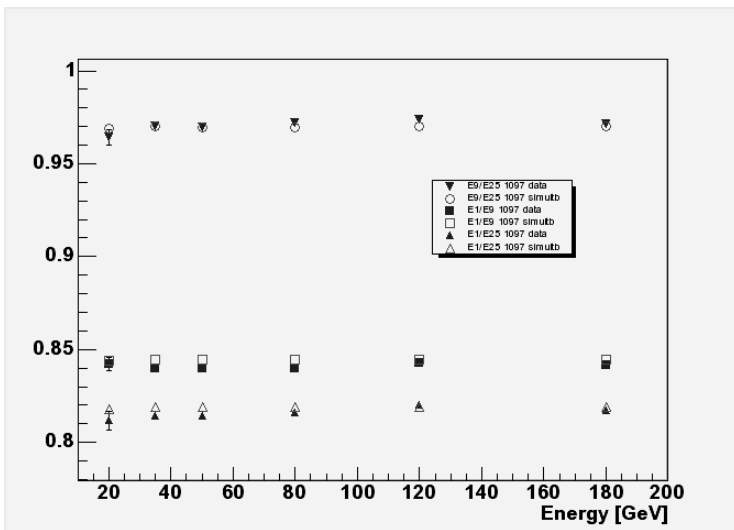


Figure 7: Confinement in a CMS ECAL crystal matrix.

5 Conclusions

By now, the LHC experiments have all switched to simulation programs based on the Geant4 framework. While the initial validation seems successful, more

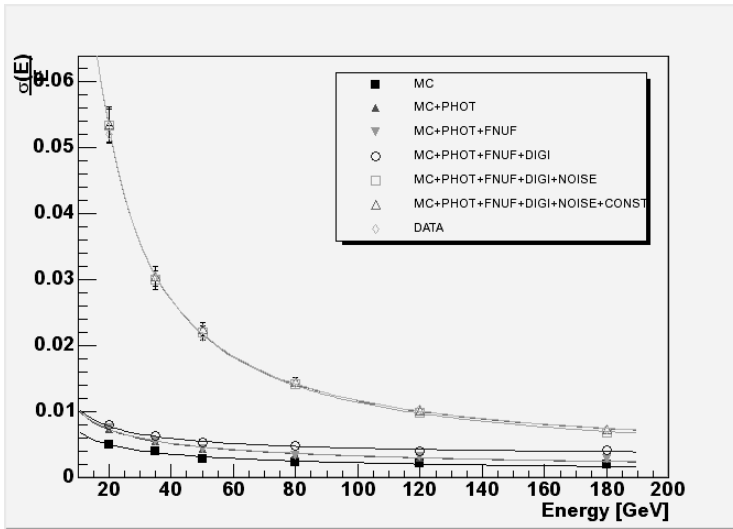


Figure 8: Energy resolution as a function of beam energy.

data is needed to prepare the simulation by the start of the LHC program. A critical eye must be kept when comparing simulations and test beam data, since for a correct understanding a very accurate understanding and simulation of the electronic and beam conditions are unavoidable.

References

1. R. Brun, et al., GEANT3, CERN DD/EE/84-1, (1986).
2. S. Agostinelli et al., “GEANT4 - a simulation toolkit”, Nucl. Instr. Meth. Phys. Res. A 506, 250-303 (2003).
3. OPAL, K. Ahmet et al., Nucl. Instr. and Meth. A305 (1991) 275.
4. <http://alice.web.cern.ch/Alice/AliceNew>.
5. <http://atlas.web.cern.ch/Atlas>.
6. <http://cmsinfo.cern.ch/Welcome.html>.

Frascati Physics Series Vol. XXXVIII (2005), pp. 57

II WORKSHOP ITALIANO SULLA FISICA DI ATLAS E CMS – Napoli, October 13 - 15, 2004

DATA CHALLENGING

Paolo Capiluppi

*Dipartimento di Fisica dell'Università di Bologna and INFN
40126 Bologna, Italy*

Written contribution not received

Frascati Physics Series Vol. XXXVIII (2005), pp. 59

II WORKSHOP ITALIANO SULLA FISICA DI ATLAS E CMS – Napoli, October 13 - 15, 2004

LHC, STATUS OF THE CONSTRUCTION AND PERSPECTIVES

Lucio Rossi

CERN, PH Department, Geneva, Switzerland

Written contribution not received

Session I – Triggers

FIRST LEVEL TRIGGERS FOR ATLAS AND CMS EXPERIMENTS AT THE LHC

S. Marcellini, *INFN Bologna*

Fr. Pastore, *INFN Rome*

Abstract

The LHC machine characteristics and the physics program requirements deeply influence the challenges of first level trigger systems of the ATLAS and CMS experiments. Due to the about 1 GHz interaction rate, the trigger front-end electronics are organized in pipeline memories, which allow few microseconds latency to the trigger logic for making decisions. In this paper a general discussion on the requirements for the design of first level triggers is presented and followed by an overview of the first-level triggers of the ATLAS and CMS experiment. In particular calorimeter and muon trigger systems are described for both experiments.

1 Trigger requirements

ATLAS (A Toroidal LHC ApparatuS) ¹⁾ and CMS (Compact Muon Solenoid) ²⁾ are the two general-purpose detectors designed to operate on the Large Hadron

Table 1: *Possible selection signature at LHC*

particles	example of physics coverage
electrons	Higgs, new gauge bosons, extra dim., SuSy, W, top
photons	Higgs, extra dim., SuSy
muons	Higgs, new gauge bosons, extra dim., SuSy, W, top
jets	SuSy, compositness, resonances
jet + miss. E_T	SuSy, leptoquarks
tau + miss. E_T	extended Higgs models, MSSM, SuSy

Collider (LHC). The LHC project has been designed to allow for a wide physics program, from the search of new physics to the precision measurements of the Standard Model (SM) ³⁾. Differently to the majority of soft products from proton-proton collisions, which have $p_t \sim 1$ GeV/c, interesting physics, including decay products of new physics heavy particles, are expected to be produced with large transverse momentum. High p_t event rate is dominated by jet production and this high QCD background does not allow to select hadronic-only final states. Moreover, low- p_t muons from K and π decays and from c and b quarks represent a large background to interesting physics, and a precise p_t measurement is therefore needed. SuSy events over all have high multiplicity jets, or leptons, and large missing transverse energy, thus isolation criteria based on energy deposited around the muon in the calorimeter or in the trackers can be used. Table 1 reports some relevant LHC physics items, and the corresponding signature in terms of physics objects (particles). ATLAS and CMS trigger systems must therefore select events containing electrons, photons, muons, jets and large missing energy.

At the design luminosity of $10^{34} \text{ cm}^{-2} \text{ s}^{-1}$, the LHC proton-proton collisions at the center of mass energy of $\sqrt{s} = 14$ TeV yield an event rate of $\sim 10^9$ Hz, with an average of ~ 25 “minimum-bias” overlapping events. Highly efficient selection criteria are then required to select “interesting” events, which are a small fraction of the total cross section: for example, the rate of $H \rightarrow \gamma\gamma$ for a SM Higgs of 120 GeV is about 10^{-13} of the total cross section.

Another challenge for the Trigger/DAQ systems of these experiments is given by the high bunch-crossing rate, equal to 40 MHz, and the large number of read-out channels which follow the highly fine granularity of detectors. The typical event size (around 1-2 MByte) limits the rate of the events that can

be stored on tape to approximately 100 Hz. This huge rate reduction ($\sim 10^7$) must be performed on-line by the trigger systems. They need high efficiency for selecting processes of interest for physics and this efficiency must be precisely known and should not have biases affecting physics results.

ATLAS and CMS experiments use multi-level triggers, which provide a rapid rejection of high rate backgrounds without incurring much dead-time. The first-level triggers, applying inclusive trigger criteria, reduce the event rate to less than 100 kHz, the maximum rate at which front-end systems can work properly. Custom trigger electronics ensures high efficiency with fast and simple selection algorithms. One or more high-level triggers use specialized processors with higher progressive rejection power to achieve rates affordable to mass storage. At this level semi-inclusive triggers are applied with more complex algorithms, like feature extraction, vertex reconstruction, global logic and simple topology variables. ATLAS and CMS have chosen a different organization for their trigger systems, even if both systems are able to shift boundaries between levels. ATLAS foresees three trigger levels, in which the Level 2 is specialized for operating on a reduced part of the data, the Regions of Interest (RoI). The full event is build at the Level-2 rate (~ 1 kHz) and then sent to the Event Filter (EF) farm. CMS has chosen to perform its rate reduction employing only two physical layers, so that the full events are build at the output of Level-1, requiring a large bandwidth for data readout (~ 100 GB/s). Reconstruction then proceeds in virtual trigger levels: in the virtual level-2 algorithms only muons and calorimeters information are used, then, in the virtual level-3, tracker data are included.

2 First-Level Trigger Requirements

First-level trigger must take a trigger decision for each Bunch Crossing (BC), every 25 ns. In ATLAS and CMS this is based on multiplicity information from clusters found in the calorimeters and from tracks found in dedicated muon trigger detectors. Since a trigger decision is issued every 25 ns, while the trigger latency is much longer, up to $2.5 \mu\text{s}$, the trigger must concurrently process many events. For this reason custom electronics works in pipelines, performing separate steps of the processing logic in parallel at each BC period. The latency includes the time needed for signals to reach the trigger electronics and to distribute the decision back to the Front End electronics. Then latency

time is fixed by the processing time plus the data transmission along cables and fibers.

A correct BC identification is crucial for event selection and for reducing the required readout bandwidth. For this reason, the muon spectrometers are projected in order to allow a maximum time-of-flight comparable with the BC period, while the calorimeters require that the pulse shape of the signals extends over many bunch crossings to be less sensitive to noise.

High trigger efficiency is ensured by the redundancy of selection criteria, the “trigger menus”, which can concurrently select events of a wide range of physics studies, and allow the measurements of efficiency using data. First level trigger must be sufficiently flexible to face possible variations of detector performance and LHC luminosity. Rates can be kept under control by adjusting energy or momentum thresholds of physics objects or by a proper prescaling of events with large cross section.

Data-processing technologies for first level triggers make large use of (radiation hard) programmable devices, commercial FPGAs or custom ASICs, which can operate at 40 MHz and above. They also allow the implementation of many trigger algorithms and offer great flexibility, since algorithms as well as parameters can be modified once the experiments have started running. Data-movement technologies includes high-speed serial links: low-power LVDS for electrical transmission at ~ 400 Mbit/s and high performance Gbit/s transmission, both electrical and optical ones.

3 Overview of the first-level trigger systems for ATLAS and CMS

The ATLAS detector is characterized by a large geometry acceptance, an extremely high-momentum resolution muon spectrometer located inside 0.5-2 T superconductive air coil toroids, a compact calorimeter system, composed by electromagnetic and hadronic calorimeter in the barrel and endcaps, and an inner tracking system located inside the internal 2 T superconductive solenoid. The level-1 trigger system ⁴⁾ is composed of a number of subsystems, as shown in Fig. 1(a), made of processors running at 40 MHz with the LHC clock signal.

The level-1 selection is dominated by local signatures, based on coarse granularity from calorimeters and muon chambers, and the rejection is gained with local analysis of full detector data. The overcome candidate thresholds (p_t for muons, E_T and E_T missing for calorimeters) with their geographical ad-

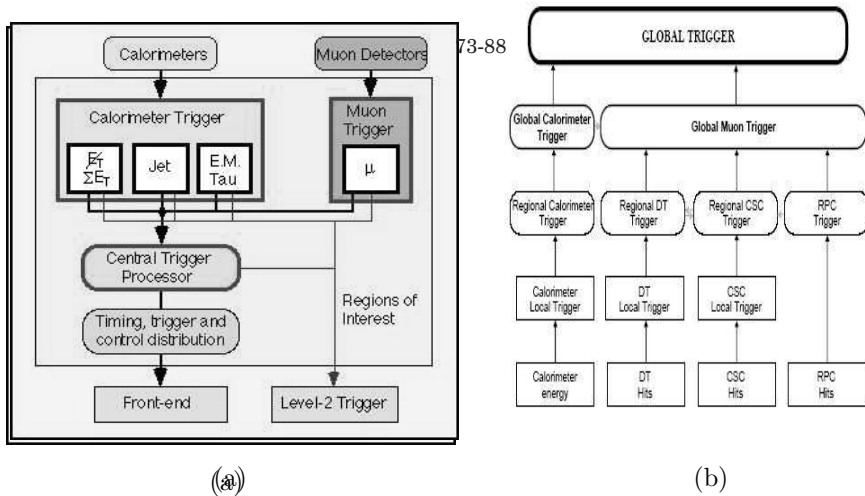


Figure 1: *The L1 Trigger System Overview for ATLAS (a) and CMS (b).*

dresses (η pseudo-rapidity and ϕ azimuth angles) are the only data sent to the higher trigger levels and represent the selected Region of Interest. Typically there are less than 2 RoIs per event accepted by the level-1 system, nominally 2% of the complete event data. Using the RoI, level-2 system accesses, in the data-buffers, only the data corresponding to the limited regions indicated. Besides these, the level-1 trigger can also provide RoI for object not participating to the selection, typically relatively low- p_t candidates.

The results of the muon and the calorimeter trigger processing are sent to the Central Trigger Processor (CTP), which takes the final decision based on multiplicities of identified trigger objects, required in coincidence or veto. Up to 96 trigger menus are available and each of them can be prescaled to accommodate trigger rates. Decisions are then sent via the TTC system to the Front End electronics to allow the readout data transmission.

CMS main feature is a strong solenoidal magnetic field ensuring high momentum resolution for charged particles ($\Delta p/p \sim 0.1 \cdot p_t$ TeV). Apart from the

superconducting coil, the apparatus consists of a silicon inner tracker with an embedded pixel detector, a lead tungstate crystal electromagnetic calorimeter, a copper-scintillator sandwich hadron calorimeter and a muon system, featuring dedicated trigger chambers, the resistive plate chambers (RPC), and a tracking system which is also used in the trigger. The latter is made up of drift tubes with BC identification capability (DT) in the barrel region, and cathode strip chambers (CSC) in the forward parts of the experiment. To improve detector coverage, a Forward Calorimeter consisting of a copper matrix with embedded quartz fibers is added in the forward regions.

The Global Trigger (GT) is the top level of L1 Trigger System ⁵⁾, and its logic structure is sketched in Fig. 1(b). The Global Trigger receives the best four (isolated and not isolated) candidates from the muon and calorimeter subsystems. The trigger objects are determined starting from local trigger information in the calorimeters and the muon system, the so called Trigger Primitives, followed by the calculations of regional and global sub-detector specific quantities. Trigger objects are sorted according to their rank, determined from transverse energy, momentum and quality informations. The highest rank objects are sent to the global trigger, which then applies threshold and other selection criteria according to physical or technical requirements. The Global Trigger of CMS also receives informations on the pseudo-rapidity and azimuthal angle of the objects. For muon candidates, charge information is also delivered. Trigger conditions based on event topology can therefore be applied already at L1. The GT logic can be programmed to calculate up to 128 different trigger algorithms in parallel for every bunch crossing. A final OR function combine all active algorithms and generates the L1 accept signal.

Table 2 shows, as an example, the expected rates for some trigger objects in ATLAS and CMS, in the case of a machine luminosity $L = 10^{33} \text{ cm}^{-2} \text{ s}^{-1}$.

4 Calorimeter Triggers

In ATLAS, the calorimeter trigger combines information from electromagnetic and hadronic calorimeter cells into trigger towers by analogue summation of the corresponding signals. There are a total of about 7200 relatively coarse granularity trigger towers, with size $\Delta\eta \times \Delta\phi = 0.1 \times 0.1$ in the region $|\eta| < 2.5$, while coarser granularity is used in the forward regions. There are two basic

Table 2: *Some of the Level-1 trigger rates, in kHz, expected in ATLAS and CMS, when applying 90 % efficiency thresholds (in GeV). The values assume a LHC luminosity of $L = 10^{33} \text{ cm}^{-2}\text{s}^{-1}$ (10^{34} for high- p_t muons in ATLAS).*

Selection	ATLAS		CMS	
	Threshold	Rate	Threshold	Rate
single e/γ	17	11	22	5.7
double e/γ	12	1.4	12	2.7
τ	20	16.3	85	3.2
jet	100	6.0	140	1.2
E_T^{miss}	51	1.0	275	0.01
total E_T	336	1.0		
single μ	6 (low p_t)	23.2	10	8.7
	20 (high p_t)	3.8		
double μ			3.3	1.6

types of calorimeters, those sampling in Liquid Argon (LAr-B, LAr-EmEC, LAr-HEC, FCAL), and the TileCal, where sampling is done by means of plastic scintillator. The signal amplitude in the branch to the trigger is weighted to transverse energy according to the tower position with respect to the beam at the nominal interaction point.

The liquid-argon based calorimeters have charge collection times of several hundred ns. This is very slow compared with the BC period of 25 ns, and so to reduce pile-up effects at high luminosity the calorimeter pulses are shaped to have a peaking time of about 40 ns and a base width of about 100 ns. The TileCal is scintillator-based, with an intrinsic time response that is short compared to the bunch-crossing period. However, its pulses are also shaped to extend over several LHC bunch-crossings in order to reduce the effect of electronic noise on the measurement of pulse height.

The ATLAS Calorimeter Trigger system is composed by a Front-End Preprocessor, which digitizes signals, extracts the E_T and assigns the correct BC. The tower thresholds, together with pedestal subtraction and final calibration in E_T units, are applied in a lookup table. These data are transmitted to the Cluster Processor, which search for isolated high- p_t electrons/photons and hadrons/taus candidates. The search is made for isolated clusters on 4×4 trigger-towers elements and looking for all possible positions of overlapping win-

dows in the detector, the so called sliding windows. The results from the window processing are combined to calculate multiplicities. There are eight sets of electron/photon and hadron/tau trigger criteria, each one being a combination of cluster thresholds and hadronic and e.m. isolation thresholds. Additional E_T sums are sent by the Preprocessor to the Jet/Energy-sum Processor, which search for high- E_T jets and calculates the missing- E_T and the scalar E_T values. The single jet element is composed by 2x2 trigger towers, while the window size used for jets depends also on the current luminosity, due to changes in the pile-up, and on the need to separate nearby jets in multi-jet events. For each of the eight thresholds, the window size can be chosen independently.

The CMS calorimetric system is made by the electromagnetic calorimeter (ECAL) and the hadronic calorimeter (HCAL) and ensures an energy resolution less than 1% for electrons and photons at 100 GeV. The ECAL is composed by a barrel and an endcap (EB, EE respectively), whereas the HCAL is subdivided into a barrel, endcap and forward section (HB, HE, and HF). The calorimeter trigger requires digitized E_T values from all its ECAL crystals and HCAL towers for every 25 ns LHC cycle. The transverse energy sum is computed for each calorimeter trigger tower, using different energy scales in different zones of the calorimeter, if needed. Programmable thresholds can be applied to individual calorimeter channels before the trigger primitives calculation, in order to improve the immunity to noise.

For the electron and photon trigger, two independent streams are considered: the isolated and non-isolated electron/photons. The isolation is determined by taking into account the lateral shower profile, the number of ECAL trigger cells involved, and the ratio of HCAL and ECAL energy deposit (which is related to the longitudinal shower profile). In each calorimeter region, defined by 4x4 trigger towers, the highest E_T non isolated and isolated electron/photon candidates are separately found. The four highest E_T candidates of both categories from each $\Delta\eta \times \Delta\phi = 3.0 \times 0.7$ region are transferred to the Global Calorimeter Trigger, where the top four candidates are retained for processing by the CMS global trigger.

The jet trigger uses the transverse energy sum, computed in calorimeter regions of 4x4 trigger towers, except in the Forward detector, where it is computed on the tower itself. Then the transverse energy is computed over

3x3 calorimeter regions. The missing E_T is computed from the sums of the calorimeter regions extending up to $|\eta| = 5.0$ and the corresponding trigger is defined by a threshold value and a prescaling factor.

5 Muon Triggers

The ATLAS Muon Trigger system makes use of hit patterns in dedicated muon detectors, RPC stations in the barrel and TGC chambers in the end-cap and forward regions, the latter having a finer segmentation albeit a larger timing resolution. Both the systems are able to provide unambiguous identification of the BC containing a high- p_t muon candidate. The logic is based on coincidence-matrix ASICs which identify muon candidates looking for coincidence of hits in different layers and discriminates their transverse momentum depending on the width of the roads used for the coincidence. In each projection, a low- p_t trigger is applied based on two planes of chambers, and a successive high- p_t trigger combines these information with the additional outer station. Further logic combines information from the two projections and track candidates are identified in 0.1×0.1 granularity regions. Among the information collected over one sector, the two highest- p_t candidates are retained and sent to the muon-trigger interface to the CTP (MuCTPI), which counts the number of muon candidates for each of the six p_t thresholds and passes the multiplicity information to the CTP.

Although using similar trigger algorithms, the barrel and end-cap systems show significant differences in electronics. The RPC fast detector signals require fine timing calibration, while the complex magnetic field map in the endcaps causes a not clear separation between the two coordinate systems, that have to be combined before making the p_t calculation.

The First Level Muon Trigger of CMS uses all three kinds of muon detectors, working independently. The excellent precision of DT and CSC ensures sharp momentum thresholds, and their multilayer structure allows an effective background rejection. They are also able to perform BC identification, although with lower precision with respect to the RPC system, which is dedicated to this purpose, due to its very high time resolution. They also respond in a different way to the various backgrounds. The DT system, with rather long drift time (about 400 ns) and CSC with charge weighting are more vulnerable

to muon radiation, for which RPC are much less insensitive. On the other hand accidental coincidence of three over four background hits can be recognized by the RPC trigger as a real muon. This is very unlikely for DT/CSC, as they look for coincidences of several planes in each muon station. Data between DT and CSC are exchanged in the overlap region ($0.8 < |\eta| < 1.2$). Optionally, coarse RPC data can be sent to the CSC trigger in order to help solving spatial and temporal ambiguities in multi-muon events.

DT and CSC electronics first processes the informations in each chamber independently, delivering vectors (with position and angle) in any muon station. Vectors from different stations are collected by the Track Finder, which combines them to form a muon track, and assigns a transverse momentum value. Up to four muon candidates from each muon sub-system are selected and sent to the Global Muon Trigger. In the case of RPC there is not a local processing, and if the hits from the different stations are aligned along a possible muon track, a p_t track is assigned.

6 Conclusions

First-level triggers for ATLAS and CMS represent a great challenge because of the large interaction rates involved by the LHC machine and the rarity of the physics processes that need to be selected. A great design work and prototyping have been done. The final prototypes systems have been tested and the production and installation phases are now going to start.

References

1. ATLAS Detector and Physics Perf. TDR, CERN/LHCC/99-15, Vol. II.
2. CMS Technical Proposal, CERN/LHCC 94-38 (1994).
3. F. Gianotti and M. Mangano, in these proceedings.
4. ATLAS First-Level Trigger TDR, CERN/LHCC/98-24 (1998).
5. The CMS Trigger and Data Acquis. Proj., CERN/LHCC 2000-038, Vol. I.

THE HIGH LEVEL TRIGGERS IN ATLAS AND CMS

Alessandro Di Mattia

Università “La Sapienza” and INFN

Marco Zanetti

Università and INFN Padova

Abstract

The High Level Trigger (HLT) systems of ATLAS and CMS provide a software based event selection after the initial Level-1 hardware trigger. It is implemented as software tasks running on large processor farms, and the foreseen rejection factor is about 10^3 for both experiments. Besides this commonalities, ATLAS and CMS have different approaches for its design which originate from an opposite philosophy of the DAQ architecture. An overview of the two architectures is presented together with examples of online reconstruction algorithms. The different trigger strategies foreseen for the LHC runs and their impact on the physics program are also discussed. Finally some remarks concerning the HLT systems commissioning are given.

1 Introduction

The ATLAS ¹⁾ and CMS ²⁾ experiments are omni-purposes detectors that will operate at the Large Hadrons Collider (LHC), a $p - p$ collider with a center of mass energy of 14 TeV and a design luminosity ranging from $2 \times 10^{33} \text{ cm}^{-2}\text{s}^{-1}$ (low luminosity phase) to $10^{34} \text{ cm}^{-2}\text{s}^{-1}$ (high luminosity phase). Although having substantial different designs, ATLAS and CMS have to face the same extreme challenges provided by the collider, in particular the reduction of the data rate approximately by a factor of 10^6 , from 40 MHz, corresponding to the interaction frequency, down to a value of the order of 100 Hz which is manageable by the persistent storage and the off-line processing. Both ATLAS and CMS split the decision whether to retain or not an event, into different stages. In both cases, the first step (Level 1), given the high interaction rate and the limited buffering capabilities, exploits algorithms implemented on custom hardware boards which process only a subset of the event data (namely from muon detectors and calorimeters) with coarse granularity and lower resolution. The output event rate of the Level 1 is designed to be of the order of 100 kHz. Subsequently, the High Level Triggers (HLT) provide a software based event selection to further reduce the Level-1 rate to ≈ 100 Hz. At the high luminosity phase, this value corresponds to a cross section of ≈ 10 nb which matches the prediction for $\sigma(pp \rightarrow W^+ \rightarrow \mu^+\nu)$; it is therefore evident how critical is the role of the HLT which has to perform *online* the first actual physics analysis.

2 DAQ and HLT Architectures

Being the identification and selection of the interesting events a real time procedure, the reliability of the entire DAQ and HLT systems is a critical issue for both the experiments in order to reach their full physics potential. The main guidelines that define the design and the development of the HLT of ATLAS and CMS are based on the following considerations:

- the performances and the working conditions of the collider and of the detectors are not precisely predictable and vary with time; in this sense the flexibility of the system is a crucial issue;
- the HLT should fulfill the physics programs as well as be inclusive enough

in order not to reject unexpected phenomena;

- the system should be robust, i.e. it should not rely too much on the changes of the calibration and detector alignment constants;
- to maximize the efficiency of the filtering process, an uninteresting event should be rejected from the data flow as soon as possible;
- it must be possible to validate the trigger and to compute the overall selection efficiency using only the data, relying as less as possible on simulation;
- the HLT should benefit of all the major features of the offline software, in particular it should be as close as possible to the offline reconstruction code;

Moreover, being the experiments life extended over 20 years, the long term maintainability is a critical issue too. Previous experiences have shown that custom electronics is more difficult to maintain and upgrade than comparable commercial products. Therefore the use of commercial computing and network equipment is required, because it helps to maintain the system over the full life time of the experiment.

2.1 ATLAS Architecture

After the initial Level-1 selection, the data coming in parallel from the detector readout are handled by the HLT/DAQ system. Taking into account the estimates of the bandwidth that will be used by the ATLAS subdetectors, the total readout bandwidth is of about 200 GBytes/s. This constitutes a formidable challenge for the switching network that accounts for the data transmission through the entire system: the use of a bare network schema would require to implement thousands of connections with a data throughput that reaches the performance limit of the current commercial equipment. Moreover, since the estimate of the total bandwidth depends on the working conditions of the detectors (luminosity delivered by LHC, fluctuations on the Level-1 rate, detector occupancy), the network must be dimensioned to face the fluctuations of the data rate.

To cope with this problem, the ATLAS architecture ³⁾ is designed to minimize the data movement towards the HLT processors. At the early stage

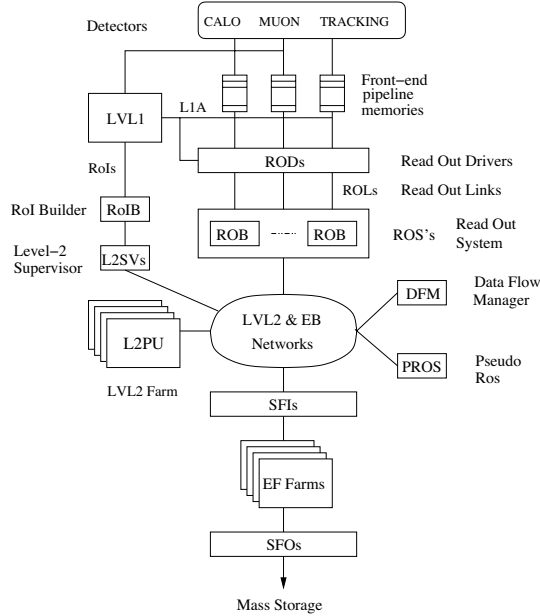


Figure 1: *The ATLAS Trigger/DAQ system.*

of the HLT processing, the event data fragments are held separately in memory buffers (the ROBIN) and wait for the decision whether to be assembled into a complete event for the final selection or to be discarded. This constitutes an intermediate step of the HLT trigger, which is called Level-2. The trigger algorithms make use of the full granularity data but access only the detector regions that has been flagged by the Level-1 as those containing the physics candidates (the Region of Interest, RoI). The RoI based access allows to use only 2% of the event data to take the Level-2 decision, thus limiting the required bandwidth of the dataflow. A further reduction of the data traffic is obtained by multiplexing the detector readout into the ROBINs in such a way as to gather together data from detector elements which are projective aligned towards the interaction vertex. This increases the probability to access a single ROBIN per RoI. The design foresees that the Level-2 will reduce the Level-1 rate by a factor of about 30 with a latency of about ~ 10 ms. To achieve this rejection power in such a small time the Level-2 algorithms will perform an approximate reconstruction of the physics candidate avoiding the use of the

fully detailed calibration constants of the detectors.

After the Level-2 decision, the data are delivered to the Event Filter processor farm to take the final decision on the event. At this stage the algorithms employed are derived from the offline reconstruction software and access to the full event data. The increase of the reconstruction accuracy provides a rejection of the Level-2 accept rate of about a factor 10. But the use of more sophisticated procedures, which make use of complete detector calibrations, requires more time to execute the algorithms. Therefore the latency time of the Event Filter is estimated to be about ~ 1 s.

Both the Event Filter and the Level-2 algorithms run into a common software framework which reuses part of the offline software components. In particular all the interfaces towards the data, and the code providing the detector description and calibration is implemented by the same offline tools. This eases the development and the study of the selection algorithms optimizing the manpower and, at the same time, increases the long term maintainability of the code. But the use of pure offline components into the online environment clashes sometimes with the latency requirement thus requiring their replacement with highly optimized code, especially in the Level-2 environment.

The general schema of the ATLAS Trigger/DAQ is shown in figure 1. The detector data flows through ~ 1600 Read Out Drivers (RODs) into the Read Out System (ROS). This is realized by standard PCs hosting several ROBIN boards. The data concentration into the ROS's is about 10, therefore ~ 150 machines will be employed to buffer the data within the Level-2 decision. On the contrary the Level-1 trigger data are processed by the RoI Builder (ROIB), and then sent to a Level-2 Supervisor (L2SV), which manages the Level-2 operations. The Level-2 algorithms run into the Level-2 Processing Units (L2PU) of the trigger farm which is made of ~ 500 biprocessor machines. In case of a "Level-2 accept", the result is stored into the pROS as a part of the event data and then is sent through the Event Builder and the SFI to the "EF farm" together with the ROS's data under the supervision of the DataFlow Manager (DFM).

2.2 CMS Architecture

The main feature and peculiarity of the CMS architecture ⁴⁾ is that the Data Acquisition system performs the HLT event selection in a single farm of com-

mercial processors, the Filter Farm (FF). This design principle has been established in order to take advantage of the extraordinary and constant rate of evolution in computing technology either in processing power and in network speed. Avoiding a physical intermediate level in the selection chain allows the HLT to be entirely software implemented, and to access full resolution and granularity data as well as calibration and alignment monitored constants. More in details, the data from each detector front-end belonging to a “L1-accepted” event, are collected by a set of Read-out Units and then delivered to the Builder Units (BUs) through a large switching network (Read-out Builder Network). The network bandwidth required is of the order of 1 Tbyte/s. The BU receiving the data fragments is responsible for the actual building of the event and serves it to a Filter Unit (FU) via another switching system, the Filter Farm Network. The FUs are the components of the FF where the HLT code is executed and the selections are applied¹. The selected events are then forwarded to the computing services for storage or for further analysis. A picture of the CMS DAQ architecture is shown in Fig. 2. A key feature of the FF is that the raw data is delivered to the FU only if requested by the specific HLT algorithm; this allows to reduce either the data traffic and the HLT processing time. The computing power needed by the FF is estimated to be as high as 10^6 *SI95* corresponding to $\mathcal{O}(10^3)$ GHz processors. Given the average event size of the order of 1 MB and the manageable output rate of $\mathcal{O}(10^2)$ Hz, 1Tbyte of data will be written on the mass storage every day.

3 Reconstruction Algorithms

The HLT selections are based on the precise and efficient reconstruction of the physical objects, i.e. e , γ , μ , τ , *jets* and *b-jets*. The higher the stage of the selection chain, the larger the amount of data and the greater the time available by the reconstruction algorithms. In the following, as examples of the way physical object are measured and identified by ATLAS and CMS HLT systems, two reconstruction algorithms will be illustrated.

¹Actually the event building and filtering is performed in eight independent slices, each one of which could in principle perform the whole process by itself. This address the issue of the scaling of the system

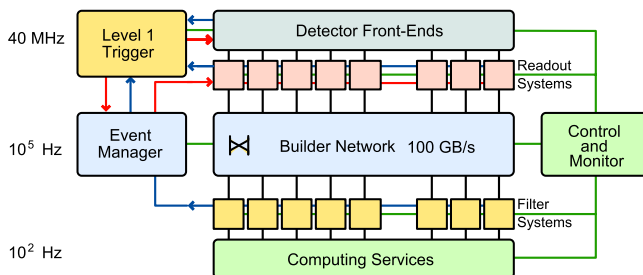


Figure 2: *Schema of CMS Data Acquisition system.*

3.1 Online muons reconstruction in ATLAS

The HLT muon selection in ATLAS comprises the Level-2 trigger and the Event Filter. The Level-2 identifies muon objects and estimates their physics properties with a set of optimized algorithms. At this stage the event selection is mostly based on the physics of the single muon, therefore the algorithms are tuned to provide the best physics performance while reconstructing the muon features around the selection threshold values. On the contrary, the Event Filter employs a complete muon reconstruction program, based on offline packages, that provides very good performance over the full spectrum of muon events. This allows to select the events using also tight invariant mass criteria. The task of the Level-2 muon trigger can be decomposed into a number of broad steps: validation of the Level-1 muon RoI, combination of the muon track with the Inner Detector tracks, check for isolation in the calorimeter and recovery of the very low- p_T muons not triggered by the Level-1 (i.e. search for secondary RoIs). The aim of the first step is to reject the fake Level-1 triggers and to operate a first reduction of the Level-1 rate by means of a more precise measurement of the muon transverse momentum² (p_T). The algorithm doesn't make use of time consuming fit methods: muon hits are recognized by means of geometrical criteria and the track is reconstructed with a set of linear segments fitted on each muon station. Nevertheless the resolution of the transverse momentum reconstruction is 6% at the low- p_T threshold (6 GeV) and 4% at the

²The better quality of the momentum measurement, with respect to that provided by Level-1, allows for a sharper p_T threshold.

high- p_T threshold (20 GeV). The good quality of the momentum measurement allows to reduce the Level-1 input rate by a factor of about 2 at 6 GeV and by a factor of about 10 at 20 GeV. The rejection of the Level-1 fake triggers is about 10^3 and is provided by requiring at least two segments per track. After the RoI is confirmed, the selected sample is refined depending on the given trigger threshold. For high- p_T muon triggers the calorimeter energy deposition around the track direction is analyzed to confirm the track is isolated. On the contrary, the low- p_T muon triggers undergo to a sharp refinement, which involve the use of the Inner Detector data. Extrapolating backward the muon flight direction, a small slice of Inner Detector is identified where to search for tracks compatible with the muon one. The matching candidate allows to refine the estimate of the muon p_T thus yielding a reduction factor of about 2.5 of the Level-1 low- p_T rate. A further reduction is obtained requiring the muon event is compatible with a $J/\psi \rightarrow \mu^+\mu^-$ decay. In this case a wide region of the Inner Detector is reconstructed to search for the second decay muon track. To be identified as a muon, the Inner Detector track is demanded to be consistent with hits in the innermost MDT station. A loose cut on the invariant mass of the dimuon system is also applied. The Inner Detector data are also employed to confirm the high- p_T triggers, but the criteria used are less stringent because the rate is not demanding.

Being seeded by the Level-2 result, the muon algorithm in the Event Filter starts to reconstruct the spectrometer data. This standalone reconstruction is implemented with offline algorithms that make use of combinatorial technique to identify the muon hits and involve the complete magnetic field map in the fit. To improve the performance on high- p_T momentum reconstruction, the multiple scattering effect along the track path is recovered taking into account the material distribution crossed by the muon. As in Level-2, the muon track is propagated backward to the Inner Detector to search for the muon hits. Once identified, these are entered in the global fit to refine the track reconstruction. After the combined reconstruction the complete definition of the muon track through the ATLAS detector is available to be used for the final trigger menu selection. Altogether the Event Filter reconstructs the muon momentum with a resolution close to that provided by the offline program, i.e. $\sim 2.5\%$ for muons up to $p_T \simeq 200\text{GeV}$. The sophisticated techniques employed by the Event Filter require a large amount of CPU time that, at present, clashes with the

latency requirement. To limit the CPU usage, the reconstruction is performed only in a wide region around the muon RoIs. Optimization studies are ongoing to see if it is possible to execute the standalone reconstruction over the full spectrometer.

3.2 Online electrons and gammas reconstruction in CMS

The CMS HLT selection of electrons and gammas proceeds in three steps. At the beginning, namely L2³ the electron/photon candidates are reconstructed exploiting only the calorimetric information with the full granularity. The reconstruction is performed in the regions indicated by the Level 1 candidates. In order to recover the energy radiated by electrons and converted by photons in the tracker material, “super clustering” algorithms are used.

The second step, L2.5, demands hits in the pixels vertex detector consistent with a L2 candidate. The expected hit position on the pixels layers is estimated by propagating inward the energy weighted average impact point of the candidate to the nominal vertex position. If at least two hits are found, the candidate is classified as an electron, otherwise as a γ . The rate of the photons candidate is further reduced applying higher thresholds energy cuts than in the electron stream. The γ selection can also use isolation requirements, lateral shower shape for π^0 s rejection and reconstruction of converted photons. In the final step, L3, the algorithm to select the electron candidates has enough time to use the tracker hit in order to perform a full track finding and reconstruction. Cuts are then applied on E/p and on difference in η between the extrapolated track and the supercluster position. Isolation is required for both electrons and photons.

4 Triggers

A major issue concerning the HLT selection is *what* to save permanently on the mass storage. More precisely, the question about which trigger streams has to be settled and how much bandwidth needs to be allocated for each of them has to be addressed. The answer is of course a compromise between the request of

³the name L2 does not represent a physical layer in the HLT chain. Given the entirely software implementation of the HLT, an arbitrary high number of intermediate stages could be implemented

Table 1: *ATLAS and CMS High Level Trigger tables.*

Streams	ATLAS		CMS	
	Thresholds (GeV)	Rate (Hz)	Thresholds (GeV)	Rate (Hz)
<i>Single μ</i>	20	40	19	25
<i>Double μ</i>	10	10	7	4
<i>Single e</i>	25	40	29	33
<i>Double e</i>	15	< 1	17	1
<i>Single Photon</i>	60	25	80	4
<i>Double Photon</i>	20	2	40,25	5
<i>Single Jet, 3 Jets, 4 Jets</i>	400, 165, 110	30	657, 247, 113	9
<i>Jet + missing E_T</i>	70, 70	20	180, 123	5
<i>τ jet + missing E_T</i>	35, 45	5		
<i>τ jet</i>			86	3
<i>Double τ jet</i>			59	1
<i>$e + \tau$</i>			19, 45	2
<i>b-jet</i>			237	5
<i>b-physics</i>	topological	10		
<i>Prescaled, calibration</i>		20		10
Totals		200		105

maximal efficiency for the physic program and the total bandwidth and CPU power available. It also depends strongly on the phase of the experiment and the actual conditions of the LHC and the detectors.

ATLAS and CMS performed the exercise⁴ of listing a feasible set of selections for standard LHC running condition at $\mathcal{L} = 2 \times 10^{33} \text{ cm}^{-2}\text{s}^{-1}$. The established outcome is summarize in Table 1. Within the streams listed in Table 1, tree kind of triggers can be identified, each one responsible of a different part of the physics program.

⁴Neither the thresholds nor the associated rates must be taken as the final ones; it is probable that a better knowledge of the detectors and of the phenomenology will lead to a better tuning of the selection cuts. Moreover the associated rated should be compared only by order of magnitude since they rely on different physics assumptions

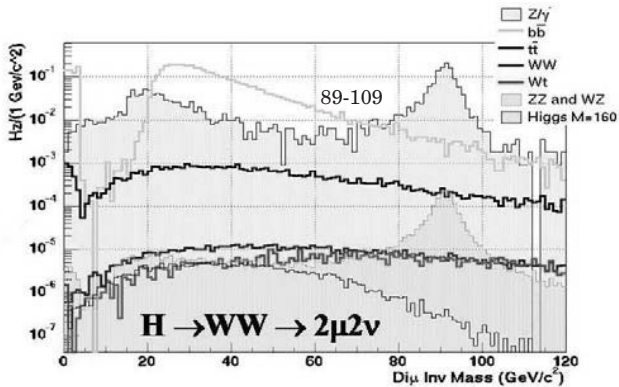


Figure 3: *Output of dimuon stream of CMS HLT for $h \rightarrow W^+W^- \rightarrow \mu^+\nu\mu^-\bar{\nu}$ and main backgrounds.*

4.1 Inclusive Triggers

By means of these, most of the physics program of the experiment will be covered as well as eventual unexpected phenomena at the TeV scale. In normal LHC run condition, most of the bandwidth will be dedicated to such streams. One of the golden processes for the Higgs boson discovery at the LHC is the decay $h \rightarrow Z^0Z^0 \rightarrow e^+e^-e^+e^-$. The ATLAS HLT will selected these events with high efficiency in the single and double isolated electron streams (97% for event with 2 e with $p_T > 20\text{GeV}/c$, $|\eta| < 2.5$).

In the case the Higgs particle has a mass within the range $[150 - 170] \text{GeV}/c^2$, because of the favorable branching ratio, the decay into W boson pairs dominates and the processes $h \rightarrow W^+W^- \rightarrow \mu^+\nu\mu^-\bar{\nu}$ becomes one of the most appealing channel for a fast discovery. In CMS the efficiency for selecting these kind of events with μ s within detector acceptance ($p_T > 3\text{GeV}/c$, $|\eta_\mu| < 2.5$) ranges from 93% for $M_h = 150$, to 95% for $M_h = 170$. In Fig. 3 the contribution of various processes to the “dimuon” stream is shown. The invariant mass of the dimuon system is reconstructed by the L3 muon algorithm.

4.2 Exclusive Triggers

Some interesting physics processes have kinematic features that do not allow the standard inclusive triggers to select them efficiently. In order not to loose

the chance to investigate such phenomena, dedicated triggers are then needed to save those kind of events for off-line analysis. The most important example is the physics related to the quark beauty whose rare decays could reveal new scenarios beyond the Standard Model. The most suitable final states, i.e. for a hadronic collider like the LHC the muonic ones, although having peculiar topological and kinematic properties, are mainly populated by low p_T muons, usually well below the single and double inclusive thresholds. In order to retain these kind of events, the HLT selection exploits part of the inner detectors information from the beginning, otherwise utilized only at the last stage.

At low luminosity ($\mathcal{L} < 2 \cdot 10^{33} \text{ cm}^{-2}\text{s}^{-1}$) the ATLAS B-physics High Level Trigger is initiated by a low- p_T muon trigger, confirmed by Level-2, in combination with an electromagnetic trigger or a jet trigger. Then, a fast track algorithm performs an unguided search for tracks in a wide region of the inner detector. These tracks serve as seeds for the semi-exclusive reconstruction of the interesting decay channels, e.g. $B_d \rightarrow \pi^+\pi^-$, $D_s^- \rightarrow \Phi(K^+K^-)\pi^-$, $J/\Psi \rightarrow \mu^+\mu^- (e^+e^-)$. It proceeds combining couple of opposite charged tracks to identify a specific parent particle on the basis of the invariant mass. The combinatorial background is reduced by means of cuts on the scalar sum of the transverse momenta and on the difference of the z-intercept of the two tracks. The minimum p_T required to a track for entering in this procedure depends on the decay channel: it is 4 GeV for events with pions, but it drops down to 2 GeV for events with electrons. These latter are the most challenging for the track reconstruction and imply the use of the TRT data at Level-2 to identify the electrons down to very low- p_T . The boundary between the Level-2 and the Event Filter is set by the techniques used to improve the track reconstruction quality. The recovery of the electron bremsstrahlung and the primary vertex reconstruction are CPU intensive calculations which are executed at the Event Filter stage. By means of these the Event Filter can apply a tighter invariant mass cut on the sample selected by the level-2.

The CMS dedicated HLT selections for b -physics are described in Ref ⁴). An important example of those is the exclusive trigger for the decay $B_s \rightarrow \mu_+\mu_-$. It happens in two stages, the first one based only on the vertex detector measurements, the second exploiting the whole tracking system. As first step a fast track and vertex reconstruction is performed looping on pixel hit

pairs; starting from the obtained track-seeds, the algorithm execute the track reconstruction in the tracker. If and only if two opposite charged tracks are founded, the dimuon invariant mass is required to met the B_s mass within a range of $\pm 150 \text{ MeV}/c^2$. In order to suppress combinatorial background, χ^2 and decay length transverse distance criteria are applied. The selection efficiency for the signal is 33.5% with an average execution time of 240 ms on 1 GHz CPU.

4.3 Prescaled, calibration and monitoring triggers

These triggers will play a crucial role for understanding, validating and debugging, either the detectors and the first LHC data during the first months of running.

The prescaled triggers are meant to extend the physics coverage of the on-line selection by enlarging the kinematic reach of the various measurements, e.g. towards smaller values of transverse momentum. A typical example is the measurement of the jet cross section over the full kinematic range, starting from the lowest achievable E_t value up to the region covered by the inclusive trigger. Prescaled triggers will be also crucial for determining the trigger efficiency from data, e.g. via bootstrap methods.

Calibration of the various subdetectors and monitoring of their performances are critical issues for every kind of physics measurement. As an example a strategy for a fast intercalibration of the different parts of the electromagnetic calorimeter must be developed. Ref ⁵⁾ addresses the latter item. The method suggested there makes use of the ϕ -symmetry of deposited energy to intercalibrate the CMS electromagnetic calorimeter (ECAL) crystals within rings at constant η ⁵. Single jet events triggered by L1 with a threshold of 120 Gev are used, the region within $\Delta R < 1.0$ of the trigger jet being excluded to avoid the most obvious trigger bias. Of these events, only the ECAL data are processed by the HLT, where the threshold is raised to 150 GeV. A dedicated high frequency (1 kHz) bandwidth is allocated for this calibration trigger. Eleven million jet trigger events, i.e. few hours of data taking during low luminosity phase, are sufficient to perform the intercalibration to a precision between 2% and 3%, depending on η .

⁵This method needs to be used in conjunction with another method to intercalibrate the ϕ rings - $Z^0 \rightarrow e^+e^-$ has been suggested

5 ATLAS and CMS commissioning

In order to be ready for the data taking and analysis in 2007 at the scheduled LHC startup, the certification and checking of the functionalities, the expected performances of the various sub-detectors and the detector as a whole must start well in advance. This should be done by means of real data to the maximum extent. In the period before the LHC installation ATLAS and CMS plans foresee to exploit cosmic muons. Later, as soon as the collider will provide the first single beam, the beam halo and the particles produced in the interactions of the beam with the gas in the vacuum pipe will be used too.

During this commissioning phase, the DAQ/HLT system carries out a twofold role: as part of the detector, it has to be commissioned as well as the other subdetectors, moreover it is a crucial tool for the commissioning of the latter. The first step is to verify the correctness of the data flow. In this context the detectors front ends synchronization, the event building from the data fragment and the actual event data flow through the HLT chain are the main issues. Because of the additional physical layer in the HLT system, ATLAS will be more focused on the precise understanding and debugging of the latter item, in particular of the RoI mechanism. On the contrary the most critical feature of the CMS HLT, the event building, will be stressed only when high rate of sizable events will be provided by the Level 1 trigger, i.e. during standard LHC runs. Because of the very low event rate in this phase no selection will be applied by the HLT. This allows part of the online reconstruction algorithms to be tested and debugged. The HLT commissioning will be completed during the LHC $p - p$ runs, when the whole infrastructure will be in place on the basis of physics performances, i.e. efficiency for interesting processes and rejection for minimum bias and underlying events.

6 Conclusions

The ATLAS and CMS HLT systems, although based on different approaches, the former on two physical layers in order to reduce the data throughput, the latter implemented on a single processors farm for exploiting the maximum flexibility, are designed to reduce the LHC event rate to $\mathcal{O}(100)$ Hz with high efficiency for the whole physics program. In both experiments the HLT system development has been going on successfully and it is ready to be commissioned

during the incoming period of cosmic muons tests and the first days of LHC activity.

References

1. the ATALS collaboration, Technical Proposal, CERN/LHCC 98-4 (1998).
2. the CMS collaboration, Technical Proposal, CERN/LHCC 94-38 (1994).
3. the ATLAS collaboration, ATLAS High-Level Trigger Data Acquisition and Controls Technical Design Report, CERN/LHCC 2003-022, ATLAS TDR 016 (2003).
4. the CMS collaboration, Data Acquisition and High-Level Trigger Technical Design Report, CERN/LHCC 2002-26 (2002).
5. D. Futyan and C. Seez, *J. Phys. G: Nucl. Part. Phys.* 29 (2003) 1299-1326

Session II – Physics Tools

MUON RECONSTRUCTION AND IDENTIFICATION IN ATLAS AND CMS

Nicola Amapane

Università di Torino and INFN Torino, Italy

Michela Biglietti

University of Michigan

Abstract

The ability to identify, reconstruct and trigger on muons is essential for LHC experiments, since most of the physics LHC is designed to explore is characterized by the signature of muons. The different design principles of the ATLAS and CMS muon spectrometers and the implications on operation and reconstruction strategies are discussed.

1 Introduction

Efficient muon identification with accurate momentum measurement is crucial to fully exploit the physics potential of the ATLAS and CMS experiments, both in the trigger and in the off-line reconstruction. To meet the LHC physics goals, a momentum resolution of about 10% up to muon transverse momenta of $p_T = 1 \text{ TeV}/c$ will be required.

Very different strategies were adopted by ATLAS and CMS to achieve this goal, starting from the choice of the magnetic field configuration: a very intense solenoidal field for CMS and a large toroidal field for ATLAS. These choices determine the requirements on the detectors to be used and on their operation.

The ATLAS air-core toroids allow measurements with large lever arm, degraded very little by multiple scattering. To reach the desired p_T resolution, however, very challenging requirements on position resolution, alignment and knowledge of the complex magnetic field have to be met. Also, a toroid does not provide the field for the inner tracker system, so an additional small solenoid is used for this purpose. The inner tracker improves the muon p_T resolution for very low- p_T muons.

The single CMS solenoid allows a very compact and relatively simple design. The 4 T field inside the solenoid allows very precise central tracking, while the return flux in the instrumented iron yoke allows an independent momentum measurement. This measurement is largely affected by multiple scattering, so the full p_T resolution can be obtained only combining it with the measurement of the inner tracker, which dominates the resolution up to $p_T \sim 200$ GeV/ c . On the other hand, the CMS muon spectrometer is subject to much less stringent requirements on resolution, alignment and knowledge of the magnetic field than the ATLAS spectrometer.

1.1 The ATLAS Muon Spectrometer

The measurement of muon momentum in ATLAS is based on the magnetic deflection of muon tracks in a system of three large superconducting air-core toroid magnets instrumented with trigger and high precision tracking chambers. The overall size of the ATLAS muon spectrometer¹⁾ is about 22 m in diameter and 44 m in length. In the pseudorapidity range $|\eta| \leq 1$ (barrel), the magnetic bending, provided by eight large barrel toroids, varies between 2 and 6 Tm, with large variations as a function of the azimuth angle. In the endcap regions ($1 < |\eta| < 2.7$) the deflection is obtained by means of two air-core toroids placed in the external parts of the barrel toroid, with a design bending power ranging from 4 to 8 Tm. The toroidal configuration permits to have high bending power and a constant transverse momentum resolution up to large values of η . Moreover, the choice of an open geometry system permits to minimize the

effects of the multiple scattering and of the magnetic force. The drawback of this design is the relatively low magnetic field that can be reached. High resolution detectors, small calibration and alignment errors are thus required.

Both in the barrel and in the endcap regions the muon trajectory is sampled in three high precision stations equipped with Monitored Drift Tubes (MDT). Each station holds a pair of MDT multi-layers, consisting of 3 (4 in the innermost station) layers of cylindrical drift tubes, and measures the muon positions with a precision of about $50 \mu\text{m}$. In the innermost region, at $2 < \eta < 2.7$, the MDTs are replaced with four layers of Cathode Strip Chambers (CSC) which show a smaller occupancy and provide measurements with resolution in the range of $50 \mu\text{m}$ both in the radial and in the azimuthal direction. The muon trigger is provided by Resistive Plate Chambers (RPC) in the barrel and by Thin Gap Chambers (TGC) in the endcaps. The trigger chambers also provide spatial measurements in the direction orthogonal to the bending plane, with a typical resolution of about 1 cm. The RPCs are pairs of detectors read out by strip panels measuring both η and ϕ . Two layers of RPCs are placed in the middle stations and one in the outer station. Two doublets and a triplet of TGC provide the trigger in the endcaps up to $\eta = 2.4$; each chamber provides coarse measurements of ϕ , via pick-up strips, and of r from the signal collected on groups of wires. Another doublet of TGC, located in the innermost layer, does not take part in the trigger system. The gas mixture used and the trigger chamber operation allow for a very limited local dead time and a time resolution of 1.5 ns, ideal for bunch crossing identification.

1.2 The CMS Muon Spectrometer

With a diameter of 6 m and a length of 13 m, the 4 T CMS solenoid provides a bending power of about 12 Tm in the in the barrel region ($\eta < 1.45$), decreasing to about 4 Tm at $\eta \sim 2.4$. The muon spectrometer is located within the iron yoke, where the return field can reach about 1.8 T and the bending power varies with η between 3 and 0.6 Tm.

The large bending power and the multiple scattering due to the amount of material in the muon spectrometer lead to relatively modest requirements on detector resolution and alignment. With a chamber spatial resolution of the order of $100 \mu\text{m}$, the muon system improves the transverse momentum resolution for $p_T \gtrsim 200 \text{ GeV}/c$, while the the inner tracker dominates the

resolution for lower momenta.

The CMS muon system ²⁾ consists of three independent subsystems. In the barrel ($|\eta| < 1.2$), where the track occupancy and the residual magnetic field are low, drift tube detectors (DT) are installed. DT chambers are arranged in four concentric cylinders (stations) of 12 or 14 chambers. Cells have a size of 42×13 mm and are operated with an Ar/CO₂ mixture at atmospheric pressure. The electric field is obtained with positively-biased insulated strips that shape the field in order to obtain a good distance-time linearity. Four staggered layers of parallel cells constitute a super-layer, which allows to resolve the left-right ambiguity of a single layer and provides the measurement of a two-dimensional segment. Also, it measures the bunch crossing originating a segment with no need of external input, using a generalisation of the meantimer technique ³⁾. A chamber is composed by two super-layers measuring the $r - \phi$ coordinates, with the wires parallel to the beam line, and an orthogonal super-layer measuring the $r - z$ coordinates. The latter is not present in the outermost station.

In the endcaps, up to $|\eta| < 2.4$, cathode strip chambers (CSC) are used. These multi-wire proportional chambers, operated with a Ar/CO₂/CF₄ mixture at atmospheric pressure, have good spatial and time resolution and can be operated at high occupancy levels and in the presence of a large inhomogeneous magnetic field. For this reason they were adopted in the endcap region. CSC chambers are arranged in four disks (stations) placed between the iron disks of the yoke. Chambers are composed of six layers, each consisting of an array of anode wires, measuring the non-bending coordinate, between segmented cathode planes, with a 9.5 mm gap. The bending coordinate is measured interpolating the charge induced on the cathode strips.

Redundancy is obtained with a system of resistive plate chambers (RPC), that are installed in both the barrel and in the endcaps up to $|\eta| < 2.1$. RPCs have limited spatial resolution, but fast response and excellent time resolution, of the order of 2 ns, providing unambiguous bunch crossing identification. They are also used to complement DTs and CSCs in the measurement of the p_T .

All three system contribute both to the muon Level-1 trigger and to the muon reconstruction in the High Level Triggers. However, at the LHC startup no trigger electronics will be installed for the innermost chambers of the first CSC station, thus limiting the Level-1 trigger acceptance to $|\eta| < 2.1$. Additionally, the outermost ring of the fourth CSC station, as well as all RPC

chambers above $|\eta| = 1.6$, will be installed in a later stage.

2 Alignment and Calibration

Calibration is a task of great importance in high precision systems like the ATLAS muon spectrometer, especially for high- p_T measurements where the resolution is dominated by wire calibrations and alignment. For the reconstruction of a track segment in a MDT multilayer, a good knowledge of the space-drift time relationship $r(t)$ is required. The error on $r(t)$ should be small ($20 \mu\text{m}$) compared to the MDT single-tube resolution ($80 \mu\text{m}$). The determination of the space-drift time relationship can be obtained with well established autocalibration procedures ⁴⁾ using data recorded by the MDT tubes during the passage of muon tracks. These procedures have been tested on test beam data, comparing the results of the procedure with the $r(t)$ calibration obtained using an external tracker.

Another ingredient for achieving the desired resolution at high transverse momenta is an excellent alignment system that enables the monitoring of the position of the different chambers in the spectrometer with a precision better than $30 \mu\text{m}$ ⁵⁾. The basic elements of this system are RASNIK ⁶⁾, optical monitors that provides a very accurate measurement for both the in-chamber deformations and the relative displacement of different chambers. Test beam data show that the required resolution on the sagitta can be achieved when the alignment system is used.

The absolute calibration of the muon spectrometer depends finally on the magnetic field knowledge. The toroidal magnetic field of the muon spectrometer will be measured using about 5000 Hall probes with 0.1% resolution, which determine the field components locally. Further refinements of the field map can be obtained via the study of the $Z \rightarrow \mu\mu$ resonance, for which we expect a rate of 1.5 Hz at low luminosity and 20 Hz for high luminosity operation, with a simultaneous fit of the magnetic field and of the energy loss in the calorimeters ⁷⁾.

The CMS muon spectrometer has much less stringent requirements on alignment and calibration, since the required detector resolution is relatively low. In the DT cells, the field shaping is such that the drift time is to a good approximation linear with the distance from the wire. Relatively simple calibration procedures have been successfully used in testbeam analysis ⁸⁾. The

residual non-linearity can be corrected using parameterizations obtained from simulations of the cell or from real data, but this will not be critical for the initial operation.

The alignment system of the CMS muon spectrometer ⁹⁾ is based on rigid frames with optical links (LEDs, lasers and CCD cameras). Special link lines are used to align the muon spectrometer with the inner tracker with a precision of the order of 80 μm . Alignment procedures with reconstructed muons are limited by the imperfect knowledge of the material budget and of the inhomogeneous magnetic field in the yoke. Due to the large multiple scattering, only high momentum muons ($p_T \gtrsim 50 \text{ GeV}/c$) can be used. Preliminary studies indicate that a quite large statistics will be needed before this procedure exceeds the precision of the mechanical alignment system.

It must be noted that the magnetic field induces large deformations in the iron yoke. A movement of up to 1 cm distributed in the longitudinal direction is expected in each half of CMS. Therefore, alignment constants cannot be determined until the field is switched on.

In winter 2005, the complete magnet system will be ramped up in the surface hall. This will allow to map the magnetic field by means of a dedicated rotating arm equipped with Hall and NMR probes, to monitor the movements of the yoke and test the alignment system. During detector operation, the field will be monitored with a set of NMR probes installed within the solenoid and flux loops installed on selected segments of the yoke.

3 Muon Reconstruction

For the muon reconstruction in ATLAS the packages MOORE/MuId ¹⁰⁾ and MUONBOX/STACO ¹¹⁾ have been developed; in this section the method of muon track reconstruction as applied in MOORE and MuId is presented. MOORE reconstructs tracks inside the muon spectrometer starting with a search for regions of activity within the detector, using mainly the measurements of the trigger chambers. Subsequently MOORE performs the pattern recognition in the precision chambers using a realistic $r(t)$ relation, and forms track candidates from the selected hits. The final reconstructed objects are successfully fitted tracks, whose parameters are expressed at the first measured point inside the muon spectrometer. The purpose of MUID consists in combining tracks found in the muon spectrometer with the corresponding inner

detector track, in order to provide the best estimate of the kinematic parameters of the muons at their production vertex. The first step is the extrapolation of tracks to the vertex region, taking into account the multiple scattering and the energy loss in the calorimeters. Inner detector and muon tracks are then matched and all combinations giving a satisfactory combined fit are retained as identified muons. The results of the muon reconstruction show that at low momenta the inner detector ($p_T < 50$ GeV/ c) has the dominant contribution to the momentum resolution. The reconstruction efficiency is about 95% for muons with $p_T > 10$ GeV/ c . Recent studies done with the startup muon spectrometer layout show a degradation of the resolution and efficiency in the the rapidity range $1 < |\eta| < 1.3$, where the station providing the middle measurement point for the sagitta reconstruction (EE wheel) are missing. On the other hand, the postponed installation of half of the CSC stations appears to be less damaging than the complete absence of the EE stations.

The reconstruction efficiency is lower for low- p_T muons because muons lose a significant part of their energy in the calorimeters, and thus some of them cannot be reconstructed in the muon spectrometer. To identify those muons a dedicated algorithm has been developed; it allows the identification of low- p_T muons by extrapolating inner detector tracks into the muon spectrometer and looking for nearby hits. Using this method the efficiency for low- p_T muons can be increased significantly ¹²⁾.

The standalone and combined muon reconstruction procedures have been validated on real data during the 2004 combined H8 test beam. The studies on the collected data include track reconstruction, both in the individual subsystems and combining all muon technologies; combined reconstruction using the information of calorimeters and inner trackers; sagitta reconstruction and comparison with simulated data; and muon energy reconstruction exploiting the magnetic system deployed in the H8 setup. All the studies have been done using the final ATLAS software, including also the simulation of the test-beam geometry and detector response and show the good performances of the muon software in a real data taking environment.

In CMS, muon reconstruction is developed within ORCA ¹³⁾, the CMS object-oriented reconstruction software. Algorithms are implemented using the concept of *regional reconstruction*, that is the ability to reconstruct an object using only the information coming from a limited region of one (or more)

subdetectors. An important goal of the CMS software is the ability to use the same algorithms for off-line reconstruction and for the High Level Triggers (HLT), the main differences being the availability of updated alignment and calibration constants and the use of the Level-1 candidates as seeds for the HLT regional reconstruction.

The first step of muon reconstruction consists of the reconstruction of individual hits, using the appropriate calibration constants. Individual hits are then fit to straight segments within the DT and CSC chambers. Using these segments in the track fit eases the selection of the hits to be actually included and, in the case of the DTs, allows to resolve the left-right cell ambiguity.

The track fit consists of regional reconstruction based on the iterative Kalman Filter method¹⁴). This is first performed using only the measurements in the muon spectrometer and exploiting the very precise information on the beam spot position in the transverse plane ($\sigma \sim 20 \mu\text{m}$). In the HLT, the seed for the Kalman filter is given by the Level-1 candidates; the resulting muon candidates are used for the Level-2 trigger selection. The algorithmic efficiency is about 99% for muons in the range $10 < p_T < 100 \text{ GeV}/c$, with typical $1/p_T$ resolutions of the order of 10% in the barrel and 16% in the endcaps. The same algorithm is used for the off-line reconstruction, except that seeds are obtained from the segments reconstructed in all DT and CSC chambers.

Full muon tracks are then reconstructed including measurements of the inner tracker. First, regional track reconstruction is performed in the silicon detectors within a “region of interest”, defined using parameters and uncertainties of the tracks previously fitted in the muon spectrometer alone. A Kalman filter fit seeded by hit pairs in the pixel detectors and in the double-sided silicon strip layers is used for this purpose. The resulting trajectories are then matched to the original candidate in the muon system and their hits are refitted together. In the HLT, the resulting candidates are used for the Level-3 trigger selection. The algorithmic efficiency of the Level-3 is about 99%, except for the region of overlap between the barrel and endcaps ($\eta \sim 1$), where it is slightly lower. The inner tracker improves dramatically the $1/p_T$ resolution to about 1.0% and 1.7% in the barrel and endcap regions respectively.

The expected muon rates in the High Level Trigger have been recently studied in detail¹⁵). It has been shown that the most critical contribution to the Level-1 and Level-2 rate is the feed-through of real, low- p_T muons that are

reconstructed at high p_T values due to the limited p_T resolution and its sizable tails caused by multiple scattering and muon brehmsstrahlung in the iron yoke. This effect is very large due to the steepness of the rate curve at very low p_T . In this respect, the improvement in resolution of the Level-3 is essential to keep the total muon trigger rate under control.

4 Commissioning

The commissioning of the ATLAS muon spectrometer is underway at various locations at CERN and underground in LHC Point 1. During this and next year a large part of muon chambers will be installed and, during 2006, significant samples of cosmic ray events will be collected. The expected rate of cosmic muons that have muon trigger chamber hits on both the upper and lower halves of ATLAS, and also hits in the pixel detector, is about 0.7 Hz ¹⁶⁾. This means that one month of fully efficient running would give, provided that a proper trigger system will be available, about 2 million of such cosmic muons, which would be a very useful sample for studies of the barrel sectors and for part of the forward chambers. During the spring of 2007, when LHC will be commissioned with a single beam, the endcap muon chambers can be tested, in addition, with beam-halo events. Assuming a two month single beam period with 30% effective data taking time, 10^8 tracks from beam-halo are expected to be collected ¹⁶⁾. With these data, a first map of dead channels can be obtained, along with the study of tube efficiencies and autocalibration and of the alignment procedure with straight tracks. Moreover, a first test of the full muon reconstruction will be possible, both with magnetic field off and on.

The CMS commissioning strategy is somewhat different. The CMS muon spectrometer is being installed on surface, where cosmic muons are used to test the functionality of the chambers. However, the data collected in this phase cannot be used to determine calibration and alignment constants, since these must be computed with the magnetic field switched on. In winter 2005, the magnet will be ramped up to perform field mapping, to monitor the movements of the yoke and to test the alignment system. During this period, a full slice of CMS will be operational, including some forward and barrel sectors of the muon spectrometer. This will be an important chance to test the integration of DAQ and trigger systems, the trigger synchronization and the HLT calibration procedures, and the reconstruction algorithms. In 2006, after the magnet test,

the detector will be lowered to its operation position in the cavern.

With the first pp collisions, the first task will be the setup and synchronization of the trigger, and the study of noise and backgrounds. In one month of data taking, each experiment will be able to collect $O(10^6)$ of $Z \rightarrow \mu\mu$ events. Such clean physics samples will be used to calibrate and align the detector and to understand the absolute energy scale of the muon spectrometers.

5 Conclusions

Though having the same physics goals, ATLAS and CMS have chosen very different designs for their muon spectrometers. The most evident difference in the choice of the magnetic field strongly influences the detector technologies to be used and the procedures for commissioning, calibration and operation. The ATLAS muon spectrometer has a better nominal performance, but will require more accurate alignment and calibration procedures and very good knowledge of the complex magnetic field. The simpler CMS configuration translates to a muon spectrometer with less critical operation, although the inner tracker is essential to reach the full performance.

In this respect, the two detectors are complementary; this complementarity will ensure LHC will meet its physics goals.

References

1. ATLAS Muon Collaboration, ATLAS Muon Spectrometer Technical Design Report, CERN/LHCC 97-22 (1997).
2. The CMS Collaboration, The Muon Project, Technical Design Report, CERN/LHCC 97-32, CMS TDR 3 (1997).
3. F. Gasparini *et al*, Nucl. Inst. & Meth. **A336**, 91 (1993).
4. C. Bacci *et al*, Nucl. Phys. Proc. Suppl. **54**, 311 (1997).
5. C. Guyot *et al*, ATL-MUON-94-062 (1994).
6. H. Groenstege, ATL-MUON-94-063 (1994).
7. M. Aleksa, ATL-MUON-99-001 (1999).
8. C. Albajar *et al*, Nucl. Inst. & Meth. **A525**, 465 (2004).

9. The CMS Collaboration, CMS Technical Proposal, CERN/LHCC 94-38 (1994).
10. D. Adams *et al*, ATLASOFT-2003-007 (2003), ATLASDAQ-2003-020 (2003).
11. M. Virchaux *et al*, ATLASMUON-97-198 (1997).
12. S. Tarem, N. Panikashvili, ATLASOFT-2004-003 (2004);
13. ORCA, Object-Oriented Reconstruction for CMS Analysis, see <http://cmsdoc.cern.ch/orca>.
14. R. E. Kalman, A New Approach to Linear Filtering and Prediction Problems, Transaction of the ASME Journal of Basic Engineering **35** (1960).
15. The CMS Collaboration, Data Acquisition and High Level Trigger Technical Design Report, CERN/LHCC 2002-26, CMS TDR 6.2 (2002).
16. M. Boonekamp *et al*, ATLASGEN-2004-001 (2004).

JET AND MISSING E_T RECONSTRUCTION AND CALIBRATION IN ATLAS AND CMS

M.D'Alfonso

INFN, Pisa

F.Sarri

INFN, Pisa

Abstract

Precise measurement of the jet energy and of missing transverse energy is requested both to detect new physics scenarios, that could show up at the LHC energy scale, and to study already known physics processes. The ATLAS and CMS experiments have developed different algorithms to reconstruct the jet energy and the missing transverse energy, because of the difference between their calorimetric systems. In this note, after a description of the ATLAS and CMS calorimeters, the reconstruction algorithms are discussed and the results obtained on test beam and simulated data are shown.

1 The ATLAS and CMS calorimeters

The ATLAS and CMS calorimetric systems have been designed for the wide physics program of LHC. Jet and missing E_T reconstruction are particularly

relevant in the search for hadronic decays of the Higgs boson and for the signatures of supersymmetric particles. An accurate determination of the jet energy scale is also a key ingredient to study the characteristics of the top quark. The detectors will work at very high luminosities thus different technologies have been employed to obtain the required radiation hardness. For precise measurements of the jet energy and missing E_T , these calorimeters have a good linearity, resolution and hermeticity.

Different choices on homogeneity, resolution and segmentation of the two calorimetric systems have been done.

1.1 The ATLAS calorimetric system

The ATLAS calorimetric system ¹⁾ is placed outside the solenoid that provides the bending field for the tracker. It is divided into three main parts: the central one, the end cap and the forward calorimeters. It covers the pseudorapidity range up to $|\eta| = 4.9$.

The electromagnetic calorimeter is a lead-liquid argon sampling calorimeter with accordion geometry both in the central and in the end cap part. It extends up to $|\eta| = 3.2$. It is segmented in three longitudinal samples, with a granularity $\Delta\eta \times \Delta\phi = 0.003 \times 0.01$ in the first one, 0.025×0.025 in the second and 0.025×0.05 in the third one. It corresponds to a total radiation length of $\simeq 25$ or to 1.2 interaction lengths.

The central hadronic calorimeter, TileCal, is a sampling calorimeter made of iron and scintillator tiles. It extends up to $|\eta| = 1.7$. It has three longitudinal samples, the first two with a cell size $\Delta\eta \times \Delta\phi$ equal to 0.1×0.1 , the third one 0.2×0.1 . It corresponds to 7.2 interaction lengths.

The Hadronic Endcap Calorimeter consists of two independent wheels made of copper plates and liquid argon that extends up to $|\eta| = 3.2$. It presents four longitudinal segmentations with a granularity of 0.1×0.1 for $1.5 < |\eta| < 2.5$ and 0.2×0.2 for $2.5 < |\eta| < 3.2$. The thickness of the active part of the Hadronic Endcap Calorimeter is $\simeq 12$ interaction lengths ²⁾.

The forward electromagnetic and hadronic calorimeters ($3 < |\eta| < 4.9$) use the same liquid argon technology, but they employ respectively copper and tungsten as absorber. They are divided into three longitudinal samples with a granularity of 0.2×0.2 and the active detector has a total of 9 interaction lengths ²⁾.

All these calorimeters are non compensating, that is the detection efficiencies of the electromagnetic and hadronic energy are different. The ratio between these two detection efficiencies (e/h) characterizes the non compensation. For the ATLAS calorimeters it is always larger than 1.

In order to calibrate the calorimeters and to understand their performances, a part of the modules has been tested with beams. Electron, pion and muon beams of different energies and with various impinging angles have been used to define the electromagnetic energy scale and to assess the performances of the detector. This data have also been used for the tuning of the Monte Carlo simulation. Because of non compensation, the pion signal in a range of energy from 20 GeV to 300 GeV has a non-linearity of 15 – 20 %. It is recovered using software algorithms.

To reconstruct the energy and to calculate the resolution for single pion events, a weighting algorithm *a la* H1³⁾ has been applied to data acquired during a combined test where a complete section, electromagnetic and hadronic, of the calorimeters was exposed to beam. This algorithm has been chosen because the ATLAS calorimetric system is highly longitudinally segmented. The total energy is reconstructed applying weights to the signal deposits in each cell. The weights depend on the cell energy and on the beam energy. They are calculated minimizing the energy resolution with the constraint that the mean reconstructed energy reproduces the nominal beam energy. To avoid any dependence of the weights on the knowledge of the beam energy, the previous method has been slightly modified⁴⁾. The beam energy is estimated from the raw reconstructed energy and used to evaluate the weights. The cell weighting algorithm is applied and the resulting energy is used to recompute the weights. This procedure is iterated until stable weights are reached. The resolution obtained with this method for a wedge of the central Atlas calorimeter with single pions is :

$$\frac{\sigma}{E} = \left(\frac{41.9\%}{\sqrt{E}} \oplus 1.8\% \right) \oplus \frac{1.8}{E} \quad (1)$$

with E expressed in GeV, while the linearity is well within $\pm 2\%$ for energies ranging from 20 to 350 GeV. This result is well in agreement with the design requirements. For single hadrons the design resolution is $(50\%/\sqrt{E} \oplus 3\%)^2$.

1.2 The CMS calorimetric system

The CMS calorimeter is located inside the 4 tesla coil of CMS solenoid magnet. The Electromagnetic calorimeter (ECAL) consists of about 76000 $PbWO_4$ scintillating crystals, arranged in a barrel part, which covers the central rapidity region $|\eta| < 1.48$ and two endcaps, which extends the coverage up to $|\eta| < 3$. The CMS hadron calorimeter is a sampling device divided into four kinds of hadronic calorimeters which provide good segmentation and hermeticity, moderate energy resolution, and full angular coverage up to $|\eta| = 5$. The Barrel Hadronic Calorimeter (HB) surrounds the electromagnetic calorimeter, and covers the central pseudorapidity region up to $|\eta| = 1.3$ and has a depth of $5.8 \lambda_I$. The HB modules consist of 17 layers of plate scintillators interleaved with brass absorber. The layers are segmented into 0.087×0.087 towers in $\eta \times \phi$ and provide one depth measurement. Central shower containment is improved with the Outer Calorimeter (HO) consisting of one or two layer scintillators located outside the magnet. The total depth of calorimeter system is thus extended to $\sim 11.8 \lambda_I$. The end regions are covered up to $|\eta| = 3$ by two Endcap Hadron Calorimeters (HE), with a depth segmentation varying from one to three. Pseudorapidity coverage is extended up to $|\eta| = 5$ with two forward calorimeters (HF) which surround the beam pipe 11 m from the interaction point. The HF is a very high radiation area and is made by quartz fiber.

Various sections of the calorimeter have been tested using pion, electron, muon beam. Linearity and energy resolution are measured during 1996⁹⁾ in presence of magnetic field, during 2002¹⁰⁾ with beam between 20-300 GeV and during 2004 with a low energy beam ($< 30\text{GeV}$). Pion energy is reconstructed from calorimeter information as $E_\pi = a \times E_{ecal} + b \times E_{hcal}$ where E_{ecal} is the energy from depositions in a 5×5 crystal matrix around the central crystal, and E_{hcal} is the total energy from depositions in a 5×5 HB tower matrix around the central tower and a and b are correction factor. The energy distributions show non Gaussian tails due to non-compensating nature of the CMS calorimeter, as well as energy leakage beyond the ECAL-HB outer boundary. The linearity is measured between 90% and 100% for pion energy between 20 and 300 GeV. The measured energy resolution is

$$\frac{\sigma}{E} = \left(\frac{115\%}{\sqrt{E}} \oplus 5.5\% \right) \quad (2)$$

2 Algorithms for jet reconstruction and calibration

Partons in the final state produce jet of collimated particles, whose energy is measured in the calorimeters. An ideal algorithm allows to associate the energy deposits in the calorimetric cells to the final state partons.

The jet reconstruction algorithm proceeds through two subsequent steps. First the cells or calorimetric clusters typically closed to each other are grouped to form a jet, then all the kinematic quantities related to the jet itself are calculated (*recombination scheme*).

For what concerns the first step clusters are associated if they are near either in angle (cone algorithm) or both in transverse momentum and angle (K_T algorithm).

When part of the detected energy is shared between two reconstructed jets, the cone algorithm must also provide a split and merging procedure to assign unambiguously this energy to one jet only.

The energy of the reconstructed jets is different from that one of the particles belonging to the jets and thus, once reconstructed, jets have to be calibrated. This difference is due to two main reasons. Detector effects such as the non compensation of the calorimeters, the presence of dead material and of cracks, lead to underestimate the jet energy. Moreover the use of different technologies in different pseudorapidity regions degrades the uniformity of the response.

Physics effects such as initial state radiation and final state radiation, the out of cone energy loss, the underlying events and pile-up, must be well evaluated to reach a good precision on the absolute parton energy scale.

The calibration algorithms explained in the next section correct only for detector effects, that can be confidently reproduced by the Monte Carlo.

The final calibration that will correct for the physics effects will be obtained with real data. To correct for energy losses and to establish the absolute energy scale, p_T balance is imposed in events in which a jet is produced back-to-back with well known particle (*in situ calibration*).

2.1 ATLAS strategy

In ATLAS a seeded cone algorithm is used for the jet reconstruction. Calorimetric towers with a transverse energy E_T greater than 2 GeV are selected

as “seeds”. Towers within a radius $\Delta R = \sqrt{(\Delta\eta)^2 + (\Delta\phi)^2} = 0.7$ ¹ around the seed are summed and the jet barycenter is calculated. This procedure is iterated until a stable cone is reached.

If two jets share an energy percentage greater than 50%, they are merged up to form one jet, otherwise common towers are assigned to the nearest jet.

The four-momentum *recombination scheme*⁵⁾ is used to calculate the transverse energy, η and ϕ of the reconstructed jet.

As for the single pion testbeam events, the H1 weighting technique is used to calibrate jets. The total energy is calculated as a weighted sum of the cell energies belonging to the jets. The cell weights w_i depend on the calorimetric sample i , on the cell energy and within each sample on the pseudorapidity.

They are calculated minimizing the energy resolution with the constraint that the jet reconstructed energy is equal to the energy of the MC particles belonging to the jet (MC jet).

Different weight parameterizations as a function of the cell energy or as a function of both the cell and MC jet energy have been studied. The results on linearity and resolution obtained on a QCD di-jet sample with electronic noise are shown in Fig.1⁶⁾. The parametrization chosen in this case is : $w_i(E_i, E_{MC}) = a_i(E_{MC}) + b_i(E_{MC})/E_i$ and a 2σ noise cut is applied to the simulated data.

The linearity is within 2% and the resolution for $|\eta| < 0.7$ is :

$$\frac{\sigma}{E} = \frac{71.0\%}{\sqrt{E}} \oplus \frac{5.4 \text{ GeV}}{E} \oplus 1.2\% \quad (3)$$

If the calibration procedure is not applied the resolution is $132.7/\sqrt{E} \oplus (2.7 \text{ GeV})/E \oplus 2.5\%$.

A sample of $Z^0 (\rightarrow \mu\mu, ee) + \text{jet}$ events generated with the fast simulation has been studied as possible candidate for the *in situ calibration*⁷⁾. The analysis shows that in two months of data taking at low luminosity the parton energy can be reconstructed with a precision of 1% in a p_T range from 50 to 400 GeV, considering only the statistical error.

¹The value of ΔR is 0.7 for the low luminosity period, while it is changed to 0.4 for the high luminosity period.

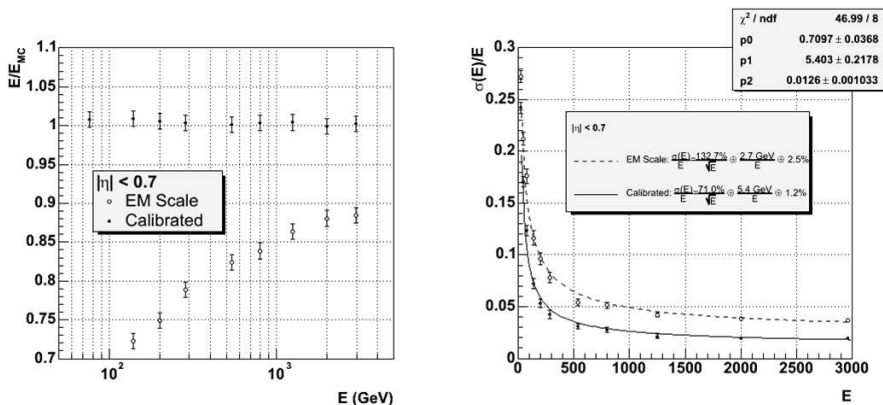


Figure 1: On the left : ratio between reconstructed energy and MC jet energy as a function of the jet energy for not calibrated (open dots) and for calibrated jets (full dots). On the right : resolution $\frac{\sigma(E)}{E}$ as a function of the jet energy for not calibrated (dashed line) and calibrated jets (continuous line).

2.2 CMS Strategy

Jet-finding algorithm developed for CMS are cone-based algorithms (simple cone, iterative cone, midpoint cone) or K_T algorithms¹¹.

In the iterative cone algorithm, calorimeter towers are sorted to decreasing E_t ; only towers passing a seed cut are used as starting points for the initial jet cones and neighboring within the radius R are added to seed towers. Then the E_t weighted centroid of this selected towers is computed and a cone of radius R is drawn around this direction. This procedure is iterated until a stable cone is found. A scalar addition of E_t or E of towers is computed to determine Jet E_t or E . Towers assigned to a jet are not used as input for an outer jet in the event. The K_T jet algorithm merges particles in order of increasing relative transverse momentum keeping their separation in η - ϕ to less than some value. Noise and pile-up are suppressed before of any of these algorithms start applying an E_t tower threshold.

Jet energy measurement (resolution, linearity, efficiencies, fake) are influenced by calorimeter response to low energy particles, electronic noise, magnetic field effects, pile-up, dead material and cracks, longitudinal leakage for high-pt jets, shower size, out of cone loss, miscalibration. These effects are studied with

a full simulation of the detector. Due to these factors the average calorimeter response is not linear and depends upon the jet rapidity.

In order to restore the jet energy scale, corrections are implemented by weighting the energies from longitudinal calorimeter compartments. This coefficient is dependent on pseudorapidity (η) and transverse energy (E_t), and a set of this parameters should be provided for each jet finding algorithm, each cone size, level of noise, pile-up. These weights are calculated using a sample of QCD di-jets, comparing the energies of jets found using the generator-level particles to jets found in the calorimeters. To set the energy scale, a correction factor is applied to an ECAL + HCAL tower $E_{jet} = a \times (E_{ecal} + E_{hcal})$ (optionally with different Ecal and Hcal weights). In figure 2 jets are reconstructed using the iterative cone with cone size of 0.5 and tower threshold $E_t = 0.5$ GeV, and the energy of final jets are calculated as sum of energies of jet constituent. E_t dependence confirms the non linearity to low energy pions and the η dependence is an effect of noise in the barrel and of pile-up and magnetic field in the end-cap. The jet energy scale can be extracted from photon plus jet events in the limit that the transverse momentum of the photon plus jet system is zero. A sample of γ + jets events are used to evaluate the systematic uncertainty due to initial state radiation, background coming from two jets with energetic π^0 and event selections.

3 E_T^{miss} reconstruction

A precise E_T^{miss} reconstruction is fundamental for the search of supersymmetry signature since these events are characterized by a large E_T^{miss} . Moreover it is required for invariant mass reconstruction in events in which neutrinos are produced among the decay products.

3.1 E_T^{miss} reconstruction in ATLAS

In ATLAS the E_T^{miss} for each event is computed summing the signal of cells within $|\eta| < 5$ over all the calorimeters. The contribution of each cell is calculated using the weights *a la* H1 ⁸⁾.

The σ of the distribution of the difference between the reconstructed E_T^{miss} and the MC E_T^{miss} of non interacting particles is considered to evaluate the resolution. The resolution is proportional to $\sqrt{\Sigma|E_T|}$ as expected.

Studies on full simulated $Z^0 \rightarrow \tau\tau$ and $A^0 \rightarrow \tau\tau$ events without noise have

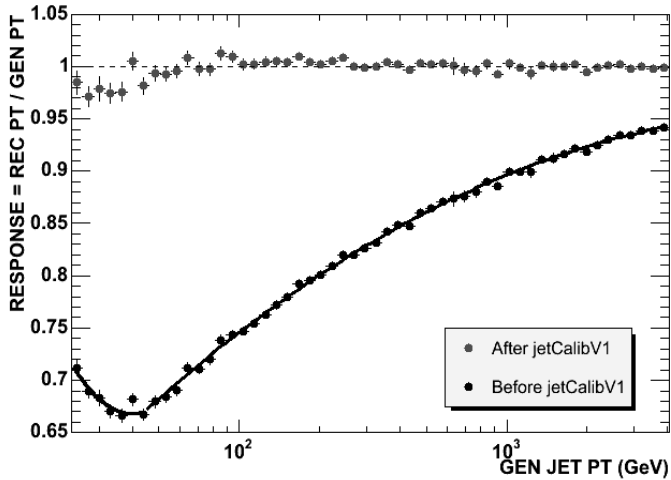


Figure 2: *Ratio between reconstructed jet energy and generated jet energy before and after jet energy scale correction. Only jets within $\eta < 1$ and $E_t > 10\text{GeV}$ are selected*

been done and the results compared to TDR (Fig.3). The obtained resolution is $\sigma(E_T^{miss}) = 0.46 \cdot \sqrt{\Sigma|E_T|}$.

Events with noise have also been generated. The noise cuts have been optimized to reduce the effect on E_T^{miss} resolution. It has been shown that introducing noise and applying a 2σ cut E_T^{miss} resolution is worsened by 30 %, and the σ of the reconstructed Z mass increases of 10% on $Z^0 \rightarrow \tau\tau$ events.

3.2 E_T^{miss} reconstruction in CMS

Also E_T^{miss} resolution (as jet energy resolution) in CMS is strongly influenced by non-compensating calorimeters, underlying event, pile-up, strong magnetic field in the tracker region, calibration algorithm biases, electronic noise, hot/dead cells (inaccessibility and eventual damage), event synchronization.

A Raw E_T^{miss} calculation is based on sum over towers. Contribution to the E_T^{miss} resolution is expected from stocastic term, noise and pile-up, constant term¹⁴). Improvement is expected from a calibrated E_T^{miss} .

A calibrated E_T^{miss} can be based on sum over calibrated jets and uncalibrated towers or on a calibrated jets and calibrated towers.

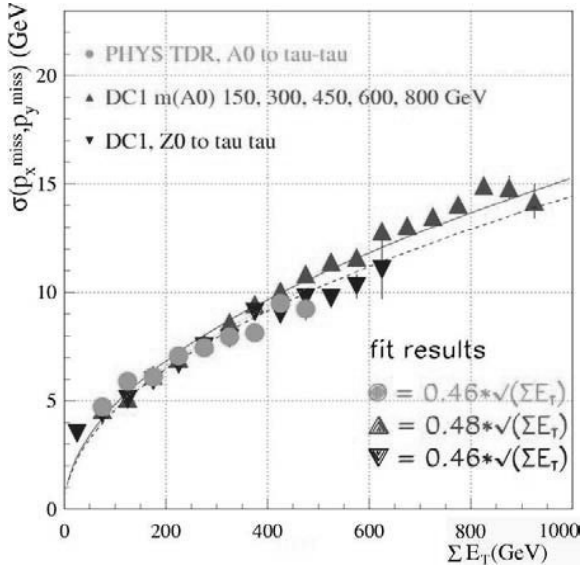


Figure 3: E_T^{miss} resolution as a function of $\Sigma|E_T|$ for DC1 $Z^0 \rightarrow \tau\tau$, $A^0 \rightarrow \tau\tau$ and TDR $A^0 \rightarrow \tau\tau$. DC1 events are without noise; TDR events are with noise and a 1.5σ cut is applied.

$$E_t = \Sigma(E_t)_j^{jet} \times C_j^{jet}(E_t, \eta) + \Sigma(E_t)_i^{tower} \times C_i^{tower}(\eta) \quad (4)$$

4 Conclusions

The LHC physics will require a precise reconstruction of jets and E_T^{miss} . The calorimetric systems of the two experiments have been tested on beam and the results on resolution and linearity are in agreement with the design requirements. Different jet and E_T^{miss} reconstruction algorithms have been developed by the two collaborations. The reconstruction quality is in good agreement with the required performance. An accurate study to evaluate physics and detectors effects is going on.

5 Acknowledgements

The authors would like to thank people of Jet- E_T^{miss} communities of ATLAS and CMS, in particular D.Cavalli, C.Roda, I.Vivarelli.

References

1. ATLAS Collaboration, "ATLAS Detector and Physics Performance Technical Design Report" - CERN/LHCC/99-14, ATLAS TDR 14 (25 May 1999).
2. ATLAS Collaboration, "ATLAS Calorimeter Performance" - CERN/LHCC/96-40, ATLAS TDR 1 (15 December 1996).
3. H1 Collaboration, Nucl. Instrum. and Methods **A386**, 348 (1997).
4. S.Akhmadaliev *et al.*, Results from a new combined test of an electromagnetic liquid argon calorimeter with a hadronic scintillating-tile calorimeter, Nucl. Instrum. and Methods **449**, 461 (2000).
5. G.C.Blazey *et al.*, Run II Jet Physics, hep-ex/0005012 v2, (10 May 2000).
6. C.Roda,I.Vivarelli,ATLAS Software Week (September 2004).
7. R.Lefevre,C.Santoni, ATLAS-PHYS-2002-026
8. D.Cavalli, Combined Performance Meeting - ATLAS Software Week (March 2004).
9. V.V Abramov *et al.*, Studies of the response of the prototype CMS hadron calorimeter, including magnetic fields effects, to pion, electron and muon beams, NIM **A 457** (2001) 75-100
10. V. Daniel Elvira, Measurement of the Pion Energy Response and Resolution in the Hadronic Barrel Calorimeter using CMS HCAL Test Beam 2002 Data, CMS Note 2004/020
11. <http://cmsdoc.cern.ch/orca/>
12. R. Harris, Jet Calibrations from QCD Jet Sample, CMS JETMET Meeting 6 october 2004
13. Konopliyanikov, Jet Energy corrections with γ /Z + jet, CMS week 8 dec 2004
14. Haipfeng Pi, Tuning jet and unclustered tower for MET correction, CMS week september 2004

ELECTRONS AND PHOTONS RECONSTRUCTION IN ATLAS AND CMS

L. Carminati

Università e INFN di Milano

P. Meridiani

INFN Sez. Roma1

Abstract

The electron/photon reconstruction and identification capabilities of the ATLAS and CMS detectors are presented. The electromagnetic calorimeters of both experiments are described and the main recent testbeam results are reported.

1 Introduction

The identification and reconstruction of electrons and photons with a p_T starting from 1-2 GeV up to 5 TeV range is mandatory for LHC physics. The lower limit comes from the need to reconstruct electrons produced in the semileptonic decays of b-quarks which is important for the $H \rightarrow b\bar{b}$ channel, for SUSY studies and for many aspects of B physics. An efficient electron reconstruction down to ~ 5 GeV is also required for the observation of the $H \rightarrow 4e$ channel.

Electrons and photons with p_T greater than about 15-20 GeV are expected from Higgs decays $H \rightarrow \gamma\gamma, 4e, WW$, from W decays and in various SUSY channels. Very high momentum (hundreds of GeV up to ~ 5 TeV) electrons are expected from the decays of new exotic physics states as $W' \rightarrow e\nu$ and $Z' \rightarrow e^+e^-$.

2 Electromagnetic calorimetry in ATLAS and CMS

The main task of the electromagnetic calorimeter is to provide an accurate measurement of the energy and position of electrons and photons. Jets and missing transverse momentum reconstruction should also be performed in association with the hadronic calorimeter. Particle identification capabilities and event selection at the trigger level are also a crucial part of the required calorimeter tasks. Although the EM calorimeter at the LHC will be involved in a variety of measurements, the performance specifications are driven by few benchmark physics channels such as the $H \rightarrow \gamma\gamma$ and $H \rightarrow 4e$ decays. The observability of such rare decays requires high hermeticity and the largest possible acceptance. In order to achieve a mass resolution of $\sim 1\%$ in the 115 – 180 GeV mass range stringent requirements on both energy and direction resolution are needed. In the $H \rightarrow \gamma\gamma$ channel, to minimize the angular contribution to the mass resolution a precise knowledge of the photon direction is needed. In low luminosity conditions ($2 \cdot 10^{33} \text{cm}^{-2}\text{s}^{-1}$) the direction reconstruction takes advantage from primary vertex determination in the Inner Detector. At high luminosity ($10^{34} \text{cm}^{-2}\text{s}^{-1}$), if this will not prove to be feasible, only the pointing information of the calorimeter can be used. Moreover, to reduce the background to this channel an excellent rejection against jets ($R \sim 3000$ for an 80 % photon efficiency) and in particular with respect to high- p_T isolated π^0 is required. Particle identification, accurate position measurement, minimization of electronic and pileup noise require a good detector granularity and fast detector response. The ATLAS and CMS collaborations have made different technology and design choices. The ATLAS collaboration has chosen an ionization sampling calorimeter equipped with a cell by cell electronic calibration system. The calorimeter is placed outside (in the radial coordinate) the magnetic field: this design while increasing the total amount of material in front of the calorimeter allows to keep the magnetic field at 2 T. The CMS electromagnetic calorimeter is an homogeneous crystal detector in a 4 T magnetic field.

Simulations and analysis of test-beam data give confidence that they will both meet the stringent LHC requirements.

2.1 The ATLAS electromagnetic calorimeter

The ATLAS EM calorimeter is a lead-liquid argon sampling calorimeter with accordion geometry ¹⁾. This choice guarantees an hermetic coverage and a stable calibration using a technique which is intrinsically radiation hard, which is a requirement in order to cope with the high dose LHC environment (from 0.18 Gy/h at $|\eta| = 0$ to 6.5 Gy/h at $|\eta| = 2.6$ in the high luminosity phase). It is located outside the solenoid and extends up to $\eta = 3.2$ (fig. 1(a)) with precision info up to $\eta = 2.5$. The calorimeter has 3 longitudinal samplings (called strips, middle and back) and excellent particle identification capability. In the barrel the middle towers have size $\Delta\eta \times \Delta\phi = 0.025 \times 0.025$ (fig. 1(b)) while the strips are finer in η (about 4 mm, $\Delta\eta \times \Delta\phi = 0.003 \times 0.1$). This last characteristic proves to be crucial in separating γ from jets (and in particular to reject π^0) and to measure the shower direction. A presampler detector for $\eta < 1.8$ is used to correct for the energy lost in the material before the calorimeter. The calorimeter has a total of about 190,000 readout channels and each channel can be calibrated using a cell by cell electronic calibration network. The readout signals are sampled every 25 ns and the peak and time offset are determined using an optimal filtering technique.

2.2 The CMS electromagnetic calorimeter

The CMS collaboration has chosen a homogeneous calorimeter composed with finely segmented crystals of lead tungstate ($PbWO_4$), a radiation resistant and chemically inert scintillator, with a very short radiation length $X_0 = 0.89$ cm and Molière radius $R_M = 2.2$ cm, which allows the construction of a compact and highly granular detector. Figure 2 shows a longitudinal view of a quarter of the electromagnetic calorimeter: it is organised in a barrel region $|\eta| \leq 1.479$ and a forward region to cover the pseudorapidity area below 3.0. Precision energy measurements will be made only in the region $|\eta| \leq 2.6$, matching the coverage of the tracker.

The calorimeter is built out of 75848 Lead Tungstate ($PbWO_4$) crystals. There are 17 different crystal types in the barrel: each crystal has a length of 230 mm ($25.8 X_0$) and a front face area close to 22×22 mm², exact dimensions

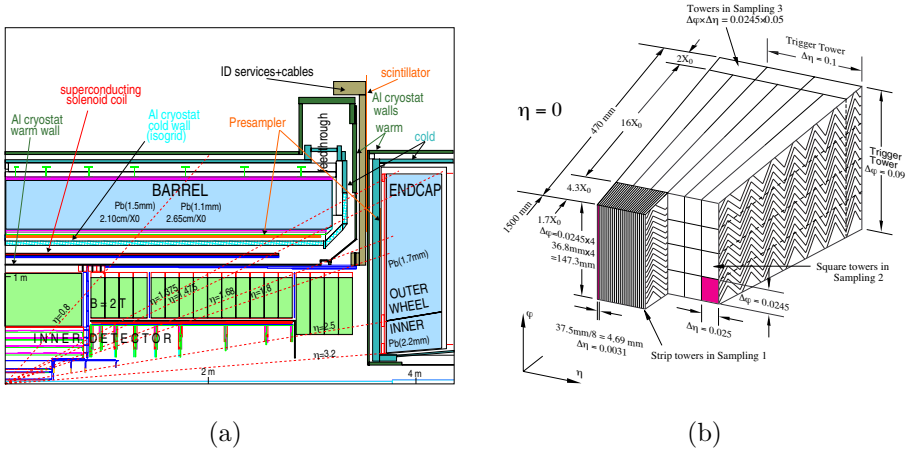


Figure 1: Longitudinal view of a quadrant of ATLAS electromagnetic calorimeter (left) and a sketch of the accordion structure of the calorimeter (right).

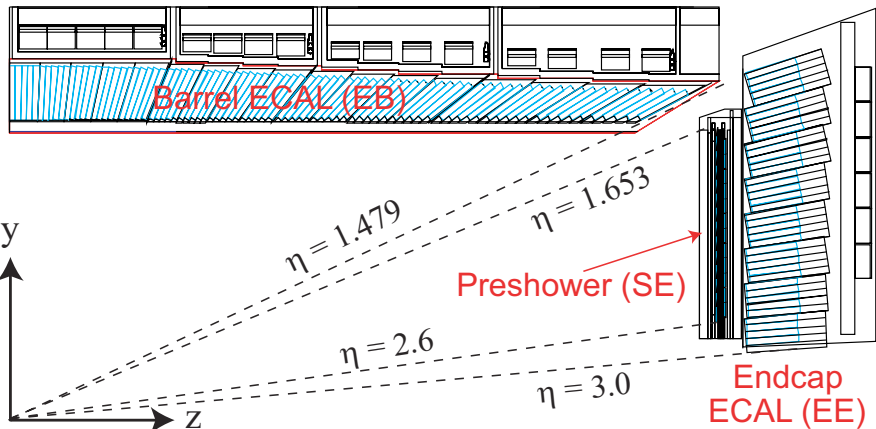


Figure 2: Longitudinal view of a quadrant of CMS electromagnetic calorimeter.

depending on crystal type, giving a granularity of $\Delta\eta \times \Delta\Phi = 0.0175 \times 0.0175$. The crystals are tapered and their axes have a constant off-pointing angle of 3° with respect to the nominal vertex position in both η and ϕ to avoid gaps that are pointing to the interaction region, increasing the overall hermeticity of the structure. The ECAL endcaps are built up of structures composed of identical 5×5 crystals, called super-crystals; endcap crystals are 220 mm long (owing to the presence of the $3X_0$ thick pre-shower detector in front) and with $24.7 \times 24.7 \text{ mm}^2$ front face dimensions: they are slightly larger in cross-section, shorter, and almost parallelepiped, compared to the barrel crystals. The front face of the endcap shall be at a distance of 3170 mm from the interaction point.

The relatively low light yield imposes the use of photo-detectors with intrinsic amplification: in the barrel avalanche photodiodes (APDs) are used, while in the endcaps, due to the higher expected neutron flux, vacuum phototriodes (VPTs) are employed.

3 Electrons and photons reconstruction issues

Both in ATLAS and CMS, an e/γ leaving the interaction point will cross several layers of tracking detectors and services before reaching the calorimeters. Material in front of the calorimeter results both in photons conversion and electrons bremsstrahlung; in particular material at low radii is the most dangerous as the electron pair (in case of conversions) and the electron and the accompanying photon(s) (in case of bremsstrahlung) might be separated enough by the magnetic field in the tracking volume so that they will not get to the same calorimeter cluster leading to a degradation of the calorimeter performance.

3.1 Electrons and photons reconstruction in ATLAS

In the electromagnetic calorimeter reconstruction software, a sliding window algorithm is used to search for clusters. The algorithm loops on all the calorimeter cells and calculates the total energy deposited in a specific window around the considered cell: a cluster is found when the energy deposition is greater than a given threshold. Both sliding window size and threshold can be selected by the user. The size of the cluster in $(\Delta\eta, \Delta\phi)$ can be chosen by the user according to the requirements of the specific physics analysis. The possibility to introduce topological clustering technique in the electrons/photons reconstruction is presently under study. The energy of the cluster is then computed by

summing the energies of all the cells of the cluster in the various samplings: corrections are applied to take into account the energy lost in the upstream material, the longitudinal leakage as well as the finite lateral containment. The position of the cluster is determined in each compartment by calculating the barycenter of the deposited energies and correcting for S-shapes effect. The global η position of the e/γ objects is obtained from an average of the η_i positions in each layer weighted on the intrinsic compartment resolutions. In the case of $H \rightarrow \gamma\gamma$ decay, the longitudinal segmentation of the calorimeter allows a calorimeter standalone primary vertex reconstruction with a resolution better than 20 mm: when the inner detector information is added, a resolution of 40 μm can be achieved. The position in ϕ is measured from the second sampling only which has the best granularity in the azimuthal coordinate.

Electrons are identified and reconstructed using information from the calorimeter and the tracking detectors, including the transition radiation detector functionality of the straw tubes¹). About 20% of the electrons lose around 50% of their energy for bremsstrahlung while traversing the inner detector. To recover the energy lost a wider cluster size along ϕ is used (3×7 cells). Various techniques have also been studied to optimize the reconstruction of the electron track. Good results have been obtained inserting the cluster baricenter in the calorimeter as an additional point in the track fit. By using shower shape analysis, track-cluster match, E/p and transition radiation, ATLAS has studied the possibility to isolate an inclusive 20 (30) GeV electron sample against the large QCD jet background. It has been estimated that for an electron efficiency of 72.7 (67.5)% a jet rejection, with respect to jets reconstructed in the calorimeter with $p_T > 17(25)$ GeV, greater than 1.5×10^5 (0.45×10^5) has been obtained at low (high) luminosity.

A critical item that should be carefully considered is the number of photons conversions in the material in front of the electromagnetic calorimeter (beam pipe, inner detector, calorimeter cryostat): the converted photons are dangerous since they start showering before the beginning of the calorimeter thus degrading the energy resolution in the detector and requiring a larger cluster size. It is estimated that about half of the $H \rightarrow \gamma\gamma$ events have at least one photon converting inside $R < 80$ cm and $|z| < 280$ cm (where track reconstruction is possible). Conversions with $R_c < 40$ cm can be recovered by fitting to a common vertex opposite charge track pairs with the right kinemat-

ics¹): the resolution on Z coordinate of the conversion from the inner detector measurement is expected to be 0.03 mm for $R_c < 20$ cm and 0.54 mm for $20 < R_c < 40$ cm with an efficiency is about 86.4%, decreasing at higher radii where track reconstruction is more difficult. To recover the energy loss due to the opening of the electrons in the solenoid, a wider cluster size is used for converted (3×7) than for unconverted photons (3×5 in the barrel, 5×5 in the endcap): these dimensions are the best compromise between the needs to collect all the particle energy and to reduce the contributions from pile-up and electronic noise. Photons can be separated from jets by looking at the shower profile (especially in the strips which have the better granularity along η), by isolation cuts, by studying conversions and by applying a track veto¹). After this selection the surviving jets are dominated by isolated high- p_T π^0 . An additional factor of three of rejection power (needed in the $H \rightarrow \gamma\gamma$ analysis) can be achieved by further cuts on the shower shape in the strip compartment. For a 80% photon efficiency approximately flat in η and E_T a total jet rejection of about 1000 for 20 GeV photons and of about 3500 for photons of E_T greater than 50 GeV has been obtained. It has been shown with test beam data that the γ/π^0 factor of three in rejection is feasible (4.1).

3.2 Electrons and photons reconstruction in CMS

3.2.1 Energy and position reconstruction with the calorimeter

The main concern in calorimeter electron and photon reconstruction in CMS is the recovery of the effects due both to the material between the interaction point and ECAL and to the very intense magnetic field (4 T). For example, electrons with $P_T = 35$ GeV and $|\eta| \leq 1.5$, loose on average 43.6% in bremsstrahlung before exiting the tracker volume. In some cases, it can also happen that not all the electron energy is reaching the calorimeter, since part of the bremsstrahlung energy can be lost in the tracker material. To minimize the effects in the energy and position reconstruction made by calorimeter, CMS has developed a topological clustering algorithm, the so-called *SuperClustering*, with the idea to recover the electron energy by making cluster of clusters along a ϕ -road (assuming that bremsstrahlung radiation lies to a good approximation only in the ϕ direction). In the barrel, the Superclustering algorithm exploits also the knowledge of the lateral shower shape in η , while dynamically searching for separated sub-clusters in ϕ . In the endcap, instead, also the preshower energy

needs to be summed up to the crystal supercluster energy. Some specific corrections to the supercluster energy are also being studied, with the aim to recover the energy lost in the tracker volume. The achieved energy resolution for electrons with $p_T = 35$ GeV/c amounts to $\sigma_{gaus}/\mu = 1.06\%$ and $\sigma_{eff}/\mu = 2.24\%$, where μ indicates the mean value of the E_{meas}/E_{true} distribution, σ_{gaus} the gaussian width and σ_{eff} the effective width containing 68.3% of the distribution. The corresponding numbers for the endcaps are $\sigma_{gaus}/\mu = 1.23\%$ and $\sigma_{eff}/\mu = 2.11\%$

SuperClustering is not used for measuring energy and position of unconverted photons, where a fixed matrix of 5×5 crystals has been found to be the optimal choice; instead, supercluster algorithms are applicable to the case of converted photons, where the energy deposit is spread in a larger area on the calorimeter. The photons energy distributions have a resolution of 0.86% for unconverted $p_T = 35$ GeV/c photons and 1.15% for converted ones.

Impact point of electrons and photons is obtained by calculating a weighted mean position of the crystals in the cluster, using a logarithmic weight instead of a linear one in order to avoid correcting for S-shape effects. In the CMS detector this simple picture is complicated by the non-pointing geometry, which requires some definition of the crystal position in (η, ϕ) , that is changing along the crystal axis due to the calorimeter non pointing geometry. Crystal position is calculated at the shower maximum depth along the crystal axis parametrized as: $0.89[\text{Log}(E) + 5.7]$ cm. Determination of parameters is described in reference 2).

3.2.2 Electron tracking

An issue of particular importance for electron reconstruction and identification is the use of tracker information, and the cluster-track matching aspects. In the current version of the online reconstruction software, track seeding is obtained propagating the calorimeter impact point back through the magnetic field, and looking for compatible hits in the pixel detector. The advantage of using this technique is that the matching of super-clusters to pixel hits is also a powerful tool to reject the jet background 3) to electrons: with an efficiency of 95% for isolated electrons in a p_T interval from 10 to 50 GeV, a rejection of 17 against QCD jets can be achieved at low luminosity. At this level, it is also possible to efficiently separate electrons from photons, since in the pixel

detector photons has a little probability to convert. The pixel matching technique, instead, is not particularly suited for low p_T electrons, such as the ones which can come from a low mass Higgs decaying into 4 electrons. In some cases, hits cannot be found in the pixel detector due to a wrong calorimeter reconstruction, with a consequent loss of efficiency. An improved electron identification strategy specifically tuned for the low p_T electrons is currently under development. Other aspects which are now being tuned are the electron track building and fitting procedures ⁴⁾. In the online reconstruction algorithms, a standard Kalman Filter algorithm ⁵⁾ is used, treating electron as if it were a muon, hence assuming both in the track building and in the fitting phase a Bethe-Bloch distribution for the electron energy loss and stopping the track as soon as a significant amount of bremsstrahlung has been emitted.

In order to be able to follow the track change of curvature, hence to measure not only the track momentum at the vertex but also the momentum at the calorimeter surface, giving a direct measure of the amount of bremsstrahlung emitted by the electron, a gaussian sum filter algorithm (GSF) has been developed ⁴⁾. The Kalman filter, in fact, relies solely on gaussian probability density functions, and it is not optimal for electron tracks, since the bremsstrahlung energy loss distribution of electrons propagating in matter is highly non-gaussian. The key component in the application of the GSF to electrons is the approximation of energy loss distribution by means of a gaussian mixture; in the actual implementation the Bethe-Heitler model has been chosen for the energy loss distribution. The different components of the mixture measure different degrees of hardness of the bremsstrahlung. A comparison with the Kalman filter, shows a clear improvement of the momentum resolution for low p_T tracks; at high momenta the results approach those of the Kalman filter ⁴⁾.

3.2.3 *Converted photons and primary vertex finding for $H \rightarrow \gamma\gamma$*

Reconstruction of converted photons is another aspect of particular importance, since as we have seen converted photons can degrade the Higgs boson mass resolution in the $H \rightarrow \gamma\gamma$ channel and lead to some inefficiency. The conversion probability for photons is 27% in the centre of barrel ($|\eta|=0$), 50% at the junction of the tracker barrel and forward region ($|\eta|=0.9$) and 62% at the end of the ECAL barrel ($|\eta|=1.4$). On average, 70% of the $H \rightarrow \gamma\gamma$ events have at least one of the two photons converted. Knowledge of the primary

vertex position is necessary to have a precise direction determination of the photon direction. The primary vertex can be determined by reconstructing all the charged particle tracks in the event; the Higgs boson production vertex can be correctly identified with efficiency of more than 90% at low luminosity, exploiting the fact that the total transverse momentum of the underlying event charged particles is larger than that of the pile up events. However, at high luminosity finding the right vertex is difficult, and the success rate decreases at around 70%. Determination of the z coordinate of the primary vertex from the tracks of a converted photon may help to choose the right vertex. Using a sample of photons with $p_T = 35$ GeV/ c , it was shown that the z coordinate of the primary vertex can be reconstructed with an accuracy of around $80\mu\text{m}$ if a conversion occurs before 20 cm in transverse radius, 1.2 cm for conversions between 20 and 65 cm. For late conversions, above 65 cm in transverse radius, the tracks are poorly reconstructed and do not offer any useful information on the primary vertex. The crucial parameter is the number of stereo layers in the tracker which are crossed by the track.

3.2.4 Use of electrons and photons for calorimeter calibration

Reconstructed electrons and photons will play a crucial role in the in-situ calorimeter calibration procedures. The CMS goal is to achieve a global intercalibration precision at a level of better than 0.5%; intercalibration precision is directly going into the constant term of energy resolution with very little scaling. High p_T isolated electrons are produced at sufficiently high rate from $W \rightarrow e\nu$ and $Z \rightarrow e^+e^-$ decays at LHC (respectively around 10 and 1 Hz at low luminosity); they can be used to obtain both the intercalibration coefficient and, exploiting the Z mass peak, the absolute scale of energy. However, in situ calibration with electrons is complicated by the bremsstrahlung effects on electron reconstruction; current strategy is to apply loose cuts on bremsstrahlung to intercalibrate regions of crystal with a uniform quantity of material in front, while, selecting electrons with no or little bremsstrahlung, intercalibrate different calorimeter regions between them. A complementary strategy is also being defined, looking at the possibility to intercalibrate the calorimeter with unconverted photons from the η^0 and π^0 decays, which are copiously produced at LHC. Preliminary results show that suitable η^0 and π^0 decays, with sufficiently energetic photons not overlapped between them, can be selected at a rate of

about 1Khz.

3.2.5 Selection efficiencies and rates

Detailed performance numbers on the online reconstruction and selection in terms of the electron and photon rates output by the HLT can be found in ⁵⁾. As an example the total HLT electron/photon rate at low luminosity is 43 Hz, of which 10 Hz are occupied by $W \rightarrow e\nu$ events and 1 Hz by $Z \rightarrow e^+e^-$; the HLT efficiency to select $H \rightarrow \gamma\gamma$ ($m_H = 115$ GeV/c²) events is 77%.

4 Testbeam results

During the last years intensive test beam programs allowed to verify some of the main design specification of the ATLAS and CMS calorimeters. Some selected results of these runs are summarized in the following sections.

4.1 ATLAS calorimeter testbeam results

Besides the module 0 (a pre-production prototype module ^{6) 7)}) a total number of 4 production barrel modules and 3 end-cap modules have been tested. The sampling term of the energy resolution has been measured at various points in η both in barrel and end-cap modules. As an example, the sampling term is 9.24% at $\eta = 0.3625$ (barrel) and 10.35% in the end-cap, at $\eta = 1.9$. The typical noise measured in a 3×3 -cell cluster in the test beam set-up is about 160 MeV. The coherent noise has been estimated to be about 5% of the incoherent noise. The results are in agreement with the expectations.

To reach the prefixed goal of keeping the constant term at the 0.7% level the ATLAS strategy is the following. By a careful mechanical construction and thanks to the electronic calibration, ATLAS aims at obtaining a local constant term of about 0.5% in a region with a size of $\Delta\eta \times \Delta\phi = 0.2 \times 0.4$ (which corresponds to 128 middle cells). There are 440 such regions that then need to be intercalibrated to correct for long-range disuniformities in the calorimeter. The intercalibration will be performed *in situ* using $Z \rightarrow ee$ events. A 0.3% intercalibration accuracy is already possible after few days of data taking thanks to the high Z production cross section at the LHC. The response uniformity has been measured on test-beam modules. It has been shown that on regions including 517(733) cells of the barrel (end-cap) module—regions which are

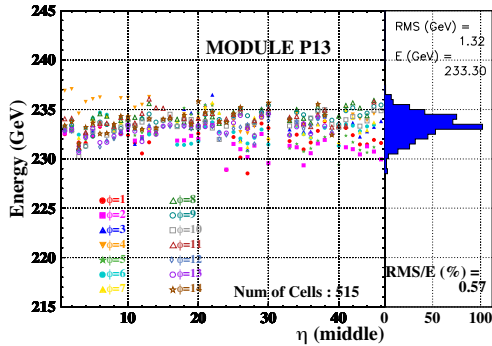


Figure 3: *Response of a ATLAS calorimeter barrel module as a function of η and ϕ*

much larger than the nominal 128 cells—a uniformity of 0.57% (0.49%) has been obtained. These results prove that the aimed uniformity has been reached (see fig. 4.1).

The linearity of the response of the calorimeter has been studied in detail with electrons beam from 10 to 180 GeV: the detector has been proved to be linear within $\pm 0.25\%$ for $E > 10\text{GeV}$ and within $\pm 0.1\%$ for $E > 40\text{ GeV}$ as reported in figure 4(a). The angular resolutions in the ϕ and θ directions have also been measured in the test-beam set-up. The θ angle can be reconstructed by using the shower direction as obtained from the strips and from the middle. The results for electrons in the barrel (see fig. 4(b)) match the design goal. Similar results have been obtained in the end-cap.

It has been shown with test beam data that the required γ/π^0 factor of three rejection on top of jets is feasible. From a photon beam, single-photon events have been superimposed offline and selected if their kinematics was consistent with that of a 50 GeV π^0 decaying to two γ 's. For a 90% efficiency, a rejection of 2.60 ± 0.05 against pions has been obtained (Montecarlo predicts 2.82 ± 0.10).

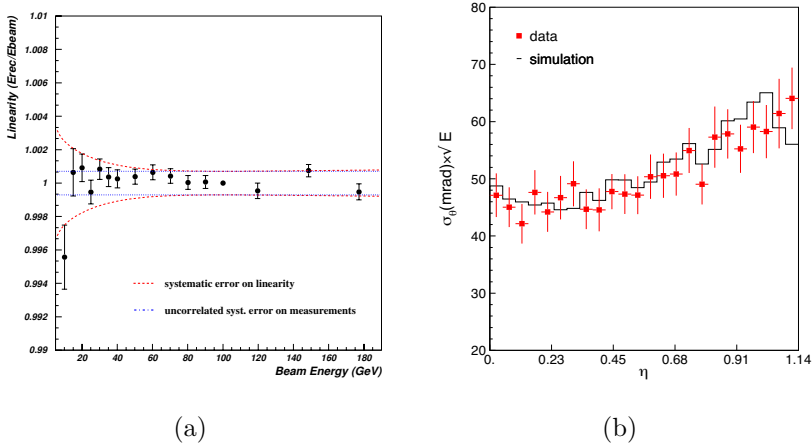


Figure 4: *Linearity of the response of the electromagnetic calorimeter (a) and θ resolution times the square root of the beam energy as a function of η for a ATLAS barrel module at 245 GeV (b)*

4.2 CMS calorimeter testbeam results

Very important calorimeter test beams have taken place in the years 2002, 2003 and 2004. Analysis of the 2004 data test beam, which for the first time involved a fully equipped calorimeter supermodule (1700 channels) with the final electronics, are still going on at the time of writing.

For what concern the energy resolution, the new MGPA electronics design showed to fulfill the design requirements in terms of noise and resolution. The data showed some low frequency noise, the result of which is a pulse baseline that varies from event to event. This effect is present with a uniform (15 - 20%) spatial correlation, and can be easily subtracted; after correction the noise for the sum of nine crystals is 129 MeV, corresponding to a noise per channel of about 43 MeV. Figure 5 shows the energy resolution for the sum of nine crystals. They confirm that the design performance can be reached.

Encouraging results have also been obtained in the area of temperature and high voltage stability. Since both light yield ($-2\%/^{\circ}C$ at 18 $^{\circ}C$) and APD gain ($-2.4\%/^{\circ}C$) depends on temperature, temperature should be stable for long periods within 0.1 $^{\circ}C$ not to affect the energy resolution, where “long

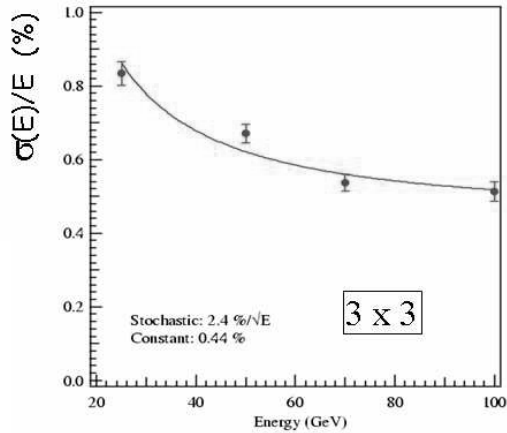


Figure 5: Energy resolution for the sum of nine crystals obtained at four different energies as obtained from test beam

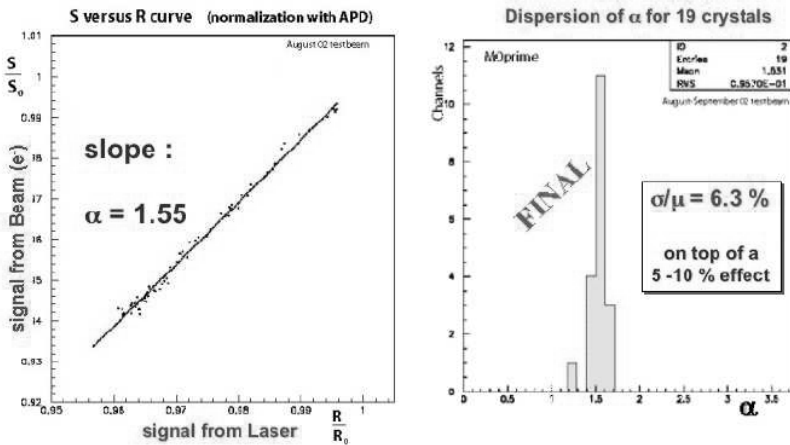


Figure 6: Left : Correlation between the signal from 120 GeV electrons in one crystal and the signal from laser light injection. Right : Dispersion of the parameter α

periods” can be understood to correspond to at least a period between two in-situ calibrations (1-2 months). The cooling system showed a stability well below the $0.1^{\circ}C$ over a period of two months. Same type of requirements are made for the APD high voltage system:

Ability to follow the crystal response monitoring the crystal transmission has been also proved. In fact, irradiation of the crystals results in a reduction of scintillation light transmission. In order to correct dynamically (between calibrations with physics events) the calibration constant of each crystal for this effect, a laser monitoring system will be installed. It distributes laser light of three frequencies through a two-level fanout system with cross-verification by precision radiation-hard PN diodes at each level, to each crystal via a radiation-hard optical fiber. The basic idea is that the loss of the scintillation signal from the laser light follows that from particles according to a ratio $\Delta_{signal} = \Delta_{laser}^{\alpha}$. As an example the results obtained for one of the crystals are shown in Fig. 6 (left). The fitted parameter $\alpha = 1.55$ is measured with a precision of 3%. Figure 6 (right) shows the dispersion of the exponent: very good uniformity is found with a spread of 6.3%. Other important results concerns the precision which can be reached in the intercalibration using the measurements which are coming from the quality control measurements on crystal and electronics performed in the calorimeter regional centers. Initial intercalibration from these measurements is quite important, since it will not be possible, due to the very tight schedule, to perform a beam intercalibration of all the crystals (this is foreseen only for a small percentage of crystals to be able to perform cross-checks and systematic studies). It has been shown that a precision of around 4% can be achieved using the light yield measurement.

Also an interesting test using cosmic muons (in this case APD gain has been increased of a factor 4 in order to increase the signal to noise ratio) has taken place. Preliminary results show that an intercalibration at a level of 3% can be reached. A more complete test will be repeated this year.

5 Conclusions

The ATLAS and CMS Collaborations have made different technology and design choices for their calorimeters and different calibration and reconstruction strategies have been adopted. Both detectors have been optimized mainly for Higgs physics and the stringent requirements set in this way make them able

to cope with a wider range of physics channels. The performance of calorimeters modules has been carefully tested during many testbeams periods and the results are within specifications. Simulations and analysis of test-beam data gives confidence that both calorimeters will meet the stringent LHC requirements.

References

1. The ATLAS Collaboration, CERN/LHCC/99-14/15 (1999).
2. E. Meschi et al., CMS Note 2001/034 (2001)
3. G. Daskalakis et al., CMS Note 2002/039 (2002)
4. W. Adam et al., CMS Note 2005/001 (2005)
5. The CMS Collaboration, CERN/LHCC/2002-26 (2002)
6. B. Aubert et al., Nucl. Instrum Methods A500 (2003) 202-231.
7. B. Aubert et al., Nucl. Instrum Methods A500 (2003) 178-201.

SELECTION OF EVENTS WITH BEAUTY AND TAU WITH THE ATLAS AND CMS DETECTORS

Susanna Cucciarelli

CERN

Carlo Schiavi

INFN Genova

Abstract

The expected selection performance for events with b quarks and τ leptons in the final state with the ATLAS and CMS detectors are discussed. Reconstruction tools and trigger strategies are also reviewed.

1 Introduction

ATLAS and CMS are general purpose detectors that will be installed at the Large Hadron Collider at CERN. Their main target is discovering new physics, especially in the Higgs and Supersymmetry sectors. In particular the Standard Model Higgs decay into $b\bar{b}$ is expected to be the dominant decay channel for a light Higgs boson ($m_H \lesssim 130$ GeV) while the Higgs decay into τ leptons is particularly important for a Minimal Supersymmetric Standard Model Higgs. The detection of b quarks and τ is therefore crucial to increase the the new physics discovery potential at LHC.

2 Tracking System Layout

Both the ATLAS ¹⁾ and CMS ²⁾ detectors have been designed in order to optimize physics coverage at an affordable cost. They essentially consist of three subdetector systems: the Tracking system, closest to the beam pipe, the Calorimetric system and the Muon chambers.

ATLAS and CMS will make use of a detector based on silicon pixels in the the innermost part of the Tracking systems. The Pixel detector grants the most precise spatial measurement in the Tracking system, providing a three-dimensional position information. In addition, the Pixel system is also characterized by a very low occupancy (with a maximum of $\mathcal{O}(10^{-4})$ hits per pixel at each bunch crossing, at LHC design luminosity) even in the high density environment of proton-proton collisions at LHC.

Table 1: *Main parameters of the ATLAS and CMS Pixel detectors.*

	ATLAS	CMS
Barrel layers	3	3
Forward disks	3	2
Minimal radius (cm)	5.05	4.3
Pixel size (μm^2)	50x400	100x150
Number of channels	$8.2 \cdot 10^7$	$6.6 \cdot 10^7$
$r\phi$ resolution (μm)	7	10
z resolution (μm)	70	15

The main characteristics of the Pixel detectors of ATLAS and CMS are summarized in Table 1. Spatial resolutions of Pixel systems strongly depend on the track impact angle and the size of clusters, so the quoted numbers only give an average rough estimation. In the transverse plane, the effect of the smaller pixel size of ATLAS with respect to CMS is partially balanced by the smaller internal radius of the CMS Pixel detector.

After the Pixel system, both ATLAS and CMS detectors have silicon-microstrip layers, some of them present a stereo tilt angle to allow a three-dimensional position measurement. For the outer tracking, the two experiments made a different choice: CMS still uses silicon micro-strips detectors, while ATLAS uses a Transition Radiation Detector to allow a better particle identification.

3 Track and Vertex Reconstruction Performance

In order to identify b and τ a very precise track and vertex reconstruction is needed. All the results given in the following refer to a track reconstruction

algorithms based on a standard Kalman Filter. The efficiency to reconstruct tracks depends on many factors, such as the event topology, luminosity conditions and detector efficiency. Single muon tracks are reconstructed with an efficiency close to 100% in the tracker acceptance assuming a perfectly aligned detector.

Figure 1: *Track reconstruction efficiency for single pions (left: the effect of pile-up events is shown by filled circles) in ATLAS and for jets (right: red and blue dots correspond to $E_t = 50, 200$ GeV respectively) in CMS.*

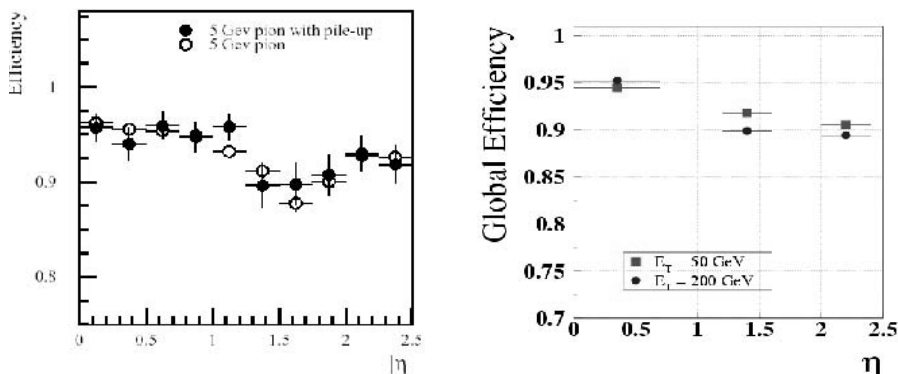


Figure 1 shows the track reconstruction efficiency as a function of the pseudorapidity for single pions with the ATLAS detector simulation and for jets with the CMS detector simulations. In both the cases the efficiency does not fall below 85%.

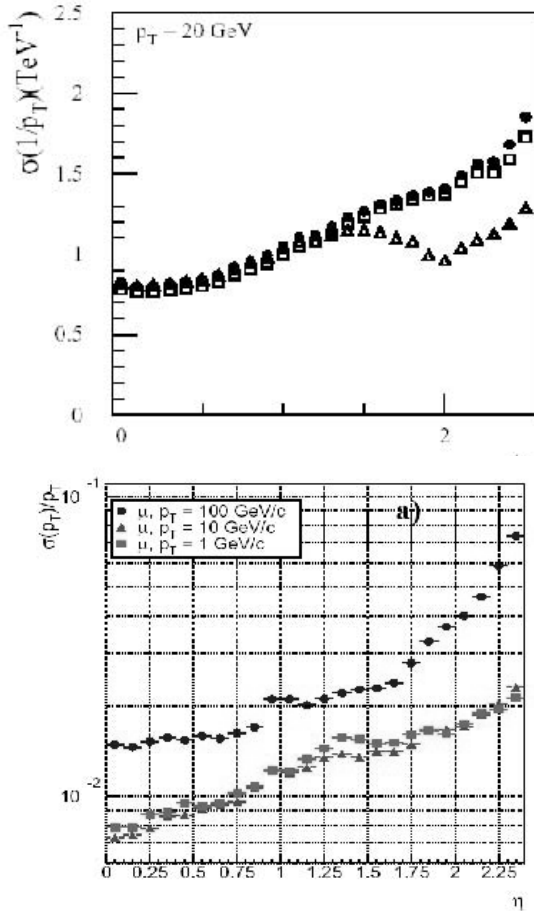
The relative transverse momentum (p_T) resolution for single muon tracks is shown in Figure 2 as a function of the pseudorapidity. ATLAS and CMS detectors reach similar performance, obtaining a relative p_T resolution of a few percent for single muons at high energies.

The impact parameter resolutions, evaluated on high p_T tracks, are listed in Table 2. ATLAS has a slightly better transverse impact parameter resolution and CMS shows a significant advantage in the longitudinal coordinate, this clearly reflects the different cell sizes in the Pixel detectors.

The vertex finding process is accomplished in two steps: first of all, primary vertices are reconstructed, identifying the one which triggered the event, and subsequently the reconstruction of displaced vertices from high lifetime particles, like b and τ , is performed. The performance on vertex reconstruction is clearly related to the quality of the track reconstruction. The reconstruction of primary vertices can also be performed at an early stage, without using the information from all the tracking system. Both ATLAS and CMS show that

it is possible to reconstruct and identify the primary vertex of the signal event using only the Pixel detector. The main advantage of such an approach is that it is fast, so that it can be used for event selection at trigger level and it can also be used to constrain the track reconstruction with the full Tracker information in order to not reconstruct tracks belonging to pile-up events.

Figure 2: *Relative p_T resolution for single muon tracks as a function of the pseudorapidity in ATLAS (top) and CMS (bottom).*



CMS has shown that in most interesting signal events at low luminosity, the efficiency to identify the primary vertex is above 95% except for some signal event, like $H \rightarrow \gamma\gamma$ where the low charged track multiplicity does not allow the primary vertex to be identified as the signal one. Dedicated algorithms have

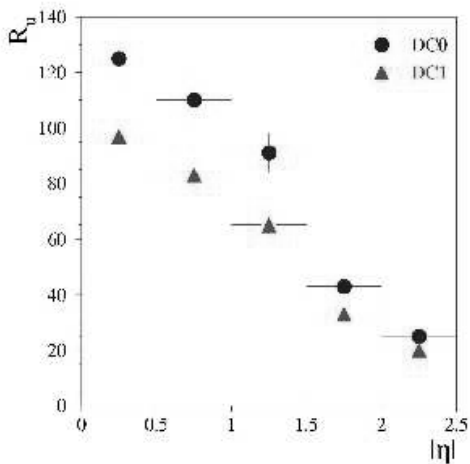
to be used to identify the primary vertex for low multiplicity signal topologies.

Table 2: *Impact parameter resolution in ATLAS and CMS.*

	ATLAS	CMS
$\sigma(d_0)$ at $\eta=1$	15 μm	20 μm
$\sigma(z_0)$ at $\eta=1$	95 μm	40 μm

The resolution in the z position determination is about $50\mu\text{m}$ for low luminosity events and improves up to $30\mu\text{m}$ using the full tracker information. To reconstruct secondary vertices the information from the all Tracker system are needed. The efficiency of secondary vertex finding depends on the impact parameter of tracks belonging to a displaced vertex and the required purity on the same set of tracks. Once the set of tracks coming from a secondary vertex have been identified, a fit is needed to estimate the position of the secondary vertex from which the decay length is computed.

Figure 3: *Light-quark rejection in WH ($H \rightarrow b\bar{b}$) events as a function of the pseudorapidity in ATLAS while 60% of b quarks are retained.*



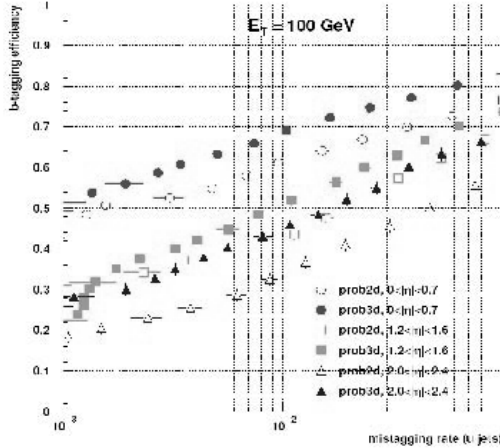
4 B-Tagging

The main characteristic of jets coming from b quarks with respect to light-quark jets is that they contain large impact parameter tracks originating from a secondary vertex, in fact the lifetime of B hadrons (1.6 ps) corresponds at a decay length of around half a millimeter in the rest frame. Track reconstruction

has to be precise enough to identify tracks with a large impact parameter in order to combine the information provided by these tracks in different ways to finally tag a jet as a “b-jet”.

To perform b-tagging online the processing time has to be reduced as much as possible, both CMS and ATLAS have performed studies to check what are the minimal tracker informations needed. For online purpose the impact parameter significances of tracks belonging to a jet are directly used to tag the jet. The High Level Trigger of CMS consists of only one trigger level using the same algorithms as offline, made faster with a regional reconstruction. Using a partially reconstructed tracks CMS studies have shown that it is possible to select about 50% of b-quark jets with a light-quark jets rejection from 25 to 50 depending on the pseudorapidity regions. The expected offline performance with the same b-tagging algorithm do not change significantly. ATLAS developed a dedicated algorithm for online track reconstruction, compatible with the latency constraint. At Level 2 trigger, a rejection of light-quark jets of about 15 is expected, while retaining an efficiency of b-quark jets of 50%. In the next trigger selection, called Event Filter, offline quality algorithms allow to improve the light quark rejection up to a factor 10.

Figure 4: *Light-quark rejection in WH ($H \rightarrow b\bar{b}$) events as a function of the efficiency in $b\bar{b}$ events in CMS for different pseudorapidity bins.*



Offline b-tagging techniques are not limited by the processing time, thus more sophisticated observables can be adopted to evaluate the probability, for a given jet, to come from a light quark.

It is not straightforward to make a direct comparison of the offline b-tagging performance in CMS and ATLAS, because different event samples are used and results are presented in a different way. Nevertheless, Figures 3 and

4 show the results obtained, in the two experiments, adopting very similar b-tagging algorithms, both based on the likelihood-ratio method and exploiting the transverse impact parameter significance of the reconstructed tracks. In particular, the left plot shows, for ATLAS, the rejection against u-jets produced in the decay of a 120 GeV Higgs boson (WH associated production, $H \rightarrow u\bar{u}$ decay) as function of the pseudorapidity, corresponding to 60% efficiency on b-jets (from the $H \rightarrow u\bar{u}$ decay). The right plot shows, instead, the mistagging rate in CMS, as a function as a function of the efficiency in $b\bar{b}$ events for different pseudorapidity ranges.

To further improve b-tagging, the information of the track impact parameter inside a jet can be combined with the search for secondary vertices and other kinematic variables (like invariant mass and charged track multiplicity at the secondary vertex). CMS is finalizing this combined b-tagging approach, while ATLAS has shown that adding the information of the secondary vertex improves by a factor up to three the b-tag performance. Even if the displaced tracks in a jet give the most powerful feature to discriminate b-quark from light-quark jets, a lepton-based b-tag can also be useful. In this case the b-tagging efficiency is limited by the branching ratio of the leptonic b decay which is around 20%. In both ATLAS and CMS experiments b-tagging techniques based on the lepton reconstruction and identification are under developing.

5 B-Tagging performance at Startup

The b-tagging performance presented in the previous section refer to a perfectly optimized detectors. The effect of the realistic conditions of the detector, like misalignment, readout inefficiency and dead channels, precise description of the magnetic field and material budget, is presently under intensive study.

In particular, it is possible that in the startup phase only the inner and middle barrel layers of the CMS pixel detector will be installed. A similar startup condition was suggested in the past also for ATLAS, but is now discarded. The effect of these staged scenarios have been deeply investigated, especially for b-tagging where the information from the pixel detectors is essential to precisely evaluate track parameters and reconstruct secondary vertices.

Table 3: *Ratios of light quark rejection for staged and not-staged ATLAS pixel scenarios, for the WH and ttH benchmark channels at low luminosity.*

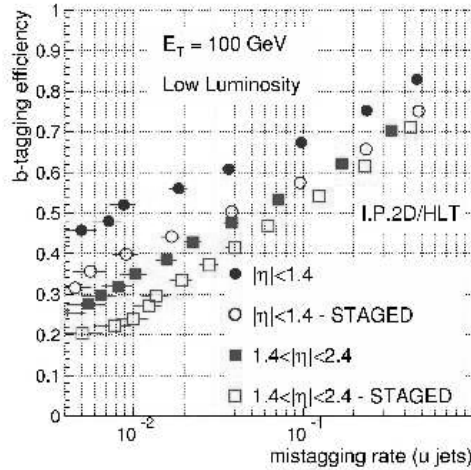
	u-jet rejection: perfect alignment	u-jet rejection: misaligned
$\epsilon_b=50\%$	164 ± 4	106 ± 2
$\epsilon_b=60\%$	53 ± 1	39 ± 1

The ATLAS Collaboration also evaluated b-tagging performance in the

benchmark channel $t\bar{t}H$ both with $H \rightarrow b\bar{b}$, in case of misalignments in the pixel detector; the results listed in Table 3 correspond to a $20 \mu\text{m}$ misalignment in the $R\Phi$ plane and $60 \mu\text{m}$ along Z . The effects of misalignment become negligible below 5 and $15 \mu\text{m}$ for the two coordinates respectively.

The effect of the CMS staged scenario is instead shown in Figure 5 in terms of b-tagging efficiency in $b\bar{b}$ events as a function of the mistagging rate in light $q\bar{q}$ events. The mistagging rate increases by a factor two with a staged scenario, while 60% of b-quark jets are retained.

Figure 5: *The b-tagging efficiency in $b\bar{b}$ events as a function of the mistagging rate in light $q\bar{q}$ events at low luminosity for a staged and not-staged CMS pixel scenarios.*



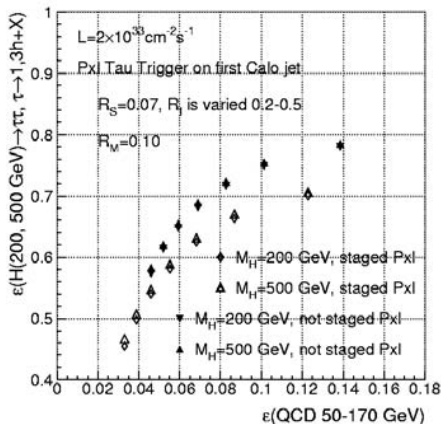
6 Tau-Tagging

The signature of a τ -lepton decaying into hadrons consists on one or three prongs jets. The τ -lepton identification is mainly based on the search for collimated jets using the information from both the Tracker and Calorimetric systems with a significant amount of missing energy due to the neutrinos. Being the τ lifetime (0.3 ps) significantly lower than the one of b hadrons, the detection of displaced tracks is only used at the offline stage, when all the precise information from the Tracker system are available. The leptonic τ decays are also considered: the electron decay is treated as the hadronic case and the muon decay needs the track impact parameter to be reconstructed.

At present, ATLAS mostly performed offline studies after the Level 1 trigger selection and CMS presented detailed strategies for the High Level Trigger chain, while offline strategies are under investigation. If the only calorimetric information are used to define an isolation variable for narrow jets, CMS shows

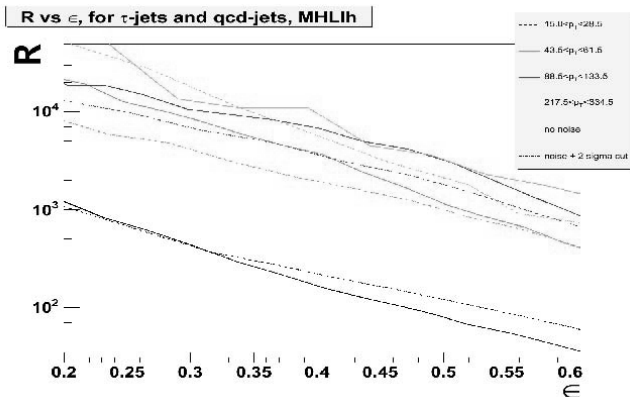
that 86% of $H \rightarrow \tau^+\tau^-$ signal can be selected when around 30% of QCD events are retained ³⁾. The performance on τ -isolation criteria can be improved by checking for tracks reconstructed in a cone around the direction of the τ jet. In order to optimize the processing time at HLT, the Pixel detector response can be used to reconstruct tracks in the cone. In Figure 6, the signal efficiency is

Figure 6: The τ -tagging efficiency at High Level Trigger in $H \rightarrow \tau^+\tau^-$ events as a function of the QCD efficiency in light $q\bar{q}$ events at low luminosity for a staged and not-staged CMS pixel scenarios.



presented as a function of the QCD efficiency varying the isolation cone in the Pixel detector.

Figure 7: The τ -tagging efficiency in $H \rightarrow \tau^+\tau^-$ events as a function of the QCD rejection and for different p_T bins with ATLAS.



No significant difference is shown for different Higgs mass hypotheses,

while in the case of a staged scenario the performance decreases of about 10%. Using all the Tracker response improves the signal efficiency of 15%, but the processing time increases of a factor 2. At the offline stage the whole information from the Tracker can be used and displaced decay vertices can be reconstructed. ATLAS uses a likelihood approach to search for $H \rightarrow \tau^+ \tau^-$ decays based on isolation variables.

ATLAS shows (Figure 7) the τ identification efficiency as a function of the QCD rejection. Rejection rates at the same signal efficiency can vary a lot, depending on the p_T of the tau.

7 Conclusions

Many interesting channels relevant for discovery physics studies at LHC, such as searches of Higgs bosons or supersymmetrical particles, will contain in the final state jets coming from b-quarks or tau leptons. Both ATLAS and CMS experiments have developed efficient trigger and offline selection strategies to identify this kind of events.

In this contribution the current performance for the two experiments was reviewed, for both the online and the offline implementations, showing that it should be well adapted to the physics requirements at LHC. Anyway, the comparisons between the experiments are far from being complete, due to many factors: different event samples are often used; different development stages for the online and offline strategies; intrinsic difficulties in comparing online results, due to infrastructural differences in the approach to the trigger selection.

The comparison between the two experiments will become even more interesting as soon as performance studies will heavily focus on the commissioning phase. Common event samples will be probably used, and a throughout review of the selection methods will be performed in similar ways. Examples of this kind of studies, such as those on the impact of misalignments or of staged detector scenarios, are already provided in this contribution.

References

1. The Atlas Collaboration, Atlas Detector and Physics Performance, CERN/LHCC 99-14.
2. The CMS Collaboration, The Tracker Project Technical Design Report, CERN/LHCC 98-6.
3. The CMS Collaboration, Data Acquisition & High Level Trigger TDR, CERN/LHCC 2002-26

STATUS OF ENERGY FLOW ALGORITHMS IN ATLAS AND CMS

B. Mangano, I. Vivarelli
INFN and Scuola Normale Superiore Pisa

Abstract

The Energy Flow method is based on the integration between the calorimeters and the tracker. The idea is to substitute the calorimetric measurement of the energy with the momentum measured by the tracker for charged tracks. The goal is to improve the final resolution on jet energy and direction and correct the energy scale. The current status of the Energy Flow algorithms for both ATLAS and CMS experiment is discussed.

1 Detectors description

The Energy Flow techniques rely on the combined performances of the tracker and the calorimeters. A brief reminder of the structure of these subdetectors for the ATLAS and CMS experiments will be useful to better understand the results discussed in the following.

The ATLAS calorimetry ¹⁾ makes use of different technologies in different pseudorapidity regions. The EM calorimeters cover up to $|\eta| \simeq 3.2$. The passive material (lead) is disposed along an accordion structure, while LAr is used as the active material. There are three longitudinal layers for a total of 24 radiation lengths (1.2 interaction lengths), while the transversal segmentation is $\Delta\eta \times \Delta\phi = 0.025 \times 0.025$. The HAD calorimetry makes use of a iron-scintillating tiles calorimeter in the central region $|\eta| < 1.7$ while, because of its intrinsic radiation hardness, lead-LAr is used again up to $|\eta| < 3.2$. The forward region $3.2 < |\eta| < 5$ is covered by the Forward Calorimeter. The goals for the resolution and linearity on single electrons and pions for the barrel region have been reached at the combined testbeams ^{2) 3)} ($10\%/\sqrt{E} \oplus 0.7\%$ for electrons, $50\%/\sqrt{E} \oplus 3\%$ for pions).

The inner tracker ⁴⁾ combines high-resolution detectors at the inner radii with continuous tracking at the outer radii (3 layers of pixels, four of silicon microstrips, and a straw tube tracker, the TRT). The tracker is included in a 2T solenoidal magnetic field. The momentum resolution is

$$\sigma\left(\frac{1}{P_T}\right) = \left(0.36 \oplus \frac{13}{P_T}\right) \text{TeV}^{-1} \quad (1)$$

where P_T is expressed in GeV, while the efficiency for isolated tracks is above 95% (87–90% for non-isolated tracks).

The CMS calorimetry ^{5) 6)} is divided in a barrel ($|\eta| < 1.5$) and 2 end-caps ($|\eta| < 3$). Two forward detectors complete the hermeticity up to $\eta = 5$. The EM section (ECAL) is composed by $PbWO_4$ crystals, with a transversal segmentation of $\Delta\eta \times \Delta\phi = 0.0174 \times 0.0174$ and one longitudinal section of $25.8X_0$. The resolution for single electrons in barrel can be parametrized by

$$\frac{\sigma(E)}{E} = \frac{2.5\%}{\sqrt{E}} \oplus 0.5\% \oplus \frac{150 \text{ MeV}}{E} \quad (2)$$

The hadronic calorimeter (HCAL) is a sampling calorimeter (brass as passive material, scintillating tiles as active material). The transversal segmentation is $\Delta\eta \times \Delta\phi = 0.087 \times 0.087$ for $|\eta| < 2$ and coarser for larger $|\eta|$. The testbeam results ⁷⁾ indicate a resolution on single “mip-in-ECAL” pions of $101\%/\sqrt{E} \oplus 4.0\%$.

The tracker ⁸⁾ has three pixel and ten silicon microstrips layers in the central region, while the end-cap region is covered by two pixel layers, three inner

and nine outer forward disks of silicon detectors. The momentum resolution is

$$\sigma\left(\frac{1}{P_T}\right) = \left(0.15 \oplus \frac{5}{P_T}\right) \text{ TeV}^{-1} \quad (3)$$

with more than 95% efficiency for isolated tracks reconstruction (90% for non-isolated tracks).

2 Energy Flow Algorithms in ATLAS

Inside the ATLAS collaboration, two different approaches to the use of the energy flow have been studied. The first one ⁹⁾ (approach A in the following) builds EnergyFlow objects from calorimeter towers and tracks and uses them as input objects for the jet reconstruction algorithm, while the second ¹⁰⁾ (approach B) applies energy flow techniques on reconstructed jets. Both of them are at present somewhat limited by the *ad interim* solutions used inside ATLAS for the clustering. While at present the standard clustering for jets is done only in the η - ϕ space, the final clustering, which is under development, will make use of the complete η - ϕ - r segmentation of the ATLAS calorimetry, thus allowing for 3D clusters, more efficient in recognizing energy deposits belonging to a jet and less sensitive to noise.

The aim of the approach A is to define consistently topologically connected EnergyFlow objects. Each charged track seeds an EnergyFlow object. The tracks are then associated to calorimeter clusters both in the EM and in the HAD calorimeter extrapolating the track trajectory using the helix and making a matching in the η - ϕ space. The energy deposit expected for the particle (given its identification and its momentum measured by the tracker) is then subtracted from the calorimeter clusters. If the remaining energy in the cluster is within $1.28 \sigma_{noise}$ from zero, the cluster is removed from the cluster list. The remaining non-zero EM clusters seed EnergyFlow objects, the η - ϕ association is repeated and the expected energy deposits in the HAD clusters is subtracted. The remaining HAD clusters seed EnergyFlow objects.

Finally, EnergyFlow objects that are topologically connected (an EM cluster can be associated to more than one HAD cluster because of the bending of the magnetic field, for example) are grouped together in only one EnergyFlow object.

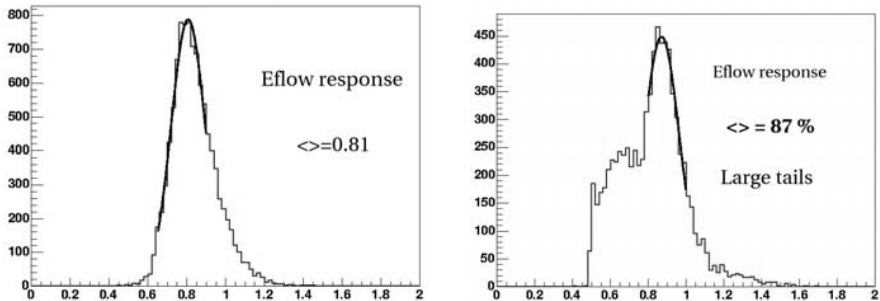


Figure 1: *The ratio between the reconstructed and reference energy is considered for events with 3 particles in the final state (γ, n, π^\pm). The shape of the distribution is degraded as they get close (on the left: $\Delta R > 0.1$, on the right: $\Delta R = 0.05$).*

Approach B considers as input for the Energy Flow algorithm the already reconstructed jets. The idea is to identify (within a jet) clusters generated from charged hadrons, photons, electrons and finally neutral hadrons. To do this, a first iteration is performed on EM clusters. The central cell of those clusters that do not have a charged track pointing to them is chosen as a seed, and all the cells within $\Delta R = 0.0375$ are labelled as EMCL. Then an iteration over the tracks is performed, and all the cells within $\Delta R = 0.0375$ from the track are labelled as CHRГ. Finally, unassigned cells are labelled as NEUH. Ideally, EMCL should take into account photons, CHRГ should account for charged pions, while NEUH should include neutrons.

It is worth to notice that the Energy Flow algorithms work at best with high granularity calorimeters and low multiplicity environment. If the subtraction of the expected energy is performed on an isolated cluster, one can expect an improvement on the resolution. But as soon as the clusters are not well separated, the subtraction of the expected value does not lead to an improvement of the resolution. This can be seen for example in fig. 1, where a “jet” composed by only three particles (γ, n, π^\pm) is considered. If the particles are far away in the η - ϕ space (left plot), the distribution of the measured energy is well shaped, but as soon as the particles become close (right figure), the Energy Flow response loose its regularity. Therefore, a refined 3D clustering algorithm is mandatory to improve the performances of the Energy Flow algorithms in

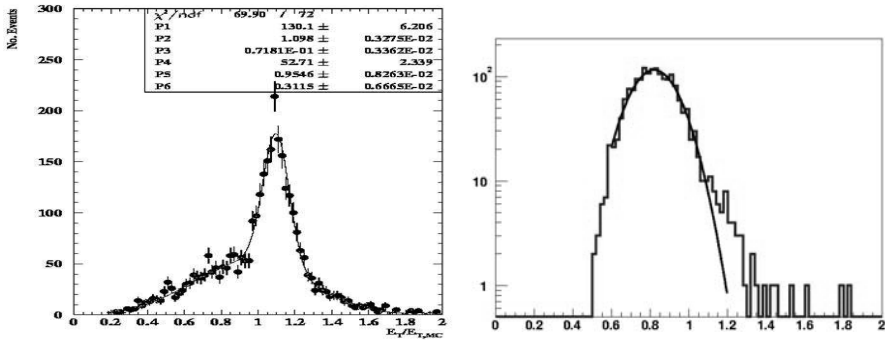


Figure 2: *On the left: the ratio between the reconstructed and the reference energy for the approach A on 50 GeV jets. The $\sigma(E)/E$ on the core of the distribution is 7%. On the right: The same for approach B for jets with energy between 20 and 60 GeV. The $\sigma(E)/E$ is 12–13%. As a reference, the TDR resolution for jets at 50 GeV is 8–9 %.*

ATLAS.

Fig. 2 shows the results of both the approaches discussed. Noise and pile-up are not included in the simulation. The left figure shows the current performances of approach A for 50 GeV jets. Two different contributions can be seen. The core of the distribution (whose $\sigma(E)/E$ is 7%) shows the performances where the track subtraction has worked, while in the broad peak, it did not work. The right figures shows the performances of approach B on jets with energy between 20 and 60 GeV. While the distribution is much more regular, the peak is broader ($\sigma(E)/E \simeq 12 - 13\%$) with respect to the core of the left plot. For comparison, the resolution quoted in the TDR for 50 GeV jets (from the standard calorimeter measurement) is 8%. The improvement of the clustering strategy could give an important improvement to the Energy Flow performances.

3 CMS algorithm description

As for ATLAS, an Energy Flow Algorithm has been developed inside the CMS collaboration. The idea that low p_t track momenta are better determined by the tracking system inside the 4T magnetic field than by their energy measurement in the calorimeter is the starting point. The current implementation ¹¹⁾

corrects the jet energy and direction after its reconstruction by the jet-finding algorithm (that uses the calorimetric deposits only). Up to now the EF algorithm works with jet provided by cone jet-finding. In fact the cone size ΔR is a basic parameter both for the jet-finding and for the EF algorithm.

The CMS jet-finding cone algorithms do not directly recover charged tracks which, for effect of the magnetic field, are swept out of the jet cone, while the ATLAS one does. Therefore the CMS EF algorithm carries out this operation too.

The integration between Calorimeter and Tracking system measurements is performed by the EF algorithm through the following steps:

- Jets in the event are reconstructed by the calorimeter using an iterative cone algorithm. The jet object is defined by the collected energy and the direction.
- In the event all tracks with $P_T > 1$ GeV and $|\eta| < 2.4$ are reconstructed and selected at the vertex in a cone ΔR around jet direction. The cone is the same of the jet-finding algorithm.
- For each track the impact point on the ECAL inner surface is extracted and extrapolated to the HCAL one.
- The expected response of the calorimeter to each charged track is subtracted from the calorimetric cluster and track momentum is added.
- Other low P_T charged tracks, swept out of the jet cone definition by the magnetic field, are added to jet energy.

The algorithm doesn't include two features that, in a future implementation, could improve its performance. The first one is the use of Particle Identification: at the current status, the response to a pion is used for every charged track, independently of its type. The second is the response subtraction: even if there is a good confidence that a cluster is formed by a single track, the current EF algorithm subtracts only the expected energy deposit of the track and not the complete cluster. This leads to a good improvement in the jet energy calibration, but not in the energy resolution.

The algorithm performance has been tested comparing Montecarlo¹ and

¹Montecarlo jets are reconstructed implementing the same jet-finding algorithm than for reconstructed jet with tracks information from the MC truth

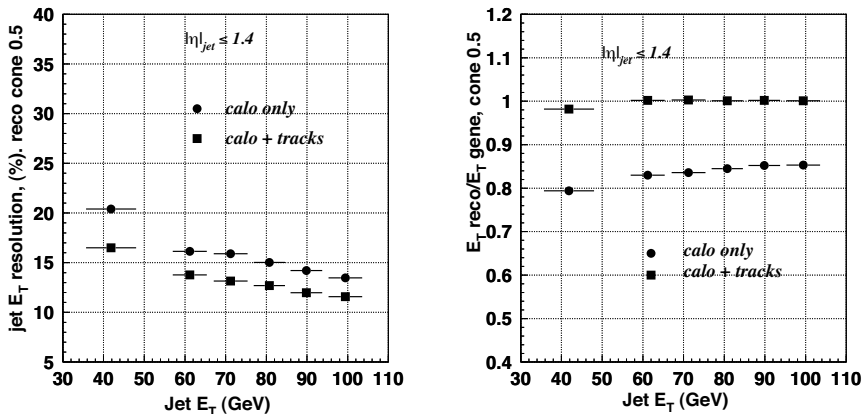


Figure 3: Jet transverse energy resolution (left) and reconstructed jet transverse energy (right) as a function of the generated jet transverse energy. Jets with $0 < |\eta| < 1.4$ (barrel) from a sample with low luminosity pile-up; reconstruction with calorimeter only (close circles), subtraction procedure of expected responses using library of responses and out-of-cone tracks (close squares).

reconstructed jets, with and without EF applied. Di-jet events with P_T between 80 and 120 GeV/c were generated with PYTHIA and fully simulated and reconstructed inside the CMS software framework¹⁴⁾ ¹³⁾. Effects due to low luminosity ($L = 2 \times 10^{33} \text{cm}^{-2} \text{s}^{-1}$) pile-up have been included. The resolution and the reconstructed jet energy fraction are shown for jets generated with $|\eta| < 1.4$ in fig. 3. When the EF algorithm is applied, the reconstructed jet energy fraction for 40 GeV generated jets increases from 0.80 to 0.99 and the same fraction for 100 GeV jets increases from 0.85 to 1.00. The resolution improves by about 20-25% as a result of adding the out-of-cone tracks.

In the endcap region (figs. 4), jets with the same E_T as in the barrel are more energetic and, in addition, the tracking efficiency is smaller in the endcap than in the barrel. Therefore, the tracker information is not relevant in the endcap above 80-90 GeV and is less rewarding for lower E_T jets than in the barrel. Besides jets in the endcap are more affected by pile-up than in the barrel.

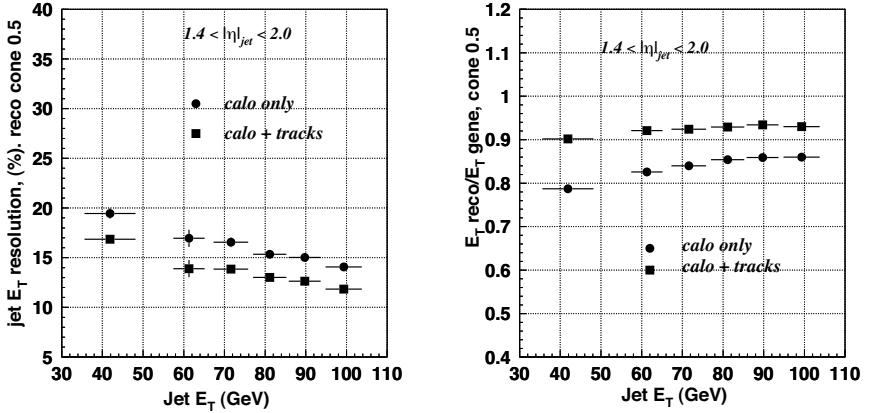


Figure 4: *Jet transverse energy resolution (left) and reconstructed jet transverse energy (right) as a function of the generated jet transverse energy. Jets with $1.4 < |\eta| < 2.0$ (endcap) from a sample with low luminosity pile-up; reconstruction with calorimeter only (close circles), subtraction procedure of expected responses using library of responses and out-of-cone tracks (close squares).*

The performance of the EF algorithm has been tested also on events with a $120 \text{ GeV}/c^2$ X object decaying into light quarks with initial and final state radiation switched on. The X mass is reconstructed from the two leading jets that are within $R = 0.5$ of the direction of the primary partons. The ratio of the X mass reconstructed to the X mass generated for calorimetry jets and calorimeter-plus-tracker jets is shown in Fig. 5. The di-jet mass is restored with a systematic shift of about 1% and the resolution is improved by 10%. The ratio of the reconstructed to the generated X mass is 0.88 before corrections with tracks and 1.01 after corrections.

A more recent extension to the EF algorithm makes use of two cones with different size ¹²⁾: a smaller one for the jet-finding step and a larger one for the out-of-cone charged tracks recovery step. The idea of two different cones is suggested by the fact that neutral tracks release their energy basically along the jet direction, since they are not deflected by the magnetic field. Therefore a small cone is sufficient to recover most of the neutral deposits

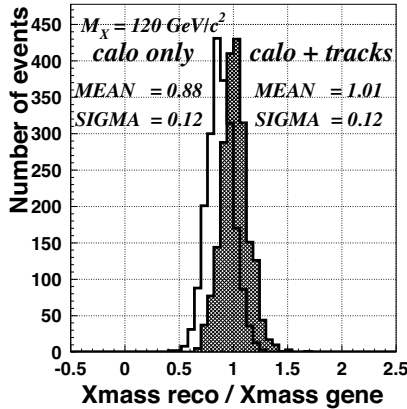


Figure 5: *Ratio of the reconstructed to the generated X mass with calorimeters only (empty histogram) and with calorimeter + tracks corrections (hatched histogram).*

in the calorimeter; the charged contribution to the jet energy is subsequently recovered by the tracker using a larger size cone. In this way, for the same amount of charged and neutral jet fragments recovered, the contamination by neutral deposit which do not belong to the jet (pile-up, underlying event, etc..) can be reduced. The performances of this extended algorithm are currently under investigation.

4 Conclusions and Outlook

The usage of EF algorithm in jet reconstruction looks more promising in the CMS experiment than in ATLAS. The latter, in fact, has placed more emphasis to the hadronic calorimeter performance. However it's important to stress that part of the power of the CMS EF algorithm is due to the recovery of out-of-cone tracks, a feature already included in ATLAS jet-finding process. In the future improvement in the EF algorithm performance are expected for both collaboration: ATLAS is developing a 3D clustering algorithm which will be more efficient in separate energy deposits; CMS plans to implement particle ID so that the correct calorimetric response for each track can be evaluated.

5 Acknowledgements

The work reported here has been produced by the effort of several individuals in the ATLAS and CMS collaboration. We would like to acknowledge in particular the contributions, precious comments and explanations from D.Tovey, D.Froidevaux, E.Richter–Was, P.Nevski from the ATLAS collaboration and from O.Kodolova, A.Nikitenko, L.Fano, A.Santocchia and D.Spiga from the CMS collaboration.

References

1. ATLAS Calorimeter performance Technical Design Report, CERN/LHCC/96-40.
2. M.P. Casado and M. Cavalli Sforza, TILECAL-NO-75,1996.
3. S.Akhmadaliev *et al.*, Nucl. Inst. and Meth., A429, pag. 461, 2000.
4. Inner Detector Technical Design Report, CERN/LHCC 97–16 and 97–17.
5. The HCAL Technical Design Report, CERN/LHCC 97–31.
6. The ECAL Technical Design Report, CERN/LHCC 97–33.
7. V.V.Abramov *et al.*, Nucl. Inst. and Meth., A457, pag. 75, 2001.
8. The Tracker Technical Design Report, CERN/LHCC 98–6.
9. Talk given at 4th ATLAS Physics Workshop, Athens, 21–25 May 2003.
10. Talk given at ATLAS Software Workshop, 4th March 2004.
11. O.Kodolova *et al.*, *Jet energy correction with charged particle tracks in CMS*, CMS NOTE 2004/015.
12. A. Santocchia, Double Cone Algorithm for Jet Energy Correction, JetMet Meeting CERN 21-09-2004.
13. <http://cmsdoc.cern.ch/orca/>
14. <http://cmsdoc.cern.ch/cmsim/cmsim.html>

Session III – Standard Model

THE TOP QUARK AT LHC

Andrea Giammanco
SNS and INFN Pisa
Guido Gagliardi
INFN Genova

Abstract

The LHC (Large Hadron Collider) at CERN will be a "top factory" given the high top quark production cross section. This paper reports the present perspectives for the top physics measurements that will be possible at CMS and ATLAS, focussing on the top mass, single top production and FCNC decays. The huge top sample collected may be used in the commissioning phase to calibrate jet energy and B-tagging algorithms.

1 Introduction

The top quark discovery ^{1, 2)} and mass measurement ³⁾ highlighted the uncommon nature of the heavier quark. Top decays proceed through the channel $t \rightarrow Wb$ with a BR of 0.99, so being a source of energetic b-jets. The fact that $\tau_{decay} < \tau_{QCD}$ implies that the top quark exists only as a free quark,

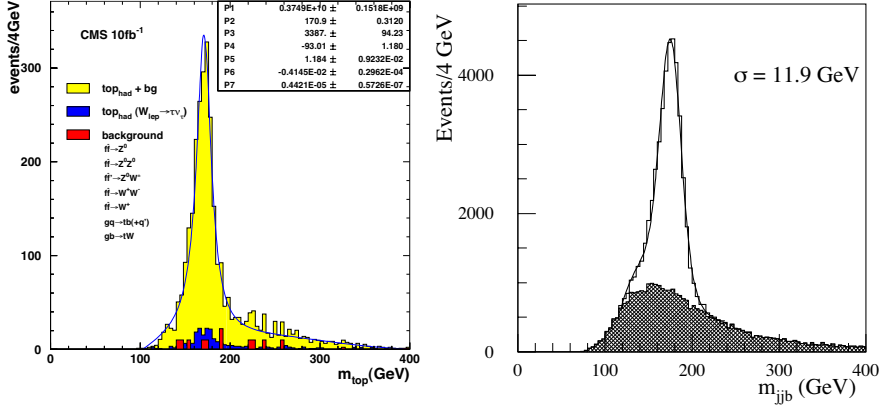


Figure 1: The mass of the reconstructed top in the semileptonic channel after all cuts including the contribution of the indicated background processes at CMS ⁶⁾ and ATLAS ⁵⁾.

so that the effects from new physics should show up very clearly on top of the precise Standard Model predictions. Some SUSY particles and heavy resonances have the top quark as decay product: as a consequence the Standard Model production of the top quark is the background to many new physics channels.

2 Top quark mass measurement at LHC

The top pair production at LHC has been computed at the NNLO-NNLL order ⁴⁾ to be $(825 \pm 150) pb$, about 100 times higher than the one at Tevatron. At low luminosity LHC will then produce $8 \cdot 10^6 t\bar{t}/y$, so being a top factory.

The top quark can be seen in the semi-leptonic (lepton + light jets + b-jets), leptonic (di-lepton + b-jets) and hadronic channels, whose signatures are respectively the presence of a lepton plus jets, a lepton pair plus b-jets and a multijets event.

2.1 Semi-leptonic channel

The lepton + jets channel is easily triggered and has a BR of 29.6%. An integrated luminosity of 10 fb^{-1} will contain a sample of $2.5 \cdot 10^6$ events. The

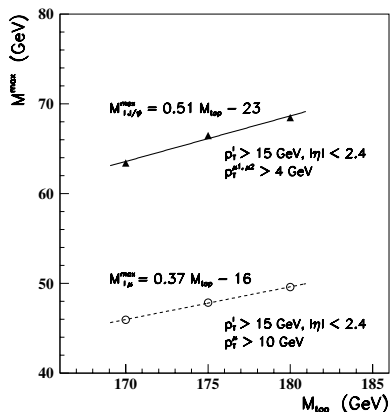


Figure 2: *Dependence on top quark mass of the isolated lepton plus J/ψ invariant mass (solid line) and of the isolated lepton plus μ -in-jet (dashed line) ¹⁵⁾.*

hadronic decaying top can be fully reconstructed and the cut over the reconstructed mass $|M_{j\bar{j}b} - M_t|$ greatly improves the background reduction. The leptonic decaying top can be partially reconstructed by imposing $E_T(\nu) = E_T(\text{missing})$ and $M_{l\nu} = M_W$. The main background to this process arises from SM W +jets and Z +jets production. The top mass peak is shown in fig.1 for both ATLAS ⁵⁾ and CMS ⁶⁾ experiments. The expected mass resolution is $1 \div 2$ GeV.

An improvement to the mass measurement can be achieved looking at $t\bar{t}$ pairs produced back-to-back with high P_T . The backgrounds and the wrong jet assignments are then reduced since the decay products will occupy two distinct emispheres.

Another interesting analysis looks for a J/ψ in the final state, which is easily reconstructed in the dimuon decay. The top mass depends on the invariant mass of the system lepton+ J/ψ (fig.2). This analysis is unrealistic at low luminosity, while it becomes promising at full luminosity with an expected sample of about 1000 events/y.

2.2 Leptonic channel

The leptonic decaying top is easily triggered by a dilepton trigger and has a BR of 4.9%. Due to the presence in the final state of two ν 's, the mass measurement relies on the MC studies for the angle between the b quark and the lepton. The pairing between the b quark and the leptons is made by minimising the invariant mass M_{lb}^2 and is correct in about the 85% of the cases.

An improvement to the top mass measurement can be done by looking at the soft lepton coming from the b quark cascade decays, the top mass being strongly correlated with the invariant mass of the lepton pair.

2.3 Hadronic channel

Although the 44.4% of the $t\bar{t}$ pairs decay into a full hadronic final state, triggering the hadronic channel is far from trivial, since only very high jet energy thresholds give reasonable QCD rejection. The S/B ratio, using b-tagging and event shape variables, may be reduced to about $1/8 \div 1/6$, the background being mostly multi-jet QCD events. The event can be fully reconstructed but the correct pairing between the jets is not trivial.

2.4 Top mass measurement from the production cross section

The $t\bar{t}$ production cross section is dependent on the top mass. The statistical contribution to the top mass measurement error is lower than 10% after a few days of low luminosity data taking. On the other hand, the systematic contribution to the top mass measurement is quite relevant: a PDF uncertainty of 10% gives a ΔM_{top} of about 4 GeV, while the uncertainty on the total cross section is estimated to account for another 5%. Measuring the top mass using the production cross section is however interesting since the systematic effects are uncorrelated with the ones for the full event reconstruction techniques.

2.5 Summary of top mass measurement

The sources of top mass uncertainty are summarized in table 1 for the techniques described so far. The values quoted refer to both ATLAS and CMS experiments. The systematic errors are correlated between the experiments and the techniques.

Source of error	Semilept.	Semilept. (high P_T)	Lept.	$\sigma_{t\bar{t}}$	Semilept. J/Ψ
Statistical	0.10	0.25	0.90 (?)	< 0.05	< 1.0
Light jet energy scale	0.20	1.2 (?)	-	-	-
b -quark jet energy scale	0.60	0.60	0.60	-	-
ISR/FSR	1.5 (?)	0.2 (?)	1.0	(?)	0.30 (?)
b -quark fragm.	0.25	0.10	0.70	-	0.60
backgrounds	0.15	0.10	0.10 (?)	negl.	0.20
PDF	negl.	negl.	negl.	4.0	0.20
Total	< 2.0 (?)	< 2.0 (?)	< 2.0 (?)	< 4.0 (?)	< 1.3 (?)

Table 1: Top mass measurements error sources (in GeV) for the various techniques described in the text.

From the reported data a combined error of about 1 GeV should be achievable.

3 Single top production

The electroweak single top production provides a direct measurement of the V_{tb} CKM element and is particularly sensitive to new physics beyond the Standard Model, entering the $W - t - b$ vertex.

This process has never been observed so far; published Tevatron analyses only give cross section upper limits ^{7, 8, 9}).

Single top quarks can be produced at hadronic colliders via the three processes shown in fig. 3: t-channel (or W -gluon fusion) is the main production mechanism with $\sigma \approx 250$ pb expected at LHC ¹⁰), Wt associated production follows with $\sigma \approx 60$ pb ¹¹), and s-channel (or W^*) process has only $\sigma \approx 10$ pb ¹⁰). It is interesting to study the three processes separately, since they are differently sensitive to new physics: the existence of a new massive vector boson W' would increase the s-channel signal, while a $FCNC$ process $gu \rightarrow t$ would signal itself in the t-channel process, and in a light SUSY scenario ¹²) the Wt production would have to be disentangled by a significant $H^{\pm}t$ production.

Furthermore, the three processes have different backgrounds and their systematic errors are different (see Table 2). The s-channel has the lowest

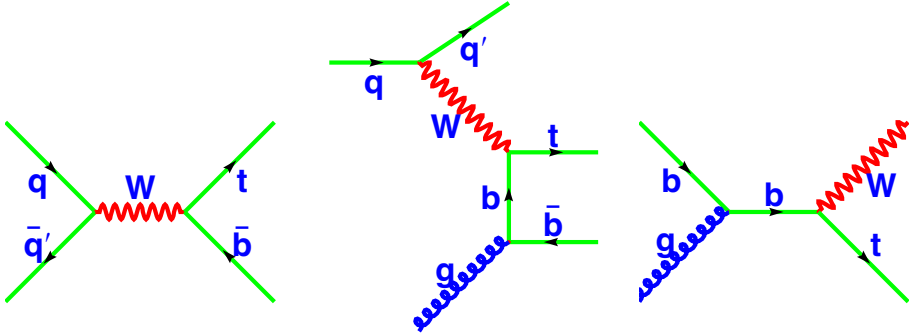


Figure 3: *Single top diagrams. From left to right: t-channel (or Wg fusion), Wt associated production, s-channel (or W^*).*

rate, but is the best theoretically understood mechanism of electroweak top production.

	$d\sigma/\sigma$ (%)	$d\sigma/\sigma$ (%)	$d\sigma/\sigma$ (%)
Source of error	s-channel	t-channel	Wt
Statistical	5.4	0.71	-
PDF	4	10	-
μ (scale)	4	5	-
$\delta m_t = 2$ GeV	5	2	-
Total theory error	7.5	11	50

Table 2: Relative errors in the cross section for the three single top production processes.

The main backgrounds, due to final states similar to the processes under study, are $t\bar{t}$ ($\sigma \approx 830$ pb) and $Wb\bar{b}$ ($\sigma > 300$ pb). To reduce the enormous QCD multi-jets background, all the published analyses require a high p_T lepton in order to select $t \rightarrow l\nu b$ decays.

3.1 t-channel production

The most striking feature of the final state for this process is the presence of a forward light jet from the “spectator” quark, i.e. the one recoiling against the W (see fig. 3). Furthermore, the \bar{b} (b) quark associated to the t (\bar{t}) quark tends

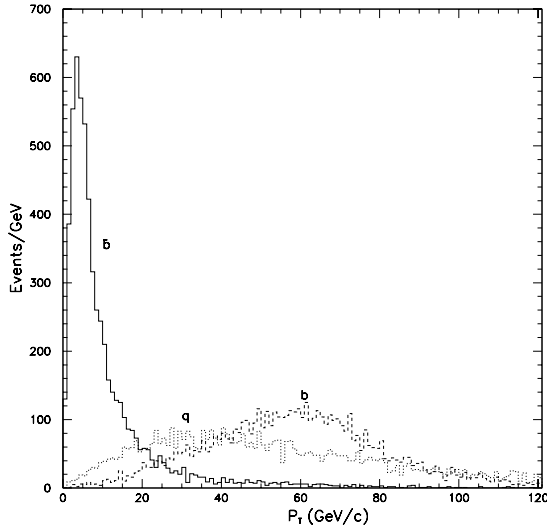


Figure 4: *Transverse momentum spectra for the final state partons in the t -channel production of single top quarks* ¹⁵⁾.

to be produced at very small angle, resulting outside of the detector acceptance in most cases (see fig. 4). So, the typical selection requires exactly two jets with only one tagged as b -jet.

ATLAS ¹³⁾ further requires that the total mass of the event be greater than 300 GeV and that the sum of the E_T 's of the lepton and all the jets be greater than 200 GeV, selecting 27000 signal and 8500 background events after 30 fb^{-1} . This corresponds to $S/B=3.1$ and give a 0.71% relative statistical uncertainty on the cross section.

CMS ¹⁵⁾ asks for a jet in the forward calorimeter ($2.5 < |\eta| < 4.0$) and another jet in the central region ($|\eta| < 2.5$), selecting 6600 signal events and 1900 background events ($S/B=3.5$) in a window around the nominal top mass after 10 fb^{-1} integrated luminosity, yielding a 1.5% relative statistical uncertainty on the cross section.

3.2 Wt production

This process yields two W 's, the one produced in association with the top and the other coming from its decay. The strategy followed by ATLAS ¹³⁾ is to

select events in which one W decayed leptonically and the other hadronically, by asking one high p_T lepton and exactly three jets, one tagged as b -jets and the other two with an invariant mass in a window around the nominal W mass. With the additional requirement of the total mass of the event smaller than 300 GeV, 6800 signal events and 30000 background events (mostly $t\bar{t}$) survive the cuts, giving $S/B=0.22$ and a 2.8% relative statistical uncertainty on the cross section.

3.3 s-channel production

Tight cuts must be applied to obtain a reasonable signal-to-background ratio for this small cross-section process. Exactly two high p_T jets are required, both tagged as b -jets. This significantly reduces the W +jets background (whose jets have softer spectra) and also $t\bar{t}$ (containing, on the contrary, too many high p_T jets on average) and t-channel background. In the ATLAS analysis¹⁴⁾ further cuts require that the invariant mass of the event be larger than 200 GeV and the scalar sum of the jet transverse momenta be larger than 175 GeV. This selects 1100 signal events and 2400 background events (mostly $t\bar{t}$) with $S/B=0.46$ and a 5.4% relative statistical uncertainty on the cross section.

4 FCNC

LHC will give the opportunity to put stringent limits on rare top decays, including the Flavour Changing Neutral Current (FCNC) ones.

According to the Standard Model, branching ratios are way too small for FCNC decays to be observed, but an opportunity for new physics to be revealed is provided.

4.1 $t \rightarrow qZ$

Standard Model and Minimal SuperSymmetric Model predict $BR(t \rightarrow qZ)$ to be of order 10^{-12} and 10^{-8} , respectively. The golden channel for this search is of course $t\bar{t} \rightarrow qZbW \rightarrow ql\bar{l}b\nu$, with two leptons in a mass window around the nominal Z mass. This way a branching ratio as small as 1.1×10^{-4} can be measured⁵⁾.

4.2 $t \rightarrow q\gamma$

SM and MSSM predict $\text{BR}(t \rightarrow q\gamma)$ to be of order 10^{-12} and 10^{-8} , respectively. Again, the best selection comes from W decaying leptonically. A branching ratio as small as 1.0×10^{-4} can be measured ⁵⁾.

4.3 $t \rightarrow qg$

This channel is so overwhelmed by backgrounds that there is apparently no hope to observe this decay. On the other hand the same tgq FCNC coupling, if enhanced by new physics, would give a spectacular and quite unambiguous same sign top production ($qq \rightarrow tt$). In this case, a branching ratio as small as 7.4×10^{-3} may be extracted ⁵⁾.

5 Top quark and commissioning of the detectors

For the LHC experiments in the commissioning phase we can assume that a leptonic trigger will be available, while the b-tagging and light quarks rejection efficiencies and the jet energy scale will still have to be calibrated and understood. In this scenario the semileptonic decaying top sample will be a tool to provide energetic b-jets in kinematical closed events.

In fig. 5 the top mass peak from the semi-leptonic sample collected in the first days of LHC operation (integrated luminosity: 150pb^{-1}) is shown over the expected background. The three jet combination with higher P_T is assigned to the hadronic decaying top.

Of the four jets from semileptonic top decays two can be assigned to the W decay by imposing tight invariant mass cuts: the remaining two jets make an high purity b-jets sample useful to calibrate the b-tagging algorithms. By rescaling the 4-vector of the non-tagged jets in order to obtain $M_{jj} = M_W$ it is possible to calibrate the jet energy in the $50 \div 200$ GeV P_T range with a 1% precision. For $P_T(\text{jet})$ of the order of 50 GeV the FSR must be taken into account by loosening the jet cones; for $P_T(\text{jet})$ greater than 200 GeV the jet overlapping becomes dominant.

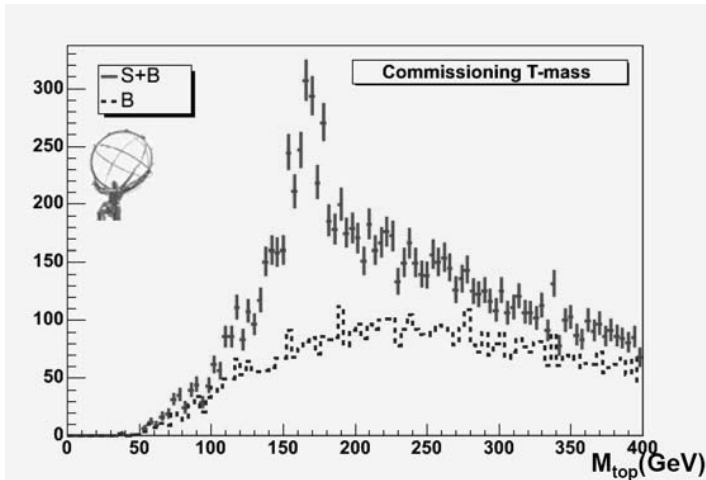


Figure 5: *Semi-leptonic top signal over the expected background after the selection described in the text, for an integrated luminosity of 150pb^{-1} .*

References

1. CDF Collaboration, Phys.Rev.Lett. **74**, 2626 (1995).
2. D0 Collaboration, Phys.Rev.Lett. **74**, 2632 (1995).
3. CDF and D0 Collaborations and Tevatron Electroweak Working Group (P. Azzi et al.), hep-ex/0404010.
4. N.Kidonakis, R.Vogt, Phys.Rev. D **68**, 114014 (2003).
5. ATLAS Collaboration, ATLAS TDR, CERN/LHCC/99-15.
6. L.Sonneschein, CMS NOTE 2001/001.
7. CDF Collaboration, Phys.Rev. D **69**, 052003 (2004).
8. CDF Collaboration, hep-ex/0410058.
9. D0 Collaboration, Phys.Lett. B **517**, 282 (2001).
10. B.W.Harris, Phys.Rev. D **66**, 054024 (2002).
11. T.Tait, Phys.Rev. D **61**, 034001 (2000).

12. M.Beccaria, F.M.Renard, C.Verzegnassi, *Phys.Rev. D* **71**, 033005 (2005).
13. M.Cobal, Proceedings of the “I Workshop Italiano sulla Fisica di ATLAS e CMS” (Pisa, 2003).
14. D.O’Neil, B.González Pineiro, M.Lefebvre, *J.Phys. G* **28**, 2657 (2002).
15. D.Green, K.Maeshima, R.Vidal, J.Womersley, W.Wu, CMS NOTE 1999/048.

W AND Z PHYSICS AT THE LHC

M. Vos

INFN - Sezione di Pisa, Italy

P. Ferrari

CERN, Switzerland

Abstract

The two general-purpose experiments in the Large Hadron Collider at CERN, ATLAS and CMS, offer a wide range of “new” and “standard” physics. In this note the Standard Model physics potential - and more specifically that of W and Z bosons - is briefly outlined. An overview is given of feasibility studies for gauge boson precision measurements. Further, the use of W and Z final states to improve the existing experimental limits on triple gauge couplings is discussed. Finally, the importance of the Z and W samples during the commissioning phase - for calibration and alignment of the detector, but also as a reference physics sample for studies of the underlying event and the determination of parton density functions - is discussed.

1 Introduction

The LHC is primarily intended as a discovery machine exploring the energy frontier. In several articles in these proceedings the “new” physics reach of ATLAS and CMS is discussed. However, the characteristics of the collider offer very interesting possibilities for Standard Model physics as well. The production rate for gauge bosons is unprecedented: during the initial years of operation, with the “low” luminosity of $2 \times 10^{33} \text{cm}^{-2} \text{s}^{-1}$, 100 million W bosons decaying into an electron and a neutrino and 10 million Z to electron-positron events per year (10fb^{-1}) are produced. In combination with the large center-of-mass energy the LHC opens up several windows for Standard Model physics. In the following, two fields are discussed: precision measurements of electroweak gauge boson properties and the study of triple gauge couplings.

Precision measurements of gauge boson properties provide an important constraint of the Standard Model. The Higgs boson mass can be predicted from the mass of the top quark and W boson via the following formula:

$$m_w = \sqrt{\frac{\pi\alpha_{EM}}{\sqrt{2}G_F \sin\theta_W} \frac{1}{\sqrt{1-\Delta r}}} \quad (1)$$

where all constants (Fermi’s constant G_F , the electro-weak fine-structure constant α_{EM} and the Weinberg weak mixing angle θ_W) are well-known. The top and Higgs mass are related through the radiative corrections Δr that have a quadratic dependence on the top mass, $\Delta r \propto m_t^2$, and a logarithmic dependence on the Higgs boson mass: $\Delta r \propto \log m_H$. The current precision of the top and W mass determination (by Tevatron ¹⁾ for the former and by LEP ²⁾ and Tevatron ³⁾ for the latter) is such that the constraint from formula 1 is considered an indirect measurement of the Higgs mass within the Standard Model: $m_H = 114_{-45}^{+69}$ GeV. Alternatively, an upper limit, again valid within the Standard Model, can be derived: $m_H < 260$ GeV at 95 % confidence level.

The LHC will produce approximately 10 million top-quark pairs per year at low luminosity, about 4 orders of magnitude more than at the Tevatron. Therefore, in the first years of the LHC, an important improvement in the (statistical) precision of the measured top mass is expected. In order for the W and top mass measurement to contribute equally to the uncertainty of the Higgs mass prediction, the W mass error should be reduced to 10-15 MeV. In section 2 the expected statistical and systematic uncertainties for the W mass

measurement at the LHC are reviewed.

The Standard Model is based on the principle of gauge invariance. The non-Abelian structure of the gauge group, leads to a specific prediction of the self-couplings of the electroweak gauge bosons W^\pm , Z and γ . The study of the triple (and quartic) couplings of gauge bosons therefore provides a powerful test of the Standard Model. The measurement of non-zero values for the neutral couplings or deviations from the Standard Model prediction for the charged couplings would be very compelling evidence for new physics. The LEP and Tevatron experiments have established that the anomalous triple gauge boson couplings, if they exist, are small. The expected sensitivity of the LHC experiments for the various types of anomalous triple gauge-boson couplings presented above, are related to the experimental limits from the LEP and Tevatron experiments in section 3.

The ATLAS and CMS collaborations are preparing large detectors with an unprecedented level of complexity. Consequently, the task of understanding and calibrating the detectors requires an unprecedented effort. Moreover, the statistical error on many measurements will be so small that a very precise control of systematic detector effect is required. In this task, the very precisely known properties of the Z boson (and to a lesser extent also the W) may well turn out to be anchors of crucial importance. In section 4, the use of Z and W events in the commissioning phase of the experiment - calibration of the energy scale, alignment, magnetic field map - is discussed.

The most important findings are summarized in section 5.

2 Precision measurements of W properties

In the introduction it was shown how precision measurements of the properties of the W boson provide an important cross-check of the Standard Model. In this section, the uncertainty on the W mass measurement is discussed in some detail. The statistical and systematic contributions to the error are analysed for the W mass measurement as performed at the Tevatron experiments. Given a set of assumptions, an expectation for the LHC is inferred. An alternative approach that could be applied at the LHC is discussed at the end of this section.

The W mass measurements by CDF and D0 are described in detail in the literature ³⁾. Here, only the basic procedure is explained. The best

results at the Tevatron are obtained in the decay channels to electron (muon) and neutrino. The signal events are selected by requiring a relatively hard and central lepton ($p_T > 25$ GeV, $|\eta| < 2.4$) to be reconstructed. Further, a significant missing energy $E_T^{miss} > 30$ GeV is required. Events containing jets with transverse momentum $p_T > 30$ GeV or a large recoil (> 20 GeV) are rejected.

As the neutrino escapes detection, its transverse momentum can only be reconstructed by measuring the unbalanced transverse energy of the recoiling system, i.e. the missing transverse energy. The longitudinal component of the neutrino momentum is unknown. The transverse mass is defined as:

$$m_T^W = \sqrt{2p_T^l p_T^\nu (1 - \cos \Delta\phi)} \quad (2)$$

where p_T^l is the lepton transverse momentum, p_T^ν the neutrino transverse momentum (inferred from missing E_T) and $\Delta\phi$ the difference in azimuthal angle between the lepton and neutrino. A distribution of the transverse mass shows the typical Jacobian peak, abruptly falling at m_W , see figure 1. The W mass is determined from the transverse mass distribution by matching the experimental distribution with Monte Carlo templates generated for different W masses.

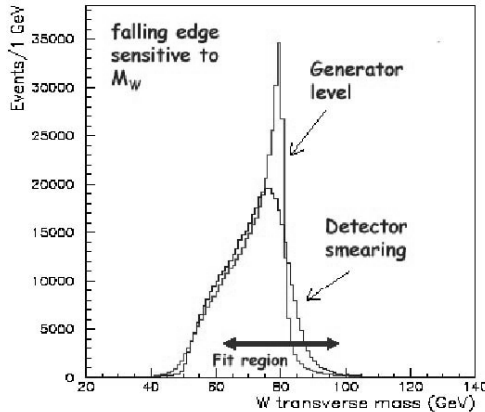


Figure 1: The distribution of the transverse W mass at generator level and with the effect of the detector smearing are shown.

Table 1: A comparison of a recent Tevatron (runIb 84 pb^{-1}) break-down of the error contributions to the W mass measurement to that expected for a single low-luminosity year at the LHC. The errors are expressed in MeV.

<i>source</i>	stat	En. scale	E/p	recoil	Γ_W	p_T^W	bkg	rad. decay	PDF	tot
<i>Teva-tron</i>	65	75	25	33	10	45	5	20	15	113
<i>LHC</i>	2	15	5	5	7	5	5	10	10	25

A large number of systematic effects have been identified that have a significant contribution to the error. Several weaknesses in the generator description of the W production and decays are contributing to the systematic errors: the uncertainty on the width of the W, on the parton density functions, on backgrounds and radiative decays. For the Tevatron measurements, a large contribution comes from the W transverse momentum distribution: the theoretical model of (hard) gluon emission does not reach the required precision. A better constraint is obtained by using a semi-empirical distribution as input to the Monte Carlo:

$$p_W^T = [p_Z^T]_{data} \times \left[\frac{p_W^T}{p_Z^T} \right]_{theory} \quad (3)$$

While at Tevatron the statistics in the $Z \rightarrow l^+l^-$ calibration channel constitutes a limiting factor for this approach, statistics won't be a problem at LHC.

While at the Tevatron the rather poor statistics in the $Z \rightarrow l^+l^-$ calibration sample limits the effectiveness of this approach, at the LHC statistics will soon cease to be a problem. Therefore, ATLAS and CMS should be able to reduce considerably the systematic error contribution from the transverse momentum spectrum. Guideline numbers for this and other physics systematics, from a recent CDF study and the expectation for the LHC, are given in table 1.

A second source of systematic uncertainty is related to the description of the detector. The uncertainty in the response of the detector to the (partly) hadronic recoiling system leads to a significant systematic error at the Tevatron. Another source is the description of the E/p resolution of electrons (the energy measured in the calorimeter, divided by the momentum as measured in the tracker). The largest source of systematic uncertainty at the Tevatron

comes from the uncertainty in the lepton energy scale. The techniques used to calibrate the energy scale and their expected performance during the initial phase of the experiment are discussed in more detail in section 4. Figure 2 shows the dependence of the systematic error on the W mass measurement on the the uncertainty in the lepton energy scale for the ATLAS detector after one year at the LHC.

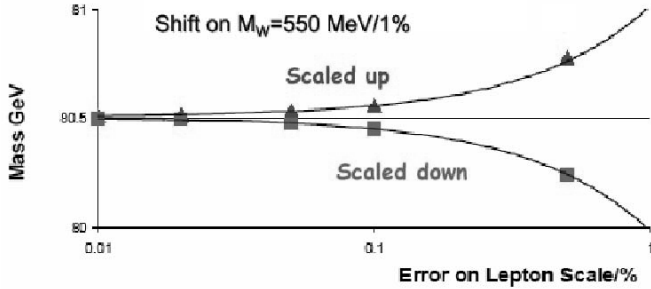


Figure 2: The dependence of the systematic error on the W mass measurement on the the uncertainty in the lepton energy scale for the ATLAS detector after one year at the LHC.

Table 1 shows how at LHC the favorable statistics for the signal and calibration samples leads to smaller errors. This is reflected not only in the smaller statistical errors, but also in the smaller contribution from the lepton energy scale that is dominated by the statistics in the Z sample. It should be noted, however, that the expectations for the LHC in table 1 are based on the assumption that the detector alignment and calibrations are very well known. This will most likely not be the case during the first year of the LHC. The W mass measurement is a strong incentive for pushing the knowledge of the detector calibrations to the limits. The total systematic error on the W mass per LHC experiment per year will be about 25 MeV, and about 15 MeV when combining ATLAS and CMS.

For an early W mass measurement it may well be worth looking for alternative approaches that depend less strongly on the calibration. A good example is the W/Z ratio method, that was studied by the D0 collaboration ⁴⁾. The

basic idea is to use the measured lepton distribution in Z-boson decay, along with the calculated ratio of the W- over Z-boson distribution, to predict the equivalent leptonic distribution in the W-boson case. By comparing this prediction to the measured leptonic distribution, the W-boson mass and width can be extracted relative to those of the Z-boson, whose properties are well known from LEP measurements.

The advantages of this method are the smaller dependence on theoretical errors in the description of the recoil and the cancellation of common systematics in the ratio, mainly the detector response to the lepton and the recoil. In a proof-of-principle study by D0 ⁵⁾, it was shown that the impact of correlated experimental errors is much reduced using this method. This gain should be balanced against the increase in the statistical error: the Z production rate is an order of magnitude smaller than that of the W. Indeed, in the D0 study the additional statistical error due to the limited statistics in the Z sample turned out to be larger than the gain in the systematical error.

The method might be more suitable to the LHC environment than the Tevatron. Recently, CMS has started to evaluate the potential of a similar approach. For an “early” measurement of the W mass, when detector and physics are likely not fully under control. The CMS approach differs from the D0 method in that the shape of the W transverse mass spectrum, rather than the lepton transverse momentum distribution, is obtained from Z events. The results of this feasibility study are very promising ⁶⁾.

3 Triple gauge couplings

The structure of the Standard Model gauge group yields a prediction for the couplings between triplets of electroweak gauge bosons. The existence of small, but non-zero, anomalous triple gauge-boson couplings has not been ruled out experimentally. The study of Triple Gauge Couplings (TGC) is appealing since the present precision on TGC is of the order of 10% despite most of the electroweak parameters of the Standard Model are known to 0.1%. In the most general Lorentz-invariant parameterisation, the triple gauge-boson vertices are described by a large number of independent couplings. For the $WW\gamma$ and WWZ vertices, a total of fourteen independent couplings can be written. Assuming electro-magnetic gauge-invariance and C and P conservation, five couplings remain ⁷⁾. At the tree level in the Standard Model these couplings have

well-defined values:

$$g_Z^1 = k_\gamma = k_Z = 1 \quad \lambda_\gamma = \lambda_Z = 0 \quad (4)$$

The existence of neutral ZZZ , $\gamma\gamma\gamma$, $ZZ\gamma$ and $Z\gamma\gamma$ vertices in the Standard Model would violate the combined CPT symmetry. The $Z\gamma$ and ZZ anomalous couplings are parametrised by $h_{1,3}^V$, $h_{2,4}^V$ and $f_{4,5}^V$, respectively, with $V=\gamma,Z$. Since the anomalous contributions to those coupling grow with the center-of-mass energy of the hard scattering process \hat{s} , the sensitivity of LHC is greatly increased with respect to previous experiments.

The existence of anomalous couplings could lead to unitarity violation at relatively low energies ⁸⁾. Unitarity violation is avoided if the couplings are introduced as form factors rather than mere constants. Often a dipole form factor is chosen

$$A = \frac{A_0}{(1 + \hat{s}/\Lambda_{FF}^2)^n} \quad (5)$$

where Λ_{FF} plays the role of a cut-off scale, related to the energy scale at which new physics becomes important in the weak boson sector. The exponent n should be chosen greater than that in the dependence of the coupling on \hat{s} to avoid unitarity violation. The choice of the value of the cut-off scale Λ_{FF} and the exponent n affect the experimentally observed distributions in machines (like the LHC) that cover a large \hat{s} range. Therefore, many analyses quote their results for different values of these two parameters.

The experimental signature of the anomalous triple gauge-boson couplings is an enhanced production cross-section of the di-boson final state with respect to the Standard Model expectation. Moreover, several differential distributions show marked differences between the Standard Model production and that due to anomalous couplings. Notably, anomalous couplings tend to yield events with larger transverse momenta for the final state bosons, see figure 3.

Limits on Anomalous TGCs can be extracted by simply comparing the expected and observed event rates. A preferable approach is to construct a likelihood that compares the experimental distribution in one or more dimensions to reference distributions. The reference distributions are generated for several values of the couplings using Monte Carlo techniques. This method has the advantage to be less dependent on the overall normalisation scale, while the analysis of the differences in the shape can give hints on the type of anomalous coupling originating them.

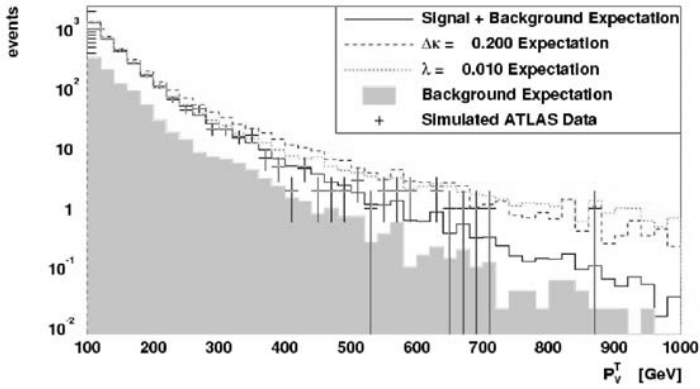


Figure 3: The distribution of the transverse momentum of the photon in $pp \rightarrow W\gamma$ events for a luminosity of 30 pb^{-1} from the ATLAS study ¹⁰⁾. The distributions predicted by Standard Model TGC as well as in the presence of anomalous couplings are shown. The contribution of the background is shown as a shaded histogram.

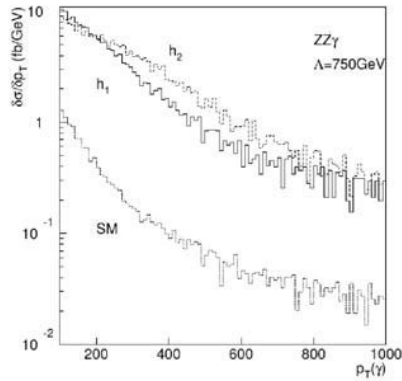


Figure 4: The distribution of $d\sigma/dp_T(\gamma)$ for the SM ($h_i=0$) and anomalous CP violating coupling limits ($h_1=0.5, h_2=0.05$) at $\Lambda = 750 \text{ GeV}$ for the $ZZ\gamma$ vertex as from the CMS study ¹⁹⁾.

The $W\gamma$ final state, with the W decaying to an electron or muon and a neutrino, is selected requiring an isolated photon with a transverse momentum of at least 100 GeV, a lepton with at least 25 GeV in the tracker acceptance and a missing p_T of at least 25 GeV. In reference ⁹⁾, an exhaustive list of background sources to this final state is studied and it is shown that, with some additional cuts, all of them can be reduced to be an order of magnitude lower than the signal when requiring $p_T^\gamma > 200$ GeV.

Both ATLAS and CMS have prepared sensitivity studies for this final state ^{10, 11, 12)}. In all cases, the detector response is parameterised in so-called “fast simulation”. ATLAS, assuming an integrated luminosity of $30fb^{-1}$ and using a constant form factor, expects the following constraints at 95 % confidence level:

$$-0.0035 < \lambda_\gamma < 0.0035 \quad -0.075 < \Delta k_\gamma < 0.076 \quad (6)$$

where statistical and systematic uncertainties are considered. CMS uses a cut-off $\Lambda_{FF} = 2$ GeV and quote their results for an integrated luminosity of $10fb^{-1}$. The expected limits at 95 % confidence level:

$$-0.0019 < \lambda_\gamma < 0.0019 \quad -0.17 < \Delta k_\gamma < 0.17 \quad (7)$$

These fast simulation studies indicate that the LHC can, even with the limited statistics of a few years’ running, tighten the existing experimental limits on the anomalous coupling λ_γ and from LEP ¹³⁾ and the Tevatron ¹⁴⁾ by roughly an order of magnitude. The improved sensitivity is mostly due to the high center-of-mass energy reach of the LHC. The sensitivity to Δk_γ is of the same order of the existing limits.

The WWZ coupling is studied using the $WZ \rightarrow l^+l^-l\nu$ final state, where l is taken to be an electron or a muon. The signal sample is selected requiring three leptons with a transverse momentum of at least 25 GeV in the tracker acceptance and a missing transverse momentum of at least 25 GeV. From this channel, ATLAS ¹⁵⁾ expects the following sensitivities on an integrated luminosity of $30fb^{-1}$:

$$-0.0086 < \Delta g_Z^1 < 0.011 \quad -0.11 < \Delta k_Z < 0.12 \quad -0.0072 < \lambda_Z < 0.00 \quad (8)$$

where the form factors are taken constant like in the $WW\gamma$ channel.

The neutral triple gauge-boson coupling show a very strong dependence on the center-of-mass energy of the hard scattering process. Therefore, one would expect these analyses to benefit most from the large beam energy at the LHC. The analyses by ATLAS (17, 18) and CMS (11, 19) concentrate on the $Z\gamma \rightarrow ll\gamma$ to constrain the $h_{1,3}^V$ and $h_{2,4}^V$, while the $f_{4,5}^V$ coupling is constrained by the $ZZ \rightarrow ll\nu\nu$ and $ZZ \rightarrow ll'l'$ final states. Figure 4 shows the distribution $d\sigma/dp_T(\gamma)$ for the SM ($h_i=0$) and anomalous CP violating coupling limits ($h_1=0.5, h_2=0.05$) at $\Lambda = 750$ GeV for the $ZZ\gamma$ vertex as from the CMS study.

For an integrated luminosity of $100 fb^{-1}$ and a cut-off energy in the form factor of 6 to 8 TeV, the sensitivity to the neutral couplings mentioned above is of the order of several 10^{-4} . Indeed, these studies indicate that three to five orders of magnitude can be gained with respect to the LEP2 sensitivity.

4 Commissioning of the experiments

The determination of the absolute energy scale for leptons and jets is one of the greatest challenges during the initial phase of the experiment. It requires the knowledge of a large number of detector parameters: the tracker alignment, the magnetic field map in the tracker volume, the tracker material distribution (for electrons), the calorimeter calibration and the muon energy loss in the calorimeters. In particular the first two items are correlated: precisely disentangling effects due to both causes may prove to be very challenging indeed.

Both ATLAS and CMS perform precision measurements during the construction and integration phase: the tracker detector module mounting precision is specified to be better than 500 microns, while the magnetic field map can be measured using an array of Hall probes. A sub-set of calorimeter modules is calibrated in test beams.

Alignment and calibration constants are expected to vary with time: thermal effects and out-gassing of the support structure lead to movements of the tracker, the gradual increase in bias voltage will lead to a change in Lorentz angle in the silicon detectors, radiation damage will change the light yield of calorimeter crystals and light guides, etc. During the operation of the experiment, the response of all detectors is extensively monitored. A laser alignment system is continuously monitoring the position of the tracker elements. Several systems based on diodes (electromagnetic calorimeter) and radioactive sources (hadronic calorimeters) are used to monitor the response of the calorimeters.

Controlling the construction dispersion and monitoring of the detector response are essential tools for the understanding the detector. It is clear, however, that these techniques do not provide the precision required by the physics analyses. The absolute energy scale has to be calibrated from data. As an example, the tracker alignment is considered.

The tracker alignment and magnetic field map are determined from tracks in the overlaps between modules. The statistics are not expected to limit the precision: one day's data should allow to obtain a statistical precision of the order of 1 micron ²¹⁾. The alignment from single tracks, however, does not fully determine the energy scale: deformed topologies are possible that satisfy the constraints. The calibration of the energy scale is obtained from a resonance with a well-known mass decaying to a lepton pair (the Z at 90 GeV and the J/Ψ and Υ at ~ 5 GeV). The scale can be determined using either of them. Then the extrapolation to different masses is cross-checked using the second resonance. Recent Tevatron studies ²²⁾ favour the use of the lighter resonances for setting the energy scale. The reconstructed Z mass is within 1.5 standard deviations of the world average.

Similarly, the jet energy scale is calibrated using hadronically decaying W bosons.

5 Summary

The LHC is expected to offer considerable new opportunities for the physics of electro-weak gauge bosons.

A precise measurement of the W mass provides a test of the Standard Model and helps to tighten the constraint on the Higgs mass. The large statistics of W and Z bosons produced at the LHC, together with a thorough control of the detector and physics systematics, will allow an improvement of the accuracy on the W mass (with respect to the Z mass) to approximately 15 MeV.

The study of triple gauge-boson couplings at LHC is very promising. A range of di-boson final states can be studied at the LHC, yielding information on a large number of couplings. The large center-of-mass energy reach is expected to lead to a much larger reach for the cut-off scale Λ_{FF} . Especially for couplings that depend strongly on the center-of-mass energy, the sensitivity is significantly improved with respect to previous experiments, in some cases by many orders of magnitude.

In many measurements the control of the detector and physics systematics is of utmost importance. Even though the information from the construction phase is vital, the most precise calibration comes, in many cases, from a reference data sample. The large production rate and well-known properties make the Z mass constraint the most important handle for the calibration of the lepton energy scale.

The authors would like to thank the convenors of the session, Marcello Manelli and Giacomo Polesello, and O. Buchmuller, C. Buttar, M. Dobbs, S. Haywood, C. Marques and A. Schmidt for useful discussions.

References

1. CDF-NOTE-6955, D0-NOTE-4417, hep-ex/0404010.
2. M. Thomson for the LEP collaborations Eur.Phys.J.C33:S689-S693, 2004.
3. CDF Collaboration and D0 Collaboration (V.M. Abazov et al.). hep-ex/0311039.
4. W.T. Giele and S. Keller Phys.Rev.D57:4433-4440, 1998.
5. S. Rajagopalan for the $D0$ collaboration FERMILAB-CONF-96-236-EF.
6. A. Schmidt, Diploma thesis, University of Karlsruhe (2004), IEKP-KA/2004-2 .
7. U. Baur and D. Zeppenfeld, Nucl. Phys. B308: 127, 1988.
8. U. Baur and D. Zeppenfeld, Physics Letters B201: 383, 1988.
9. G. Azuelos et al. CERN-TH-2000-102, hep-ph/0003275.
10. ATL-PHYS-2002-022.
11. Th. Müller, D. Neuberger, W.H. Thümmel. CMS note 2000/017.
12. C.K. Mackay, P.R. Hobson CMS note 2001/056.
13. D. Abbaneo et al. CERN-EP-2000-016 (2000).
14. B. Abbott et al. (D0 collaboration) Phys. Rev. D 58:3102 (1998).

15. M. Dobbs and M Lefebvre ATL-PHYS-2002-023.
16. C.K. Mackay, P.R. Hobson CMS note 2001/052.
17. S. Hassani ATL-PHYS-2002-023.
18. S. Hassani ATL-PHYS-2002-022.
19. C.K. Mackay, P.R. Hobson CMS note 2002/028.
20. P.J. Bell ATL-PHYS-2004-015.
21. EPJdirect A1, 1-11 (2004).
22. W. Hays presented at ICHEP 2004, submitted to World Scientific.

Session IV – Higgs and Beyond

STANDARD MODEL AND MSSM HIGGS BOSON SEARCHES AT LHC

Simone Gennai

Scuola Normale Superiore and INFN, Italy

Evelin Meoni

Università degli Studi della Calabria and INFN, Italy

Abstract

The search for the Higgs boson in the Standard and Minimal Super Symmetric Model at the Large Hadron Collider is presented. The results of new analysis based on multivariate techniques are shown. Some considerations on the impact of possible staged scenarios on the analysis performances are reported.

1 Introduction

The LHC collider is expected to give the final answer to the question whether the Higgs boson exists and to measure its properties with good precision. The first pp collisions are expected in 2007. Two large detectors, ATLAS and CMS^{1, 2)}, with the main goal to find the Higgs boson, are presently under construction. The experimental reach of these two detectors are expected

to be similar, although different and complementary design concepts and technologies are used in many detector elements.

Actual limits to the Higgs boson mass come from both direct and indirect searches at LEP, Tevatron and SLC. The upper mass limit for a Standard Model (SM) Higgs boson like is set to $251 \text{ GeV}/c^2$ at 95% confidence level, while the direct searches exclude a Higgs boson with a mass lower than $114.4 \text{ GeV}/c^2$ at 95% confidence level. The ATLAS and CMS collaborations have established the expected discovery ranges for the most important production and decay channels of the (SM) Higgs bosons ^{3, 4)}. Different search strategies are triggered by different Higgs boson mass value: the $H \rightarrow \gamma\gamma$ is the golden channel for a light Higgs boson ($m_H < 140 \text{ GeV}/c^2$), while the four leptons final state ($H \rightarrow ZZ \rightarrow 4 \ell^\pm$) provides an excellent signature over a large mass range, from $m_H \sim 130 \text{ GeV}/c^2$ to $m_H \sim 500 \text{ GeV}/c^2$. To increase the sensitivity of the experiments, the associated production of the Higgs boson with a pair of top quark and the production in the vector boson fusion mechanism are also considered in the analysis.

During the last period a big improvement in the development of new Monte Carlo packages has been done. The most important innovation it is the use of Monte Carlo packages that combine the matrix element at next to leading order calculation with the parton shower approach as the MC@NLO ⁵⁾ package. These new tools allow better description of the kinematics for most of the backgrounds.

For what concerns the MSSM scenario: the neutral Higgs boson decaying into a pair of τ leptons, and the charged Higgs boson decaying into a top and b quarks, offer the best discovery opportunities in the whole $\tan\beta - m_A$ plane. Some considerations on the first years of data taking and the impact of not calibrated (or staged) detector are presented.

2 The SM Higgs boson search

The main production mechanism of the SM Higgs boson, over the entire mass range, is the gluon-gluon fusion ($gg \rightarrow H$). The cross section for the weak boson fusion channel ($qq \rightarrow qqH$) is $\sim 10\%$ of the $gg \rightarrow H$ cross section for $m_H < 200 \text{ GeV}/c^2$ and becomes comparable to it for very heavy Higgs boson. The associated processes $qq \rightarrow HW$, $qq \rightarrow HZ$, $gg/qq \rightarrow ttH$ and $gg/qq \rightarrow bbH$ have cross sections lower by a factor of ~ 100 with respect to the gluon fusion but

in a number of cases provide better signal to background ratios.

The branching ratios for the $H \rightarrow \gamma\gamma$ decay mode is only about 2×10^{-3} but due to the clean signature it is one of the major Higgs boson discovery channels at LHC. Figure 1 shows the expected statistical significance for the SM Higgs boson in the ATLAS detectors for 10 fb^{-1} as a function of m_H , while fig. 2 shows the same in the CMS detector for 30 fb^{-1} (6, 4). Beyond the corresponding mass thresholds the decays to weak boson pairs strongly dominate and provide several useful final states for the Higgs boson searches.

The intermediate mass range from $\sim 130 \text{ GeV}/c^2$ to $\sim 500 \text{ GeV}/c^2$ is covered with several final states: $H \rightarrow ZZ^* \rightarrow 4 \ell^\pm$, $H \rightarrow WW^* \rightarrow \ell^+ \ell^- \nu\nu$, $H \rightarrow WW \rightarrow \text{lepton} + \text{jets}$. The 4 leptons and $H \rightarrow \gamma\gamma$ channels provide an excellent Higgs mass measurement, while only the transverse Higgs boson mass can be reconstructed for the $H \rightarrow WW^* \rightarrow \ell^+ \ell^- \nu\nu$ channel. The search of the Higgs boson in the associated production channel, $t\bar{t}H$ and WH , is less sensitive to the $\gamma\gamma$ mass resolution as in this case the backgrounds can be effectively reduced by the lepton or jet requirement giving $S/B \sim 1$.

2.1 $H \rightarrow \gamma\gamma$

This channel allows the best resolution for the measurement of the Higgs boson mass. A precision less than 1% in the reconstructed mass can be achieved, for a mass range between 100 and $150 \text{ GeV}/c^2$, using the primary vertex position to reconstruct the correct angle between the photons directions and the converted photons. An excellent electromagnetic calorimeter resolution is mandatory for the inclusive $H \rightarrow \gamma\gamma$ channel due to the large prompt $\gamma\gamma$ background with a signal to background ratio (S/B) close to 0.1. Figure 3 shows the reconstructed Higgs boson mass superimposed on the total background for $m_H = 120 \text{ GeV}/c^2$ with 100 fb^{-1} (4). Statistical significance better than 5σ is expected for $120 \text{ GeV}/c^2 < m_H < 140 \text{ GeV}/c^2$ in the inclusive $H \rightarrow \gamma\gamma$ channel already with 30 fb^{-1} in both experiments.

2.2 $H \rightarrow ZZ/ZZ^* \rightarrow 4\ell$

For a Higgs boson mass range between 130 and $150 \text{ GeV}/c^2$, the four-electron and four-muons final states have been studied with full simulation and complete reconstruction (4, 7). The main backgrounds for this channel are represented by the ZZ^* , $t\bar{t}$ and Zbb processes, that can be suppressed using kinematical and

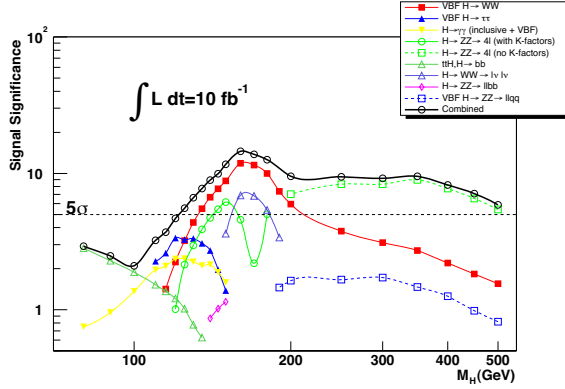


Figure 1: Expected statistical significance for the Standard Model Higgs boson in the ATLAS detector for 10 fb^{-1} as a function of m_H .

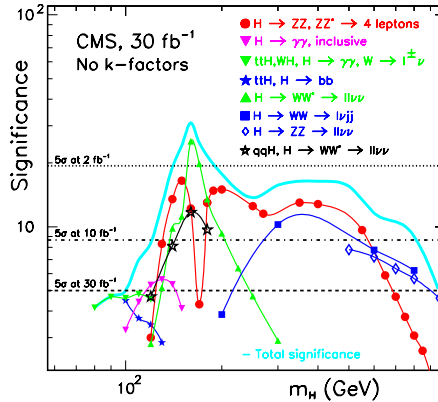


Figure 2: Expected statistical significance for the Standard Model Higgs boson in the CMS detector for 30 fb^{-1} as a function of m_H .

isolation criteria on the leptons in the final state. Two different analysis have been developed: the first one is based on standard selections on kinematical variables, the second one is based on a neural network approach. The second approach gives an improvement up to 20% in the extracted significance.

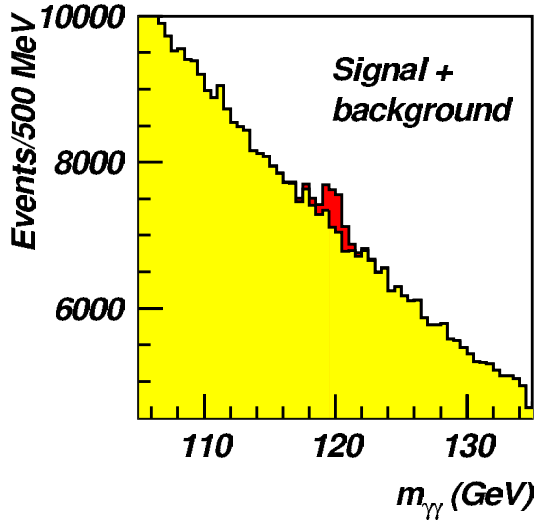


Figure 3: Signal superimposed on the total background for $H \rightarrow \gamma\gamma$ with $m_H = 120 \text{ GeV}/c^2$ for 100 fb^{-1} in the CMS detector.

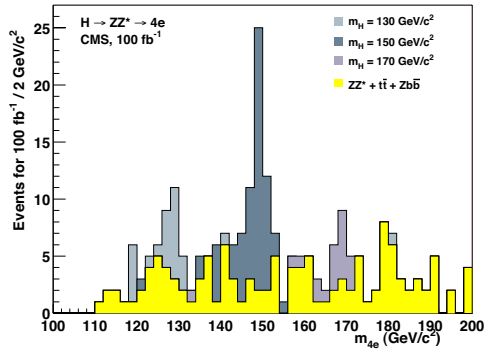


Figure 4: Signal superimposed on the total background for $H \rightarrow ZZ^* \rightarrow 4e$ with $m_H = 130, 150$ and $170 \text{ GeV}/c^2$ for 100 fb^{-1} in the CMS detector.

The reconstructed four-electron invariant mass distribution of the $H \rightarrow ZZ^* \rightarrow e^+ e^- e^+ e^-$ signal and the background with $m_H = 130, 150$ and $170 \text{ GeV}/c^2$ for 100 fb^{-1} is shown in Fig. 4.

2.3 The weak boson fusion

The weak boson fusion channels ($qq \rightarrow qqH$) are the most promising for the searches of the heavy Higgs boson ($m_H > 500 \text{ GeV}/c^2$), recently these studies have been applied also to medium mass Higgs boson⁸⁾. The dynamics of the process lead to energetic jets in the forward and backward directions, and the absence of colour exchange in the hard process leads to small jet activity in the central region. Thus imposing a veto on the jet activity leads to a large reduction against the backgrounds from $t\bar{t}$, single W and Z production and the QCD jet events. The $qq \rightarrow qqH$, $H \rightarrow WW^*$ channels is particularly interesting as it contains the HWW coupling at production and decay. The two-lepton plus transverse missing energy final state from $H \rightarrow WW^* \rightarrow ll \nu\nu$ is promising and provides a discovery for $m_H > 120 \text{ GeV}/c^2$ as is shown in Fig. 2. Due to the spin correlations a Jacobian type structure is visible in the Higgs boson transverse mass reconstructed from the lepton pair and missing transverse energy. The transverse invariant mass distribution superimposed on the total background for $m_H = 160 \text{ GeV}/c^2$ in the ATLAS detector is shown in Fig. 5. The use of neural network analysis can improve the signal significance up to 50% (for very high Higgs boson mass).

Several investigations on how to extract the background shape (and normalization) using the data, are being carried out by both the collaborations.

3 MSSM Higgs boson

The neutral sector of the MSSM Higgs boson can be studied mainly in the double τ final state^{9, 10)}. Figure 6 shows the Higgs boson reconstructed mass ($500 \text{ GeV}/c^2$) in the double τ jet final state after all selections superimposed on the background events for 60 fb^{-1} with the CMS experiment.

The best way to investigate the properties of the charged Higgs boson is in the tb final state with the top quark decaying semileptonically.

Figures 7 show the discovery potential for all the MSSM Higgs bosons as a function of m_A and $\tan\beta$, assuming maximal stop mixing, $m_{\text{top}} = 175 \text{ GeV}/c^2$ and $m_{\text{SUSY}} = 1 \text{ TeV}/c^2$ for 30 fb^{-1} .

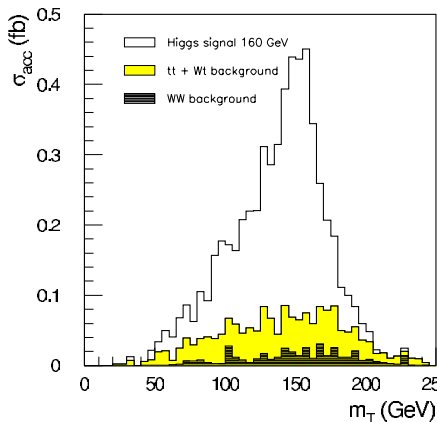


Figure 5: Signal superimposed on the total background (fb) for qqH , $H \rightarrow WW^* \rightarrow ll\nu\nu$ with $m_H = 160$ GeV/c^2 in the ATLAS detector.

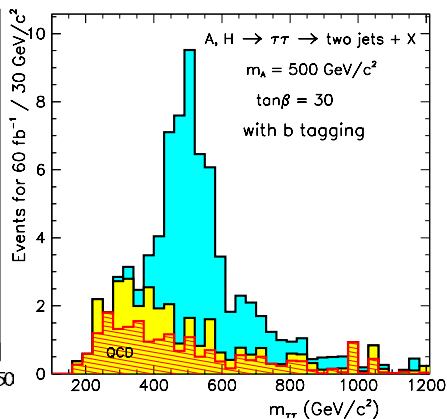


Figure 6: Signal superimposed on the total background for $A, H \rightarrow \tau\tau \rightarrow \text{two jets} + X$ with $m_A = 500$ GeV/c^2 and $\tan\beta = 30$, after all the analysis selections, with the CMS experiment.

4 Start up and staged scenarios

In the first year of data taking, there will be no searches for new physics but an extensively work to debug the several detectors and understand the response of the experiments. The Z and W bosons production will be used to calibrate the calorimeters and to align the tracker. The importance of these calibration is showed in the following example taken from the $H \rightarrow \gamma\gamma$ study. In order to extract the signal from the background, a mass resolution of about 1% is needed, to achieve this resolution, the constant term of the calorimeter resolution must be $< 0.7\%$. The testbeam measurements on single electromagnetic calorimeter modules and the calibration of the electromagnetic calorimeter using the Z decay into electrons, should guarantee to achieve this result. In case of modules disuniformity and missing calibration the constant term could not be lower than 2% and the signal significance would be lowered by a 25% which means a 50% more in integrated luminosity to achieve the discovery.

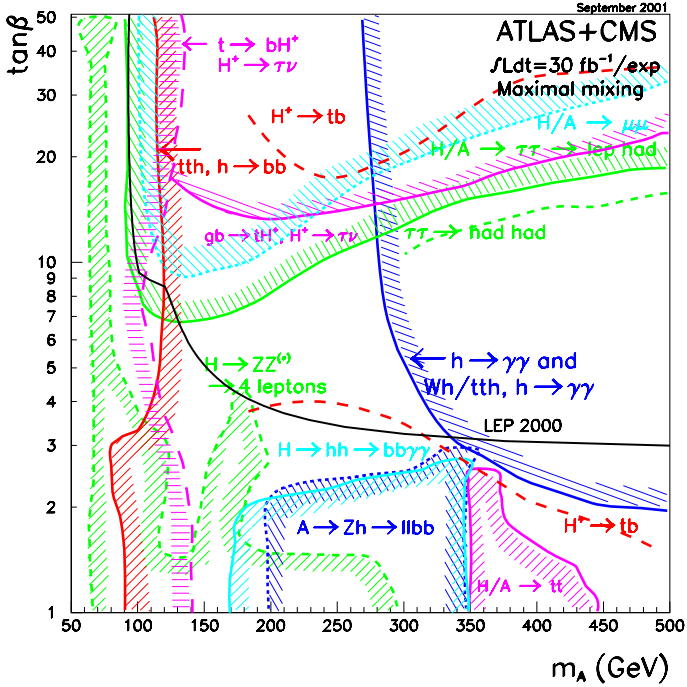


Figure 7: Expected 5 sigma discovery region in the $m_A - \tan\beta$ plane for all the MSSM Higgs bosons with several final state for 30 fb^{-1} .

Both experiments are considering a possible start with staged detectors, as missing pixel layers or gap scintillators. First studies show an average decrease in signal significance of about 10% and, in some cases, an increase up to 15% in the integrated luminosity is needed to achieve the discovery ¹¹⁾.

5 Conclusions

A review of the updated analysis for the Higgs boson search at LHC has been presented. With perfectly calibrated and aligned detectors, the discovery of a SM-like Higgs boson would be possible with only 10 fb^{-1} for a mass range between 115 and $700 \text{ GeV}/c^2$.

Both collaborations have started to use more sophisticated analysis based on multivariate techniques and a big improvement in the background estimation has been done using NLO Monte Carlo generators as MC@NLO.

The presence of not perfectly calibrated or staged detectors would imply an increase up to 15% in the integrated luminosity to achieve a significance above the 5 sigma.

6 Acknowledgements

The authors would like to thank both collaborations for having provided the material shown and for the useful discussions and comments.

References

1. ATLAS Collaboration, ATLAS Technical Proposal, CERN/LHCC 94-43, CERN 1994.
2. CMS Collaboration, CMS Technical Proposal, CERN/LHCC 94-38, CERN 1994.
3. ATLAS Collaboration, ATLAS Detector and Physics Performance Technical Design Report, CERN/LHCC/99-14.
4. S. Abdullin, *et al.*, Summary of the CMS Potential for the Higgs Boson Discovery, CMS NOTE 2003/033.
5. Stefano Frixione, Bryan R. Webber, Matching NLO QCD computations and parton shower simulations, J. High Energy Phys. JHEP06(2002)029.
6. K. Cranmer *et al.*, Prospect for Higgs Searches via VBF at the LHC with the ATLAS Detector, ATL-PHYS-2004-005.
7. I. Iashvili, *et al.*, Study of the $H \rightarrow ZZ/ZZ^* \rightarrow 4\ell^\pm$ Channel in CMS, CMS TN/95-059 (1995);
M. Dzelalija, *et al.*, Study of the heavy $H \rightarrow ZZ \rightarrow 4\ell^\pm$ Channel in CMS, CMS TN/95-076 (1995).
K. Cranmer *et al.*, Application of K Factors in the $H \rightarrow ZZ^* \rightarrow 4\ell$ Analysis at the LHC, ATL-PHYS-2003-025(2003), hep-ph/0307242.

8. H. D. Yildiz *et al.*, Study of $pp \rightarrow jjH$ with $H \rightarrow WW \rightarrow l \nu qq$ in CMS for $m_H=300$ and $600 \text{ GeV}/c^2$, CMS NOTE-2001/050;
S.Asai *et al.*, Prospects for the Search for a Standard Model Higgs Boson in ATLAS using Vector Boson Fusion, SN-ATLAS-2003-024;
K. Cranmer *et al.*, Search for Higgs Boson Decay $H \rightarrow \gamma\gamma$ Using Vector Boson Fusion, ATL-PHYS-2003-036 hep-ph/0401088, 2004;
V. Zmushko, Search for $H \rightarrow \gamma\gamma$ in association with one jet, ATL-PHYS-2002-020;
K. Cranmer *et al.*, Neural Network Based Search for Higgs Boson Produced via VBF with $H \rightarrow W^+ W^- \rightarrow \ell^+ \ell^- p_T$ missing for $115 < m_H < 130 \text{ GeV}/c^2$, ATL-PHYS-2003-007.
9. D. Cavalli *et al.*, The Higgs Working Group : Summary Report (2001), Workshop on Physics at TeV Colliders, Les Houches, France, 2001, hep-ph/0203056.
10. R. Kinnunen *et al.*, Study of $H \rightarrow \tau\tau$ with Hadronic τ Decays in CMS, CMS NOTE 2003/006.
11. F. Gianotti, P. Jenni Physics Impact of Staging ATLAS Detector Components, ATL-GEN-2001-002.

SEARCH FOR PHYSICS BEYOND THE STANDARD MODEL AT THE LARGE HADRON COLLIDER

Massimiliano Chiorboli

University and INFN of Catania, Catania, Italy

Davide Costanzo*

Lawrence Berkeley National Laboratory, Berkeley, CA, USA

Abstract

Proton-proton collisions at the Large Hadron Collider will represent a unique chance to discover physics phenomena beyond the Standard Model. In this paper we discuss how the two LHC general purpose experiments, ATLAS and CMS, can unveil new physics and explain the origin of the Electroweak symmetry breaking. We will first discuss Supersymmetry as one of the most popular models, which can be discovered at the early running of the collider machine. Other models, like extra-dimension and Little Higgs, are also discussed.

1 Introduction

One of the main purposes of the experiments at the Large Hadron Collider (LHC) is to investigate the mechanism of Electroweak symmetry

breaking. The possible discovery of a Higgs boson would complete the picture of the Standard Model (SM). However the presence of a Higgs boson and no other new physics phenomena would require a rather unlikely fine tuning of the parameters of the model.

New physics phenomena from a rich variety of models, are proposed to solve this problem also known as “hierarchy problem”. A comprehensive description of all these models is beyond the purpose of these proceedings. We will highlight here only a few popular models like Supersymmetry, extra-dimensions and little Higgs. From an experimental point of view we can divide new phenomena in two categories. The first category is composed by those model for which the LHC experiments are expected to provide a proof within the first year of running, eg with about 10fb^{-1} of integrated luminosity. The second category is made up of models where new particles are produced with a small cross section of the order of the fb, that would require a longer time to discover.

It is of great interest nowadays to assess the potential for discovery of particles that can be copiously generated at the LHC energy. It is also very important to understand how the detectors at their initial operation can be used to show the existence of new particles, and how to reduce the level of instrumental background due to a partially instrumented or non completely optimized detector. The tools needed for the discovery of new particles were discussed in a different session of this workshop, and further reference is found in these proceedings.

Two general purpose experiments (ATLAS and CMS) are being constructed to start taking data at the LHC in 2007.

2 Direct search for SuperSymmetry

Supersymmetry (SUSY) is one of the oldest and best motivated of the theories predicting the existence of physics beyond the Standard Model. SUSY models require the existence of at least one SUSY partner for each Standard Model particle, together with a considerably enlarged Higgs sector. With the exception of spin, these SUSY particles (“sparticles”) possess the same quantum numbers as their SM counterpart. Such states in nature have never been experimentally observed, and one of the major

tasks of the experiments at the Large Hadron Collider(LHC) will be to measure them or to reject SUSY models. A feature of many SUSY models is the conservation of a multiplicative quantum number known as R-parity, which causes SUSY particles to be pair produced and forces the Lightest Supersymmetric Particle (LSP) to be stable. Missing transverse energy generated by the escape of two such LSPs from SUSY events provides the typical signature for R-parity conserving SUSY at hadron colliders.

SUSY searches will be one of the most important tasks for the LHC experiments in the first few years of operation of the collider.

2.1 Supersymmetry reach at the LHC

The experimental sensitivity to supersymmetry is, of course, model dependent. Here we concentrate on the sensitivity to the gravity-mediated model (mSUGRA). The mSUGRA model assumes that at the GUT scale all bosons (squarks, leptons and Higgs bosons) have a common mass m_0 , all fermions (gauginos and higgsinos) have a common mass $m_{1/2}$, and all the trilinear Higgs-sfermion-sfermion couplings have a common value A_0 . Thus, the model can be parameterized in terms of these three constants and of the ratio of the Higgs expectation values, $\tan(\beta)$. Figure 1 (left) shows the region of the $(m_{1/2}, m_0)$ parameter space which can be accessed by ATLAS and CMS for different luminosity scenarios, 10 fb^{-1} being the total integrated luminosity that each experiment is expected to collect during the first year of operation. Instead of exploring all the allowed parameter space, several points are chosen to cover the main experimental signatures arising in the mSUGRA model.

Cascade decays of SUSY particles will generate missing energy for the escaping LSP, but also multiple hadron jets. The SUSY mass scale, defined as $M_{\text{SUSY}} = \min(\tilde{q}_R, \tilde{g})$, can be inferred by measuring the peak of the effective mass distribution M_{eff} defined as the sum of the missing transverse energy and the P_T of the four leading jets in the event. The expected distribution of M_{eff} in jet+ \cancel{E}_T +0 lepton events is plotted in figure 1(right) for SUSY and background events for a model that was studied using a full GEANT simulation of the ATLAS detector. It can be seen that the SUSY signal is more than one order of magnitude over

the background for $M_{\text{eff}} > 1$ TeV. From a fit to the M_{eff} distribution, the SUSY mass scale can be measured in a model independent fashion with an ultimate error $\leq 10\%$. The normalization of this distribution also provides a measure of the total SUSY production cross-section and together these two pieces of information can be used to constrain the SUSY breaking mechanism.

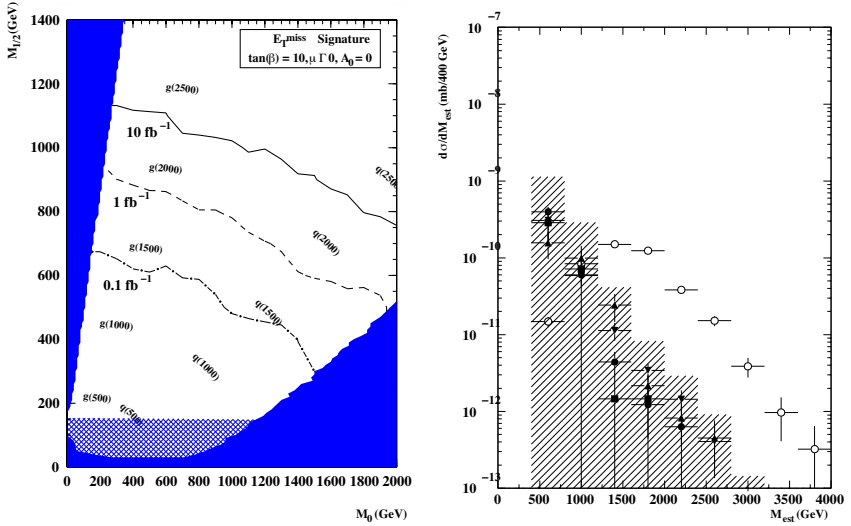


Figure 1: Left: ATLAS 5 σ discovery potential of the inclusive jets + \cancel{E}_T channel in the $m_0 - m_{1/2}$ plane for mSUGRA models with $\tan(\beta) = 10$, $\mu > 0$ and $A_0 = 0$ assuming 0.1fb^{-1} , 1fb^{-1} and 10fb^{-1} integrated luminosity. Full dark region are excluded by theory, hatched regions by experiment (LEP2 and elsewhere). Right: Effective mass distribution for SM background channels and SUSY signal at ATLAS mSUGRA point 5.

2.2 Sparticles mass measurement

The measurement of the mass of SUSY particles can be used to further constrain the theoretical model. However the SUSY decay chains will always end with an invisible LSP ($\tilde{\chi}_1^0$), so no mass peaks can directly

measured. The kinematic end points of invariant mass distributions in multi-step SUSY decays, have to be used to determine the mass of the sparticles. An example is given by the decay chain:

$$\tilde{q}_L \rightarrow \tilde{\chi}_2^0 q \rightarrow \tilde{\chi}_1^0 \ell^+ \ell^- q \quad (1)$$

The invariant mass distribution of same-flavor opposite-sign charged leptons from this chain is expected to have a kinematical end point at:

$$M_{\ell\ell}^{max} = M_{\tilde{\chi}_2^0} \sqrt{1 - \frac{M_{\tilde{\ell}_R}^2}{M_{\tilde{\chi}_2^0}^2}} \sqrt{1 - \frac{M_{\tilde{\chi}_1^0}^2}{M_{\tilde{\ell}_R}^2}} = 108.92 GeV \quad (2)$$

The invariant mass distribution for the model previously mentioned is shown in figure 2 (left) for an integrated luminosity of 100 fb^{-1} , with same-flavor lepton pairs weighted positively and opposite-flavor leptons pairs weighted negatively. The $e^+e^- + \mu^+\mu^- - e^\pm\mu^\pm$ combination cancels all contributions from two independent decays (assuming $e - \mu$ universality) and strongly reduces combinatorial background. The fitted end-point is at $108.71 \pm 0.087 \text{ GeV}$ in good agreement with the expected value.

The other kinematic end-points which can be measured involve the presence of hadronic jets and give access to the left-hand side of the decay chain in eq. (1). However, the resolution and energy scale calibration for jets are worse than those for leptons, as jets are much more complicated objects to be reconstructed. It is expected that the hardest jets will be those coming directly from the decay $\tilde{q}_L \rightarrow \tilde{\chi}_2^0 q$. Therefore the smaller of the two masses formed by combining the leptons with one of the two highest P_t jets, should be smaller than the four-body kinematic end-point. The distribution of the smaller l^+l^-q mass is plotted in figure 2 (right). This distribution is expected to vanish linearly as the end-point is approached. In a similar way the invariant mass of one of the leptons and the jet used in the previous distribution will show an upper-edge. It can also be shown that the maximum invariant mass of the two leptons together with one of the two hardest jets of the event will exhibit a lower edge, that can be used to further constrain the sparticle masses.

Using the knowledge of the edge positions, the mass of the squarks can be measured with a precision of about 3%, while the mass of the invisible LSP can be inferred with a 12% precision.

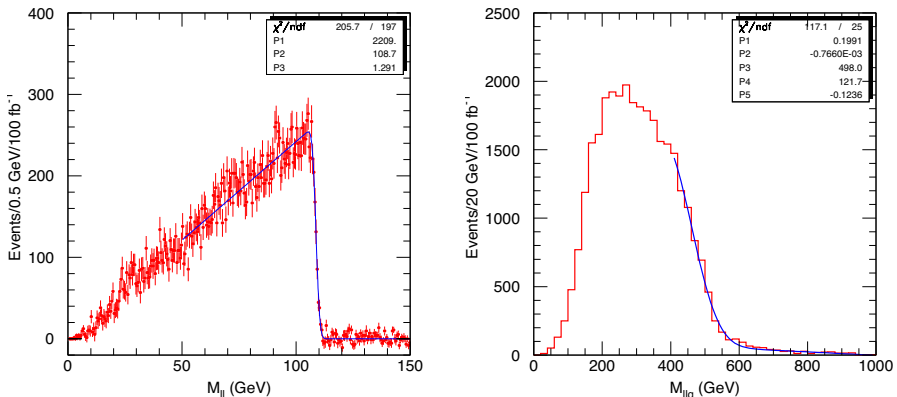


Figure 2: Left: Distribution of the flavor subtracted $\ell^+\ell^-$ invariant mass. Right: Distribution for the smaller of the two $\ell^+\ell^-q$ masses. A linear fit to the edge region is performed.

3 Search for small scale extra-dimensions

Models with Extra Dimensions try to solve the hierarchy problem in a geometrical way: recent theories involve the idea that the three spatial dimensions in which we live could be a three-spatial-dimensional “membrane” embedded in a much larger extra dimensional space, and that the hierarchy is generated by the geometry of the additional dimensions. Several scenarios have been proposed. We will discuss here some of them that are of interest for the ATLAS and CMS Collaborations.

3.1 The ADD Model

In 1999 Arkani-Hamed, Dimopoulos and Dvali (ADD) proposed a framework to solve the gauge hierarchy problem by introducing n large extra

dimensions ³⁾. In this model, the Standard Model fields are confined to our 4-dimensional world, and new dimensions are felt only by gravity. The observed Planck scale, $M_{Pl} \sim 10^{19}$ GeV is only an effective scale, related to the fundamental scale M_D through the volume of the compactified dimensions, $M_D^{n+2} R^n = M_{Pl}^2$. The hierarchy problem is solved without fine-tuning, setting M_D equal or close to the electroweak scale $M_{EW} \sim 10^3$ GeV. This assumption gives a R of the size of the solar system for $n = 1$, which is obviously ruled out by experiments. However for $n \geq 2$ the expected R is less than 1 mm, and therefore do not contradict existing gravitational experiments. The gravitons freely propagating in extra dimensions appear in the 4D point of view as a tower of infinite number of Kaluza-Klein states with masses $M_k = 2\pi k/R$ ($k = 0, 1, 2, \dots, \infty$). The coupling of the SM particles to each of these KK states is of the order of $1/M_{Pl}$, but the overall coupling is, however, obtained by summing over all the KK states and is therefore of the order of $1/M_D$. For particles colliding at energies much larger than the KK mass splitting, the discrete spectrum can be approximated by a continuum with a density of states $dN/dm \sim m^{n-1}$. Being M_D in the TeV range, the effective gravitational interaction is as strong as the electroweak one, and thus gives rise to phenomenological consequences visible at the TeV accelerators.

The relevant processes at LHC are $gg \rightarrow gG$, $qg \rightarrow qG$ and $q\bar{q} \rightarrow gG$. Since gravitons interact weakly with the detectors, the typical signature of these events will be jets plus missing transverse energy. This signature was studied by the ATLAS collaboration ⁴⁾ using a parameterized simulation of the detector (ATLFAST).

Figure 3(left) shows the missing transverse energy distribution for this signal together with the backgrounds, for different choices of n and M_D . With an integrated luminosity of $100 fb^{-1} cm^{-2} s^{-1}$ values of M_D up to 9 TeV (6 TeV) can be explored for $n=2$ ($n=4$).

3.2 TeV^{-1} sized Extra Dimensions

Variations of the ADD model ⁶⁾ assume that only fermions are confined in the 4-D brane, whereas the gauge fields propagate also in a number of additional “small” extra dimensions orthogonal to the brane with

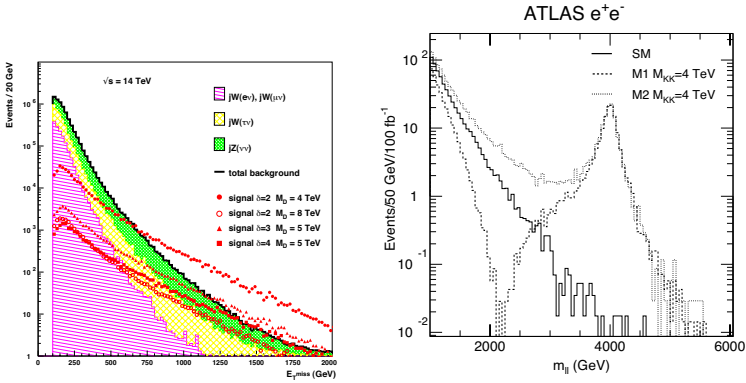


Figure 3: Left: Distribution of the missing transverse energy in background events and in signal events after the selection and for 100 fb^{-1} for graviton production in the ADD model. Right: Invariant mass distribution of e^+e^- pairs for the Standard Model (full line) and for models M1 (dashed line) and M2 (dotted line). The mass of the lowest lying KK excitation is 4 TeV. The histograms are normalized to 100 fb^{-1} .

compactification radius of the order of 1 TeV^{-1} . The so-called M1 model assumes only one “small” extra dimension with all the SM fermions confined to the 4-D brane in the same fixed point. The main signature is the appearance of KK resonances for each of the gauge fields propagating in the bulk. This model is completely specified by the compactification scale M_c . The masses M_n of the KK modes of the gauge bosons are given by:

$$M_n^2 = (nM_c)^2 + M_0^2, \quad (3)$$

where M_0 is the mass of the zero-mode excitation, corresponding to the Standard Model gauge bosons. Depending on the value of the M_c parameter, the heavy gauge bosons could be produced at LHC and observed by ATLAS and CMS.

The model M2⁹⁾, is built as M1, but quarks and leptons are confined to opposite fixed points in the fifth dimension. In this case the signs of the quark couplings of the bosons are reversed for excitations with n odd, yielding a somewhat different phenomenology.

Fig. 3(right) shows the e^+e^- invariant mass distribution for a $Z^{(1)}$ boson with a mass of 4 TeV as obtained with a fast simulation of the ATLAS detector for both M1 and M2 models. Comparing the two-electron invariant mass spectrum for the Drell-Yan production (full line) and for the $Z^{(1)} \rightarrow e^+e^-$ decay in the M1 and M2 models a suppression of the cross section with respect to the SM for masses below the resonance in the model M1, due to negative interference terms between the SM gauge bosons and the whole tower of the KK excitations, can be observed. The model M2 would instead yield to an enhancement of the peak cross section.

A study to evaluate the potential of the CMS experiment to discover a heavy Z' gauge boson in the $Z' \rightarrow \mu^+\mu^-$ channel has also been performed¹⁰⁾, for six different models using the CMS GEANT3-based full simulation of the detector¹¹⁾.

Fig. 4a shows the mass spectra for signal and Standard Model fully reconstructed events, with histograms normalized to an integrated luminosity of 0.1 fb^{-1} . Fig. 4 (right) shows the integrated luminosity needed to reach 5σ significance as a function of Z' mass for the six considered models.

It can be observed that: (i) A very low luminosity, less than 0.1 fb^{-1} , should be sufficient to discover the Z' boson at 1 TeV; (ii) An integrated luminosity of 10 fb^{-1} is sufficient to reach 5σ significance at 3 TeV for some (but not for all) of the Z' model: depending on the model the mass reach is in the range between 2.6 and 3.4 TeV. (iii) An integrated luminosity of 100 fb^{-1} does not allow to obtain 5σ significance at 5 TeV with only the $Z' \rightarrow \mu^+\mu^-$ channel for any of the models considered: the corresponding mass reach lies in the region between 3.4 and 4.3 TeV.

3.3 The Randall-Sundrum Model

The Randall-Sundrum model (RS)¹³⁾ is based on a five dimensional non-factorizable geometry. A solution to 5-dimensional Einstein's equations, preserving 4-dimensional Poincare invariance, is given by the metric

$$ds^2 = e^{-2kr_c\phi} \eta_{\mu\nu} dx^\mu dx^\nu + r_c^2 d\phi^2 \quad (4)$$

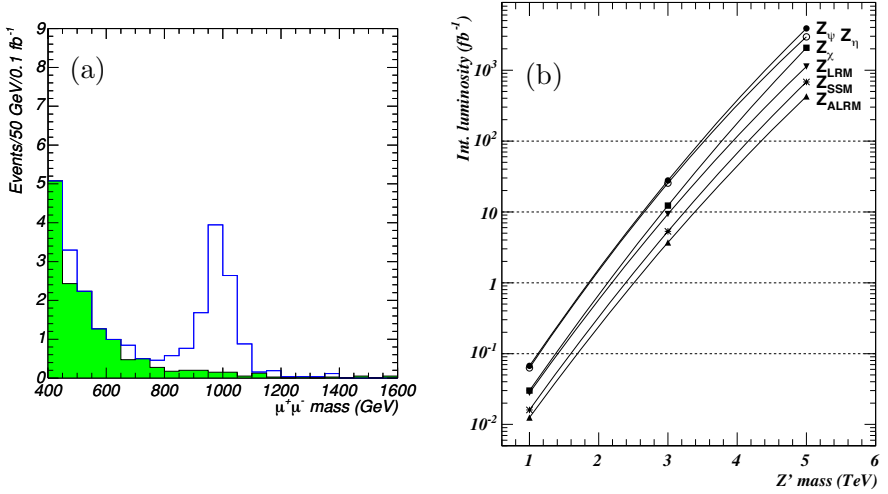


Figure 4: Left: Distribution of the $\mu^+\mu^-$ invariant mass for 1 TeV Z' plus background (open histogram) and for background only (shaded histogram). The number of events per bin is normalized to an integrated luminosity of 0.1 fb^{-1} . Right: Integrated luminosity needed to reach 5σ significance as a function of the Z' mass for the six models considered. Symbols indicate fully simulated mass-luminosity points, lines are the results of interpolations between the points.

where ϕ is the fifth dimension, x^μ are the ordinary 4-dimensional coordinates, $k \sim M_{\text{Pl}}$ is the curvature and r_c is the compactification radius. With this geometry, two 4-dimensional branes are located at $\phi = 0$ and $\phi = \pi$, respectively called the Plank brane and the Standard Model brane. All the ordinary Standard Model fields are confined in the second brane.

In this set-up, a fundamental 5-dimensional mass scale M_{Pl} appears in the 4-dimensional brane at $\phi = \pi$ as

$$\bar{M}_{\text{Pl}} = e^{-kr_c\pi} M_{\text{Pl}} \quad (5)$$

The hierarchy between the Plank and the electroweak scales is hence removed by the exponential warp factor, if $kr_c \sim 11 \div 12$. Because of the small compactification radius, there are no deviations from the Newton's law at experimentally accessible distances. On the other hand, massive graviton excitations appear, with masses given by $M_n = kx_n e^{-kr_c\pi}$, where x_n is the n^{th} root of the Bessel function J_1 . These masses are of order of TeV, and Kaluza-Klein gravitons can be detected as massive resonances in collider experiments. Couplings of the gravitons to matter are given by $1/\Lambda_\pi$, where $\Lambda_\pi = \bar{M}_{\text{Pl}} e^{-kr_c\pi}$. Two parameters control the properties of the RS model: the mass of the first Kaluza-Klein graviton excitation $M_G = M_1$ and the constant $c = k/M_{\text{Pl}}$, related to the graviton couplings and widths.

Fig. 5a shows the e^+e^- invariant mass distribution obtained using the CMS full GEANT simulation. ¹⁴⁾ Three different graviton mass hypothesis were considered: $M_G = 1.5, 1.75$ and 2 TeV and for $c=0.01$. Histograms are normalized to 100 fb^{-1} of integrated luminosity. Fig. 5b shows the significance as a function of the Graviton mass for different integrated luminosities. A 5σ discovery is possible for masses as high as to 1775 GeV . And the whole region of interest can be covered with 100 fb^{-1} .

Another CMS study ¹⁵⁾ takes into account the possibility to observe the radion, a scalar field which describes the fluctuations in the metric of the fifth dimension, which in general mixes with the Higgs. This scalar sector of the RS model is parametrized in terms of a dimensionless parameter, ξ , of the Higgs and radion masses, m_H and m_ϕ

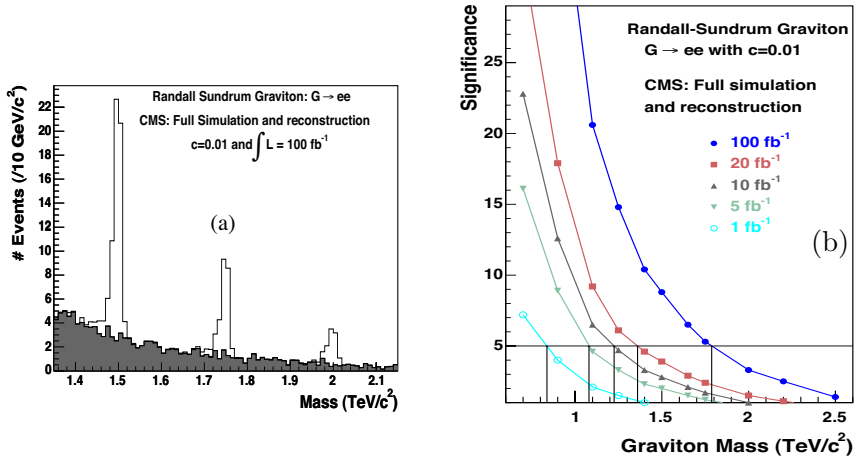


Figure 5: (a) Three Graviton mass hypothesis $M_G = 1.5, 1.75$ and 2 TeV plotted over the background for $c=0.01$ and 100 fb^{-1} of integrated luminosity, with histograms normalized to the expected number of events. (b) Significance as a function of the mass for different integrated luminosities (from 1 to 100 fb^{-1}) for $c=0.01$

and the vacuum expectation value of the radion field, Λ_ϕ . The presence in the Higgs radion sector of trilinear terms opens up the important possibility of $\phi \rightarrow hh$ and $h \rightarrow \phi\phi$ decays. Using the decay modes $\phi \rightarrow hh \rightarrow \gamma\gamma + b\bar{b}$ and $\phi \rightarrow hh \rightarrow \tau\tau + b\bar{b}$ a big fraction of the parameter space for this model can be covered already for 30 fb^{-1} of data. The decay mode $\phi \rightarrow hh \rightarrow b\bar{b} + b\bar{b}$ was found not to give a comparable discovery potential because of the b background from QCD jet production.

3.4 The little Higgs Model

A theoretical model which has been recently proposed to solve the hierarchy problem of the Standard Model is the “little Higgs” model. New particles are introduced to cancel the loop corrections to the Higgs mass due to W , Z , Higgs and top particles which require fine tuning of the parameters of the model in order to keep the Higgs mass finite. For each of the SM particles a new heavy particle is introduced, and the detection of these particles can be used to confirm the model. The production cross section of particles in the little Higgs model is predicted to be of the order of a few fb, so final conclusions on this model can be drawn only with after several years of running of the LHC. The results reported here assume an integrated luminosity of 300 fb^{-1} for one experiment.

In the “littlest Higgs” model considered here the top loop is canceled by a heavy boson T whose mass is expected to be in the TeV range. This particle is expected to decay into tZ , tH or bW with a branching ratio of 25% for the first two channels and 50% for the latter one. The detection of the T particle is important to establish the model and the measurement of its mass can be used to extract some of the parameters of the model. The decay $T \rightarrow Wb \rightarrow l\nu b$ can be used to discover the T particle up to a mass of about 2 TeV. This signature, however, is the same as that expected from a fourth generation quark which is coupled to the third family, so additional evidence has to be searched for by looking at channels with a lower event yield. The decay chain $T \rightarrow tZ \rightarrow 3l + 1b\text{-jet} + X$ is by a flavor changing neutral current and is expected to be suppressed for a fourth generation quark. The invariant mass reconstructed (see if one or two plots fit here)

4 Conclusion

Protons will start colliding at the Large Hadron Collider in two years from now, representing a unique opportunity to unveil new, unexpected physics. In this paper we reviewed just a few examples of the new physics that could be discovered by the ATLAS and CMS experiments, from Supersymmetry, to extra-dimension to more exotic models. Although none of these may be the one Nature chose, the study of these models enable us to prepare for new signals exploiting a wide range of experimental signatures. The potential for discovering new Physics with ATLAS and CMS is huge, and we should get ready to “expect the unexpected”.

Acknowledgments

The authors wish to thank Lucia Silvestris and Fabio Cerutti for the invitation and the organizers of the Workshop for the wonderful organization and the pleasant atmosphere at the University of Naples.

5 References

References

1. J.H. Christenson *et al*, Phys. Rev. Lett. **13**, 138 (1964).
2. M.B. Green, Superstrings and the unification of forces and particles, in: Proc. fourth M. Grossmann Meeting on General Relativity (ed. R. Ruffini, Rome, June 1985), **1**, 203 (North-Holland, Amsterdam, 1986).
3. N. Arkani-Hamed, S. Dimopoulos, G. Dvali, *The Hierarchy Problem and New Dimensions at a Millimeter*, Phys. Lett. **B429**, 263 (1998), hep-ph/9803315;
4. -L. Vacavant, I. Hinchliffe, *Signals of Models with Large Extra Dimensions in ATLAS*, J. Phys. **G27** 1839 (2001);
5. E. Richter-Was, D. Froidevaux, L. Poggioli, *ATLFAST 2.0: a fast simulation package for ATLAS*, ATL-PHYS-98-131;

6. K. Dienes, E. Dudas, T. Gerghetta, Nucl. Phys. **B537** 46 (1999);
A. Pomarol, M. Quiros, Phys. Lett. **B438** 255 (1998);
M. Masip, A. Pomarol, Phys. Rev. **D60** 096005 (1999);
I. Antoniadis, K. Benakli, M. Quiros, Phys. Lett. **B460** 176 (1999);
7. G. Azuelos, G. Polesello, *Prospects for the detection of Kaluza-Klein excitations of gauge bosons in the ATLAS detector at LHC*, Eur. Phys. J. **C39** 1 (2005);
G. Polesello, M. Prata, *Prospects for observing the Kaluza-Klein excitations of the W boson in the ATLAS detector at the LHC*, Eur. Phys. J. **C32** 55 (2004);
8. T.G. Rizzo, Phys. Rev. **D61** 055005 (2000);
9. N. Arkani-Hamed, M. Schmaltz, Phys. Rev. **D61** 033005 (2000);
10. R. Cousins, J. Mumford, V. Valuev, *Detection of Z' Gauge Bosons in the Dimuon Decay Mode in CMS*, CMS NOTE-2005/002;
11. CMS Collaboration, CMS Simulation Package,
<http://cmsdoc.cern.ch/cmsim/cmsim.html>;
12. CMS Collaboration, CMS Reconstruction Packeg,
<http://cmsdoc.cern.ch/orca>;
13. L. Randall, R. Sundrum, *A Large Mass Hierarchy from a Small Extra Dimension*, Phys. Rev. Lett. **83**, 3370 (1999);
14. C. Collard, M.C. Lemaire, *Search with the CMS Detector for Randall-Sundrum Excitations of Gravitons Decaying into Electron Pairs*, CMS NOTE-2004/024;
15. D. Dominici, G. Dewhirst, A. Nikitenko, S. Gennai, L. Fanó, *Search for radion decays into Higgs boson pairs in the $\gamma\gamma bb$, $\tau\tau bb$ and $bbbb$ final state*, CMS NOTE-2005/007;
16. S. Abdulli *et al.*, CMS TN/94-180.

Session V – QCD

QCD at LHC

V. Del Duca

Instituto Nazionale di Fisica Nucleare, Sez. di Torino
via P. Giuria, 1 - 10125 Torino, Italy

Abstract

QCD is an extensively developed and tested gauge theory, which models the strong interactions in the high-energy regime. After more than 30 years from *asymptotic freedom*, QCD is alive and well. I shall review the considerable progress which has been achieved in the last few years in the most actively studied QCD topics: higher-order corrections, PDFs and Monte Carlo models. Thanks to that, QCD in the high-energy regime is becoming more and more an essential precision toolkit to analyse Higgs and New Physics scenarios at LHC.

1 Introduction

Quantum chromodynamics (QCD) is by now widely accepted as the theory which describes the strong interactions between hadrons and their components, the quarks and gluons. From a theoretical point of view, it is a gauge field

theory featuring asymptotic freedom, i.e. a coupling that grows weaker at smaller distances. However, the strong interactions also feature confinement, that is the lack of colour of the observed hadrons. An adequate theoretical solution to confinement is not yet available and is difficult to obtain, because the QCD Lagrangian is formulated in terms of quarks and gluons, rather than the observed hadrons, and because at large distances the coupling is strong. Conversely, at small distances, i.e. in the high-energy regime, the coupling is weak and thus it is possible to make use of the perturbative framework. I shall focus on the fact that perturbative QCD, i.e. QCD in the weak-coupling regime, has emerged as an essential precision toolkit for exploring Higgs and Beyond-the-Standard-Model (BSM) physics; and that is even more so at the Large Hadron Collider (LHC), because of the strongly interacting colliding protons. What's in the box of the precision toolkit ? A precise determination of the strong coupling constant, α_S , of the parton distributions, of the electroweak parameters and of the LHC parton luminosity; and a precise prediction for Higgs production and New-Physics processes, and for their backgrounds.

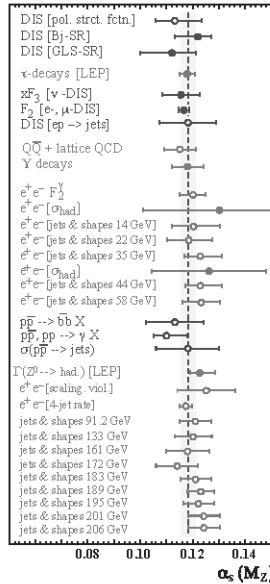


Figure 1: Summary of $\alpha_S(M_Z)$ measurements, from S. Bethke¹). Filled symbols are NNLO results.

In any scattering process in high-energy QCD, the value of any observable can be expanded in principle as a series in α_s . Thus α_s represents the single most important piece of information we need. In the $\overline{\text{MS}}$ scheme and using next-to-next-to-leading-order (NNLO) results only, the 2004 world average ¹⁾ yields $\alpha_s(M_Z) = 0.1182 \pm 0.0027$ ¹. However, the fact that in the detectors experiments observe hadrons, while through the QCD Lagrangian we can only compute the scattering between partons, calls for a framework where the short-distance physics, which is responsible for the primary scattering between partons, can be separated from the long-distance physics, which describes the parton densities in the initial state and the hadronisation in the final state. That framework is provided by factorisation, which expresses a physical observable, typically a cross section, as a convolution of short- and long-distance pieces, with the matching between the two pieces occurring at an arbitrary scale μ_F , called factorisation scale. Then the short-distance piece is perturbatively calculable, which is the partonic cross section occurring at a hard scale Q^2 ; the long-distance pieces, like the parton distribution functions (PDF) in the initial state and eventually the fragmentation functions in the final state, cannot be computed – they must be given by the experiment – but their dependence on μ_F can. In a scattering process, factorisation is not guaranteed. It holds for inclusive processes and infrared (IR) safe observables, like jets or event shapes, and it is valid up to contributions which are suppressed by inverse powers of the typical energy scale, with respect to the leading-power contribution. There are several examples of factorisation-breaking contributions: the underlying event in hadron collisions – for an analysis in $p\bar{p}$ collisions at Tevatron, see Ref. ²⁾; power-correction contributions ²⁾; double-parton scattering, which has been observed by Tevatron CDF in the inclusive sample $p\bar{p} \rightarrow \gamma + 3 \text{ jets}$ ⁵⁾; diffractive events ⁶⁾ – for violations of factorisation in diffractive production at Tevatron,

¹It is worth keeping in mind that for many of the measurements compiled in Fig.1 the errors are mostly theoretical, due to unknown non-perturbative contributions or higher-order corrections. Thus the error on the combined value of $\alpha_s(M_Z)$ cannot be evaluated through the usual statistical techniques ¹⁾.

²Monte Carlo and theory modelling of power corrections were laid out and tested at LEP, where they provided an accurate determination of α_s ³⁾; however, models still need be tested in hadron collisions – see e.g. Ref. ⁴⁾ for Tevatron studies at different centre-of-mass energies.

see Refs. 7, 8).

2 The partonic cross section

The partonic cross section $\hat{\sigma}$ is computed as a power series in α_s . There are basically three different approaches to the calculation of $\hat{\sigma}$. One approach is through matrix-element Monte Carlo (MC) generators, which provide an automatic computer generation of processes with many jets, and/or vector W, Z or Higgs bosons. There are several such generators, like e.g. ALPGEN⁹⁾, MADGRAPH/MADEVENT^{10, 11)}, COMPHEP¹²⁾, GRACE/GR@PPA^{13, 14)}, HELAC¹⁵⁾. They are multi-purpose generators, thus are not optimised for any particular process. A different example is PHASE¹⁶⁾, a MC generator dedicated to processes with six final-state fermions only – thus suitable to $t\bar{t}$ production, WW scattering, vector-boson fusion in Higgs production and vector-boson gauge coupling studies, but where no approximation is used. Matrix-element MC generators are particularly suitable to studies which involve the geometry of the event, because the jets in the final state are generated at the matrix-element level, and thus exactly at any angle. In addition, they can be interfaced with parton-shower generators, to include showering and hadronisation. However, there is also a stand-alone matrix-element MC generator, SHERPA¹⁷⁾, which has got its own showering and hadronisation. Another approach to $\hat{\sigma}$ is through shower MC generators, like HERWIG¹⁸⁾ or PYTHIA¹⁹⁾. The advantage of this approach is that full information is available at the hadron level, since showering and hadronisation are included. However, shower MC generators have only an approximate coverage of the phase space at large angles, because the generation of any additional jets beyond the lowest possible order is done through branching. Finally, MC@NLO²⁰⁾ is available, which is a procedure and a code to match exact next-to-leading order (NLO) computations to shower MC generators. In a way, this is the most desirable procedure, because it embodies the precision of NLO partonic calculations in predicting the overall normalisation of the event, while generating a realistic event set up through showering and hadronisation. It cannot be, though, multi-purpose, being obviously limited to the processes for which the NLO corrections are

known³.

The third approach to the computation of $\hat{\sigma}$ is through fixed-order computations. These yield only a limited access to the final-state structure, but have the advantage that higher-order corrections, real and virtual, can be included exactly. The virtual corrections will depend on a fictitious scale μ_R , at which the scattering amplitudes are renormalised to take care of the ultraviolet divergences. By a rather obvious terminology, the lowest-order term is called the leading order, the first higher order is the NLO, the second higher order is the NNLO and so on⁴. Nowadays, the state of the art in computing partonic cross sections is to NNLO.

3 NLO calculations

NLO calculations have several desirable features. *a)* the jet structure: while in a leading-order calculation the jets have a trivial structure because each parton becomes a jet, to NLO the final-state collinear radiation allows up to two partons to enter a jet; *b)* a more refined PDF evolution through the initial-state collinear radiation; *c)* the opening of new channels, through the inclusion of parton sub-processes which are not allowed to leading order; *d)* a reduced sensitivity to the fictitious input scales μ_R and μ_F allows to predict the normalisation of physical observables, which is usually not accurate to leading order. That is the first step toward precision measurements in general, and in particular toward an accurate estimate of signal and background for Higgs and New Physics at LHC; *e)* finally, the matching with a parton-shower MC generator, like MC@NLO, allows both for a control over the normalisation of an observable and for a realistic final-state event set up.

To sketch how a NLO calculation is done, let us consider the production of n jets in hadron collisions. There are two types of contributions to $\hat{\sigma}$: the

³For both the matrix-element and the shower MC generator approaches, see Ref. 21).

⁴In particular regions of the phase space, characterised by two or more different scales, it is possible to resum towers of logarithms of the ratios of those scales, like the threshold, transverse momentum, energy logs, and so on. The highest-power tower of logs is called the leading log; the second highest is the next-to-leading log (NLL), the third highest is next-to-next-to-leading log (NNLL), and so on.

tree-level production with $n + 1$ final-state partons, with one of the partons that is undetected, and the one-loop production with n final-state partons. Schematically,

$$\hat{\sigma} = \sigma^{\text{LO}} + \sigma^{\text{NLO}} = \int_n d\sigma^B + \sigma^{\text{NLO}} \quad (1)$$

where $d\sigma^B$ is the Born cross section, and

$$\sigma^{\text{NLO}} = \int_{n+1} d\sigma^R + \int_n d\sigma^V . \quad (2)$$

Both real and virtual contributions to Eq. (2), contain IR, i.e. collinear and soft, singularities. If in order to regulate those divergences one uses the dimensional regularisation, which fixes the dimensions of space-time to be $d = 4 - 2\epsilon$, then one finds that both terms on the right-hand side of Eq. (2) are divergent at $d = 4$. However, the structure of QCD is such that those singularities are *universal*, i.e. they do not depend on the process under consideration, but only on the partons involved in generating the singularity. Thus, in the 90's process-independent procedures were devised to regulate those divergences. They are conventionally called *slicing* ^{22, 23)}, *subtraction* ^{24, 25)} and *dipole subtraction* ²⁶⁾, and use universal counterterms to subtract the divergences. The NLO contribution, Eq. (2), can be written as,

$$\sigma^{\text{NLO}} = \int_{n+1} [(d\sigma^R)_{\epsilon=0} - (d\sigma^A)_{\epsilon=0}] + \int_n \left(d\sigma^V + \int_1 d\sigma^A \right) , \quad (3)$$

such that both sums of bracketed terms on the right-hand side of Eq. (3) are finite at $d = 4$, and thus readily integrable numerically via a computer code, with arbitrary selection cuts on the final-state particles and jets, as eventually required by a detector simulation. The organisation of NLO computations in process-independent and user-friendly procedures has made them an essential tool in the comparison with the experimental data.

Let us look briefly at the history of NLO calculations: the first final-state distribution to NLO was done for $e^+e^- \rightarrow 3$ jets ²⁷⁾. The addition of just one more jet in the final state, to produce $e^+e^- \rightarrow 4$ jets, took about 15 years ^{28, 29)}. This trend is repeated in all the other NLO calculations. Namely, in Drell-Yan with one associated jet ²³⁾, and with two associated jets ³⁰⁾; in one- or two-jet production in hadron collisions ^{23, 31)}, and in three-jet production ³²⁾; in di-photon production in hadron collisions ^{33, 34)},

and in the same with one associated jet ³⁵⁾. Finally, for other distributions in hadron collisions, like heavy-quark pair production ³⁶⁾, vector-boson pair production (including the spin correlations) ^{37, 38)}, Drell-Yan with a heavy-quark pair ³⁰⁾, the addition of just one more jet has not been achieved yet to NLO. Thus, although a lot of progress has been done in making NLO computations simpler, we are not able yet to apply systematically NLO computations to studies of signals and backgrounds for Higgs and New Physics: Why in a NLO calculation is it so difficult to add more particles in the final state ? The loop integrals occurring in the virtual contributions to Eq. (2) are involved and process dependent. In addition, more final-state particles imply more scales in the process, and so lengthier analytic expressions in the loop integral. Thus, although it is known how to compute loop integrals with $2 \rightarrow n$ particles, no integrals with $n > 4$ have been computed, either analytically or numerically.

4 NNLO calculations

Are NLO computations accurate enough to describe the data ? The answer to that question is of course process dependent. Here I shall give a few examples:

- *b production at Tevatron* It has been long thought that the CDF data for *b* quark production were not in agreement with the NLO prediction (for a historical overview, see Ref. ³⁹⁾). However, in the comparison of the CDF Run II data ⁴⁰⁾ for the J/ψ momentum distribution in inclusive $B \rightarrow J/\psi + X$ decays to the NLO prediction ⁴¹⁾ and to MC@NLO ⁴²⁾, Fig.2, one finds that the data lie within the uncertainty band and are in good agreement with the theory predictions.
- *W production at LHC* The Drell-Yan *W* cross section, with leptonic decay of the *W*, has been proposed as a luminosity monitor of LHC ⁴³⁾, warranting a greater accuracy, of the order of a few percent, than the standard determination of the luminosity through the total hadronic cross section. However, the experimental *W* cross section depends on the acceptance, i.e. the fraction of events which pass the selection cuts. Thus, the accuracy of the luminosity monitor, the “standard candle”, depends on the one of the acceptance, which is related to the precision by which the hard cross section is known. In Ref. ⁴⁴⁾ the *W* cross section has been computed at different accuracies: to leading order, the same + HERWIG,

NLO, MC@NLO, always including the spin correlations between the decay leptons and the partons entering the hard scattering. For a couple of reasonable selection cuts over the lepton decays, it was found that the difference between the NLO calculation and MC@NLO is about 2 – 3%, which is much less than the difference between the same calculations with and without spin correlations. Therefore, to whatever accuracy we may compute the W cross section, if we want to use it as a standard candle it is mandatory to include the spin correlations.

- *Higgs production at LHC* At hadron colliders, the leading production mode for the Higgs is via gluon-gluon fusion through the mediation of a heavy-quark (mostly top-quark) loop. The NLO corrections to fully inclusive Higgs production via gluon-gluon fusion, including the heavy-quark mass dependence, required an evaluation at two-loop accuracy. They were found to be as large ^{45, 46)} as the leading-order calculation. That situation was unsatisfactory, because it called for a calculation to NNLO⁵, which required an evaluation at three-loop accuracy. That was beyond the possibilities of the coeval (and also present) technology. However, if the Higgs mass is smaller than the threshold for the creation of a top-quark pair, $m_H \lesssim 2m_t$, the coupling of the Higgs to the gluons via a top-quark loop can be replaced by an effective coupling. That simplifies calculations tremendously, because it effectively reduces the number of loops in a given diagram by one. It is called the *large- m_t limit*. The NNLO corrections have been evaluated in the large- m_t limit ^{48, 49)} and display a modest increase with respect to the NLO evaluation, showing that the calculation stabilises to NNLO.

⁵One must keep in mind that the calculation of Ref. ^{45, 46)} is fully inclusive, thus for an ideal detector with a 4π coverage. If selection cuts are applied, like in Ref. ⁴⁷⁾, where Higgs production via gluon-gluon fusion is computed to NLO and to NNLO with a jet veto, the higher-order corrections may be not so large as in the fully inclusive calculation. Thus the ultimate judgement on the usefulness of a NNLO evaluation rests on an analysis with the cuts which will be used in the realistic simulations of the ATLAS and CMS detectors.

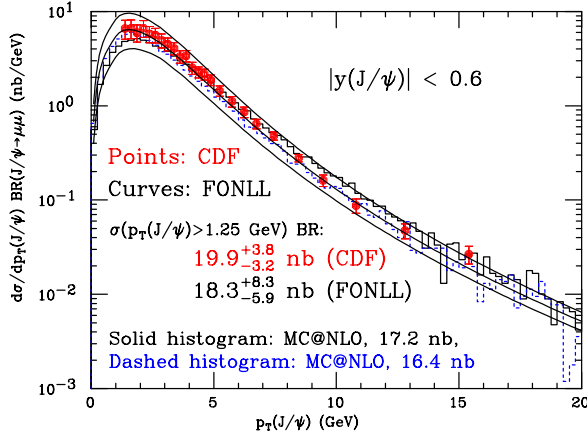


Figure 2: CDF J/ψ momentum distribution from B decays, from M. Cacciari, S. Frixione, M. L. Mangano, P. Nason and G. Ridolfi ⁴¹⁾. The CDF cross section in the inset was the preliminary value available to the authors of Ref. ⁴¹⁾. The recently published value ⁴⁰⁾ is $19.4 \pm 0.3(stat)_{-1.9}^{+2.1}(syst)$ nb.

In the examples above I stressed how the central value of a prediction may change when going from leading order to NLO and eventually to NNLO. However, a benefit of going from leading order to NLO and then to NNLO is the reduction of the uncertainty band, due to the lesser sensitivity to the fictitious input scales μ_R and μ_F of the calculation. Thus, a lot of theoretical activity has been directed in the last years toward the calculation of cross sections to NNLO accuracy.

The total cross section ^{48, 50)} and the rapidity distribution ⁵¹⁾ for Drell-Yan W, Z production are known to NNLO accuracy. So are the total cross section ^{48, 49)} and the rapidity distribution ⁴⁷⁾ for Higgs production via gluon-gluon fusion, in the large- m_t limit. However, only the calculation of Ref. ⁴⁷⁾, which has been extended to include the di-photon background ⁵²⁾, allows the use of arbitrary selection cuts, Fig.3. As we said in Sect.3, the universality of the IR divergences of gauge theories has made possible to organise NLO computations in process-independent and user-friendly procedures, where arbitrary selection cuts can be implemented. Since the universality of the IR divergences is a feature which holds to all orders, it would be desirable to exploit it also in NNLO computations. However, the cancellation of the IR divergences to

NNLO is very intricate, and although several individuals or groups have been working on it (53, 54, 55, 56, 57, 58, 59, 60), no process-independent procedure has been devised yet.

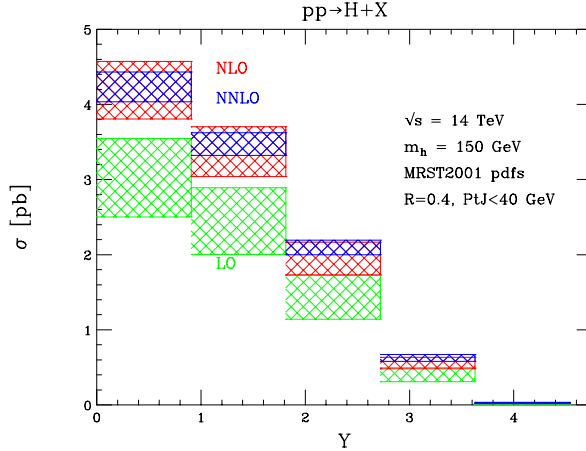


Figure 3: Bin-integrated rapidity distribution for Higgs production via gluon-gluon fusion, with a jet veto of $|p_T| < 40$ GeV, from C. Anastasiou, K. Melnikov and F. Petriello (52). The jets are identified with the cone algorithm, using a cone size of $R = 0.4$. The uncertainty bands are obtained equating the renormalisation and factorisation scales $\mu_R = \mu_F = \mu$, and then varying μ in the range $m_H/2 \leq \mu \leq 2m_H$.

5 The parton distribution functions

As we said in the Introduction, at hadron colliders the theory cross section can be written using factorisation as a convolution of the partonic cross section with the parton distribution functions. The dependence of the PDFs on Q^2 is given by the DGLAP evolution equations. In those equations, the evolution in Q^2 of the PDFs is driven by the splitting functions, which are perturbatively computable. By consistency, in the factorisation formula the partonic cross section and the splitting functions must be determined to the same accuracy. The leading-order (61, 62) and NLO (63) splitting functions have been known for a long time. The calculation of the NNLO splitting functions has been completed recently (64, 65), setting the record as the toughest calculation ever performed in perturbative QCD: it took the equivalent of 20 man-years, and

about a million lines of dedicated algebra code. The PDF's obtained by global fits ⁶⁶⁾ of all accessible collider and fixed-target data can be evolved to the large kinematic range accessible through the LHC, Fig.4. In global fits, the fit is performed by minimising the χ^2 to all the data. The evolution is started at some value Q_0^2 , where the PDF is some suitable function of x . In addition, to avoid higher-twist contaminations, the data are selected above a certain momentum transfer and energy, $Q^2 > Q_{\min}^2$ and $W^2 > W_{\min}^2$. Recently, though, also an evaluation of the $\Delta\chi^2$, i.e. of the uncertainties arising from the errors on the experimental data, has been performed ^{67, 68, 69, 70, 71)}, using either the Hessian or the Lagrange-multiplier methods. Accordingly, in connection with the use of W, Z production as a parton luminosity monitor mentioned in Sect.4, Ref. ⁷¹⁾ estimates a +4% uncertainty on the Drell-Yan W, Z production cross section.

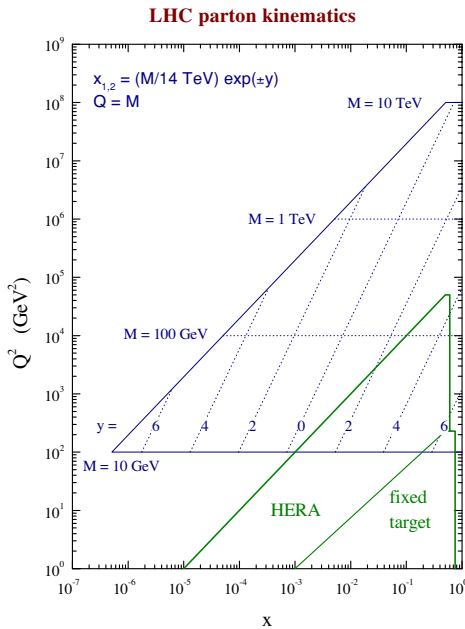


Figure 4: LHC kinematic range, from MRST ⁷²⁾.

⁶In Ref. ⁶⁶⁾, which pre-dates Refs. ^{64, 65)}, the NNLO global fit is based on a few NNLO fixed moments, which were known at that time.

6 Conclusions

QCD in the high-energy regime is constantly making progress. Here I have reviewed the considerable advances achieved in the last few years in the sectors of QCD which are most actively studied: higher-order corrections, PDFs and Monte Carlo models. Thanks to those, high-energy QCD allows for an ever more precise determination of α_s , the PDFs and the parton luminosity at LHC, thus becoming more and more an essential precision toolkit to analyse Higgs and New Physics scenarios at LHC.

7 Acknowledgements

Many thanks to Babis Anastasiou, Sigi Bethke, M.L. Mangano and James Stirling for providing the figures used in the text.

References

1. S. Bethke, Nucl. Phys. Proc. Suppl. **135** (2004) 345 [arXiv:hep-ex/0407021].
2. D. Acosta *et al.* [CDF Collaboration], Phys. Rev. D **70** (2004) 072002 [arXiv:hep-ex/0404004].
3. Y. L. Dokshitzer, G. Marchesini and B. R. Webber, Nucl. Phys. B **469** (1996) 93 [arXiv:hep-ph/9512336].
4. M.L. Mangano, “Monte Carlos” presented at the KITP Collider Physics Conference, January 2004, http://online.kitp.ucsb.edu/online/collider_c04/mangano/
5. F. Abe *et al.* [CDF Collaboration], Phys. Rev. D **56** (1997) 3811.
6. J. C. Collins, L. Frankfurt and M. Strikman, Phys. Lett. B **307** (1993) 161 [arXiv:hep-ph/9212212].
7. K. Terashi [CDF Collaboration], Int. J. Mod. Phys. A **16S1A** (2001) 265.
8. D. Acosta *et al.* [CDF Collaboration], Phys. Rev. Lett. **93** (2004) 141601 [arXiv:hep-ex/0311023].

9. M. L. Mangano, M. Moretti, F. Piccinini, R. Pittau and A. D. Polosa, *JHEP* **0307** (2003) 001 [arXiv:hep-ph/0206293].
10. T. Stelzer and W. F. Long, *Comput. Phys. Commun.* **81** (1994) 357 [arXiv:hep-ph/9401258].
11. F. Maltoni and T. Stelzer, *JHEP* **0302** (2003) 027 [arXiv:hep-ph/0208156].
12. A. Pukhov *et al.*, arXiv:hep-ph/9908288.
13. T. Ishikawa, T. Kaneko, K. Kato, S. Kawabata, Y. Shimizu and H. Tanaka [MINAMI-TATEYA group Collaboration], KEK-92-19
14. F. Yuasa *et al.*, *Prog. Theor. Phys. Suppl.* **138** (2000) 18 [arXiv:hep-ph/0007053].
15. A. Kanaki and C. G. Papadopoulos, *Comput. Phys. Commun.* **132** (2000) 306 [arXiv:hep-ph/0002082].
16. E. Accomando, A. Ballestrero and E. Maina, *Nucl. Instrum. Meth. A* **534**, 265 (2004) [arXiv:hep-ph/0404236].
17. F. Krauss, A. Schalicke, S. Schumann and G. Soff, *Phys. Rev. D* **70** (2004) 114009 [arXiv:hep-ph/0409106].
18. G. Marchesini, B. R. Webber, G. Abbiendi, I. G. Knowles, M. H. Seymour and L. Stanco, *Comput. Phys. Commun.* **67** (1992) 465.
19. T. Sjostrand, *Comput. Phys. Commun.* **82** (1994) 74.
20. S. Frixione and B. R. Webber, *JHEP* **0206** (2002) 029 [arXiv:hep-ph/0204244].
21. S. Frixione, these proceedings.
22. W. T. Giele and E. W. N. Glover, *Phys. Rev. D* **46** (1992) 1980.
23. W. T. Giele, E. W. N. Glover and D. A. Kosower, *Nucl. Phys. B* **403** (1993) 633 [arXiv:hep-ph/9302225].
24. S. Frixione, Z. Kunszt and A. Signer, *Nucl. Phys. B* **467** (1996) 399 [arXiv:hep-ph/9512328].

25. Z. Nagy and Z. Trocsanyi, Nucl. Phys. B **486** (1997) 189 [arXiv:hep-ph/9610498].
26. S. Catani and M. H. Seymour, Nucl. Phys. B **485** (1997) 291 [Erratum-ibid. B **510** (1997) 291] [hep-ph/9605323].
27. R. K. Ellis, D. A. Ross and A. E. Terrano, Nucl. Phys. B **178** (1981) 421.
28. L. J. Dixon and A. Signer, Phys. Rev. D **56**, 4031 (1997) [arXiv:hep-ph/9706285].
29. Z. Nagy and Z. Trocsanyi, Phys. Rev. Lett. **79** (1997) 3604 [arXiv:hep-ph/9707309].
30. J. Campbell and R. K. Ellis, Phys. Rev. D **65** (2002) 113007 [arXiv:hep-ph/0202176].
31. S. D. Ellis, Z. Kunszt and D. E. Soper, Phys. Rev. Lett. **64** (1990) 2121.
32. Z. Nagy, Phys. Rev. Lett. **88** (2002) 122003 [arXiv:hep-ph/0110315].
33. B. Bailey, J. F. Owens and J. Ohnemus, Phys. Rev. D **46** (1992) 2018.
34. T. Binoth, J. P. Guillet, E. Pilon and M. Werlen, Eur. Phys. J. C **16** (2000) 311 [arXiv:hep-ph/9911340].
35. V. Del Duca, F. Maltoni, Z. Nagy and Z. Trocsanyi, JHEP **0304** (2003) 059 [arXiv:hep-ph/0303012].
36. M. L. Mangano, P. Nason and G. Ridolfi, Nucl. Phys. B **373** (1992) 295.
37. J. M. Campbell and R. K. Ellis, Phys. Rev. D **60** (1999) 113006 [arXiv:hep-ph/9905386].
38. L. J. Dixon, Z. Kunszt and A. Signer, Phys. Rev. D **60** (1999) 114037 [arXiv:hep-ph/9907305].
39. M. L. Mangano, arXiv:hep-ph/0411020.
40. D. Acosta *et al.* [CDF Collaboration], arXiv:hep-ex/0412071.
41. M. Cacciari, S. Frixione, M. L. Mangano, P. Nason and G. Ridolfi, JHEP **0407** (2004) 033 [arXiv:hep-ph/0312132].

42. S. Frixione, P. Nason and B. R. Webber, *JHEP* **0308** (2003) 007 [arXiv:hep-ph/0305252].
43. M. Dittmar, F. Pauss and D. Zurcher, *Phys. Rev. D* **56** (1997) 7284 [arXiv:hep-ex/9705004].
44. S. Frixione and M. L. Mangano, *JHEP* **0405** (2004) 056 [arXiv:hep-ph/0405130].
45. D. Graudenz, M. Spira and P. M. Zerwas, *Phys. Rev. Lett.* **70** (1993) 1372.
46. M. Spira, A. Djouadi, D. Graudenz and P. M. Zerwas, *Nucl. Phys. B* **453** (1995) 17 [arXiv:hep-ph/9504378].
47. C. Anastasiou, K. Melnikov and F. Petriello, arXiv:hep-ph/0409088.
48. R. V. Harlander and W. B. Kilgore, *Phys. Rev. Lett.* **88** (2002) 201801 [arXiv:hep-ph/0201206].
49. C. Anastasiou and K. Melnikov, *Nucl. Phys. B* **646** (2002) 220 [arXiv:hep-ph/0207004].
50. R. Hamberg, W. L. van Neerven and T. Matsuura, *Nucl. Phys. B* **359** (1991) 343 [Erratum-ibid. *B* **644** (2002) 403].
51. C. Anastasiou, L. J. Dixon, K. Melnikov and F. Petriello, *Phys. Rev. D* **69** (2004) 094008 [arXiv:hep-ph/0312266].
52. C. Anastasiou, K. Melnikov and F. Petriello, arXiv:hep-ph/0501130.
53. S. Weinzierl, *JHEP* **0303** (2003) 062 [arXiv:hep-ph/0302180].
54. S. Weinzierl, *JHEP* **0307** (2003) 052 [arXiv:hep-ph/0306248].
55. D. A. Kosower, [arXiv:hep-ph/0311272].
56. A. Gehrmann-De Ridder, T. Gehrmann and G. Heinrich, *Nucl. Phys. B* **682** (2004) 265 [arXiv:hep-ph/0311276].
57. S. Frixione and M. Grazzini, [arXiv:hep-ph/0411399].
58. A. Gehrmann-De Ridder, T. Gehrmann and E. W. N. Glover, arXiv:hep-ph/0501291.

59. A. Gehrmann-De Ridder, T. Gehrmann and E. W. N. Glover, arXiv:hep-ph/0502110.
60. G. Somogyi, Z. Trocsanyi and V. Del Duca, arXiv:hep-ph/0502226.
61. D. J. Gross and F. Wilczek, Phys. Rev. D **8** (1973) 3633.
62. G. Altarelli and G. Parisi, Nucl. Phys. B **126** (1977) 298.
63. G. Curci, W. Furmanski and R. Petronzio, Nucl. Phys. B **175** (1980) 27.
64. S. Moch, J. A. M. Vermaseren and A. Vogt, Nucl. Phys. B **688** (2004) 101 [arXiv:hep-ph/0403192].
65. A. Vogt, S. Moch and J. A. M. Vermaseren, Nucl. Phys. B **691** (2004) 129 [arXiv:hep-ph/0404111].
66. A. D. Martin, R. G. Roberts, W. J. Stirling and R. S. Thorne, Phys. Lett. B **531** (2002) 216 [arXiv:hep-ph/0201127].
67. D. Stump *et al.*, Phys. Rev. D **65** (2002) 014012 [arXiv:hep-ph/0101051].
68. J. Pumplin *et al.*, Phys. Rev. D **65** (2002) 014013 [arXiv:hep-ph/0101032].
69. J. Pumplin, D. R. Stump, J. Huston, H. L. Lai, P. Nadolsky and W. K. Tung, JHEP **0207** (2002) 012 [arXiv:hep-ph/0201195].
70. A. D. Martin, R. G. Roberts, W. J. Stirling and R. S. Thorne, Eur. Phys. J. C **28** (2003) 455 [arXiv:hep-ph/0211080].
71. A. D. Martin, R. G. Roberts, W. J. Stirling and R. S. Thorne, Eur. Phys. J. C **35** (2004) 325 [arXiv:hep-ph/0308087].
72. A. D. Martin, R. G. Roberts, W. J. Stirling and R. S. Thorne, Eur. Phys. J. C **14** (2000) 133 [arXiv:hep-ph/9907231].

BOTTOM PRODUCTION FROM PAST TO FUTURE

Matteo Cacciari

LPTHE - Université Pierre et Marie Curie (Paris 6), France

Abstract

We review the history of comparisons between bottom production measurements and QCD predictions. We challenge the existence of a ‘significant discrepancy’, and argue that standard approaches to QCD calculations do a good job in describing the experimental findings.

1 Introduction

For the past ten years or so, a rumour has been making the rounds of particle physics Conferences and Workshops: measured bottom quark production rates are significantly larger than predicted by next-to-leading order QCD.

Such a state of affairs casts doubts on the ability of QCD to properly describe this process, and opens the way to speculations that either drastic

improvements to QCD calculations are needed, or even that effects beyond the Standard Model might be at work.

We shall challenge the rumour under two main aspects, aiming especially at the words “measured” and “significantly”. It is our hope that, once done, we shall have convinced the reader that standard approaches to QCD calculations do a good job in describing the experimental findings.

Let us first briefly review the history of the experimental results. Measurements of the bottom transverse momentum (p_T) spectrum at colliders began in the late 80’s, when the UA1 Collaboration, taking data at the CERN $SppS$ with $\sqrt{S} = 546$ and 630 GeV, published results for the $p_T > m_b$ (the bottom quark mass) region [1, 2]. These results were compared to the then recently completed next-to-leading order (NLO) calculation [3], and found in good agreement.

During the 90’s the CDF [4–10] and D0 [11–14] Collaborations also measured the bottom quark p_T distribution in $p\bar{p}$ collisions at the Fermilab Tevatron at $\sqrt{S} = 1800$ GeV. Apparently at odds with the UA1 results, the Tevatron data appeared to display an excess with respect to NLO QCD predictions. At the same time, rates for bottom production which appeared higher than QCD predictions were also reportedly observed in $\gamma\gamma$ and ep collisions.

Despite this seemingly overwhelming evidence, we shall argue that QCD is instead rather successful in predicting bottom production rates. Improved theoretical analyses [15, 16] and more recent experimental measurements by the CDF [17] and ZEUS [18] Collaborations support this claim, which is also borne out by a critical revisitation of previous results.

2 The Paradigm

We shall take NLO QCD calculations as a benchmark for comparisons. We shall require the experimental measurements to be genuine observable quantities. By this we mean that in principle we do not wish to compare “data” for, e.g., b -quark p_T distributions, since such a quantity is clearly an unphysical one. The quark not being directly observed its cross sections have to be inferred rather than directly measured.

A meaningful comparison will therefore be one between a physical cross section and a QCD calculation with at least NLO accuracy. Non-perturbative information, where needed, will have to be introduced in a minimal and self-

consistent way. This means that we refrain from using unjustified models, and we shall only include non-perturbative information which has been extracted from one experiment and then employed in predicting another observable, using the same underlying perturbative framework in both cases.

In practice, the non-perturbative information relative to the hadronization of the b -quarks into B -hadrons is extracted from LEP data with a calculation which has NLO + NLL accuracy. The framework presented in [15] is used: the LEP (or SLD) data [19–22] are translated to Mellin moments space, and only the moments around $N = 5$ are fitted. This ensures that it is the *relevant* part of the non-perturbative information which is properly determined [23, 24]. These non-perturbative moments are then used together with a calculation having the same perturbative features, FONLL, [25] to evaluate the cross sections in $p\bar{p}$ collisions.

The expectation is then that total cross sections be reproduced by the NLO calculations for b quarks, and that differential distribution for B hadrons be correctly described by a proper convolution of the FONLL perturbative spectrum for b quarks and the non-perturbative information extracted from LEP data. A successful comparison will see data and theory in agreement within their *combined* uncertainties.

3 The Data

Hadronic collisions were historically the first to produce bottom production data in collider physics. The first results were published by the UA1 Collaboration [1, 2], which compared bottom quark transverse momentum distributions to the then recently completed NLO prediction [3], and found a good agreement.

The first results from the Tevatron were given in 1992 by the CDF Collaboration [4]. The inclusive cross bottom cross section was published deconvoluted to the quark level. Its central value was found to be a factor of six larger than the NLO prediction, but the very large errors only made it a 1.6 sigma distance and therefore not a significant one.

One year later CDF started publishing [5, 6] the plot of the transverse momentum distribution which will then become the icon of the supposed ‘excess’. The data were shown at the unphysical quark level and, while reporting differences of the order of 1-2 sigmas between data and theory, the papers still

conclude that “...the next-to-leading order QCD calculation tends to underestimate the inclusive b -quark cross section”, hinting therefore for the first time that a discrepancy might be present. The same conclusion was reached in a subsequent paper [8], where cross sections for real particles, B mesons, were finally published.

Around the same time CDF published the first data on bottom quarks, the D0 Collaboration also released some preliminary results which were presented at a number of conferences. Somewhat at odds with the CDF ones, they were in very good agreement with the NLO predictions. Therefore, weighing the data from both collaborations, speakers at the conferences (see e.g. [26,27]) generally reported a good agreement between bottom quark data and NLO QCD. Given this state of affairs, the final D0 data must have caused some surprise when, published in final form [11], they became more CDF-like, now lying around the upper edge of the theoretical uncertainty band. The prediction of NLO QCD, however, was still considered to be giving an adequate description of the data.

The subsequent pair of D0 papers on this subject [13,14] should have caused an even larger surprise. Despite the conclusions of the previous paper (“adequate description” [11]), in the Introduction of [13] the previously measured b quark cross section is now considered to have been found “systematically larger” than the central value of NLO QCD predictions. This helps accepting the news that the data now show a considerable excess: “*The ratio of the data to the central NLO QCD prediction is approximately three...*”. [13] This strong statement is even upped in the following paper which, already in the Abstract, states that “*We find that next-to-leading-order QCD calculations underestimate b -quark production by a factor of 4 in the forward rapidity region*”. [14]

Two more experimental papers were then added to the field: both are worth examining closely, albeit for different reasons. The D0 Collaboration performed a measurement [28] of the transverse energy distribution of jets containing a bottom quarks, the so called b -jets. These objects are real observables, while at the same time being largely independent of the fragmentation properties of the bottom quarks. By contrast, other observables like the B mesons do instead of course depend on the way the bottom quarks fragment into the bottomed hadrons. D0 found that the cross section for b -jets was compatible with the NLO QCD prediction [29].

A couple of years later the CDF Collaboration updated [9] its measurement for the B mesons transverse momentum distribution, superseding [8] and representing the final analysis for bottom production with the Tevatron Run I data: “*The differential cross section is measured to be 2.9 ± 0.2 (stat \oplus syst $_{p_T}$) ± 0.4 (syst $_{f_c}$) times higher than NLO QCD predictions...*”. A couple of comments are worth making. The first is that the errors on this ratio do not include the theoretical uncertainty. The second is that the ‘NLO QCD’ prediction must of course include the non-perturbative information needed to fragment the bottom quark into the B meson. In this experimental paper this fragmentation was performed using the Peterson et al. functional form, with its free parameter set to $\epsilon_b = 0.006$. Such a procedure however neglects the notion that neither the bottom quark nor its fragmentation into B hadrons are physical observables. Neither of them is separately measurable, only their final combination is. It is therefore wrong in principle (and also, as we will see, in practice) to rely on a fixed and standard determination of the non-perturbative fragmentation function and to convolute it with whatever perturbative calculation is being used. The non-perturbative fragmentation must rather be determined from data (usually from e^+e^- collisions) using the same perturbative framework and parameters (bottom mass, strong coupling) of the calculation which will then be employed to calculate bottom quark production in $p\bar{p}$ collisions.

This is precisely what was done in [15]. The non-perturbative information was determined, as described above, from LEP data in moment space, and employed to predict the B mesons transverse momentum distribution at the Tevatron. The resulting data/theory ratio was estimated to be 1.7 ± 0.5 (expt) ± 0.5 (th), showing therefore no significant discrepancy between the data and the theory.

4 The Recent Comparisons

The understanding of the potentially large biases related to the description of the non-perturbative fragmentation phase, and the proper inclusion of uncertainties from all the sources, allowed to conclude that no significant discrepancies were probably present in the bottom data collected at the Tevatron during the Run I. These data were however always above a minimum p_T of about 5 GeV. Since a harder or softer non-perturbative fragmentation function will

leave the total cross section unchanged while shifting contributions to larger or smaller p_T values respectively, it was still possible that such a shift was only faking a larger cross section. Small- p_T data, and possibly a total cross section measurement, are therefore crucial for establishing whether the NLO QCD prediction is indeed accounting or not for the number of bottom quarks produced at the Tevatron.

Table 1: Measured and predicted integrated cross sections, from [17] and [16]. (See [16] for detailed experimental cuts and branching ratios included in cross sections given in the Table)

	CDF	Theory (FONLL)
$\sigma(H_b \rightarrow J/\psi)$	19.9 ^{$\beta+3.8$} _{$\beta-3.2$} <i>stat+syst</i> nb	18.3 ^{$\beta+8.1$} _{$\beta-5.7$} nb
$\sigma(H_b)$	24.5 ^{$\beta+4.7$} _{$\beta-3.9$} <i>stat+syst</i> nb	22.9 ^{$\beta+10.6$} _{$\beta-7.8$} nb
$\sigma(b)$	29.4 ^{$\beta+6.2$} _{$\beta-5.4$} <i>stat+syst</i> μb	25.0 ^{$\beta+12.6$} _{$\beta-8.1$} μb

Such data, from the Tevatron Run II, have indeed been recently made public in preliminary form ¹ by the CDF Collaboration [17], and promptly compared [16] to the predictions given by the framework put forward in [15]. These predictions depend solely on the following calculations and parameters:

- Perturbative inputs

- FONLL calculation (i.e. full massive NLO calculation plus matching to NLL resummation, both for e^+e^- and for $p\bar{p}$ collisions)
- bottom quark pole mass m_b (varied between 4.5 and 5 GeV)
- strong coupling ($\Lambda^{(5)} = 0.226$ GeV, i.e. $\alpha_s(M_Z) = 0.118$)
- renormalization and factorization scales (varied between $\mu_0/2 \leq \mu_{R,F} \leq 2\mu_0$, with $1/2 \leq \mu_R/\mu_F \leq 2$ and $\mu_0 \equiv \sqrt{m_b^2 + p_T^2}$)

- Non-perturbative/phenomenological inputs

¹The final data were successively published in [30].

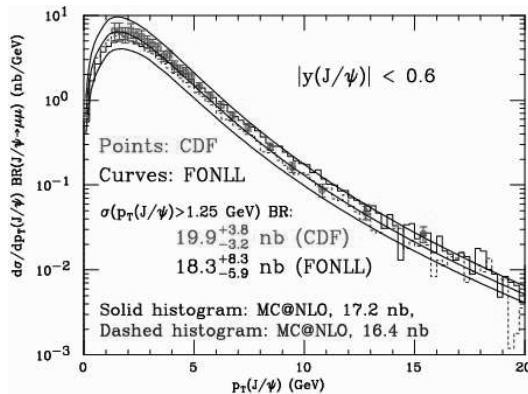


Figure 1: CDF J/ψ spectrum from H_b decays, compared to theoretical predictions [16].

- gluon and light quarks PDFs (e.g. the CTEQ6M set)
- b quark to H_b hadron fragmentation (fitted to moments of LEP data, see [15])
- H_b to J/ψ branching ratio, 1.15%, and decay spectrum (from CLEO or BABAR Collaborations)

After extensive exploration of all the numerically meaningful uncertainties, the predictions compare to the measured total cross sections as shown in Table 1.

These results clearly indicate full consistency between theory and experiment within the uncertainties. The transverse momentum spectrum of the J/ψ 's from b 's, shown in figure 1, is equally well described.

5 Bottom Production at the LHC

The LHC will be able to explore much larger transverse momentum ranges, and therefore probe the regions where heavy bottom quarks behave really very much like light ones. This will make the collinear resummation included in the FONLL approach, so far needed only for the extraction from LEP data of the non-perturbative fragmentation component, absolutely mandatory also in the

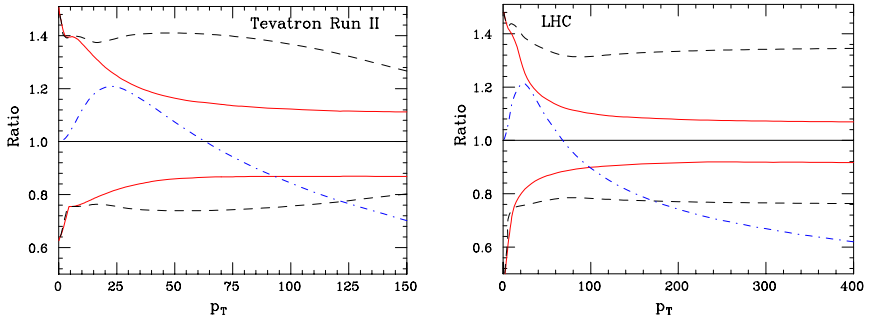


Figure 2: Uncertainty bands for the NLO (dashed) and the FONLL (solid) calculations at the Tevatron Run II (left) and LHC (right). The single dot-dashed line represents the FONLL/NLO ratio.

calculation of the hadronic cross sections. This is shown in figure 2: only at bottom transverse momenta larger than 100-200 GeV the difference between the FONLL and the NLO calculations becomes larger than the intrinsic uncertainty of the calculations themselves. Probing this large- p_T region will therefore allow to fully validate the resummation framework.

6 Conclusions

Next-to-leading order QCD appears to be doing a good job in predicting bottom quark production cross sections at the Tevatron. Comparisons performed at the *observed hadron* level, rather than at the unphysical *quark* level, do not seem to show significant discrepancies. Tevatron Run II preliminary results are even in very good agreement. We argue that discrepancies pointed out in the past were either not very significant - in that the real size of the uncertainties might have been underestimated or simply overlooked, or that the ‘data’ might have been tainted by excessive use of Monte Carlo simulation in their extraction, deconvolution to parton level, and extrapolation to full phase space.

New physics has been advocated at some point in order to explain the presumed discrepancy. While there is of course still room for it within the uncertainties, at the level of about 30% in the Tevatron data case, we argue that its presence is not needed in order to explain the single inclusive bottom

production data. The LHC data will undoubtedly allow to perform further comparisons and test the QCD predictions at even larger transverse momenta.

Finally, we wish to point out that much of the progress done in the last couple of years has been permitted by the possibility of comparing theoretical predictions to real data, rather than to deconvoluted/extrapolated ones. This is not always the case, as sometimes the original data are not published and are forever lost. We urge therefore the experimental Collaborations to always publish also results which do not depend (or depend as little as possible) on theoretical prejudices (e.g. in the form of a Monte Carlo code) for their extraction. This will avoid the risk of biasing them, and will leave open the possibility of performing updated comparisons in the future.

Acknowledgments. It is a pleasure to thank my collaborators, and the Organizers for the invitation to this Workshop.

References

1. C. Albajar *et al.* [UA1 Collaboration], Phys. Lett. B **186** (1987) 237.
2. C. Albajar *et al.* [UA1 Collaboration], Phys. Lett. B **256** (1991) 121 [Erratum-ibid. B **262** (1991) 497].
3. P. Nason, S. Dawson and R. K. Ellis, Nucl. Phys. B **303** (1988) 607; Nucl. Phys. B **327** (1989) 49 [Erratum-ibid. B **335** (1990) 260]; W. Beenakker, H. Kuijf, W. L. van Neerven and J. Smith, Phys. Rev. D **40** (1989) 54; W. Beenakker, W. L. van Neerven, R. Meng, G. A. Schuler and J. Smith, Nucl. Phys. B **351** (1991) 507.
4. F. Abe *et al.* [CDF Collaboration], Phys. Rev. Lett. **68** (1992) 3403.
5. F. Abe *et al.* [CDF Collaboration], Phys. Rev. Lett. **71** (1993) 500.
6. F. Abe *et al.* [CDF Collaboration], Phys. Rev. Lett. **71** (1993) 2396.
7. F. Abe *et al.* [CDF Collaboration], Phys. Rev. D **50** (1994) 4252.
8. F. Abe *et al.* [CDF Collaboration], Phys. Rev. Lett. **75** (1995) 1451 [arXiv:hep-ex/9503013].

9. D. Acosta *et al.* [CDF Collaboration], Phys. Rev. D **65** (2002) 052005 [arXiv:hep-ph/0111359].
10. D. Acosta *et al.* [CDF Collaboration], Phys. Rev. D **66** (2002) 032002 [arXiv:hep-ex/0206019].
11. S. Abachi *et al.*, [D0 Collaboration], Phys. Rev. Lett. **74** (1995) 3548;
12. S. Abachi *et al.* [D0 Collaboration], Phys. Lett. B **370** (1996) 239.
13. B. Abbott *et al.*, [D0 Collaboration], Phys. Rev. Lett. **84** (2000) 5478 [arXiv:hep-ex/9907029].
14. B. Abbott *et al.* [D0 Collaboration], Phys. Lett. B **487** (2000) 264 [arXiv:hep-ex/9905024].
15. M. Cacciari and P. Nason, Phys. Rev. Lett. **89** (2002) 122003 [arXiv:hep-ph/0204025].
16. M. Cacciari, S. Frixione, M. L. Mangano, P. Nason and G. Ridolfi, JHEP **0407** (2004) 033 [arXiv:hep-ph/0312132].
17. CDF Note 6285; C. Chen, [CDF Collaboration], presentation at “Beauty 2003”, <http://www-cdf.fnal.gov/physics/new/bottom/030904.blessed-bxsec-jpsi/>; M. Bishai [CDF Collaboration], presentation at Fermilab, Dec 5, 2003, <http://www-cdf.fnal.gov/~bishai/papers/wandc.pdf>
18. S. Chekanov *et al.* [ZEUS Collaboration], arXiv:hep-ex/0312057.
19. A. Heister *et al.* [ALEPH Collaboration], Phys. Lett. B **512** (2001) 30 [arXiv:hep-ex/0106051].
20. K. Abe *et al.* [SLD Collaboration], Phys. Rev. D **65** (2002) 092006 [Erratum-ibid. D **66** (2002) 079905] [arXiv:hep-ex/0202031].
21. G. Abbiendi *et al.* [OPAL Collaboration], arXiv:hep-ex/0210031.
22. G. Barker *et al.* [DELPHI Collaboration], DELPHI 2002-069 CONF 603.
23. S. Frixione, M. L. Mangano, P. Nason and G. Ridolfi, Adv. Ser. Direct. High Energy Phys. **15** (1998) 609 [arXiv:hep-ph/9702287].

24. P. Nason *et al.*, Report of the 1999 CERN Workshop on SM physics (and more) and the LHC, arXiv:hep-ph/0003142.
25. M. Cacciari, M. Greco and P. Nason, JHEP **9805** (1998) 007 [arXiv:hep-ph/9803400].
26. A. Zieminski [D0 Collaboration], <http://www.slac.stanford.edu/spires/find/www?irn=4294769>, *La Thuile, Italy, March 1994*
27. K. A. Bazizi [CDF and D0 Collaborations], FERMILAB-CONF-94-300-E, <http://www.slac.stanford.edu/spires/find/hep/www?r=fermilab-conf-94-300-e>, *Moriond QCD, France, March 1994*
28. B. Abbott *et al.* [D0 Collaboration], Phys. Rev. Lett. **85** (2000) 5068 [arXiv:hep-ex/0008021].
29. S. Frixione and M. L. Mangano, Nucl. Phys. B **483** (1997) 321 [arXiv:hep-ph/9605270].
30. D. Acosta *et al.* [CDF Collaboration], Phys. Rev. D **71** (2005) 032001 [arXiv:hep-ex/0412071].

Concluding Remarks

**CONCLUDING TALK:
STATUS OF THE STANDARD MODEL AND BEYOND**

Guido Altarelli

TH Division, Physics Department, CERN, Geneva, Switzerland

Abstract

In view of the LHC we present a concise review of the status of the Standard Model and of the models of new physics.

1 Preamble

I have chosen the formula "Concluding Talk" in the title of my contribution to this very interesting Workshop. Indeed this is not a "Summary Talk": it is impossible to review in 30 minutes/10 pages the great variety of results, ideas and projects for the future that have been presented at this Conference. Also, I am not really competent on some purely experimental areas which were discussed in many impressive talks. It is not a "Conclusion" talk either: the subject of LHC physics is at present a gigantic work in progress and we are not at the end of a particular phase where a sharp line can easily be drawn.

Rather, in my presentation I will briefly review the conceptual status of particle physics at present while we eagerly wait for the start up of the LHC.

2 The Result of Precision Tests of the Standard Model

The results of the electroweak precision tests as well as of the searches for the Higgs boson and for new particles performed at LEP and SLC are now available in nearly final form. Taken together with the measurements of m_t , m_W and the searches for new physics at the Tevatron, and with some other data from low energy experiments, they form a very stringent set of precise constraints ¹⁾ to compare with the Standard Model (SM) or with any of its conceivable extensions. When confronted with these results, on the whole the SM performs rather well, so that it is fair to say that no clear indication for new physics emerges from the data ²⁾. The main lesson of precision tests of the standard electroweak theory can be summarised as follows. The couplings of quark and leptons to the weak gauge bosons W^\pm and Z are indeed precisely those prescribed by the gauge symmetry. The accuracy of a few per-mille for these tests implies that, not only the tree level, but also the structure of quantum corrections has been verified. To a lesser accuracy the triple gauge vertices γWW and ZWW have also been found in agreement with the specific prediction of the $SU(2) \otimes U(1)$ gauge theory. This means that it has been verified that the gauge symmetry is unbroken in the vertices of the theory: the currents are indeed conserved. Yet there is obvious evidence that the symmetry is otherwise badly broken in the masses. Thus the currents are conserved but the spectrum of particle states is not at all symmetric. This is a clear signal of spontaneous symmetry breaking. The practical implementation of spontaneous symmetry breaking in a gauge theory is via the Higgs mechanism. The Higgs sector of the SM is still very much untested. What has been tested is the relation $m_W^2 = m_Z^2 \cos^2 \theta_W$, modified by computable radiative corrections. This relation means that the effective Higgs (be it fundamental or composite) is indeed a weak isospin doublet. The Higgs particle has not been found but in the SM its mass can well be larger than the present direct lower limit $m_H \gtrsim 114 \text{ GeV}$ obtained from direct searches at LEP-2. The radiative corrections computed in the SM when compared to the data on precision electroweak tests lead to a clear indication for a light Higgs, not too far from the present lower bound. No signal of new physics has been found. However, to make a light

Higgs natural in presence of quantum fluctuations new physics should not be too far. This is encouraging for the LHC that should experimentally clarify the problem of the electroweak symmetry breaking sector and search for physics beyond the SM.

3 Outlook on Avenues beyond the Standard Model

Given the success of the SM why are we not satisfied with that theory? Why not just find the Higgs particle, for completeness, and declare that particle physics is closed? The reason is that there are both conceptual problems and phenomenological indications for physics beyond the SM. On the conceptual side the most obvious problems are that quantum gravity is not included in the SM and the related hierarchy problem. Among the main phenomenological hints for new physics we can list coupling unification, dark matter, neutrino masses, baryogenesis and the cosmological vacuum energy.

The computed evolution with energy of the effective SM gauge couplings clearly points towards the unification of the electro-weak and strong forces (Grand Unified Theories: GUT's) at scales of energy $M_{GUT} \sim 10^{15} - 10^{16} \text{ GeV}$ which are close to the scale of quantum gravity, $M_{Pl} \sim 10^{19} \text{ GeV}$. One is led to imagine a unified theory of all interactions also including gravity (at present superstrings provide the best attempt at such a theory). Thus GUT's and the realm of quantum gravity set a very distant energy horizon that modern particle theory cannot ignore. Can the SM without new physics be valid up to such large energies? This appears unlikely because the structure of the SM could not naturally explain the relative smallness of the weak scale of mass, set by the Higgs mechanism at $\mu \sim 1/\sqrt{G_F} \sim 250 \text{ GeV}$ with G_F being the Fermi coupling constant. This so-called hierarchy problem is related to the presence of fundamental scalar fields in the theory with quadratic mass divergences and no protective extra symmetry at $\mu = 0$. For fermion masses, first, the divergences are logarithmic and, second, they are forbidden by the $SU(2) \otimes U(1)$ gauge symmetry plus the fact that at $m = 0$ an additional symmetry, i.e. chiral symmetry, is restored. Here, when talking of divergences, we are not worried of actual infinities. The theory is renormalisable and finite once the dependence on the cut off is absorbed in a redefinition of masses and couplings. Rather the hierarchy problem is one of naturalness. We should see the cut off as a parameterization of our ignorance on the new physics that

will modify the theory at large energy scales. Then it is relevant to look at the dependence of physical quantities on the cut off and to demand that no unexplained enormously accurate cancellations arise.

The hierarchy problem can be put in very practical terms: loop corrections to the higgs mass squared are quadratic in Λ . The most pressing problem is from the top loop. With $m_h^2 = m_{bare}^2 + \delta m_h^2$ the top loop gives

$$\delta m_{h|top}^2 \sim \frac{3G_F}{\sqrt{2}\pi^2} m_t^2 \Lambda^2 \sim (0.3\Lambda)^2 \quad (1)$$

If we demand that the correction does not exceed the light Higgs mass indicated by the precision tests, Λ must be close, $\Lambda \sim o(1 \text{ TeV})$. Similar constraints arise from the quadratic Λ dependence of loops with gauge bosons and scalars, which, however, lead to less pressing bounds. So the hierarchy problem demands new physics to be very close (in particular the mechanism that quenches the top loop). Actually, this new physics must be rather special, because it must be very close, yet its effects are not clearly visible (the "LEP Paradox" ³⁾). Examples of proposed classes of solutions for the hierarchy problem are:

Supersymmetry. In the limit of exact boson-fermion symmetry the quadratic divergences of bosons cancel so that only log divergences remain. However, exact SUSY is clearly unrealistic. For approximate SUSY (with soft breaking terms), which is the basis for all practical models, Λ is replaced by the splitting of SUSY multiplets, $\Lambda \sim m_{SUSY} - m_{ord}$. In particular, the top loop is quenched by partial cancellation with s-top exchange.

Technicolor. The Higgs system is a condensate of new fermions. There are no fundamental scalar Higgs sector, hence no quadratic divergences associated to the μ^2 mass in the scalar potential. This mechanism needs a very strong binding force, $\Lambda_{TC} \sim 10^3 \Lambda_{QCD}$. It is difficult to arrange that such nearby strong force is not showing up in precision tests. Hence this class of models has been disfavoured by LEP, although some special class of models have been devised a posteriori, like walking TC, top-color assisted TC etc (for recent reviews, see, for example, ⁵⁾).

Large compactified extra dimensions. The idea is that M_{PL} appears very large, that is gravity seems very weak because we are fooled by hidden extra dimensions so that the real gravity scale is reduced down to $o(1 \text{ TeV})$. This possibility is very exciting in itself and it is really remarkable that, in

some forms, it is compatible with experiment.

”Little Higgs” models. In these models extra symmetries allow $m_h \neq 0$ only at two-loop level, so that Λ can be as large as $o(10 \text{ TeV})$ with the Higgs within present bounds (the top loop is quenched by exchange of heavy vectorlike new charge-2/3 quarks).

We now briefly comment in turn on these possibilities.

SUSY models are the most developed and most widely accepted. Many theorists consider SUSY as established at the Planck scale M_{Pl} . So why not to use it also at low energy to fix the hierarchy problem, if at all possible? It is interesting that viable models exist. The necessary SUSY breaking can be introduced through soft terms that do not spoil the good convergence properties of the theory. Precisely those terms arise from supergravity when it is spontaneously broken in a hidden sector. This is the case of the MSSM ⁶⁾. Of course, minimality is only a simplicity assumption that could possibly be relaxed. For example, adding an additional Higgs singlet S helps in addressing naturalness constraints ⁴⁾. The MSSM is a completely specified, consistent and computable theory which is compatible with all precision electroweak tests. In this most traditional approach SUSY is broken in a hidden sector and the scale of SUSY breaking is very large of order $\Lambda \sim \sqrt{G_F^{-1/2}} M_{Pl}$. But since the hidden sector only communicates with the visible sector through gravitational interactions the splitting of the SUSY multiplets is much smaller, in the TeV energy domain, and the Goldstino is practically decoupled. But alternative mechanisms of SUSY breaking are also being considered. In one alternative scenario ⁷⁾ the (not so much) hidden sector is connected to the visible one by ordinary gauge interactions. As these are much stronger than the gravitational interactions, Λ can be much smaller, as low as 10-100 TeV. It follows that the Goldstino is very light in these models (with mass of order or below 1 eV typically) and is the lightest, stable SUSY particle, but its couplings are observably large. The radiative decay of the lightest neutralino into the Goldstino leads to detectable photons. The signature of photons comes out naturally in this SUSY breaking pattern: with respect to the MSSM, in the gauge mediated model there are typically more photons and less missing energy. The main appeal of gauge mediated models is a better protection against flavour changing neutral currents but naturality problems tend to increase. As another possibility it has been pointed out that there are pure gravity contributions to

soft masses that arise from gravity theory anomalies ⁸⁾. In the assumption that these terms are dominant the associated spectrum and phenomenology have been studied. In this case gaugino masses are proportional to gauge coupling beta functions, so that the gluino is much heavier than the electroweak gauginos, and the wino is most often the lightest SUSY particle.

What is really unique to SUSY with respect to all other extensions of the SM listed above is that the MSSM or similar models are well defined and computable up to M_{Pl} and, moreover, are not only compatible but actually quantitatively supported by coupling unification and GUT's. At present the most direct phenomenological evidence in favour of supersymmetry is obtained from the unification of couplings in GUTs. Precise LEP data on $\alpha_s(m_Z)$ and $\sin^2 \theta_W$ show that standard one-scale GUTs fail in predicting $\sin^2 \theta_W$ given $\alpha_s(m_Z)$ (and $\alpha(m_Z)$) while SUSY GUTs are in agreement with the present, very precise, experimental results. If one starts from the known values of $\sin^2 \theta_W$ and $\alpha(m_Z)$, one finds ¹¹⁾ for $\alpha_s(m_Z)$ the results: $\alpha_s(m_Z) = 0.073 \pm 0.002$ for Standard GUTs and $\alpha_s(m_Z) = 0.129 \pm 0.010$ for SUSY GUTs to be compared with the world average experimental value $\alpha_s(m_Z) = 0.119 \pm 0.003$. Another great asset of SUSY GUT's is that proton decay is much slowed down with respect to the non SUSY case. First, the unification mass $M_{GUT} \sim \text{few } 10^{16} \text{ GeV}$, in typical SUSY GUT's, is about 20-30 times larger than for ordinary GUT's. This makes p decay via gauge boson exchange negligible and the main decay amplitude arises from dim-5 operators with higgsino exchange, leading to a rate close but still compatible with existing bounds (see, for example, ⁹⁾). It is also important that SUSY provides an excellent dark matter candidate, the neutralino. We finally recall that the range of neutrino masses as indicated by oscillation experiments, when interpreted in the see-saw mechanism, point to M_{GUT} and give additional support to GUTs ¹⁰⁾.

In spite of all these virtues it is true that the lack of SUSY signals at LEP and the lower limit on m_H pose problems for the MSSM. The lightest Higgs particle is predicted in the MSSM to be below $m_h \lesssim 135 \text{ GeV}$ (the recent increase of m_t helps in this respect). The limit on the SM Higgs $m_H \gtrsim 114 \text{ GeV}$ considerably restricts the available parameter space of the MSSM requiring relatively large $\tan \beta$ ($\tan \beta \gtrsim 2 - 3$: at tree level $m_h^2 = m_Z^2 \cos^2 2\beta$) and rather heavy s-top (the loop corrections increase with $\log \tilde{m}_t^2$). Stringent naturality constraints also follow from imposing that the electroweak symmetry break-

ing occurs at the right place: in SUSY models the breaking is induced by the running of the H_u mass starting from a common scalar mass m_0 at M_{GUT} . The squared Z mass m_Z^2 can be expressed as a linear combination of the SUSY parameters m_0^2 , $m_{1/2}^2$, A_t^2 , μ^2 , ... with known coefficients. Barring cancellations that need fine tuning, the SUSY parameters, hence the SUSY s-partners cannot be too heavy. The LEP limits, in particular the chargino lower bound $m_{\chi^+} \gtrsim 100 \text{ GeV}$, are sufficient to eliminate an important region of the parameter space, depending on the amount of allowed fine tuning. For example, models based on gaugino universality at the GUT scale are discarded unless a fine tuning by at least a factor of 20 is not allowed. Without gaugino universality ¹²⁾ the strongest limit remains on the gluino mass: $m_Z^2 \sim 0.7 m_{gluino}^2 + \dots$ which is still compatible with the present limit $m_{gluino} \gtrsim 200 \text{ GeV}$.

The non discovery of SUSY at LEP has given further impulse to the quest for new ideas on physics beyond the SM. Large extra dimensions ¹³⁾ and "little Higgs" ¹⁴⁾ models are the most interesting new directions in model building. Large extra dimension models propose to solve the hierarchy problem by bringing gravity down from M_{Pl} to $m \sim o(1 \text{ TeV})$ where m is the string scale. Inspired by string theory one assumes that some compactified extra dimensions are sufficiently large and that the SM fields are confined to a 4-dimensional brane immersed in a d-dimensional bulk while gravity, which feels the whole geometry, propagates in the bulk. We know that the Planck mass is large because gravity is weak: in fact $G_N \sim 1/M_{Pl}^2$, where G_N is Newton constant. The idea is that gravity appears so weak because a lot of lines of force escape in extra dimensions. Assume you have $n = d - 4$ extra dimensions with compactification radius R . For large distances, $r \gg R$, the ordinary Newton law applies for gravity: in natural units $F \sim G_N/r^2 \sim 1/(M_{Pl}^2 r^2)$. At short distances, $r \lesssim R$, the flow of lines of force in extra dimensions modifies Gauss law and $F^{-1} \sim m^2(mr)^{d-4}r^2$. By matching the two formulas at $r = R$ one obtains $(M_{Pl}/m)^2 = (Rm)^{d-4}$. For $m \sim 1 \text{ TeV}$ and $n = d - 4$ one finds that $n = 1$ is excluded ($R \sim 10^{15} \text{ cm}$), for $n = 2$ R is at the edge of present bounds $R \sim 1 \text{ mm}$, while for $n = 4, 6$, $R \sim 10^{-9}, 10^{-12} \text{ cm}$. In all these models a generic feature is the occurrence of Kaluza-Klein (KK) modes. Compactified dimensions with periodic boundary conditions, as for quantization in a box, imply a discrete spectrum with momentum $p = n/R$ and mass squared $m^2 = n^2/R^2$. There are many versions of these models. The SM brane can itself

have a thickness r with $r < \sim 10^{-17} \text{ cm}$ or $1/r > \sim 1 \text{ TeV}$, because we know that quarks and leptons are pointlike down to these distances, while for gravity there is no experimental counter-evidence down to $R < \sim 0.1 \text{ mm}$ or $1/R > \sim 10^{-3} \text{ eV}$. In case of a thickness for the SM brane there would be KK recurrences for SM fields, like W_n , Z_n and so on in the TeV region and above. There are models with factorized metric ($ds^2 = \eta_{\mu\nu} dx^\mu dx^\nu + h_{ij}(y) dy^i dy^j$, where y (i,j) denotes the extra dimension coordinates (and indices), or models with warped metric ($ds^2 = e^{-2kR|\phi|} \eta_{\mu\nu} dx^\mu dx^\nu - R^2 \phi^2$ 15). In any case there are the towers of KK recurrences of the graviton. They are gravitationally coupled but there are a lot of them that sizably couple, so that the net result is a modification of cross-sections and the presence of missing energy.

Large extra dimensions provide a very exciting scenario 16). Already it is remarkable that this possibility is compatible with experiment. However, there are a number of criticisms that can be brought up. First, the hierarchy problem is translated in new terms rather than solved. In fact the basic relation $Rm = (M_{Pl}/m)^{2/n}$ shows that Rm , which one would apriori expect to be $0(1)$, is instead ad hoc related to the large ratio M_{Pl}/m . In this respect the Randall-Sundrum variety is more appealing because the hierarchy suppression m_W/M_{Pl} could arise from the warping factor $e^{-2kR|\phi|}$, with not too large values of kR . Also it is not clear how extra dimensions can by themselves solve the LEP paradox (the large top loop corrections should be controlled by the opening of the new dimensions and the onset of gravity): since m_H is light $\Lambda \sim 1/R$ must be relatively close. But precision tests put very strong limits on Λ . In fact in typical models of this class there is no mechanism to sufficiently quench the corrections. No simple, realistic model has yet emerged as a benchmark. But it is attractive to imagine that large extra dimensions could be a part of the truth, perhaps coupled with some additional symmetry or even SUSY.

In the extra dimension general context an interesting direction of development is the study of symmetry breaking by orbifolding and/or boundary conditions. These are models where a larger gauge symmetry (with or without SUSY) holds in the bulk. The symmetry is reduced in the 4 dimensional brane, where the physics that we observe is located, as an effect of symmetry breaking induced geometrically by suitable boundary conditions. There are models where SUSY, valid in $n > 4$ dimensions is broken by boundary conditions 17), in particular the model of ref. 18), where the mass of the Higgs is computable

and can be estimated with good accuracy. Then there are "Higgsless models" where it is the SM electroweak gauge symmetry which is broken at the boundaries¹⁹⁾. Or models where the Higgs is the 5th component of a gauge boson of an extended symmetry valid in $n > 4$ ²⁰⁾. In general all these alternative models for the Higgs mechanism face severe problems and constraints from electroweak precision tests²¹⁾. Some modern versions of technicolour can also be obtained from extra dimensions and the AdS/CFT correspondence²²⁾. At the GUT scale, symmetry breaking by orbifolding can be applied to obtain a reformulation of SUSY GUT's where many problematic features of ordinary GUT's (e.g. a baroque Higgs sector, the doublet-triplet splitting problem, fast proton decay etc) are improved²³⁾,¹⁶⁾.

In "little Higgs" models the symmetry of the SM is extended to a suitable global group G that also contains some gauge enlargement of $SU(2) \otimes U(1)$, for example $G \supset [SU(2) \otimes U(1)]^2 \supset SU(2) \otimes U(1)$. The Higgs particle is a pseudo-Goldstone boson of G that only takes mass at 2-loop level, because two distinct symmetries must be simultaneously broken for it to take mass, which requires the action of two different couplings in the same diagram. Then in the relation between δm_h^2 and Λ^2 there is an additional coupling and an additional loop factor that allow for a bigger separation between the Higgs mass and the cut-off. Typically, in these models one has one or more Higgs doublets at $m_h \sim 0.2 \text{ TeV}$, and a cut-off at $\Lambda \sim 10 \text{ TeV}$. The top loop quadratic cut-off dependence is partially cancelled, in a natural way guaranteed by the symmetries of the model, by a new coloured, charge-2/3, vectorial quark χ of mass around 1 TeV (a fermion not a scalar like the s-top of SUSY models). Certainly these models involve a remarkable level of group theoretic virtuosity. However, in the simplest versions one is faced with problems with precision tests of the SM²⁴⁾. Even with vectorlike new fermions large corrections to the epsilon parameters arise from exchanges of the new gauge bosons W' and Z' (due to lack of custodial $SU(2)$ symmetry). In order to comply with these constraints the cut-off must be pushed towards large energy and the amount of fine tuning needed to keep the Higgs light is still quite large. Probably these bad features can be fixed by some suitable complication of the model (see for example,²⁵⁾). But, in my opinion, the real limit of this approach is that it only offers a postponement of the main problem by a few TeV, paid by a complete loss of predictivity at higher energies. In particular all connections

to GUT's are lost.

Finally, we stress the importance of the dark matter and of the cosmological constant or vacuum energy problem ²⁶⁾. In fact, we know by now ²⁷⁾ that most of the (flat) Universe is not made up of atoms: $\Omega_{tot} \sim 1$, $\Omega_{baryonic} \sim 0.044$, $\Omega_{matter} \sim 0.27$, where Ω is the ratio of the density to the critical density. Most is Dark Matter (DM) and Dark Energy (DE). We also know that most of DM must be cold (non relativistic at freeze-out) and that significant fractions of hot DM are excluded. Neutrinos are hot DM (because they are ultrarelativistic at freeze-out) and indeed are not much cosmo-relevant: $\Omega_\nu \lesssim 0.015$. Identification of DM is a task of enormous importance for both particle physics and cosmology. If really neutralinos are the main component of DM they will be discovered at the LHC and this will be a great service of particle physics to cosmology. Also, these results on cosmological parameters have shown that vacuum energy accounts for about 2/3 of the critical density: $\Omega_\Lambda \sim 0.65$, Translated into familiar units this means for the energy density $\rho_\Lambda \sim (2 \cdot 10^{-3} \text{ eV})^4$ or $(0.1 \text{ mm})^{-4}$. It is really interesting (and not at all understood) that $\rho_\Lambda^{1/4} \sim \Lambda_{EW}^2/M_{Pl}$ (close to the range of neutrino masses). It is well known that in field theory we expect $\rho_\Lambda \sim \Lambda_{cutoff}^4$. If the cut off is set at M_{Pl} or even at $0(1 \text{ TeV})$ there would an enormous mismatch. In exact SUSY $\rho_\Lambda = 0$, but SUSY is broken and in presence of breaking $\rho_\Lambda^{1/4}$ is in general not smaller than the typical SUSY multiplet splitting. Another closely related problem is "why now?": the time evolution of the matter or radiation density is quite rapid, while the density for a cosmological constant term would be flat. If so, then how comes that precisely now the two density sources are comparable? This suggests that the vacuum energy is not a cosmological constant term, but rather the vacuum expectation value of some field (quintessence) and that the "why now?" problem is solved by some dynamical mechanism.

Clearly the cosmological constant problem poses a big question mark on the relevance of naturalness as a relevant criterion also for the hierarchy problem: how we can trust that we need new physics close to the weak scale out of naturalness if we have no idea on the solution of the cosmological constant huge naturalness problem? The common answer is that the hierarchy problem is formulated within a well defined field theory context while the cosmological constant problem makes only sense within a theory of quantum gravity, that there could be modification of gravity at the sub-eV scale, that the vacuum

energy could flow in extra dimensions or in different Universes and so on. At the other extreme is the possibility that naturalness is misleading. Weinberg²⁸⁾ has pointed out that the observed order of magnitude of Λ can be successfully reproduced as the one necessary to allow galaxy formation in the Universe. In a scenario where new Universes are continuously produced we might be living in a very special one (largely fine-tuned) but the only one to allow the development of an observer. One might then argue that the same could in principle be true also for the Higgs sector. Recently it was suggested²⁹⁾ to abandon the no-fine-tuning assumption for the electro-weak theory, but require correct coupling unification, presence of dark matter with weak couplings and a single scale of evolution from the EW to the GUT scale. A "split SUSY" model arises as a solution with a fine-tuned light Higgs and all SUSY particles heavy except for gauginos, higgsinos and neutralinos, protected by chiral symmetry. Or we can have a two-scale non-SUSY GUT with axions as dark matter. In conclusion, it is clear that naturalness can be a good heuristic principle but you cannot prove its necessity.

4 Summary and Conclusion

Supersymmetry remains the standard way beyond the SM. What is unique to SUSY, beyond leading to a set of consistent and completely formulated models, as, for example, the MSSM, is that this theory can potentially work up to the GUT energy scale. In this respect it is the most ambitious model because it describes a computable framework that could be valid all the way up to the vicinity of the Planck mass. The SUSY models are perfectly compatible with GUT's and are actually quantitatively supported by coupling unification and also by what we have recently learned on neutrino masses. All other main ideas for going beyond the SM do not share this synthesis with GUT's. The SUSY way is testable, for example at the LHC, and the issue of its validity will be decided by experiment. It is true that we could have expected the first signals of SUSY already at LEP, based on naturalness arguments applied to the most minimal models (for example, those with gaugino universality at asymptotic scales). The absence of signals has stimulated the development of new ideas like those of large extra dimensions and "little Higgs" models. These ideas are very interesting and provide an important reference for the preparation of LHC experiments. Models along these new ideas are not so completely formulated

and studied as for SUSY and no well defined and realistic baseline has so far emerged. But it is well possible that they might represent at least a part of the truth and it is very important to continue the exploration of new ways beyond the SM.

References

1. The LEP EW Working Group, hep-ex/0212036.
2. G. Altarelli and M. Grunewald, hep-ph/0404165.
3. R. Barbieri and A. Strumia, hep-ph/0007265.
4. H. P. Nilles, M. Srednicki and D. Wyler, *Phys. Lett. B* **120** (1983) 346;
J. P. Derendinger and C. A. Savoy, *Nucl. Phys. B* **237** (1984) 307;
M. Drees, *Int. J. Mod. Phys. A* **4** (1989) 3635;
J. R. Ellis, J. F. Gunion, H. E. Haber, L. Roszkowski and F. Zwirner, *Phys. Rev. D* **39** (1989) 844;
T. Elliott, S. F. King and P. L. White, *Phys. Lett. B* **314** (1993) 56 [hep-ph/9305282]; *Phys. Rev. D* **49** (1994) 2435 [hep-ph/9308309];
U. Ellwanger, M. Rausch de Traubenberg and C. A. Savoy, *Phys. Lett. B* **315** (1993) 331 [hep-ph/9307322];
B. R. Kim, A. Stephan and S. K. Oh, *Phys. Lett. B* **336** (1994) 200.
5. K. Lane, hep-ph/0202255,
R.S. Chivukula, hep-ph/0011264.
6. For a recent introduction see, for example, S. P. Martin, hep-ph/9709356.
7. M. Dine and A. E. Nelson, *Phys. Rev. D* **48** (1993) 1277;
M. Dine, A. E. Nelson and Y. Shirman, *Phys. Rev. D* **51** (1995) 1362;
G.F. Giudice and R. Rattazzi, *Phys. Rept.* **322** (1999) 419.
8. L. Randall and R. Sundrum, *Nucl. Phys. B* **557** (1999) 79;
G.F. Giudice et al, *JHEP* **9812** (1998) 027.
9. G. Altarelli, F. Feruglio and I. Masina, *JHEP* 0011:040,2000.
10. For a review see, for example, G. Altarelli and F. Feruglio, hep-ph/0405048.
11. P. Langacker and N. Polonsky, *Phys. Rev. D* **52** (1995) 3081.

12. G. Kane et al, *Phys.Lett.* **B551** (2003) 146.
13. For a review and a list of refs., see, for example, J. Hewett and M. Spiropulu, hep-ph/0205196.
14. For a review and a list of refs., see, for example, M. Schmaltz, hep-ph/0210415.
15. L. Randall and R. Sundrum, *Phys. Rev. Lett.* **83** (1999) 3370, **83** (1999) 4690.
16. For a review, see F. Feruglio, hep-ph/0401033.
17. I. Antoniadis, C. Munoz and M. Quiros, *Nucl. Phys.* **B397** (1993) 515; A. Pomarol and M. Quiros, *Phys. Lett.* **B438** (1998) 255.
18. R. Barbieri, L. Hall and Y. Nomura, *Nucl. Phys.* **B624** (2002) 63; R.Barbieri, G. Marandella and M. Papucci, hep-ph/0205280, hep-ph/0305044, and refs therein.
19. see for example, C. Csaki et al, hep-ph/0305237 , hep-ph/0308038, hep-ph/0310355; S. Gabriel, S. Nandi and G. Seidl, hep-ph/0406020 and refs therein.
20. see for example, C.A. Scrucca, M. Serone and L. Silvestrini, hep-ph/0304220 and refs therein.
21. R. Barbieri, A. Pomarol and R. Rattazzi, hep-ph/0310285.
22. R. Contino, Y. Nomura and A. Pomarol, *Nucl. Phys.* **B671** (2003) 148 (hep-ph/0306259); K. Agashe, R. Contino and A. Pomarol, hep-ph/0412089.
23. Y. Kawamura, *Progr. Theor. Phys.* **105** (2001) 999.
24. J. L. Hewett, F. J. Petriello, T. G. Rizzo, hep-ph/0211218; C. Csaki et al, hep-ph/0211124, hep-ph/0303236. H-C. Cheng and I. Low, hep-ph/0405243.
25. H-C. Cheng and I. Low, hep-ph/0405243.
26. For orientation, see, for example, M. Turner, astro-ph/0207297.

-
27. The WMAP Collaboration, D. N. Spergel et al, astro-ph/0302209.
 28. S. Weinberg, *Phys. Rev. Lett.* **59** (1987) 2607.
 29. N.Arkani-Hamed and S. Dimopoulos, hep-th/0405159; G. Giudice and A. Romanino, hep-ph/0406088.

Participants

Duccio Abbaneo	CERN Duccio.abbaneo@cern.ch
Cristina Adorisio	Università della Calabria Cristina.adorisio@cern.ch
Guido Altarelli	CERN Guido.altarelli@cern.ch
Mariagrazia Alviggi	Università di Napoli “Federico II” Mariagrazia.alviggi@na.infn.it
Nicola Amapane	INFN Torino Nicola.amapane@to.infn.it
Silvia Amerio	Università and INFN di Trento Silvia.Amerio@tn.infn.it
Azzurra Autieri	Università di Napoli “Federico II” Azzurra.autieri@na.infn.it
Giuseppe Avolio	Università della Calabria Giuseppe.avolio@cern.ch
Giuseppe Bagliesi	INFN Pisa Giuseppe.bagliesi@pi.infn.it
Alessandro Ballestrero	INFN Torino ballestrero@to.infn.it
Lucia Barbone	Università and INFN di Bari Lucia.barbone@ba.infn.it
Luciano Maria Barone	Università di Roma “La Sapienza” Luciano.barone@roma1.infn.it
Franco Bedeschi	INFN Pisa bed@fnal.gov
Massimiliano Bellomo	Università di Pavia Massimiliano.bellomo@pv.infn.it
Leonardo Benucci	INFN Pisa Leonardo.benucci@pi.infn.it
Umberto Berzano	Università di Pavia Umberto.berzano@pv.infn.it
Michela Biglietti	INFN Napoli Michela.biglietti@na.infn.it
Halina Bilokon	INFN LNF Halina.bilokon@lnf.infn.it

Tommaso Boccali	SNS/INFN Pisa Tommaso.boccali@pi.infn.it
Matteo Cacciari	LPTHE UPMC Parigi Matteo.cacciari@cern.ch
Vincenzo Canale	Università di Napoli “Federico II” Vincenzo.canale@na.infn.it
Paolo Capiluppi	Università and INFN Bologna Paolo.capiluppi@bo.infn.it
Mario Caprio	Università di Napoli “Federico II” Mario.caprio@na.infn.it
Gianpaolo Carlino	INFN Napoli Gianpaolo.carlino@na.infn.it
Leonardo Carminati	Università and INFN Milano Leonardo.carminati@mi.infn.it
Rino Castaldi	INFN Pisa Rino.castaldi@pi.infn.it
Andrea Castro	Università di Bologna Andrea.castro@bo.infn.it
Ariella Cattai	CERN Ariella.cattai@cern.ch
Donatella Cavalli	INFN Milano Donatella.cavalli@mi.infn.it
Nicola Cavallo	INFN Napoli Nicola.cavallo@na.infn.it
Fabio Cerutti	INFN LNF Fabio.cerutti@lnf.infn.it
Vitaliano Chiarella	INFN LNF Vitaliano.Chiarella@lnf.infn.it
Gianni Chiefari	Università di Napoli “Federico II” Giovanni.chiefari@na.infn.it
Gabriele Chiodini	INFN Lecce Gabriele.chiodini@le.infn.it
Massimiliano Chiorboli	Università di Catania Massimiliano.chiorboli@ct.infn.it
Anna Cimmino	Università di Napoli Anna.cimmino@na.infn.it

Claudia Ciocca	Università and INFN di Bologna Claudia.ciocca@bo.infn.it
Manuela Cirilli	CERN Manuela.cirilli@cern.ch
Francesco Conventi	Università di Napoli “Federico II” Francesco.conventi@na.infn.it
Davide Costanzo	Lawrence Berkeley Laboratory Davide.costanzo@cern.ch
Giovanni Crosetti	Università della Calabria crosetti@fis.unical.it
Susanna Cucciarelli	CERN Susanna.cucciarelli@cern.ch
Mariarosaria DAlfonso	INFN Pisa Mariarosaria.dalfonso@pi.infn.it
Giancarlo DAmbrosio	INFN Napoli Giancarlo.dambrosio@na.infn.it
Riccardo de Asmundis	INFN Napoli Riccardo.deasmundis@na.infn.it
Nicola De Filippis	Università and INFN di Bari Nicola.defilippis@ba.infn.it
Alberto De Min	Università and INFN di Milano Alberto.demin@mi.infn.it
Mauro De Palma	Università di Bari Mauro.depalma@ba.infn.it
Guido De Zorzi	Università di Roma “La Sapienza” Guido.dezorzi@roma1.infn.it
Vittorio Del Duca	INFN Torino Vittorio.delduca@to.infn.it
Massimo Della Pietra	Università di Napoli “Federico II” Massimo.dellapietra@na.infn.it
Domenico Della Volpe	Università di Napoli “Federico II” Domenico.dellavolpe@na.infn.it
Natale Demaria	INFN Torino Natale.demaria@to.infn.it
Marcella Diemoz	INFN Roma I Marcella.diemoz@roma1.infn.it

Alessandro Di Mattia	INFN Roma I Alessandro.dimattia@roma1.infn.it
Carlo Dionisi	Università di Roma “La Sapienza” Carlo.dionisi@roma1.infn.it
Fabrizio Fabbri	INFN Bologna Fabrizio.fabbri@bo.infn.it
Francesco Fabozzi	INFN Napoli Francesco.fabozzi@na.infn.it
Speranza Falciano	INFN Roma I Speranza.falciano@roma1.infn.it
Pamela Ferrari	CERN Pamela.ferrari@cern.ch
Roberto Ferrari	INFN Pavia Roberto.ferrari@pv.infn.it
Lorenzo Fo	Scuola Normale Superiore Pisa Lorenzo.foa@pi.infn.it
Stefano Frixione	INFN Genova Stefano.frixione@ge.infn.it
Guido Gagliardi	INFN Genova Guido.gagliardi@ge.infn.it
Fabrizio Gasparini	Università di Padova Fabrizio.gasparini@pd.infn.it
Ugo Gasparini	INFN Padova Ugo.gasparini@pd.infn.it
Paolo Gauzzi	Università di Roma “La Sapienza” Paolo.gauzzi@roma1.infn.it
Simone Gennai	INFN e SNS Pisa Simone.gennai@pi.infn.it
Andrea Giammarco	Scuola Normale Superiore Pisa Andrea.giammarco@pi.infn.it
Fabiola Gianotti	CERN Fabiola.gianotti@cern.ch
Edoardo Gorini	Università di Lecce Edoardo.gorini@le.infn.it
Claudio Grandi	INFN Bologna Claudio.grandi@bo.infn.it

Mario Greco	Università Roma III Mario.greco@roma3.infn.it
Paolo Iengo	INFN Napoli Paolo.iengo@na.infn.it
Fabio Iervolino	Università di Napoli “Federico II” Fabio.iervolino@na.infn.it
Vincenzo Izzo	Università di Napoli “Federico II” Vincenzo.izzo@na.infn.it
Stefano La Caprara	Università and INFN di Padova Stefano.lacaprara@pd.infn.it
Laura La Rotonda	Università della Calabria larotonda@fis.unical.it
Francesco La Cava	Università di Roma “La Sapienza” Francesco.lacava@roma1.infn.it
Paolo Lariccia	Università di Perugia Paolo.lariccia@pg.infn.it
Ignazio Lazzizzera	INFN di Trento lazi@tn.infn.it
Franco Ligabue	Scuola Normale Superiore Franco.ligabue@pi.infn.it
Luca Lista	INFN Napoli Luca.lista@na.infn.it
Egidio Longo	Università di Roma “La Sapienza” Egidio.longo@roma1.infn.it
Claudio Luci	Università di Roma “La Sapienza” Claudio.luci@roma1.infn.it
Lamberto Luminari	INFN Roma I Lamberto.luminari@roma1.infn.it
Boris Mangano	Scuola Normale Superiore Pisa Boris.mangano@pi.infn.it
Michelangelo Mangano	CERN Michelangelo.mangano@cern.ch
Stefano Marcellini	INFN Bologna Stefano.marcellini@bo.infn.it
Anna Teresa Meneguzzo	Università di Padova Anna.meneguzzo@unipd.it

Lorenzo Menici	Università di Roma “La Sapienza” Lorenzo.menici@roma1.infn.it
Evelin Meoni	Università della Calabria meoni@fis.unical.it
Paolo Meridiani	Università di Roma “La Sapienza” Paolo.meridiani@roma1.infn.it
Leonardo Merola	Università di Napoli “Federico II” Leonardo.merola@na.infn.it
Agostino Migliaccio	Università di Napoli “Federico II” Agostino.migliaccio@na.infn.it
Ernesto Migliore	Università and INFN di Torino Ernesto.migliore@to.infn.it
Aleandro Nisati	INFN Roma I Aleandro.nisati@roma1.infn.it
Pasquale Noli	Università di Napoli “Federico II” Pasquale.noli@na.infn.it
Maria Margherita Obertino	Università di Torino Margherita.obertino@cern.ch
Marco Paganoni	Università Bicocca and INFN di Milano Marco.paganoni@mib.infn.it
Fabrizio Palla	INFN Pisa Fabrizio.palla@pi.infn.it
Pierluigi Paolucci	INFN Napoli Pierluigi.paolucci@na.infn.it
Riccardo Paramatti	INFN Roma Riccardo.paramatti@roma1.infn.it
Andrea Parenti	Università and INFN di Padova Andrea.parenti@pd.infn.it
Francesca Pastore	INFN Roma I Francesca.pastore@roma1.infn.it
Sergio Patricelli	Università di Napoli “Federico II” Sergio.patricelli@na.infn.it
Andrea Perrotta	INFN Bologna Andrea.perrotta@bo.infn.it
Davide Piccolo	INFN Napoli Davide.piccolo@na.infn.it

Giovanni Polese	Università di Napoli “Federico II” Giovanni.polese@na.infn.it
Giacomo Polesello	CERN Giacomo.polesello@cern.ch
Guy Umberto Poloni	Università di Milano Guy.poloni@mi.infn.it
Antonino Pullia	Università Bicocca and INFN di Milano Antonino.pullia@mib.infn.it
Stefano Ragazzi	Università Bicocca and INFN di Milano Stefano.ragazzi@mib.infn.it
Francesco Ragusa	Università di Milano Francesco.Ragusa@mi.infn.it
Riccardo Ranieri	Università and INFN di Firenze Riccardo.ranieri@fi.infn.it
Marco Rescigno	INFN Roma I Marco.rescigno@roma1.infn.it
Adele Rimoldi	Università di Pavia Adele.rimoldi@pv.infn.it
Andrea Rizzi	Scuola Normale Superiore Pisa Andrea.rizzi@sns.it
Gigi Rolandi	CERN Gigi.rolandi@cern.ch
Lucio Rossi	CERN Lucio.rossi@cern.ch
Matteo Sani	Università and INFN di Firenze Matteo.sani@fi.infn.it
Pietro Santarelli	Università di Napoli “Federico II” Pietro.santorelli@na.infn.it
Francesca Sarri	INFN Pisa Francesca.sarri@pi.infn.it
Carlo Schiavi	Università and INFN di Genova Carlo.schiavi@ge.infn.it
Crisostomo Sciacca	Università di Napoli “Federico II” Crisostomo.sciacca@na.infn.it
Lucia Silvestris	INFN Bari Lucia.silvestris@ba.infn.it
Stefania Spagnolo	Università di Lecce Stefania.spagnolo@le.infn.it

Tommaso Tabarelli de Fatis	Università Bicocca and INFN di Milano defatis@mib.infn.it
Roberto Tenchini	INFN Pisa Roberto.tenchini@pi.infn.it
Guido Tonelli	Università di Pisa Guido.tonelli@pi.infn.it
Ezio Torassa	INFN Padova Ezio.torassa@pd.infn.it
Andrea Ventura	INFN Lecce Andrea.ventura@le.infn.it
Valerio Vercesi	INFN Pavia Valerio.vercesi@pv.infn.it
Ilaria Villella	INFN Napoli Ilaria.villella@na.infn.it
Iacopo Vivarelli	Scuola Normale Superiore Pisa Iacopo.vivarelli@pi.infn.it
Marcel Vos	INFN Pisa Marcel.vos@pi.infn.it
Marco Zanetti	INFN Padova Marco.zanetti@pd.infn.it

FRASCATI PHYSICS SERIES VOLUMES

Volume I

Heavy Quarks at Fixed Target
Eds. S. Bianco and F.L. Fabbri
Frascati, May 31–June 2, 1993
ISBN—88-86409-00-1

Volume II – Special Issue

*Les Rencontres de Physique de la Vallée d'Aoste –
Results and Perspectives in Particle Physics*
Ed. M. Greco
La Thuile, Aosta Valley, March 5–11, 1995
ISBN—88-86409-03-6

Volume III

Heavy Quarks at Fixed Target
Ed. B. Cox
University of Virginia, Charlottesville
October 7–10, 1994, 11
ISBN—88-86409-04-4

Volume IV

Workshop on Physics and Detectors for DAΦNE
Eds. R. Baldini, F. Bossi, G. Capon, G. Pancheri
Frascati, April 4–7, 1995
ISBN—88-86409-05-2

Volume V – Special Issue

*Les Rencontres de Physique de la Vallée d'Aoste –
Results and Perspectives in Particle Physics*
Ed. M. Greco
La Thuile, Aosta Valley, March 3–9, 1996
ISBN—88-86409-07-9

Volume VI

Calorimetry in High Energy Physics
Eds. A. Antonelli, S. Bianco, A. Calcaterra, F.L. Fabbri
Frascati, June 8–14, 1996
ISBN—88-86409-10-9

Volume VII*Heavy Quarks at Fixed Target*

Ed. L. Köpke

Rhinefels Castle, St. Goar, October 3–6, 1996

ISBN—88-86409-11-7

Volume VIII*ADONE a milestone on the particle way*

Ed. V. Valente 1997

ISBN—88-86409-12-5

Volume IX – Special Issue*Les Rencontres de Physique de la Vallée d'Aoste –
Results and Perspectives in Particle Physics*

Ed. M. Greco

La Thuile, Aosta Valley, March 2–8, 1997

ISBN—88-86409-13-3

Volume X*Advanced ICFA Beam Dynamics**Workshop on Beam Dynamics Issue for e^+e^- Factories*

Eds. L. Palumbo, G. Vignola

Frascati, October 20–25, 1997

ISBN—88-86409-14-1

Volume XI*Proceedings of the XVIII International Conference on
Physics in Collision*

Eds. S. Bianco, A. Calcaterra, P. De Simone, F. L. Fabbri

Frascati, June 17–19, 1998

ISBN—88-86409-15-X

Volume XII – Special Issue*Les Rencontres de Physique de la Vallée d'Aoste –
Results and Perspectives in Particle Physics*

Ed. M. Greco

La Thuile, Aosta Valley, March 1–7, 1998

ISBN—88-86409-16-8

Volume XIII

Bruno Touschek and the Birth of the e^+e^-

Ed. G. Isidori

Frascati, 16 November, 1998

ISBN—88-86409-17-6

Volume XIV – Special Issue

Les Rencontres de Physique de la Vallée d'Aoste –

Results and Perspectives in Particle Physics

Ed. M. Greco

La Thuile, Aosta Valley, February 28–March 6, 1999

ISBN—88-86409-18-4

Volume XV

Workshop on Hadron Spectroscopy

Eds. T. Bressani, A. Feliciello, A. Filippi

Frascati, March 8-2 1999

ISBN—88-86409-19-2

Volume XVI

Physics and Detectors for DAΦNE

Eds. S. Bianco, F. Bossi, G. Capon, F.L. Fabbri,

P. Gianotti, G. Isidori, F. Murtas

Frascati, November 16-19, 1999

ISBN—88-86409-21-4

Volume XVII – Special Issue

Les Rencontres de Physique de la Vallée d'Aoste –

Results and Perspectives in Particle Physics

Ed. M. Greco

La Thuile, Aosta Valley, February 27-March 4, 2000

ISBN—88-86409-23-0

Volume XVIII

LNF Spring School

Ed. G. Pancheri

Frascati 15-20 May, 2000

ISBN—88-86409-24-9

Volume XIX*XX Physics in Collision*

Ed. G. Barreira

Lisbon June 29–July 1st. 2000

ISBN—88-86409-25-7

Volume XX*Heavy Quarks at Fixed Target*

Eds. I. Bediaga, J. Miranda, A. Reis

Rio de Janeiro, Brasil, October 9–12, 2000

ISBN—88-86409-26-5

Volume XXI*IX International Conference on Calorimetry in**High Energy Physics*

Eds. B. Aubert, J. Colas, P. Nédélec, L. Poggioli

Annecy Le Vieux Cedex, France, October 9–14, 2000

ISBN—88-86409-27-3

Volume XXII – Special Issue*Les Rencontres de Physique de la Vallée d'Aoste –**Results and Perspectives in Particle Physics*

Ed. M. Greco

La Thuile, Aosta Valley, March 4–10, 2001

ISBN—88-86409-28-1

Volume XXIII*XXI Physics in Collision*

Ed. Soo-Bong Kim

Seoul, Korea, June 28–30, 2001

ISBN—88-86409-30-3

Volume XXIV*International School of Space Science – 2001 Course on:**Astroparticle and Gamma-ray Physics in Space*

Eds. A. Morselli, P. Picozza

L'Aquila, Italy, August 30–September 7, 2000

ISBN—88-86409-31-1

Volume XXV

*TRDs for the 3rd Millennium Workshop on
Advanced Transition Radiation Detectors for
Accelerator and Space Applications*

Eds. N. Giglietto, P. Spinelli

Bari, Italy, September 20–23, 2001

ISBN—88-86409-32-X

Volume XXVI

KAON 2001 International Conference on CP Violation

Eds. F. Costantini, G. Isidori, M. Sozzi

Pisa Italy, June 12th 17th, 2001

ISBN—88-86409-33-8

Volume XXVII – Special Issue

*Les Rencontres de Physique de la Vallée d’Aoste –
Results and Perspectives in Particle Physics*

Ed. M. Greco

La Thuile, Aosta Valley, March 3–9, 2002

ISBN—88-86409-34-6

Volume XXVIII

Heavy Quarks at Leptons 2002

Eds. G. Cataldi, F. Grancagnolo, R. Perrino, S. Spagnolo

Vietri sul mare (Italy), May 27th June 1st, 2002

ISBN—88-86409-35-4

Volume XXIX

*Workshop on Radiation Dosimetry: Basic Technologies,
Medical Applications, Environmental Applications*

Ed. A. Zanini

Rome (Italy), February 56, 2002

ISBN—88-86409-36-2

Volume XXIX – Suppl.

*Workshop on Radiation Dosimetry: Basic Technologies,
Medical Applications, Environmental Applications*

Ed. A. Zanini

Rome (Italy), February 56, 2002

ISBN—88-86409-36-2

Volume XXX – Special Issue

*Les Rencontres de Physique de la Vallée d'Aoste –
Results and Perspectives in Particle Physics*

Ed. M. Greco

La Thuile, Aosta Valley, March 9–15, 2003

ISBN—88-86409-39-9

Volume XXXI

*Frontier Science 2002 – Charm, Beauty and CP,
First International Workshop on Frontier Science*

Eds. L. Benussi, R. de Sangro, F.L. Fabbri, P. Valente

Frascati, October 6–11, 2002

ISBN—88-86409-37-0

Volume XXXII

19th International Conference on x-ray and Inner-Shell Processes

Eds. A. Bianconi, A. Marcelli, N.L. Saini

Università di Roma La Sapienza June 24–28, 2002

ISBN—88-86409-39-07

Volume XXXIII

Bruno Touschek Memorial Lectures

Ed. M. Greco, G. Pancheri

Frascati, May 11, 1987

ISBN—88-86409-40-0

Volume XXXIV

*Les Rencontres de Physique de la Vallée d'Aoste –
Results and Perspectives in Particle Physics*

Ed. M. Greco

La Thuile, Aosta Valley, February 29 – March 6, 2004

ISBN—88-86409-42-7

Volume XXXV

Heavy Quarks And Leptons 2004

Ed. A. López

San Juan, Puerto Rico, 1–5 June 2004

ISBN—88-86409-43-5

Volume XXXVI*DAΦNE 2004: Physics At Meson Factories*

Eds. F. Anulli, M. Bertani, G. Capon, C. Curceanu-Petrascu,

F.L. Fabbri, S. Miscetti

Frascati, June 7–11, 2004

ISBN—88-86409-53-2

Volume XXXVII*Frontier Science 2004, Physics and Astrophysics in Space*

Eds. A. Morselli, P. Picozza, M. Ricci

Frascati, 14–19 June, 2004

ISBN—88-86409-52-4

